Protection of Renewable Energy Systems

by

Ali Hooshyar

A thesis
presented to the University of Waterloo
in fulfillment of the
thesis requirement for the degree of
Doctor of Philosophy
in
Electrical and Computer Engineering

Waterloo, Ontario, Canada, 2014

Abstract

The recent progress in renewable energy (RE) technologies has led to the erection of RE power plants (REPPs) up to the order of several hundred megawatts. Unlike their predecessors, which generally appeared in the form of dispersed generation (DG) coupled mainly with distribution systems, such large REPPs are naturally part of high-voltage transmission networks and hold non-negligible proportions of the generation. On the other hand, RE-based DGs are becoming pervasive in modern distribution systems. As a result, the fault ride-through (FRT) requirement has become an essential part of modern grid codes.

This dissertation investigates the challenges brought about by the FRT requirement now affecting protection of systems with which REPPs are integrated. On the transmission level, it explores the performance of distance relays that are installed at an REPP substation and protect the neighboring line. The analyses are founded upon time-domain simulation of detailed REPP models with FRT capability. The studies include squirrel cage induction generator and doubly-fed induction generator (DFIG)-based wind farms, as well as full-scale converter-interfaced REPPs. The exclusive fault behavior of REPPs is scrutinized to identify possible relay maloperations and their root causes. The relay malfunctions revealed by this dissertation are restricted to systems with REPPs, and are not among the known distance relay failures that can occur in conventional power systems. If a communication link with minimal bandwidth requirement is in place, distance relays provide non-delayed fast tripping over the entire length of the line. This feature is retained by devising modified relaying algorithms.

On the distribution level, the dissertation examines the effects of RE-based DGs on directional relays and on fault type classification methods. DFIG-based wind turbines constitute an appreciable portion of today's DG power. Conventional directional elements are shown to be adversely affected when a distribution system incorporates DFIG-based wind DG. An effective method is proposed to identify the fault direction using the waveshape properties of fault signals.

Microgrids are the building blocks of future smart distribution systems. Protective devices of smart and fault-resilient microgrids are not expected to trip the healthy phases during unbalanced short-circuits. Thus, some utilities as well as relay manufacturers have started contemplating single- and double-pole tripping for distribution systems. Selective phase tripping demands fault type classification. This dissertation reveals that existing industrial methods that exploit the phase difference between sequence currents and the magnitudes of phase and sequence currents misidentify the fault type in microgrids that include photovoltaic and/or Type IV wind DGs. Using phase and sequence voltages, two new classifiers are proposed to determine the fault type for not only microgrids with different DGs, but for any three-phase system.

Acknowledgements

During the last three years, I always came out of my Ph.D. advisor's office more inspired, motivated, and confident about my abilities than when I had entered that office. For that, and for his useful guidance throughout my research, I sincerely thank Dr. Ehab El-Saadany.

I am honored that this dissertation has been examined by Dr. Claudio Canizares, Dr. Thomas Ortmeyer, Dr. Magdy Salama, and Dr. Andrea Scott. I owe respect and thanks to them for their time and insight.

Special thanks go to my officemate, soon-to-be Dr. Maher Azzouz, for the fruitful collaborations we had over these years.

I will always be indebted to Ms. Mary McPherson of the writing center who spent her, often personal, time helping me out of sheer benevolence. I hope we will remain in touch, as there is still a lot I have to learn from her.

I have consistently been on the receiving end of my M.Sc. advisor's kind attention, even during my Ph.D. studies, when I was no longer inside his jurisdiction. I am truly grateful to Dr. Majid Sanaye-Pasand for the grand clear vision he offered me on how to complete a research project successfully, and how to present its findings in a scholarly article.

I can hardly ever express my feelings to my parents, whose clear trace of devotion and concern is visible in all of my accomplishments to date. My mother's single mission has been keeping me and my sister successful and happy. This is what her life is all about. If there is one thing I miss in this world, it is her hugs. Skype fails to give me that. Any progress I have made in my education stems from the fact that my father sacrificed countless things, including his own graduate studies, for my and my sister's welfare. The importance of making sure everything is prepared for our success has made him one of the most hardworking people I have seen in my life. I cannot thank my sister, Hooria, enough for those phone calls, which were often short but could make the day for me.

It is really unfair that my Azadeh's name does not appear on the first page of this thesis. Her contribution is by no means smaller than mine. Behind whatever I have achieved in the last ten years lie Azadeh's encouragement, patience and dedication to our marriage. She made the happy-time celebrations unforgettable. When struggling over some difficult moments, the feeling that I had Azi with me and supporting me no matter what, helped me persevere and fight back. For my Ph.D. research, specifically, had it not been for her, this thesis work would have lasted for another three years. She is not only my wife, but also my acting-mother and friend in Canada. Although she is also a student, everything has always been in its place at home, and I have just had to take care of my research. Azadeh, I owe you a massive debt of gratitude that I can never hope to erase.

to
Maman and Baba,
Azadeh,
and Hooria

Table of Contents

List of Tables

List of Figures

List of Abbreviations

ABG	Phase A to Phase B to Ground
AB	Phase A to Phase B
AG	Phase A to Ground
BCG	Phase B to Phase C to Ground
BC	Phase B to Phase C
BG	Phase B to Ground
CAG	Phase C to Phase A to Ground
CA	Phase C to Phase A
CG	Phase C to Ground
CIREPP	Converter-Interfaced Renewable Energy Power Plant
CLES	Conventional Least Error Squares
DD	Disturbance Detector
DFIG	Doubly-Fed Induction Generator
DG	Distributed Generation
EHV	Extra High Voltage

ENTSO–E	European Network of Transmission System Operators for Electricity
EU-GCs	European Grid Codes
FCDFT	Full-Cycle Discrete Fourier Transform
FFT	Fast Fourier Transform
FRT	Fault Ride-Through
GC	Grid Code
HVDC	High Voltage Direct Current
HV	High Voltage
IG	Induction Generator
KVL	Kirchhoff's Voltage Law
LLG	Line to Line to Ground
LL	Line to Line
LPF	Low-Pass Filter
LUT	Look-Up Table
LV	Low Voltage
MLES	Modified Least Error Squares
NA-GCs	North American Grid Codes
PF	Power Factor
PI	Proportional Integral
PLL	Phase-Locked Loop

PMT	Phasor Measurement Techniques
POI	Point Of Interconnection
POTT	Permissive Overreach Transfer Trip
PUTT	Permissive Underreach Transfer Trip
PVDG	Photovoltaic Distributed Generation
REPP	Renewable Energy Power Plant
RE	Renewable Energy
SCIG	Squirrel Cage Induction Generator
SDG	Synchronous Distributed Generation
SG	Synchronous Generator
SLG	Single Line to Ground
TOV	Temporary Overvoltage
VDF	Voltage Dip Flag
VSC	Voltage-Sourced Converter
WF	Wind Farm

Chapter 1

Introduction

1.1 Description of the Problem

Non-hydro renewable energy (RE) sources used to be integrated primarily with distribution systems in the form of distributed generation (DG). These sources constituted an insignificant share of the generation and were inconsequential to the balance of power in the grid. In addition, depending on the RE technology involved, these sources were subject to a variety of transient disturbances that could potentially damage certain components of an RE facility in the event of grid faults. On the other hand, grid connection of the DGs over short-circuit conditions formed non-controlled islands within distribution systems, which led to power quality and public safety issues. As a result, RE sources were always tripped once the voltage at their point of interconnection (POI) dropped following the inception of a fault [1,2].

The past decade, however, has observed major technical developments in the RE industry as well as increased concerns over climate change. Hence, REs are now among the key players in the global supply of energy, and RE power plants (REPPs) up to the order of several hundred megawatts have been erected in many countries. These changes have necessitated new measures to assure stable operation of power systems in the presence of REPPs and to get maximum benefit from existing resources. Consequently, grid codes

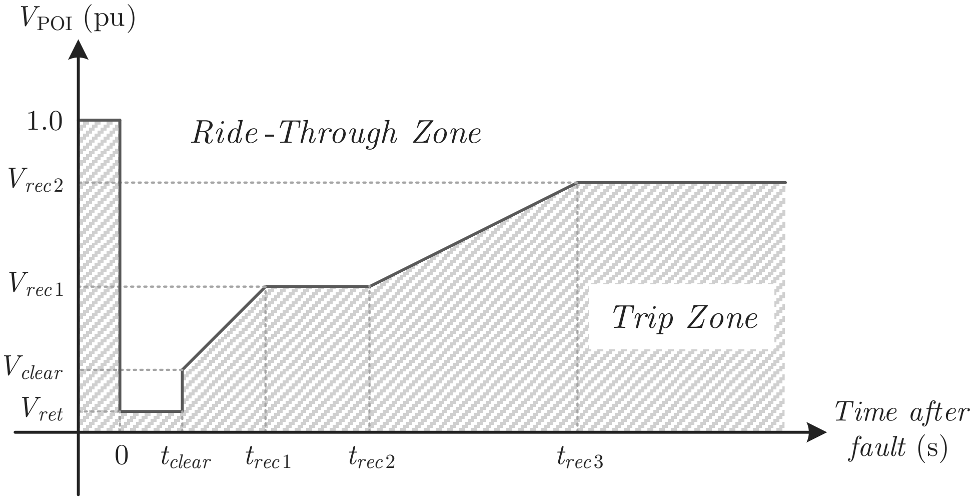

Figure 1.1. FRT curve for REPPs in the European Union.

(GCs) have evolved in recent years putting new constraints on REPPs. With respect to operation during stressed conditions, one major concern of system operators has been concurrent tripping of all REPPs in the vicinity of a short-circuit, which reduces the accessible power substantially and exacerbates the disturbance further. Therefore, the requirement for REPPs to ride through faults was among the early GC changes; doing so facilitates recovery from disturbances by raising the available generation capacity [3].

The fault ride-through (FRT) article of a GC introduces a time-voltage curve that specifies the conditions under which an REPP must remain connected to the grid after a fault is initiated. Although variations exist among different GCs in regard to the specifics of the FRT curve, it normally is a stepwise/linear graph. Take, for instance, the FRT profile of the European union countries, displayed in Figure 1.1 [4]. The time and voltage values in this figure are specified at a national level. An REPP must avoid tripping for the operating points that lie above the curve. This area includes very low, or even for some countries zero, POI voltages within the first ten cycles after the fault inception. The REPP is then allowed to be disconnected from the grid unless the voltage recovers in a linear/stepwise fashion [5].

The FRT requirement has made protection of the systems that incorporate REPPs an avenue of research over the last few years. The challenges faced are twofold.

1.1.1 Protection of REPPs during Faults

The internal components of an REPP undergo a variety of transients during grid faults. The type of the transient and the components that are in danger depend on the RE source, e.g., wind or solar, as well as on the technology involved in the REPP. For instance, as soon as a disturbance causes a voltage drop at the terminal of an induction generator (IG) based wind farm (WF), large overcurrents flow in the IGs' rotor circuits, which may damage the rotor-side converter of a doubly-fed IG (DFIG) [6]. Similar overcurrents are observed during voltage recovery. Various FRT techniques have been proposed to enable REPPs to ride through faults without inflicting any damage on REPP facilities [7–9].

1.1.2 Protection of Systems with REPPs

The DGs' contribution to faults can create several adverse effects on protective relaying of distribution systems. The DGs can cause mis-coordination of overcurrent elements in distribution networks, or may result in bidirectional fault currents for distribution systems in which power flow has traditionally been unidirectional. Some RE-based DGs have also limited short-circuits, to which overcurrent elements are hardly sensitive [10]. Many publications have studied such DG effects on distribution protection and presented creative solutions [11, 12]. Nevertheless, many of the offered remedies include requirements such as communication infrastructure that cannot be readily met in today's distribution systems. In addition, the unique fault properties of some types of RE-based DGs, e.g., DFIG-based wind DGs, have not been fully analyzed in the literature to date. For example, the next chapters of this dissertation will demonstrate that the fault current relation used in [13], which is one of the main studies on the protection of DFIG-equipped distribution systems, is not fully accurate.

On the other hand, the ratings of modern REPPs are increasing rapidly. For example, more than 50 photovoltaic farms rated above 50 MW are currently operating. Furthermore, many large photovoltaic farm projects, some of which are rated up to about 1 GW, have been planned and are under development [14]. Moreover, gigawatt level WF projects are already operational in Europe [15]. Consequently, an ever increasing share of REs, particularly wind and solar, is connected to high-voltage (HV) and extra HV (EHV) transmission grids in several countries [16]. Fault analysis and setting of the protective relays throughout such grids have historically been founded upon the fact that synchronous generators (SGs) energize the system. SGs, however, are either absent or not directly coupled with the grid in REPPs. Hence, REPPs' fault behavior is different from that of conventional power plants. This difference can directly affect the performance of relays, especially the ones in the proximity of REPPs, such as the relays that protect the lines emanating from REPPs.

While the aforementioned FRT challenge and protection of distribution systems have been researched extensively, the negative impacts of REPPs on protective relaying of HV and EHV grids have not received particular attention in the literature. For example, one main study among the few publications on this topic is [17], which proposes new zone characteristics for distance relays of WFs' neighboring lines. Meanwhile, WFs are represented in [17] by voltage sources in the same way that conventional power plants are modeled. Later chapters of this dissertation will prove that such modeling is not precise for relaying purposes and leads to maloperation of protection systems. Another example is [18], which discusses the effect of offshore WFs with HV dc (HVDC) links on distance protection. The phenomena described in [18] can occur in any system, not just systems that include offshore WFs, and has been dealt with by protection engineers for decades. Moreover, this paper studies the operation of only the relays that are located at the remote end of the line connected to an HVDC converter station and does not investigate the relay installed at the converter station. Another drawback is the limitation of the solution proposed in [18] to three-phase short circuits. Besides shortcomings in the literature, even in practical applications, protective relays are currently installed in transmission systems that include REPPs without taking certain distinctive features of the fault behavior of RE sources into account.

1.2 Research Objectives

Protection challenges of RE systems can be approached from two different angles.

1. Altering the control systems of REPPs such that their adverse effects on protection systems are eliminated,
2. Modifying protective relaying schemes so as to accommodate the changes made by REPPs.

The first approach normally leads to fault signals that are not GC-compatible. Moreover, a new control strategy that addresses the effect of an REPP on a specific type of relay in a certain part of the grid may aggravate the response of another relay type in a different part of the grid. For instance, the methods that attempt to reduce the fault current of REPPs, e.g., [19], address the overcurrent relay coordination problems in distribution systems, but violate the GC requirements for short-circuit contribution of REPPs [20, 21]. Additionally, they can result in malfunction of non-overcurrent-based relays deployed in HV and EHV networks. This latter is not a minor drawback, as the manufacturers of power electronic converters used in RE facilities do not design system-specific products, and are not normally aware of the protection system details of the network that a converter is going to be integrated with. That is why, to the best of the author's knowledge, the methods that follow the first approach have not reached a practical level.

As a protective relaying study, the outcome of this research work is intended to assist relay manufacturers in developing relays that operate successfully in systems with REPPs. To reach this goal, the REPPs are modeled according to the existing industrial practices, without requiring any change in their converter or control system details. Thus, the need for communication between relay manufacturers and wind turbine and solar panel manufacturers, which are by and large separate entities, is obviated.

On this basis, the dissertation has been driven by two objectives.

1. To investigate the transmission level challenges, impedance-based distance relays, which are usually utilized as either the primary, or the back-up protection for HV and EHV lines [22], are inspected. The focus is on the performance of distance relays that are installed at an REPP substation and protect the neighboring line. The analyses are founded upon time-domain simulation of detailed practical REPP models with FRT capability. The studies include squirrel cage IG (SCIG) and DFIG-based WFs, as well as

full-scale converter-interfaced WFs and photovoltaic farms. The unique fault properties of REPPs is scrutinized to identify possible relay maloperations and their root causes. The relay malfunctions revealed by this research are restricted to systems with REPPs, and are not among distance relays' imperfections that have been identified in conventional power systems. If a communication link with minimal bandwidth requirement is in place, distance relays provide non-delayed fast tripping over the entire length of the line. The objective is to retain this feature of distance protection by devising modified relaying algorithms.

2. On the distribution level, this study investigates the effect of the exclusive fault behavior of RE-based DGs on the operation of protective relaying systems. Furthermore, the protection of microgrids, as the building blocks of future smart distribution systems, are studied. Protective devices of smart and fault-resilient microgrids are not expected to trip the healthy phases during unbalanced short-circuits. Thus, some utilities as well as relay manufacturers have started contemplating single- and double-pole tripping for distribution systems. Selective phase tripping demands fault type classification. Fault type classification methods in microgrids that incorporate RE-based sources are discussed in detail.

In meeting these objectives, the following constraints are placed on the developed solutions to facilitate their practical implementation.

1. No extra hardware other than the currently available facilities should be required.
2. The solutions should not involve alteration of the existing GCs.

1.3 Dissertation Outline

This dissertation is divided into two main parts: the next three chapters, which concentrate on transmission system protection, and the subsequent two chapters, which focus on distribution system protection. The individual chapters are organized as follows.

Chapter 2 reveals some serious defects of distance protection for the lines connected to IG-based WFs during balanced faults. Detected failures can easily result in unnecessary WF tripping, thus jeopardizing the objectives pursued by the FRT articles of the GCs. In response, a novel pilot scheme along with a fault current classification technique is proposed to address these problems for both types of IG-based WFs, and the accurate non-delayed protection of a distance relay over the entire line length is restored.

Chapter 3 demonstrates that the interactions between full-scale converter-interfaced REPPs (CIREPPs) and distance relays are profoundly and adversely influenced by the CIREPPs' fault properties. A CIREPP model developed for relaying studies highlights the CIREPP characteristics that most endanger the protection system. The scenarios elaborated in this chapter include in-zone short-circuits missed by the relay at the CIREPP substation, and incorrect tripping for out-of-zone faults, which would neutralize FRT schemes. The findings of Chapter 3 also hold true for the ac lines emanating from voltage-sourced converter (VSC)-based HVDC connections.

Chapter 4 begins by explaining why the countermeasures currently deployed by relays to tackle the infeed problems identified in Chapter 3 fail in the presence of a CIREPP. Then, a new formula to calculate impedance which prevents maloperation in the event of line to line to ground (LLG) faults is devised for the relay's phase element. In addition, a communication-assisted method with minimal bandwidth requirement is proposed for balanced and line to line (LL) faults. The issues that should be taken into consideration for single line to ground (SLG) faults are also discussed.

Chapter 5 shows how the fault behavior of DFIG-based wind DGs can result in maloperation of directional overcurrent relays of distribution systems. A fault current classification technique is also suggested to replace the conventional directional element during problematic conditions and provide accurate fault direction quickly based on the current's waveshape properties.

Chapter 6 ascertains that existing industrial fault type classifiers, which operate based on the angles and magnitudes of phase and sequence currents, misidentify the fault type in microgrids that include photovoltaic and Type IV wind DGs. Two new classifiers are developed to determine the fault type for not only microgrids with different DGs, but for any three-phase system. The effects of system imbalance, high-impedance faults and different DG control strategies over disturbances on the proposed classifiers are examined.

Chapter 7 concludes the dissertation, highlights its contributions, and suggests topics for future research.

Chapter 2

Distance Protection of Lines Connected to IG-Based WFs

Although Type IV wind turbine is a rapidly expanding technology, the majority of today's wind energy facilities still incorporate IGs [23]. The SCIG was the dominant technology in early WFs. Despite some drawbacks, SCIGs are cost-effective and continue to constitute a non-negligible share of the currently installed wind capacity [24, 25]. More importantly, DFIGs are widely employed in modern wind energy systems, particularly for the high power level, due to various advantages, e.g., variable speed operation accompanied by reduced converter size [26].

As mentioned in Chapter 1, WFs are increasingly integrated with transmission systems, for which distance relaying is normally the protection of choice. This chapter unveils some major problems with distance protection of the lines connected to IG-based WFs during balanced short-circuits. It is shown that for the SCIG-based WFs, distance protection becomes insecure, while for the DFIG-based WFs, the relay performance is utterly unreliable, due to operating scenarios that are unique to such WFs, and are not addressed in the existing relaying practices. As a result of the incorrect impedances measured by the distance relay at the WF substation, the very objectives sought by the FRT requirement of the new GCs are not met.

A modified permissive overreach transfer trip (POTT) scheme together with a fault current classification technique are devised to address these new problems for both SCIG- and DFIG-based WFs. Similar to a conventional distance relay, non-delayed tripping is obtained over the full length of the line by means of a communication link with minimal bandwidth. A thorough performance evaluation verifies the merits of the suggested method for all possible scenarios. The most likely condition confronted by distance relays is DFIG-based WFs with crowbar resistance, for which the obtained results are particularly promising.

2.1 IG-Based WFs and Distance Relays: Problem Statement

The short-circuit behavior of IGs has been extensively analyzed in several publications [27–29]. This section investigates how this behavior affects a distance relay that is installed at a WF substation and is intended to protect the line that connects the WF to the rest of the grid.

2.1.1 SCIG-Based WFs

The general relation for an SCIG balanced fault current consists of a decaying dc and a decaying ac component, expressed by (2.1) [29].

$$i_f(t) = \frac{V_{\mathrm{m}}}{1-s}\left(\left(\frac{1}{X'} - \frac{1}{X_{\sigma s} + 1.5X_{ms}}\right) e^{-t/T'} \cos\left((1-s)\,\omega_1 t + \theta\right) + \frac{1}{X'}\, e^{-t/T_a} \cos(\theta)\right) \tag{2.1}$$

For simplicity and without loss of generality for the purpose of this study, a single cage SCIG is considered. V_{m} is the voltage amplitude, ω_1 is the fundamental angular frequency, s is the IG slip, X' is the motor transient reactance, $X_{\sigma s}$ and X_{ms} are the leakage and magnetizing reactances of the stator winding, T' is the short-circuit transient time constant, which is inversely proportional to the rotor resistance, T_a is the stator time constant, and θ is the fault inception angle.

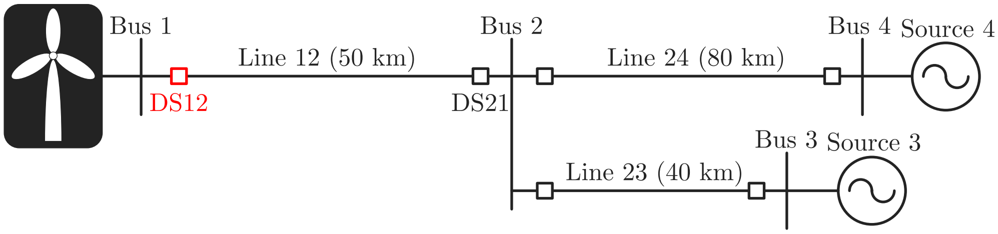

Figure 2.1. Single line diagram of the test power system with IG-based WF.

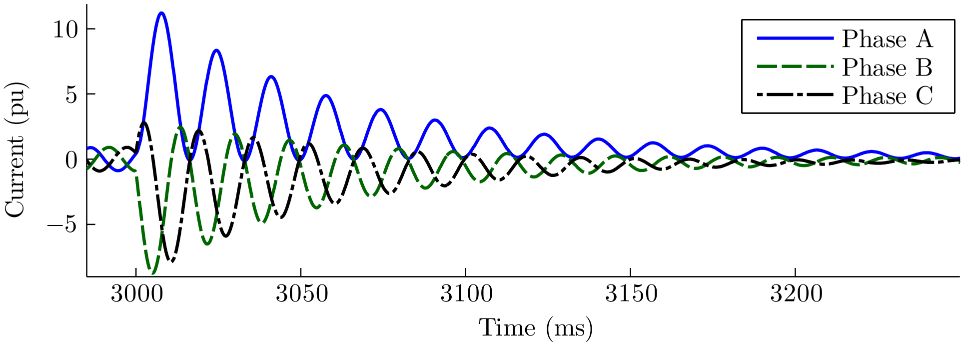

Figure 2.2. Typical current of a single SCIG for a balanced grid fault.

Figure 2.1 shows the test system, which is simulated using PSCAD/EMTDC program. The system details are presented in Appendix A. Figure 2.2 displays the current at the terminal of one of the SCIGs in the test system. A balanced short-circuit occurs at $t = 3$ s with a fault resistance, R_f, of 1 Ω. The post-fault period in Figure 2.2 consists of the following three stages.

1. Immediately after the onset of the fault, based on the constant flux linkage theorem [30], the SCIG can be represented by a voltage source in series with an impedance [31]. During this initial short interval, the current rises appreciably.
2. Afterward, the decrease in the SCIG air-gap flux, caused by the voltage drop at the machine terminal, reduces the fault current. The decrease in the fault current is for both the ac and the dc components.
3. The current described by (2.1) is derived based on the assumption that the fault causes exactly zero voltage at the SCIG terminal and leads to its complete demagnetization.

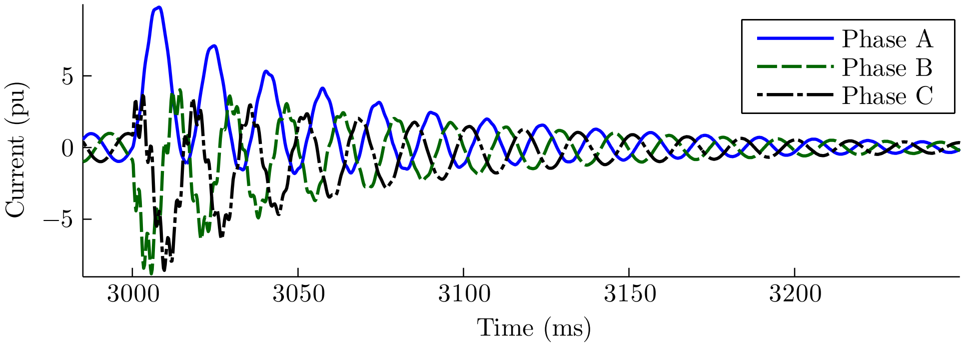

Figure 2.3. Fault current of the SCIG-based WF for a balanced fault on line 24.

As a result, the current finally reaches zero. In practice, overhead line faults typically include some levels of fault resistance, which cause nonzero fault voltage, and hence the SCIG does not fully demagnetize. Thus, the current of Figure 2.2 does not fall to zero in the third stage due to the fault resistance, and the SCIG eventually sustains a fairly small fault current.

Let us analyze how the above sequence of stages in the fault current is reflected in the impedance plane and affects the performance of a distance relay located at the WF substation. Figure 2.3 displays the fault current flowing out from bus 1 of the system in Figure 2.1 when bus 1 is connected to the SCIG-based WF. The fault location is on line 24 next to bus 2, and the fault instant is $t = 3$ s. The high-frequency content of phases B and C currents is caused by resonance between the line inductance and the power factor (PF) correction capacitor required for SCIGs.

DS12 is the distance relay that is located at bus 1 and protects line 12 of the system. A quadrilateral characteristic is used for DS12. Meanwhile, the findings of this study are applicable to other distance relay characteristics, such as mho, as well. Also, the results of this study are independent of the relay polarization type. Therefore, for the sake of simplicity, DS12 is self-polarized. The currents and voltages are sampled at 3840 Hz. DS12 measures the voltage phasor using full-cycle discrete Fourier transform (FCDFT) digital filters. The current phasor is obtained by means of the conventional least error squares (CLES) based digital filters discussed in [32], which utilize Taylor series expansion to suppress the decaying dc offset of fault current.

For the above-mentioned fault, line 24 must be tripped instantaneously, and the remainder of the system, i.e., the area including the WF, bus 2, and source 3, can continue to operate faultlessly. The fault lies in zone two of DS12, and so, DS12 must trip as the backup relay if the fault persists for more than a delay time, typically of around 200 ~ 300 ms. The resistance and reactance measured by the phase A to ground (AG) element of DS12 are plotted with respect to time in Figure 2.4(a). It is observed that, unlike distance relay measurements for conventional systems, the resistance and reactance calculated for this case are not constant after the fault and exhibit significant variations.

The above fluctuations are directly reflected in the impedance plane of the relay in Figure 2.4(b). Once the fault happens, the impedance correctly moves from the load region to zone two of DS12; however, after the considerable decline in the ac component of the fault current, the measured impedance moves away from zone two. As shown in Figure 2.5, soon after the initial post-fault transients disappear, the SCIG-based WF acts as a source that produces active power, but absorbs reactive power. The base power in Figure 2.5 is 1 MVA. Active power generation is due to the incomplete demagnetization of the SCIGs. Reactive power, however, is absorbed since the reactive power generated by the PF correction capacitors decreases because of the voltage drop after the fault. Active power generation and reactive power consumption by the WF explain why the impedance eventually lies in the fourth quadrant of Figure 2.4(b).

Figure 2.4(c), which zooms in on the impedance plane around zones one and two of DS12, depicts that the impedance stays at zone two only for a limited time after the fault. In its way toward the fourth quadrant, the impedance enters zone one at $t = 3.123$ s, resulting in instantaneous false tripping of line 12 before the 200 ~ 300 ms delay time of zone two is passed. Even if the measured impedance does not enter zone one in its transient path toward the fourth quadrant, still DS12 does not operate correctly, as it fails to perform the backup operation for a fault at the beginning of the next line since the impedance leaves zone two quickly. As a result, except for the very short interval after the fault, a distance relay installed at an SCIG-based WF substation exhibits a totally inaccurate performance, which includes incorrect disconnection of the WF from the grid and/or failure to provide the backup functionalities. Similar observations are made for the other five elements of DS12, as well.

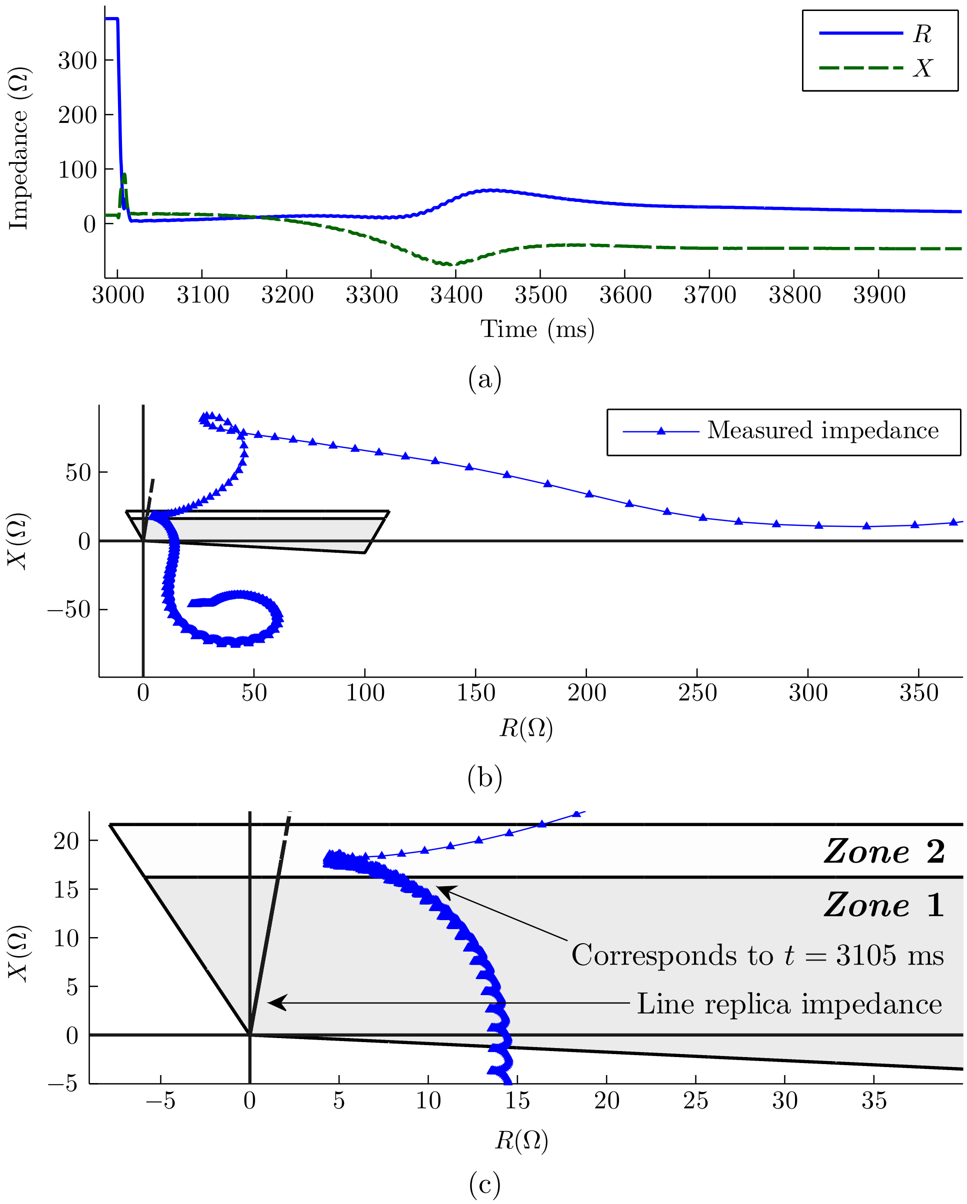

(a)

(b)

(c)

Figure 2.4. Performance of the AG element of DS12 for SCIG-based WF after the fault of Figure 2.3, (a) Time variations of the measured R and X, (b) Operating point in the impedance plane, (c) Magnified view of the impedance trajectory.

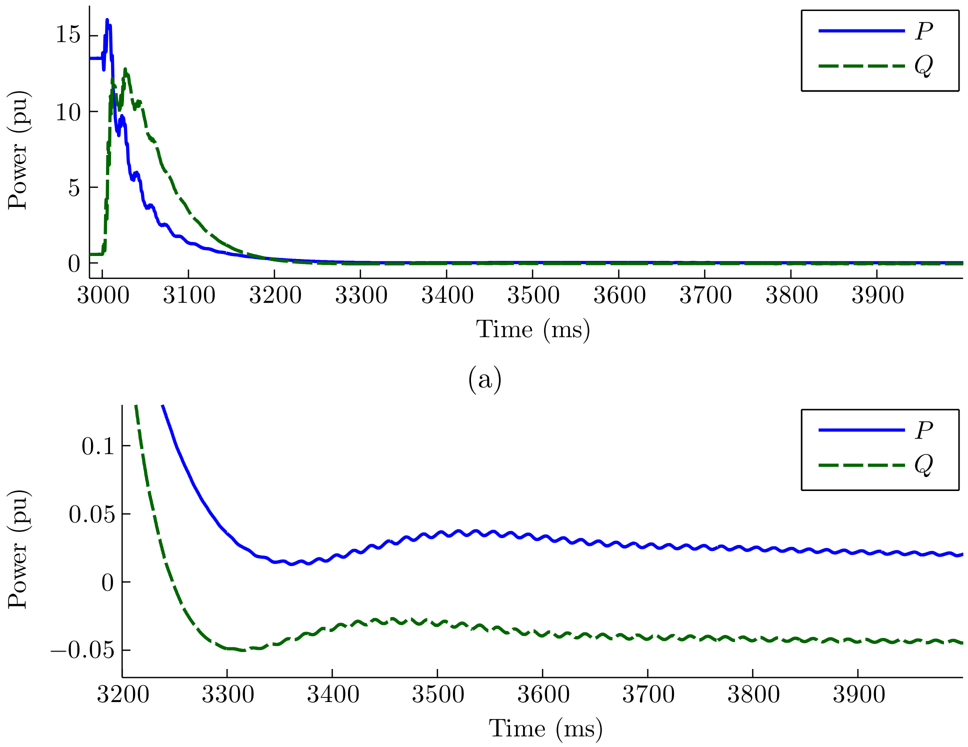

(a)

(b)

Figure 2.5. Power at the WF terminal after the fault of Figure 2.3, (a) Wide view, (b) Magnified view.

2.1.2 DFIG-Based WFs

Although a variety of FRT techniques have been proposed for DFIGs in the literature, these generators are, in practice, almost always equipped with crowbar circuits by the manufacturers to protect the converters during severe voltage drops [33, 34]. A balanced fault on the line connected to the WF is among the most severe faults and results in crowbar activation. Once the crowbar is activated, the short-circuit behavior of a DFIG is conceptually the same as that of an SCIG [33]. Nonetheless, some parameters of the fault current can be quite different in the case of a DFIG, the most important of which, from the distance relaying perspective, is the machine slip. The slip of an SCIG is very small, so the $(1 - s)$ factor in (2.1), which appears in the frequency of the ac component, can be neglected. In contrast, the slip of a DFIG changes in a range of ±30%, commensurate with wind speed. Thus, $(1-s)$ would no longer be a negligible term and causes a range of $42\sim78$ Hz for DFIG fault currents in 60 Hz systems. As will be demonstrated in the following, the effect of off-nominal frequency of a DFIG fault current proves fatal to distance protection. A distance relay operates based on the fundamental frequency voltage and current phasors. For example, the phase B ground (BG) element of a distance relay computes the impedance by

$$Z_{BG} = \frac{V_B}{I_B + K^{\circ} I^{\circ}} \tag{2.2}$$

where V_B and I_B are the fundamental frequency phasors for phase B voltage and current, K° is the zero-sequence compensation factor, and I° is the zero sequence current. Protective relays are actually equipped with frequency tracking techniques, as in [35], to adaptively modify their digital filters in the event of frequency excursion conditions and compute the voltage and current phasors accurately. During frequency excursions, both voltage and current frequency exhibit the same deviation from the nominal frequency. Hence, impedance measurement relations, such as (2.2), still offer a true measure of the distance to the fault location.

Conversely, in the case of DFIG-based WFs during balanced faults, only the current frequency significantly deviates from the nominal frequency. The voltage frequency is dictated by the bulk grid and remains within a narrow margin of 60 Hz. Moreover, modern commercial distance relays employ complete or partial memory polarization. The frequency of the pre-fault memorized voltage is closely tied with the nominal frequency.

Fairly different voltage and current frequencies make balanced short-circuit behavior of DFIG-based WFs a unique operating condition, which is an unfamiliar situation from the protective relaying perspective. For such conditions, (2.2) and other relations for impedance calculation do not hold true anymore, since these formulas are founded upon manipulating phasor quantities that correspond to the same frequency.

To validate the above analysis, the SCIG-based WF in the system discussed in Section 2.1.1 is replaced by the DFIG-based WF detailed in Appendix A. Again, a balanced fault is placed on line 24 next to bus 2 at $t=3$ s, and the performance of DS12 is analyzed. At this stage, the crowbar resistance is kept at zero. The effect of nonzero crowbar resistances is studied later on. Figure 2.6 shows the phase B fault current contribution of the DFIG-based

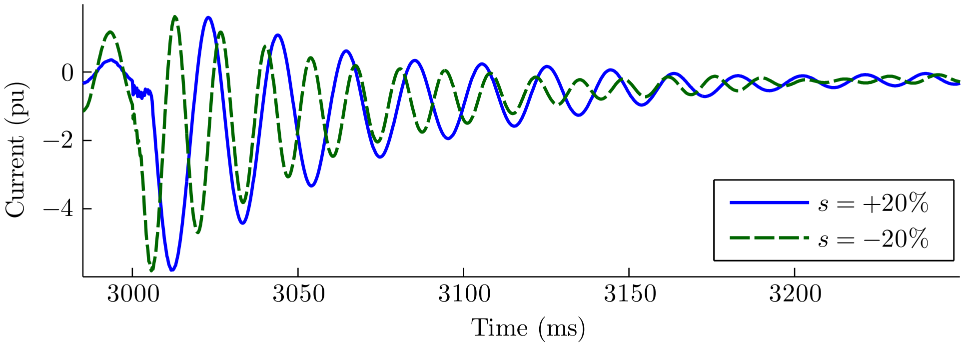

Figure 2.6. Phase B fault current of DFIG-based WF after a fault on line 24.

WF for a sub-synchronous and a super-synchronous rotor speed, which result in positive and negative slips, respectively. This figure illustrates the direct relationship between the fault current frequency and the rotor speed. To present a quantitative analysis of the frequencies, the normalized spectrum for the currents and voltages of the faults of Figure 2.6 is displayed in Figure 2.7. The spectrums are obtained by applying fast Fourier transform (FFT) to the first 300 ms of the fault signals. In the case of the sub-synchronous speed, the main peak of the current spectrum in Figure 2.7(a) is around 50 Hz, whereas the main peak of the voltage spectrum is at 60 Hz. For the super-synchronous case, however, the current spectrum is centered around 73 Hz in Figure 2.7(b), while the main peak of the voltage spectrum is again at 60 Hz. The nonzero values of the current spectra in Figure 2.7 for frequencies other than 50 and 73 Hz originate from the exponential terms in the current relation.

For a synchronous rotor speed, DS12 performance for a DFIG-based WF is similar to that for an SCIG. To investigate DS12 operation for sub- and super-synchronous speed conditions, two different frequency tracking approaches are tested.

1. The common frequency tracking practice of modern digital relays is to calculate the voltage frequency. The obtained frequency is used to update all of the relay subroutines, including the digital filters that measure the current phasor [36, 37]. Figure 2.8 depicts the time variations of the resistance and reactance measured by the BG element of DS12 using this method for the sub- and super-synchronous cases of Figure 2.6. The resultant impedances, shown in the characteristic plane of DS12 in Figure 2.9, exhibit

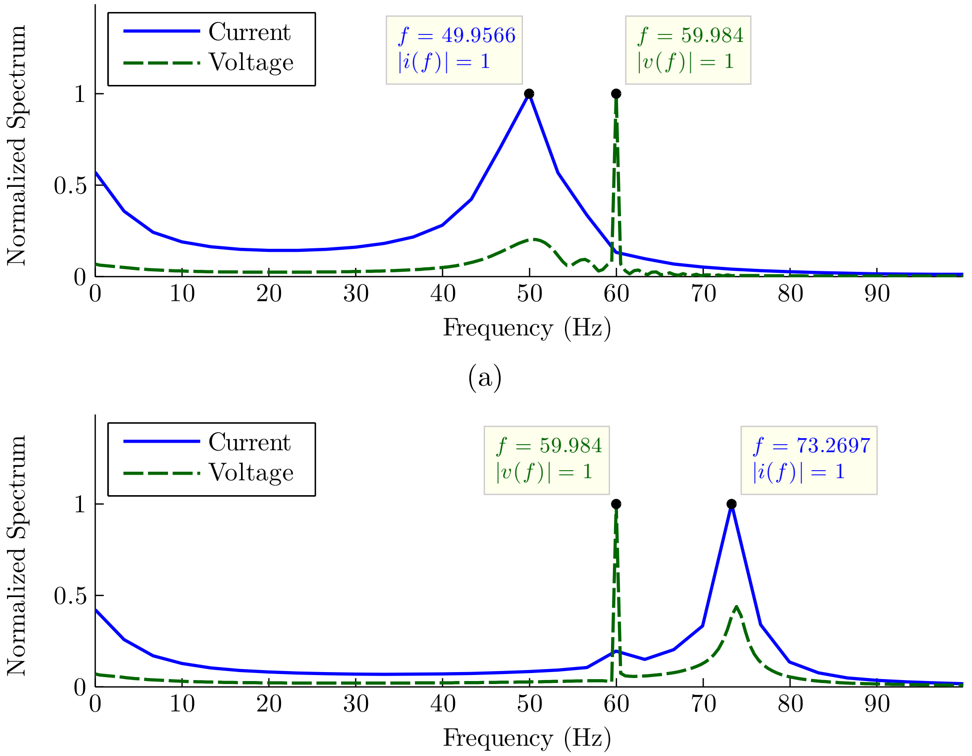

(a)

(b)

Figure 2.7. Current and voltage spectra for the faults shown in Figure 2.6, (a) $s = +20\%$, (b) $s = -20\%$.

chaotic and completely unreliable trajectories after the fault, because the digital filters that compute the current phasor are based on the voltage's 60 Hz frequency, while the actual current frequencies are substantially different. For Figures 2.9(a) and (b), the impedance spuriously enters the first zone 44 ms and 18.5 ms after the fault, respectively, and causes incorrect disconnection of line 12 and the WF from the system.

2. In the second approach, the voltage and current frequencies are found separately, and the corresponding digital filters are updated accordingly. This approach provides correct phasors for both voltage and current. However, as discussed earlier and shown in Figure 2.10, since the voltage and current phasors correspond to different frequencies, the BG element of DS12 again fails to measure the correct impedance to the fault. For Figures 2.10(a) and (b), the impedance enters zone one 54.7 ms and 17 ms after the fault,

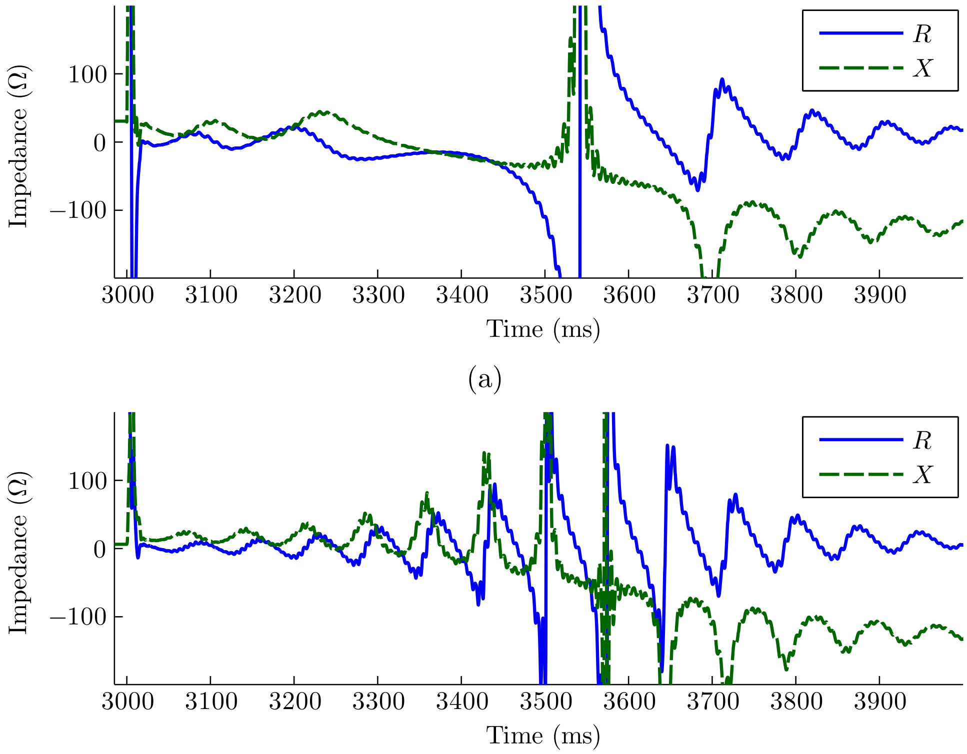

(a)

(b)

Figure 2.8. Time variation of the impedance of DS12 for DFIG-based WF during the faults of Figure 2.6 using the first frequency tracking approach, (a) $s = +20\%$, (b) $s = -20\%$.

respectively, leading to unnecessary disconnection of line 12 and the WF.

It should be noted that, unlike the DS12 performance for SCIG-based WFs, the impedance measured by DS12 is not correct even for the very short interval immediately after the fault. Furthermore, the discussed problem obviously applies to all six elements of DS12.

2.2 Proposed Solution

This section devises a solution for protecting the lines connected to IG-based WFs. The objective is to address the previously-discussed problems while maintaining distance relays' fast non-delayed protection over the entire line length. First, the layout of a new modi-

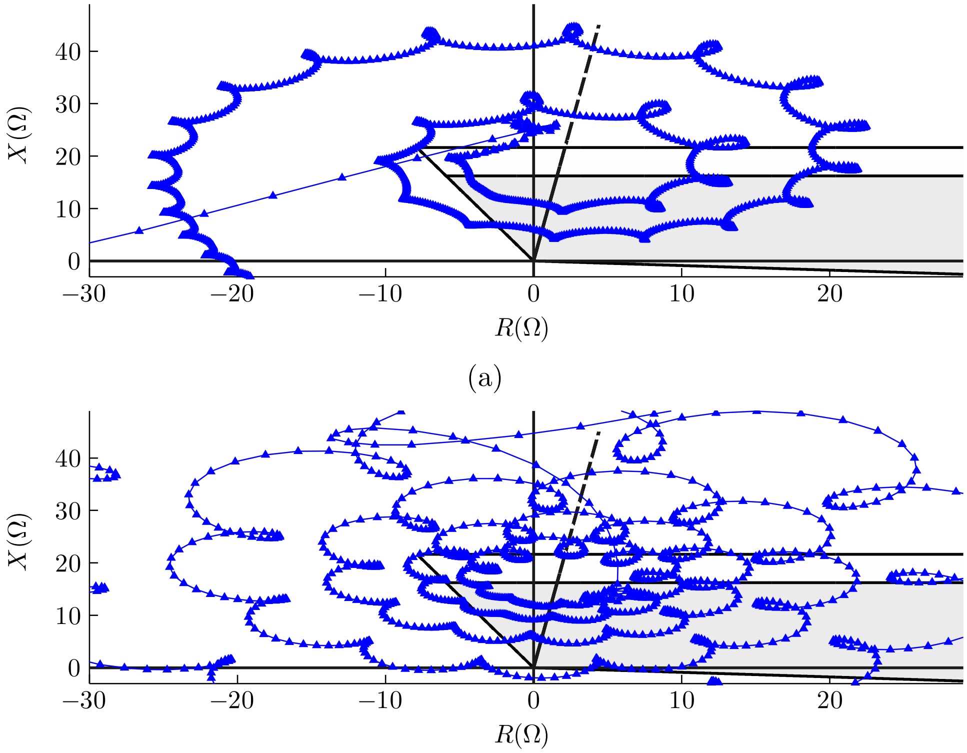

(a)

(b)

Figure 2.9. Performance of DS12 for DFIG-based WF during the faults of Figure 2.6 using the first frequency tracking approach, (a) $s = +20\%$, (b) $s = -20\%$.

fied POTT scheme is outlined. Then, the details of a proposed fault current classification technique used by the modified POTT scheme are discussed.

2.2.1 Modified POTT Scheme

A distance relay is not able to provide non-delayed tripping over 100% of the line length unless it is linked with the relay on the other end of the line through a communication link. The key feature of this channel that distinguishes distance relays as a preferred choice for HV grids is its very low bandwidth requirement. A variety of pilot schemes are already deployed to reach fast and selective distance relaying. Among them, POTT is a relatively simple, yet competent one, and is widely practiced in industrial applications [38].

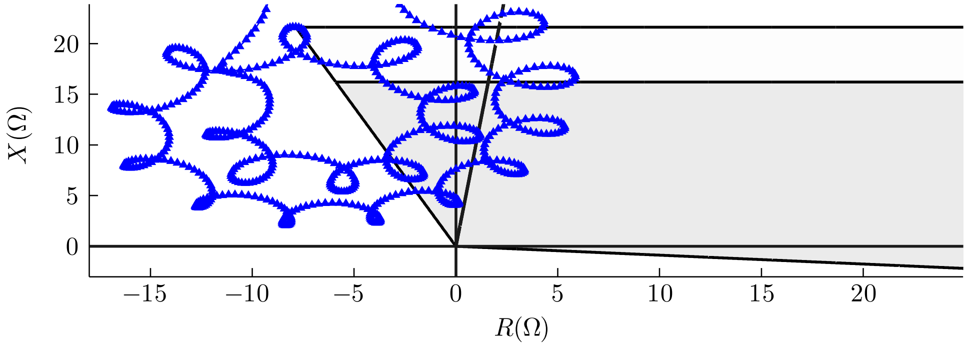

(a)

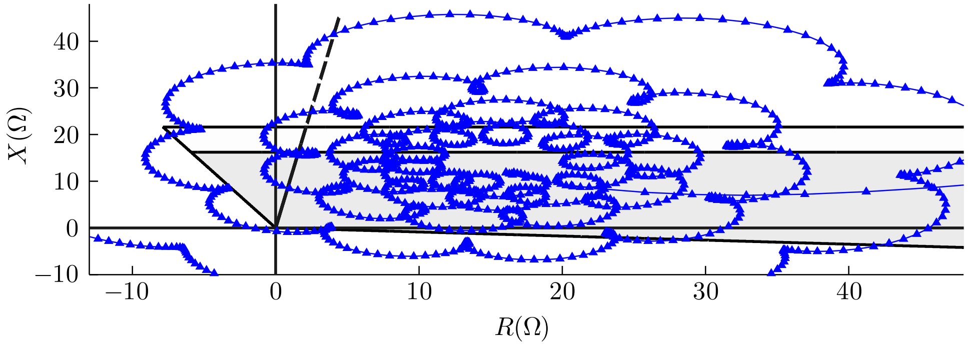

(b)

Figure 2.10. Performance of DS12 for DFIG-based WF during the faults of Figure 2.6 using the second frequency tracking approach, (a) $s = +20\%$, (b) $s = -20\%$.

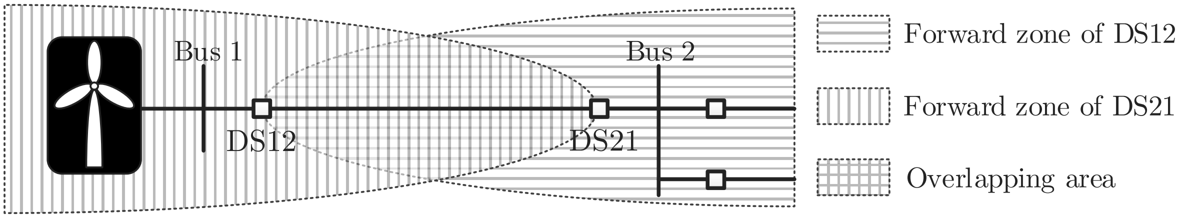

Figure 2.11. POTT scheme operation principle.

Figure 2.11 illustrates an overview of the conventional POTT logic for line 12 of the test system. DS21 is the distance relay located next to bus 2 and protects line 12. If the impedance measured by DS21 falls within the reach of its directional over-reaching zone, there is a fault either on line 12, or on bus 1, or inside the WF. The setting of this over-reaching zone is about 150% of the line length. On the other hand, if the impedance measured by DS12 drops below its directional over-reaching zone setting, there exists a fault on either line 12, or on bus 2, or on the lines connected to the right of bus 2. The only overlap between the DS12 and DS21 zones is line 12. As a result, once DS21 detects a fault within its over-reaching zone, it sends a trip signal to DS12. DS12 trips line 12 if a trip signal sent by DS21 is accompanied by the detection of a fault within its own over-reaching zone. DS21 also operates based on the same logic. The communication channel over which the data is exchanged requires minimal bandwidth, since each relay transmits only a trip/no-trip signal.

The conventional POTT scheme fails to operate accurately for the lines connected to IG-based WFs during balanced short-circuits, due to incorrect impedances measured by the relays. A modified POTT scheme is developed to tackle this problem. For this modified POTT scheme, the relays at the two line extremities detect fault direction, not based on the measured impedance, but according to the fault current waveshape attributes. As will be demonstrated later on, the waveshapes of balanced fault currents of IG-based WFs possess distinctive features, which can be utilized to distinguish them from fault currents of bulk HV power systems that the WFs are integrated with. Also, the instantaneous tripping signal of DS21 is blocked if the fault current features the short-circuit behavior of IGs.

Figure 2.12 illustrates the decision making process of DS12 according to the modified POTT scheme. This scheme is triggered by a disturbance detector (DD) unit similar to the ones developed in [39, 40], which detects the occurrence of a disturbance promptly using a few current samples. Then, a fault type classifier that compares the negative and zero sequence components of voltage and current with a suitable threshold, e.g., 0.1 pu, determines whether the fault is balanced. The modified POTT scheme is then implemented. If the later-discussed fault current classification technique identifies the current to be generated by the IG-based WF, the fault lies in the forward direction of DS12, and it transmits a trip signal to DS21. In addition, if such condition is accompanied by the receipt of a trip signal from DS21, then DS12 trips the line. Also, DS21 issues a trip command if the receipt of a trip signal from DS12 is simultaneous with the detection of a forward fault. As a result, non-delayed tripping is obtained over the full length of the line. It is to be noted that both relays send only a trip/no-trip signal.

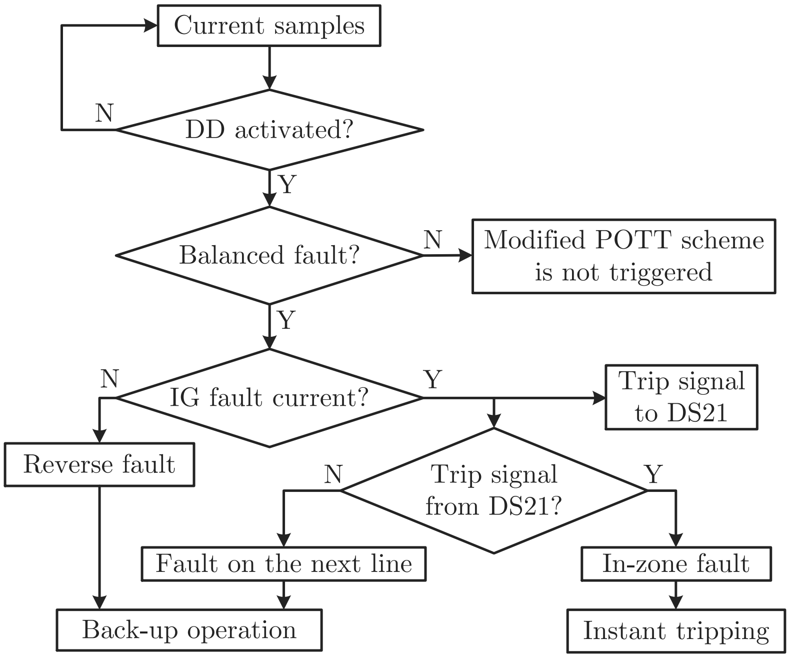

Figure 2.12. Flowchart of the proposed approach for DS12 operation.

2.2.2 Fault Current Classification

As suggested by the fault currents depicted in Figures 2.2, 2.3 and 2.6, the ac components of IG balanced fault currents exhibit a fast decaying nature. This rapid decline leads to a marked contrast between the initial peak-to-peak values of the current. The relative percentage difference between the first two peak-to-peak values of the fault current for each phase is defined by

$$\delta_{1\phi} = \frac{PtP_1 - PtP_2}{PtP_2} \times 100 \tag{2.3}$$

in which PtP_1 and PtP_2 are the first and the second peak-to-peak values of the fault current, respectively. The SCIG fault current of Figure 2.2 in phase A has been redrawn in Figure 2.13(a). It is shown that PtP_1 and PtP_2 are 11.27 pu and 8.47 pu, respectively, which yields $\delta_{1\phi} = 33.03\%$. Also, $\delta_{1\phi}$ for phases B and C of the fault current, shown in Figure 2.2 is 32.94% and 33.51%, respectively. The sum of $\delta_{1\phi}$ for all three phases is denoted by $\delta_{3\phi}$, and equals 99.48% for this SCIG fault current. Section 2.3.1 will demonstrate that

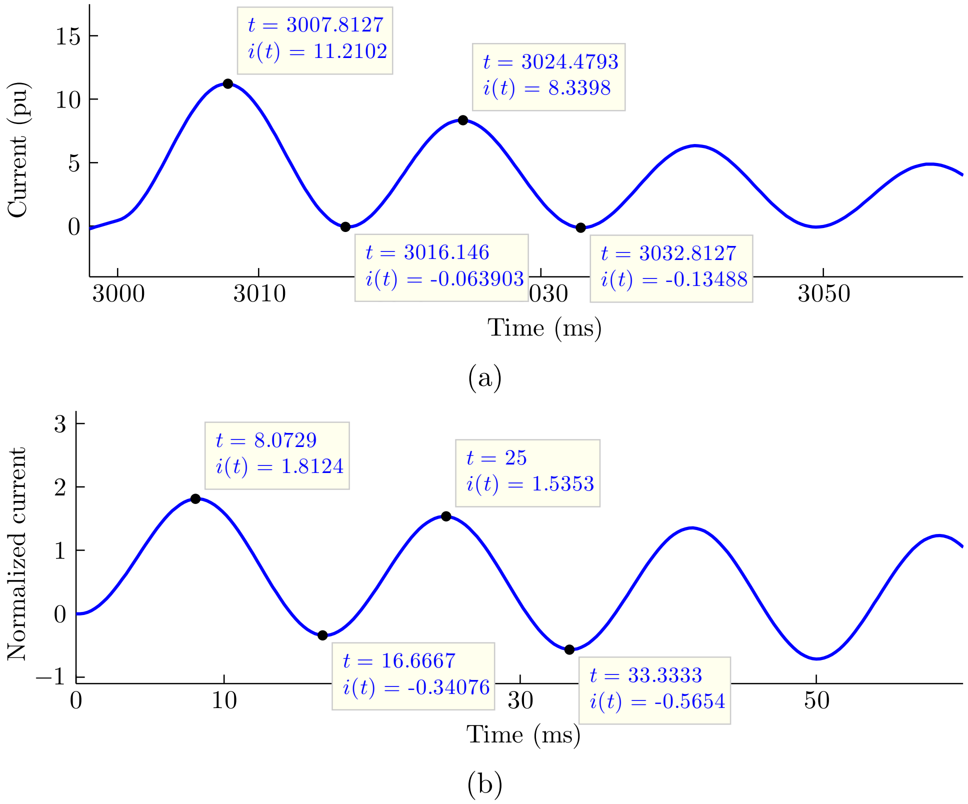

Figure 2.13. Comparison between fault currents of IG-based WFs and bulk power systems, (a) Phase A current of Figure 2.2, (b) Current described by (2.4) for $\tau = 40$ ms and $\theta = -\pi/2$ rad.

$\delta_{3\phi}$ even grows considerably larger in the case of DFIGs, which are the typical IG type employed in the WFs connected to HV grids, where distance protection is used.

Equivalent Thevenin sources are conventionally used to find the aggregate fault current of bulk HV power systems. This practice has been historically proved to be successful for protective relaying studies [41], and results in fault currents that are comprised of a fundamental frequency signal, some levels of its harmonics and a decaying dc offset. Since harmonics affect the peak-to-peak values similarly, they can be neglected for the present analysis, and the phase A fault current is expressed by

$$i_{fa}(t) = I_{\mathrm{m}} \left(\sin(\omega_1 t + \theta) - \sin(\theta)\, e^{-t/\tau} \right) \tag{2.4}$$

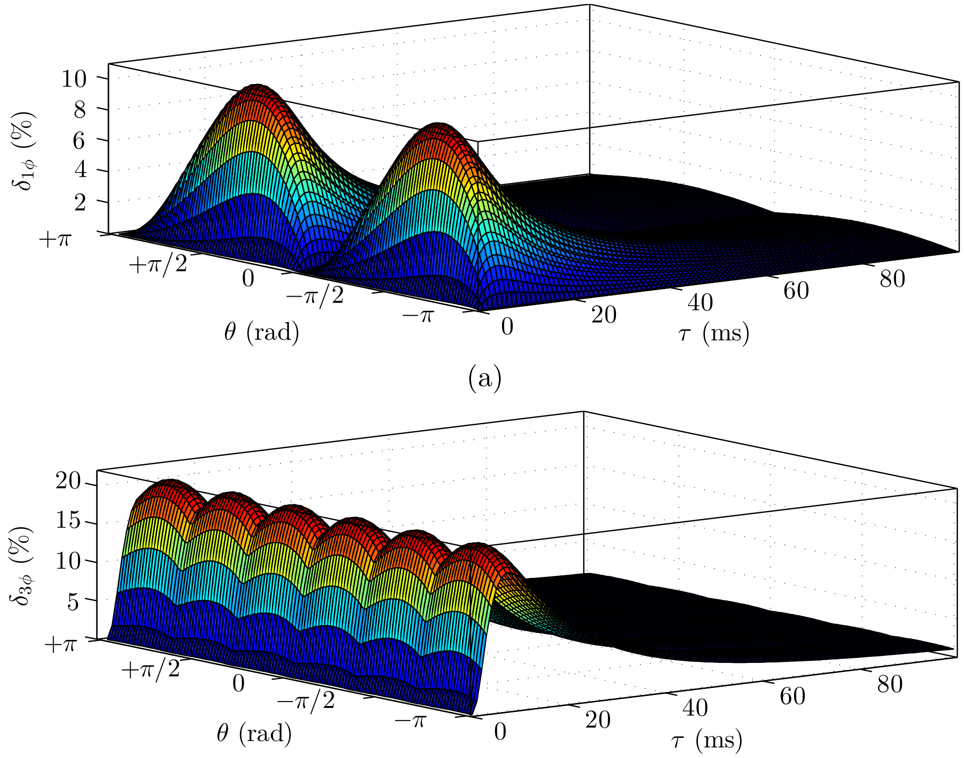

(a)

(b)

Figure 2.14. Indices obtained for bulk power system fault currents with respect to the dc offset magnitude and time constant, (a) $\delta_{1\phi}$, (b) $\delta_{3\phi}$.

where τ is the decaying dc time constant and θ determines the decaying dc initial magnitude [42]. The normalized $i_{fa}(t)$ of (2.4) for $\tau = 40$ ms and $\theta = -\pi/2$ rad (i.e., the maximum amplitude for the decaying dc) has been displayed in Figure 2.13(b). Comparing Figures 2.13(a) and (b) reveals a marked difference between the fault currents produced by IGs and the fault currents of bulk power systems. Unlike Figure 2.13(a), in Figure 2.13(b), the difference between the two initial peak-to-peak values is small because it is due to only the decaying dc component of current, even though maximum amplitude is considered for the dc offset in this figure. PtP_1 and PtP_2 are 2.15 pu and 2.10 pu, respectively, resulting in $\delta_{1\phi} = 2.50\%$, which is negligible compared to the $\delta_{1\phi}$ obtained for Figure 2.13(a).

To find the highest possible value of $\delta_{1\phi}$ for the current described by (2.4), θ and τ of (2.4) were varied in the ranges of $[-\pi, \pi]$ rad and $[1, 100]$ ms, respectively. Figure 2.14(a)

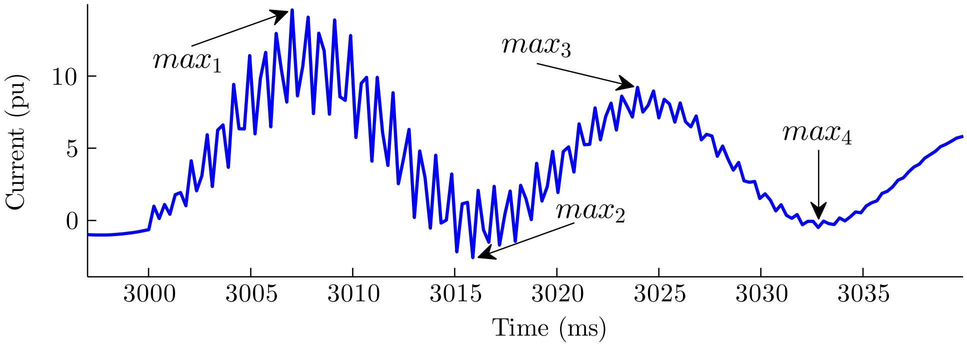

Figure 2.15. Fault current of SCIG-based WF with high-frequency pollution.

plots $\delta_{1\phi}$ measured for each pair of θ and τ. The largest $\delta_{1\phi}$ equals 10.84% and corresponds to $\theta = 1.22$ rad and $\tau = 8$ ms. The same value is obtained for $\delta_{1\phi}$ of the other two phases by shifting θ in (2.4) by $\pm 2\pi/3$ rad. Adding up $\delta_{1\phi}$ of the three phases would yield $\delta_{3\phi}$ for each pair of θ and τ, which is plotted in Figure 2.14(b). It should be noted that the maximum of $\delta_{1\phi}$ does not happen for all three phases simultaneously, as $\delta_{1\phi}$ depends on θ. $\delta_{3\phi}$ reaches 21.05% at its maximum in Figure 2.14(b). This maximum $\delta_{3\phi}$ along with a security margin can distinguish the two classes of fault current. An extensive analysis, a portion of which will be presented in the next section, revealed that by considering a security margin of about 200%, $\delta_{3\phi} = 60\%$ is an effective threshold for fault current classification. In other words, the 60% threshold is used to discriminate between the currents that correspond to the above classes of fault current.

To find the peak-to-peak values, appropriate extremums of the fault current must be located first. This stage should be immune to the effect of high-frequency components superimposed on the fault current due to noise, resonance, etc. Such high-frequency content is observed in Figure 2.15, which shows a fault current of the SCIG-based WF in the test system. The PF correction capacitor has been increased in this case to boost the resonance and display a fault current with larger high-frequency contamination. A simple pair of rules is established for finding extremums, so that only the extremums that best represent the fundamental frequency signal variations are located. These rules are as follows.

1. The extremums caused by the high-frequency contents are larger than only a few samples around them. To avoid such extremums, therefore, the proposed method determines a

current sample as a maximum or minimum if that sample is larger or smaller, respectively, than all samples inside a sufficiently long symmetrical neighborhood. A 10 ms long interval was found to be effective.

2. Resonance exhibits a rapidly decaying nature, and the resultant extremums occur in the initial few milliseconds after the fault. On the other hand, the extremums associated with the fundamental frequency signal appear after at least a quarter of a period, depending on the dc offset of the current. Therefore, no extremum is located during the first quarter-cycle of the fault current.

It is also possible to remove high-frequency pollution by means of a low-pass filter (LPF). However, thanks to the simplicity and effectiveness of the above approach, applying an LPF is not needed.

2.3 Performance Evaluation

To investigate the merits of the proposed method, the test system shown in Figure 2.1 and described in Appendix A was simulated. Bus 1 was connected either to an SCIG-based or to a DFIG-based WF. The overhead lines were simulated using the frequency-dependent line model. The generated fault signals were imported to Matlab, where they were processed according to the developed scheme. The objective was to determine whether this scheme could provide reliable protection for line 12 of the system using the waveshape properties of the fault current.

Numerous studies were carried out to scrutinize the performance of the proposed technique. Various parameters that affect the fault current waveshape of IG-based WFs, such as wind speed, crowbar resistance, fault resistance, fault inception angle, fault location, etc., were changed, and the operation of the proposed method was verified. Wind speed was kept constant throughout each case, as the decision-making process is much faster than the time span of wind speed variations. Table 2.1 displays some of the results obtained when bus 1 is connected to the SCIG-based WF. This table highlights $\delta_{1\phi}$ and $\delta_{3\phi}$ measured by DS12 for different faults on line 12 (i.e., in the forward direction of DS12), SCIGs' slip

Table 2.1
Performance of the Proposed Method for SCIG-Based WF

Fault location	R_f (Ω)	Slip (%)	$\delta_{1\phi}$ (%)			$\delta_{3\phi}$ (%)
			Phase A	Phase B	Phase C	
Next to Bus 2	10	-0.213	28.1	28.5	28.8	85.4
		-0.565	27.7	28.0	28.1	83.8
		-1.069	27.5	27.7	27.6	82.8
	5	-0.213	33.4	30.6	30.0	94.0
		-0.565	33.1	30.2	29.4	92.7
		-1.069	32.6	29.8	29.0	91.4
	0.5	-0.213	37.1	33.2	35.9	106.2
		-0.565	36.7	33.0	35.2	104.9
		-1.069	36.1	32.4	34.9	103.4
Middle of the line	10	-0.213	28.6	29.1	29.2	86.9
		-0.565	29.1	28.5	27.5	85.1
		-1.069	29.1	28.3	27.4	84.8
	5	-1.069	32.2	30.8	31.8	94.8
		-0.565	32.0	30.5	31.5	94.0
		-0.213	31.6	29.9	31.2	92.7
	0.5	-0.213	37.1	33.7	35.9	106.7
		-0.565	36.8	33.2	35.5	105.5
		-1.069	36.1	32.5	35.1	103.7
Next to Bus 1	10	-0.213	30.6	29.4	28.6	88.6
		-0.565	30.3	29.0	28.1	87.4
		-1.069	29.9	28.7	27.8	86.4
	5	-0.213	34.0	31.5	30.9	96.4
		-0.565	33.4	30.9	30.6	94.9
		-1.069	33.1	30.5	30.1	93.7
	0.5	-0.213	38.3	33.7	36.4	108.4
		-0.565	38.0	33.5	36.0	107.5
		-1.069	37.4	33.2	35.6	106.2

at the fault instant and fault resistances. Slip variations occur because of different wind speeds at the fault time. $\delta_{1\phi}$ shown in Table 2.1 is safely above the maximum value depicted in Figure 2.14(a). Furthermore, the values obtained for $\delta_{3\phi}$ exceed the 60% threshold by a wide margin. In addition, some of the achieved results when the DFIG-based WF was connected to bus 1 are reported in Table 2.2. Crowbar resistance for all cases of Table 2.2 is zero. The displayed indices can correctly classify the fault currents. The proposed method was also examined when underground cable, instead of overhead line, connected the WF to the grid, and equally successful results were obtained.

Apart from the results displayed in Tables 2.1 and 2.2, some cases are graphically discussed. First, the effect of crowbar resistance for DFIG-based WFs is studied. Then, the performance of the proposed method for internal WF faults is reviewed.

2.3.1 Effect of Crowbar Resistance

For the DFIG fault currents discussed so far, the crowbar resistance was zero. Meanwhile, non-zero crowbar resistance improves the fault behavior of a DFIG by decreasing the reactive power consumption, reducing the fault current magnitude and damping torque oscillations [33]. Such positive effects together with the higher power ratings of DFIGs explain why a DFIG-based WF with non-zero crowbar resistance is the most likely IG-based WF to be connected to HV grids, where distance relaying is practiced.

Figure 2.16 shows the fault currents measured at bus 1 for a balanced short-circuit on line 12 at $t = 3$ s. Rotor speed is 1.2 pu at the fault time. The crowbar resistance is $R_{cb} = 0.03$ pu for this case. The two initial peak-to-peak values of the phase A fault current are 4.35 pu and 2.69 pu, which yields $\delta_{1\phi} = 61.81\%$. Furthermore, similar significant differences between the fault current peak-to-peak values lead to $\delta_{1\phi}$ equal to 62.48% and 63.22% for phases B and C, respectively. Consequently, $\delta_{3\phi}$ is 187.51%, which is more than triple the 60% threshold. Hence, the relay at the WF substation can accurately recognize the forward direction of the fault, and the modified POTT scheme trips line 12 instantaneously. Obviously, $\delta_{3\phi}$ increases further if a larger R_{cb}, such as the 0.3 pu value suggested in [43], is involved.

Table 2.2
Performance of the Proposed Method for DFIG-Based WF

Fault location	R_f (Ω)	Slip (%)	$\delta_{1\phi}$ (%)			$\delta_{3\phi}$ (%)
			Phase A	Phase B	Phase C	
Next to Bus 2	10	25	44.4	45.2	44.8	134.4
		-0.1	35.2	36.1	36.5	107.8
		-25	27.3	27.6	27.5	82.4
	5	25	49.8	48.8	49.5	148.1
		-0.1	40.4	38.1	40.1	118.6
		-25	31.5	30.1	30.9	92.5
	0.5	25	54.1	53.7	54.2	162.0
		-0.1	44.7	42.2	45.1	132.0
		-25	35.0	33.2	34.6	102.8
Middle of the line	10	25	44.8	45.7	45.7	136.2
		-0.1	36.9	37.1	36.6	110.6
		-25	28.4	29.1	28.8	86.3
	5	25	50.8	49.5	50.3	150.6
		-0.1	41.1	40.2	40.8	122.1
		-25	32.0	30.6	31.7	94.3
	0.5	25	54.8	54.3	54.9	164
		-0.1	44.5	44.4	45.2	134.1
		-25	35.2	34.3	34.9	104.4
Next to Bus 1	10	25	45.9	46.1	46.5	138.5
		-0.1	37.5	38.1	37.9	113.5
		-25	28.7	29.5	29.3	87.5
	5	25	51.5	49.9	51.2	152.6
		-0.1	42.1	40.6	41.9	124.6
		-25	32.2	31.4	32.1	95.7
	0.5	25	55.4	54.8	55.1	165.3
		-0.1	44.9	45.1	46.2	136.2
		-25	35.3	35.3	36.0	106.6

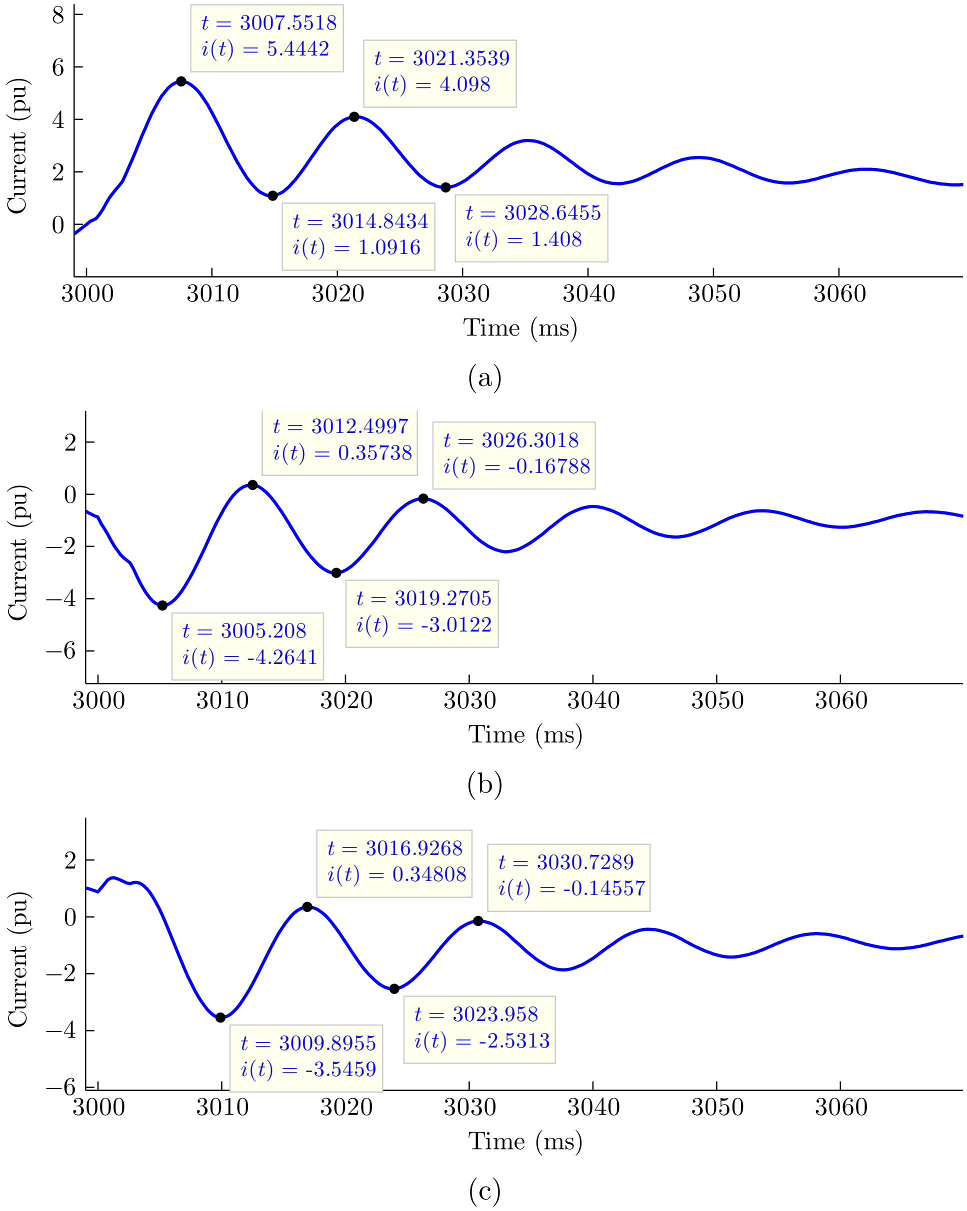

Figure 2.16. Fault currents of DFIG-based WF for nonzero crowbar resistance, (a) Phase A, (b) Phase B, (c) Phase C.

$\delta_{3\phi}$ for the fault of Figure 2.16 is substantially larger than $\delta_{3\phi}$ for the previously-discussed SCIG cases and the DFIG cases that had zero crowbar resistance. The positive impact of the crowbar resistance on the operation of the proposed technique was expected. R_{cb} is connected in series with the rotor winding, and raises the effective resistance of the rotor circuit. As noted in Section 2.1.1, the decaying rate of the ac component of an IG fault current is determined by the short-circuit transient time constant, i.e., T' of (2.1), which is inversely proportional to the rotor resistance.

2.3.2 Internal WF Faults

Fault currents passing through DS12 during internal WF faults are generated by the sources at buses 3 and 4, which account for the bulk grids connected to these buses. Various short-circuits were placed inside the WF and on bus 1 during different operating conditions, and the proposed method was tested. Two of the studied cases are discussed here.

2.3.2.1 Thevenin sources at buses 3 and 4

The common and historical practice for fault analysis is to employ equivalent Thevenin circuits to represent part of a power system that feeds the faulted section [41]. This approach, particularly, leads to very accurate results if that part of the system is large. This is the actual scenario for the HV and EHV networks that deploy distance relays. Therefore, the same approach is adopted in this subsection to represent the power systems behind buses 3 and 4. Figure 2.17 shows the currents sensed by DS12 during an out-of-zone short-circuit at bus 1 at $t = 10$ s, for which the line relay must avoid instantaneous tripping. $\delta_{1\phi}$ for phases A, B and C is 2.96%, 2.71% and 1.92%, respectively, leading to $\delta_{3\phi} = 7.59\%$, which is far less than the 60% threshold. Thus, the proposed method considers reverse direction for the fault, and prevents instantaneous line tripping.

2.3.2.2 SGs at buses 3 and 4

If the grids connected behind buses 3 and 4 are not large, their Thevenin source representation is not fully accurate. Although this is not the typical situation for the HV and EHV grids that the WFs are integrated with, it is worth investigating. To analyze this

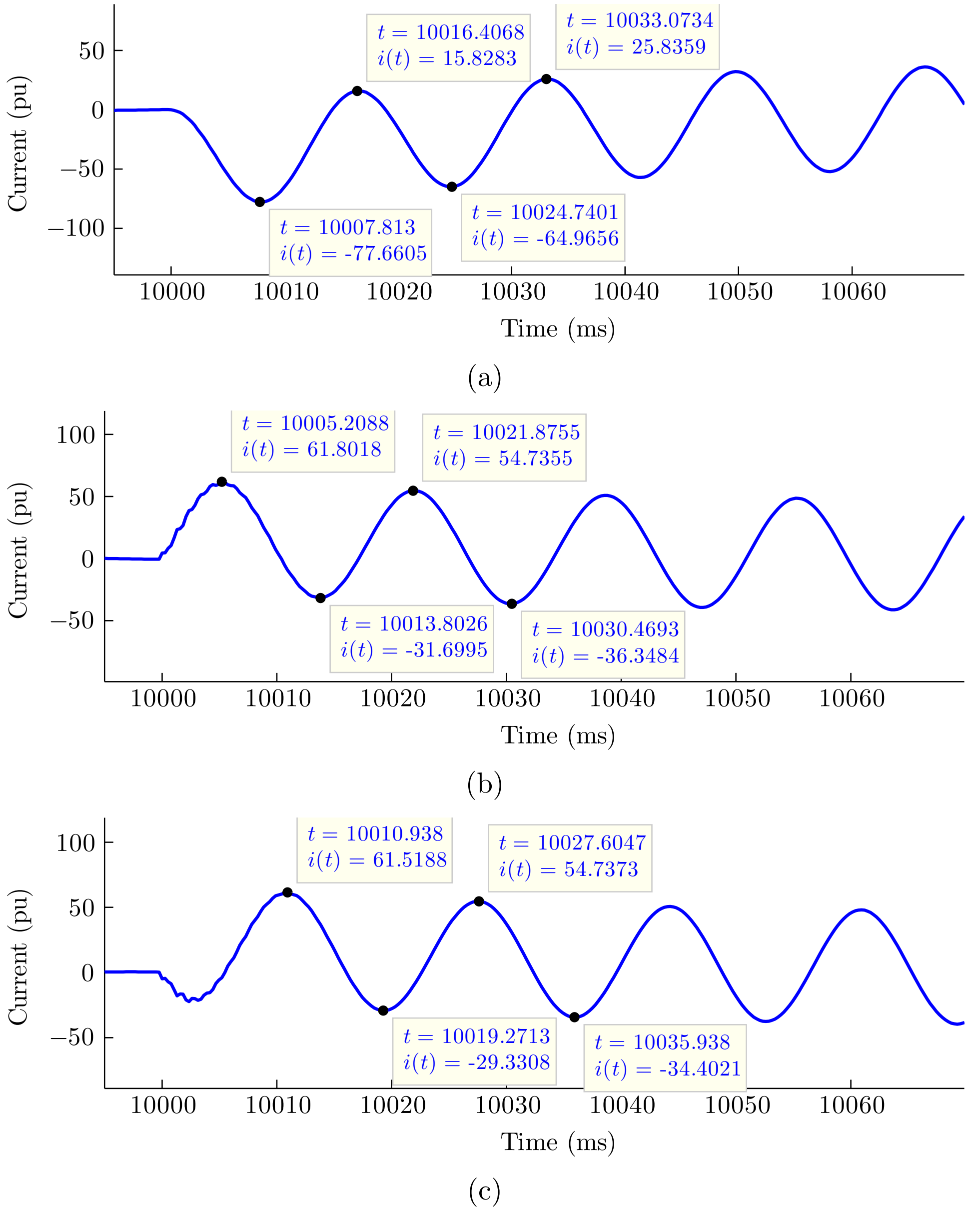

Figure 2.17. Currents for a reverse fault,
(a) Phase A, (b) Phase B, (c) Phase C.

condition, actual SG models are used in this study. Apart from the steady-state ac and the transient dc components, the three-phase fault current of an SG also includes transient and subtransient decaying ac components. The time constant of the transient ac component is in the order of seconds, and its amplitude variation is not sensed within the short window used by the proposed method. The subtransient component might vary inside the window under study. However, the subtransient component is only one of the four main components of an SG fault current, and also its relative magnitude with respect to the other fault current components drops significantly as the fault location moves away from the SG terminal [29]. Consequently, the decline in the magnitude of the entire ac component becomes very gradual for the faults that are not very close to the SG terminal. Actually, the almost uniform magnitude of the ac component of SG fault currents is a main reason behind the successful practice of using Thevenin sources for fault studies [41].

On this basis, the worst case scenario during reverse faults for DS12 occurs when, instead of an HV grid, buses 3 and 4 are each connected directly to an SG through a transformer with very low leakage impedance. Therefore, the relative magnitude of the subtransient component of the SG fault current becomes maximum, and in turn, the ac component of the current has the highest possible decay rate. Indeed, single SGs connected to buses 3 and 4 is a hypothetical scenario, which cannot be the case for real HV grids, but it is considered here to demonstrate the performance of the proposed method for the worst possible condition. The currents measured by DS12 after a fault on bus 1 at $t = 10$ s are shown in Figure 2.18. The difference between the two initial peak-to-peak values of the fault currents has increased with respect to Figure 2.17, and $\delta_{1\phi}$ has reached 10.14%, 14.72% and 15.06% for phases A, B and C, respectively. Nevertheless, $\delta_{3\phi}$ equals 39.92%, which is securely below the threshold. Hence, the reverse direction of the fault is correctly identified.

2.4 Conclusion

The impedance measured by a relay at an SCIG-based WF substation does not truly represent the fault location a few cycles after a balanced short-circuit occurs. The consequences are zone one operation for the faults located on the next lines and failure to perform back-up functionalities. For DFIG-based WFs, it is impossible to measure a meaningful

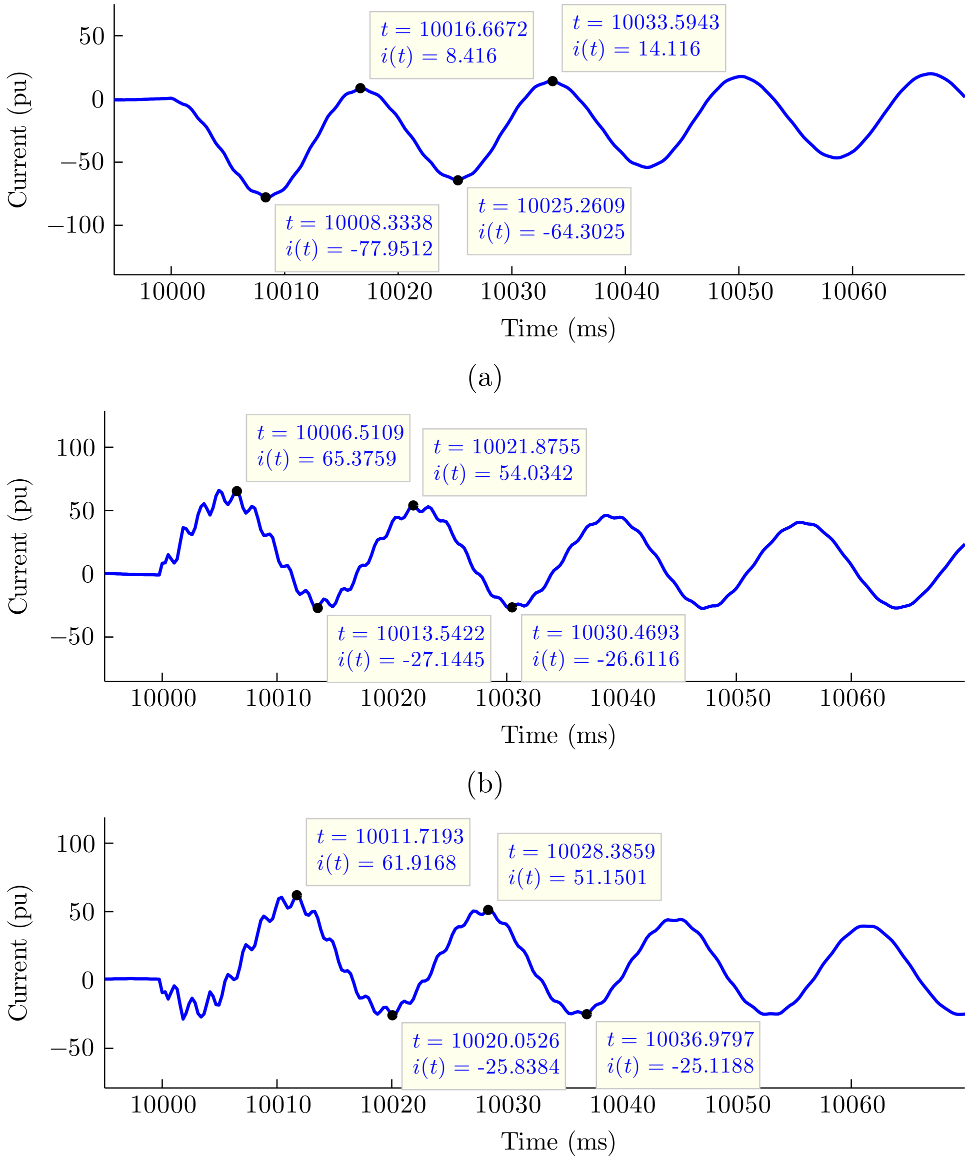

(a)

(b)

(c)

Figure 2.18. Currents for a reverse fault on bus 1 when buses 3 and 4 are connected to SGs, (a) Phase A, (b) Phase B, (c) Phase C.

impedance, as the frequencies of the fault current and voltage can be well apart. The impedance exhibits a totally chaotic trajectory, which is not reliable even for the short period after the fault. The likely corollaries are zone one operation of the WF substation relay for the faults requiring back-up operation and delayed tripping for the faults inside zone one.

The proposed modified POTT scheme provided quick and non-delayed protection over the entire line, while the minimal bandwidth requirement of distance relays for the communication link was maintained. The relay detects the fault direction according to the current waveshape properties. The developed current classification technique takes advantage of the high decay rate for the peak-to-peak values of IG fault currents. Encouraging results were obtained for both types of IG-based WFs, particularly for the DFIG-based WFs with crowbar resistance, which is the typical scenario where distance relaying is practiced.

Chapter 3

Distance Protection of Lines Emanating from CIREPPs: Problem Statement

This chapter investigates the problems associated with distance protection of transmission lines connected to CIREPPs, which have been left unnoticed in relaying literature. CIREPPs consist primarily of photovoltaic farms and Type IV WFs, which are both growing globally at exponential rates. Due to converter similarities, this study is equally applicable to the ac lines emanating from VSC-based HVDC substations, another rapidly expanding technology [44].

As power plants have been traditionally composed of SGs, modeled by Thevenin equivalent circuits for fault studies [41], the conventional wisdom from the protective relaying perspective has been that CIREPPs can also be represented similarly, with the only consideration being a large source impedance to take account of the CIREPPs' modest fault current contribution. However, a CIREPP's fault behavior is governed by its control system that determines the switching pulses of the grid-side converter [45]. The objectives and settings of this control system can be quite different depending on the host system GC, the internal references, and the adopted reference frame, among other factors. Thus, modeling a CIREPP with all of its complications by a simple source is not accurate, especially over fault conditions.

On this basis, Section 3.1 proceeds with a brief overview of the GC articles that a CIREPP's control system must take into consideration and are found to influence the CIREPP-relay interactions by later sections. Section 3.2 describes the system under study, the control structure of the CIREPP coupled with this system, and how it satisfies GC requirements. The analysis of the distance relay's possible maloperation for zone one balanced faults is covered in Section 3.3, and is extended to unbalanced faults in Section 3.4. Section 3.5 studies relay failures during zone two faults. The different relay operation for a conventional source is demonstrated in Section 3.6. Section 3.7 presents the concluding remarks.

3.1 GC Articles for Fault Conditions

Besides FRT capability, modern GCs determine active and reactive power requirements that REPPs have to comply with. Apart from the power requirements that are to be met over normal operation, European GCs (EU-GCs) impose regulations specific for faulty conditions, and typically give higher priority to reactive power support from REPPs [46]. Take, for instance, the Spanish grid; within 150 ms after the beginning of a voltage dip at the POI, the reactive current generated by a WF must be situated inside the shaded area of Figure 3.1 [3, 47]. With the exception of a handful of utilities, POI is always the HV side of the REPP main transformer. In Figure 3.1, V^+ and I^+ are the positive sequence voltage and current, respectively, V_n is the nominal voltage, and I_Q^+ is the positive sequence reactive current, given by

$$I_Q^+ = \frac{I^+}{I_{tot}} \sin(\phi^+) \tag{3.1}$$

in which ϕ^+ is the angle between V^+ and I^+, and I_{tot} is the total fault current. The lower the voltage level, the larger the reactive current generated by the WF must be. Meanwhile, during the 150 ms period, the WF is allowed to consume both active and reactive power at the POI as long as they are limited to 10% and 60% of the rated power, respectively. A broadly similar requirement with a faster response time is imposed by the German

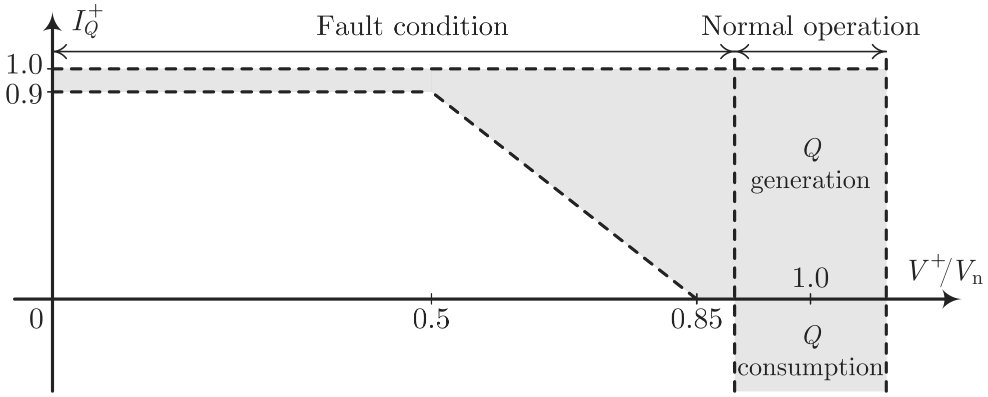

Figure 3.1. WFs' reactive current during disturbances according to the Spanish GC.

GC [20]. The GCs that comply with the reactive current requirements of [46] are referred to as EU-GCs in this dissertation.

On the issue of disturbance behavior, the current North American GCs (NA-GCs) focus only on how REPPs must ride through the fault, and do not enforce any specific regulation on the active or reactive components of REPP fault currents [48, 49]. Thus, the control system of an REPP would naturally attempt to satisfy the NA-GCs' normal power demand, which is 0.95 plus positive sequence PF, lead or lag.

HVDC links normally operate at a high PF. To the best of the author's knowledge, there is currently no unified GC that mandates reactive power generation during fault conditions for HVDC substations. Only one very recent draft of a GC for HVDC connections, prepared for public consultation by the European Network of Transmission System Operators for Electricity (ENTSO–E), allows regional utilities to have specific reactive power demands over fault conditions [50]. This draft does not impose any obligation in this regard, and has not gained final approval yet. Therefore, similar to REPPs conforming to the NA-GCs, HVDC links should be expected to operate at high PFs after a fault, particularly during the immediate narrow time frames when transmission system relays have to take action.

3.2 Description of Test System and CIREPP

The following describes a test power system that includes a CIREPP, the structure of this CIREPP and how it complies with different GC articles.

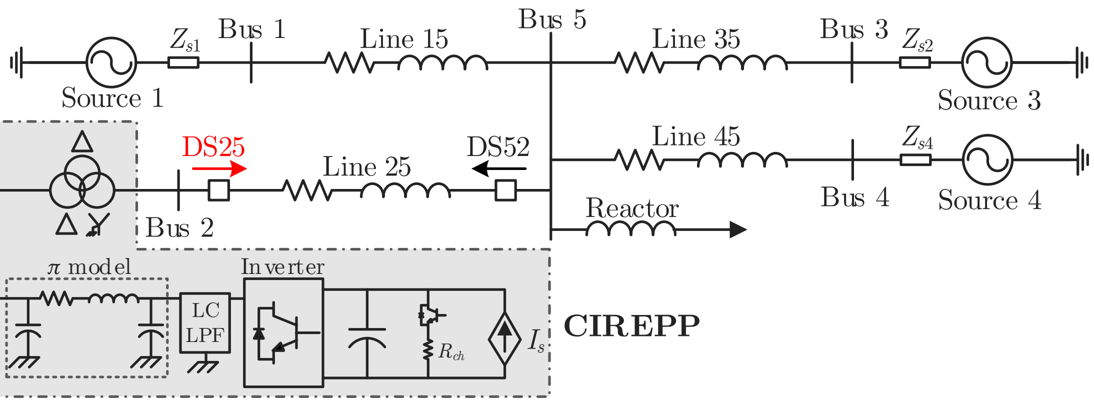

Figure 3.2. Single line diagram of the test system, including the CIREPP.

3.2.1 Test System

Simulated using PSCAD/EMTDC program, the 230 kV, 60 Hz power system depicted in Figure 3.2 was used to study the protection of line 25 connected to the 100 MW CIREPP on bus 2. DS25 and DS52 are the distance relays located at buses 2 and 5, respectively, and protect line 25. The voltage angles along with the positive- and zero-sequence impedances of the sources at buses 1, 3 and 4 are

- Source 1: $\measuredangle V_{s1} = -7.1°$, $Z_{s1}^{+} = 12.66 \measuredangle 83°\ \Omega$, $Z_{s1}^{o} = 11.1 \measuredangle 83°\ \Omega$,
- Source 3: $\measuredangle V_{s1} = -2.0°$, $Z_{s1}^{+} = 7.76 \measuredangle 86°\ \Omega$, $Z_{s1}^{o} = 5.0 \measuredangle 86°\ \Omega$,
- Source 4: $\measuredangle V_{s1} = -6.9°$, $Z_{s1}^{+} = 12.7 \measuredangle 82°\ \Omega$, $Z_{s1}^{o} = 11.2 \measuredangle 82°\ \Omega$.

The reactor at bus 5 is rated 75 MVAr. When the CIREPP generates its rated capacity at unity PF, the voltages at buses 2 and 5 are $230.6 \measuredangle 3.0°$ and $228.2 \measuredangle{-2.4°}$ kV, respectively. The lines are simulated using the frequency-dependent model, and their positive- and zero-sequence impedances are $Z_L^{+} = 0.0357 + j0.5077\ \Omega/\text{km}$ and $Z_L^{o} = 0.3630 + j1.3262\ \Omega/\text{km}$. The lengths of lines 15, 25, 35 and 45 are 155, 100, 110 and 120 km, respectively.

3.2.2 CIREPP Structure

The time spans associated with both wind speed and solar intensity variations are appreciably longer than the short intervals considered for fault studies. In addition, the fast dynamics of the RE source are essentially decoupled from the grid by the dc capacitor. Hence, the RE source together with the converter that provides the dc voltage are represented by a controllable current source.

A large WF is composed of dozens of turbines connected to the farm substation through underground cable. Each unit includes a back-to-back converter, an LPF and a transformer that boosts the voltage up to the medium level. Modeling each turbine unit separately and the cable system with its fine details is computationally intensive. Furthermore, it has been shown that a single aggregated unit along with a π model representing the cable system is able to simulate a WF accurately [51,52]. This process, designated as equivalencing, can be similarly carried out for photovoltaic farms as well. As shown in Figure 3.2, equivalencing practice was used to model the CIREPP in this study.

The main transformer of large REPPs is commonly three-winding, regularly configured as ygdYG or ddYG. On the grid side, both configurations result in the same behavior. For this study, the ddYG configuration is chosen. The transformer ratings are 150 MVA, 34.5/34.5/230 kV and $X = 0.1$ pu.

3.2.3 CIREPP's Control System and GC Compliance

The findings of this study are independent of the reference frame in which the CIREPP's control system is implemented. The synchronous *dq* frame with proportional integral (PI) controllers, voltage feed-forward compensation and cross-coupling terms, detailed in [53], is chosen, as it is widely deployed in the RE industry [54]. The phase-locked loop (PLL) of the control system is immunized against unbalanced conditions using the method described in [55].

After a voltage drop at the CIREPP's POI, the active power transfer capability of the grid-side converter reduces and, in turn, the dc link voltage rises [56]. In order for the CIREPP to ride through faults, the dc link voltage must be restricted. Hence, as shown

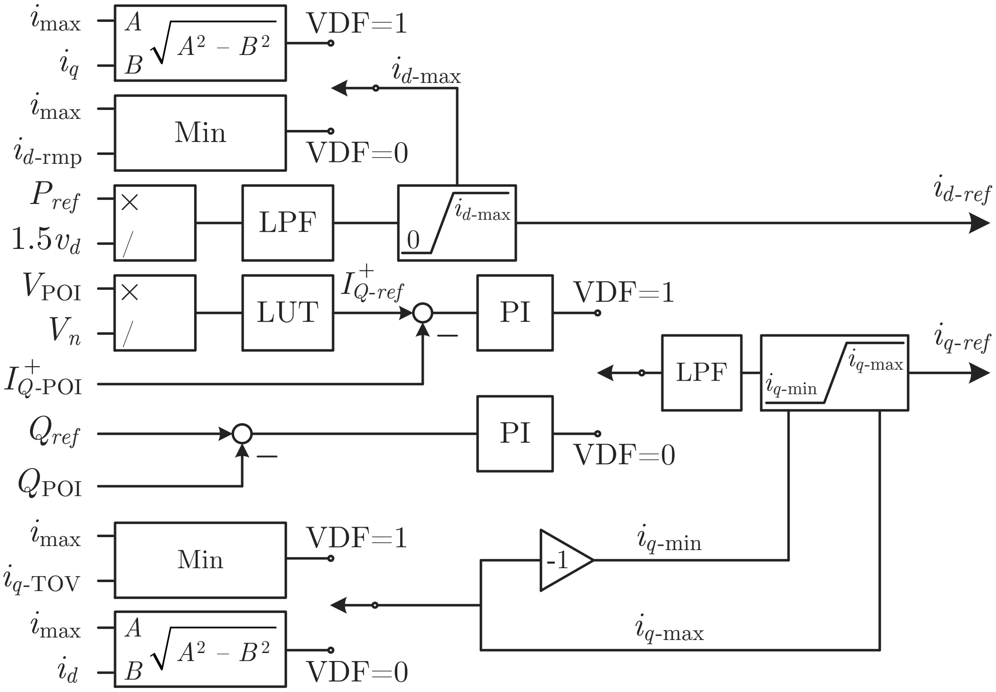

Figure 3.3. Structure of CIREPP's higher level control system for GC compliance.

in Figure 3.2, a braking chopper circuit is connected in parallel with the capacitor to suppress the dc voltage during disturbances. The maximum dc voltage allowed is 1.2 times the nominal value, which is a common practice in industrial converters [57].

Figure 3.3 shows a simplified model of the reference current generation block used by the control system. This system, which is similar to the ABB generic Type IV wind turbine model discussed in [58], can comply with the aforementioned reactive power requirements of the EU-GCs. The reference powers P_{ref} and Q_{ref} determine the references for the d and q components of the current, i_{d-ref} and i_{q-ref}, respectively, during normal operation. P_{ref} is provided by the dc link voltage control loop, and Q_{ref} is determined based on the reactive power control strategy adopted, e.g., to reach a certain PF. The GCs measure reactive power at the POI, Q_{POI}, while i_{q-ref} determines the reactive current of the inverter's filter inductor. Therefore, a closed-loop control is used to regulate Q_{POI}.

As discussed in [59], i_{d-ref} and i_{q-ref} are passed through a saturation block to protect the switches by limiting the short-circuit currents to 1.2 times the rated current. Over normal operation, priority is given to active power; thus, the limit for i_{q-ref}, that is, $i_{q-\max}$, is determined based on the 1.2 pu maximum current of the converter, $i_{\max}$, and the actual d-axis current, i_d. The maximum allowed i_{d-ref} is the minimum of $i_{\max}$ and $i_{d-\mathrm{rmp}}$, a limit that keeps active power ramp levels within the GC's acceptable range. The reference signals are finally passed through LPFs to remove noise and alleviate abrupt changes.

Once a voltage dip is detected, the reference current generation strategy switches in a discrete manner. After the voltage dip flag (VDF) is raised, i_{q-ref} is determined according to the POI voltage and a look-up table (LUT) prepared based on the host system reactive current requirement during disturbances. Similar to normal operation, I_Q^+ is regulated by controlling i_{q-ref} in a closed-loop manner. i_{d-ref} control loop remains the same; however, higher priority is given to reactive power during disturbances in the case of EU-GCs. In other words, $i_{d-\max}$ is determined based on $i_{\max}$ and the actual i_q. Being determined for the positive sequence circuit, the reactive current requirements of EU-GCs are not phase selective and potentially pose the risk of temporary overvoltages (TOVs) in healthy phases during unbalanced faults. Therefore, $i_{q-\mathrm{TOV}}$ is a limit applied to i_q during disturbances to keep the reactive power injection in the healthy phases and consequently the TOVs within the GC's acceptable range.

3.3 Zone One Balanced Faults

This section inspects the performance of DS25 for balanced faults in zone one, which covers 90% of line 25. Several case studies will be presented, through which the problematic and non-problematic conditions from the line protection perspective and the underlying causes for relay maloperation will be identified. The case studies take both the EU-GCs and NA-GCs into account, and include different properties of fault, such as its resistance and location within DS25's zone one. The problem is described using a self-polarized impedance-based relay with a quadrilateral characteristic and a large 100 Ω resistive reach. Furthermore, to validate the existence of the discussed problems in practical applications, the responses of memory-polarized mho characteristics commonly deployed in commercial re-

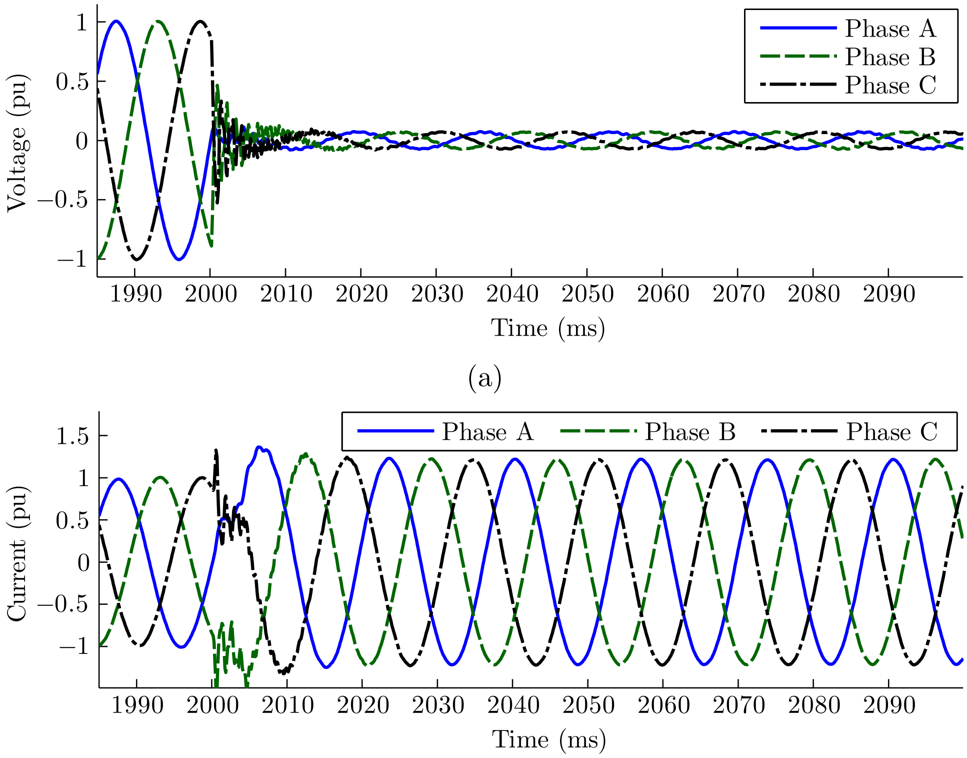

(a)

(b)

Figure 3.4. Measurements at the CIREPP's POI for case 1, (a) Voltage, (b) Current.

lays are also scrutinized.

The voltages and currents are passed through a second-order Butterworth anti-aliasing filter with a 1 kHz cut-off frequency. The voltage is measured by FCDFT, while the current phasor is computed by FCDFT for control system and GC compliance application, and by the one-cycle CLES-based digital filters for relaying purposes. At the sampling rate of 64 times per fundamental cycle, the measured impedance was updated for every 4 new pair of voltage and current samples.

3.3.1 Case 1

Case 1 includes a bolted balanced fault at 60% of line 25. The fault occurs at $t = 2$ s, and the greater than 90% voltage drop in Figure 3.4(a) is accompanied by the converter's

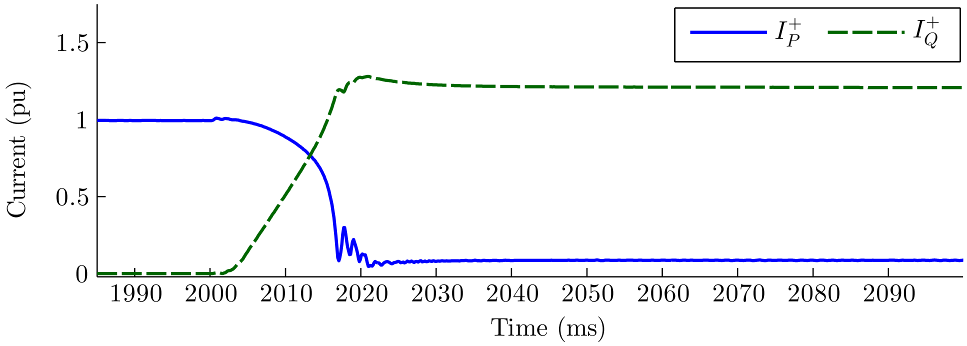

Figure 3.5. The active and reactive current of the CIREPP for EU-GC compliance in case 1.

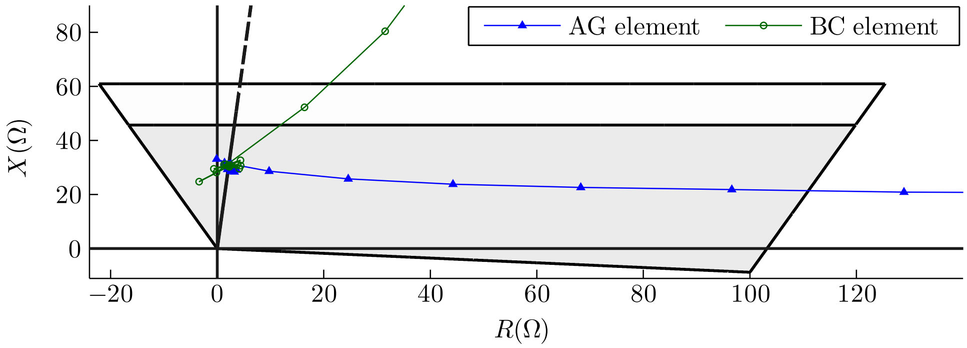

Figure 3.6. The impedance measured by DS25 for case 1.

maximum current in Figure 3.4(b). Before the fault, the CIREPP generates the nominal power at unity PF. During the fault, the CIREPP attempts to meet the EU-GCs. The CIREPP GC compliance is illustrated in Figure 3.5, which shows the significant quick jump of the per-unit reactive current after the fault is initiated. In this figure, I_P^+ is the positive sequence active current. The CIREPP's rated peak current is used to per-unitize the quantities displayed in Chapters 3 and 4. The impedances measured by the AG and phase B to phase C (BC) elements of DS25, depicted in Figure 3.6, enter zone one in 14.5 ms and 13 ms, respectively, and the line is correctly tripped.

3.3.2 Case 2

The voltage and current of the previous case while the NA-GC is applied by the CIREPP are shown in Figure 3.7. The PF curve of the CIREPP in Figure 3.8 indicates that the

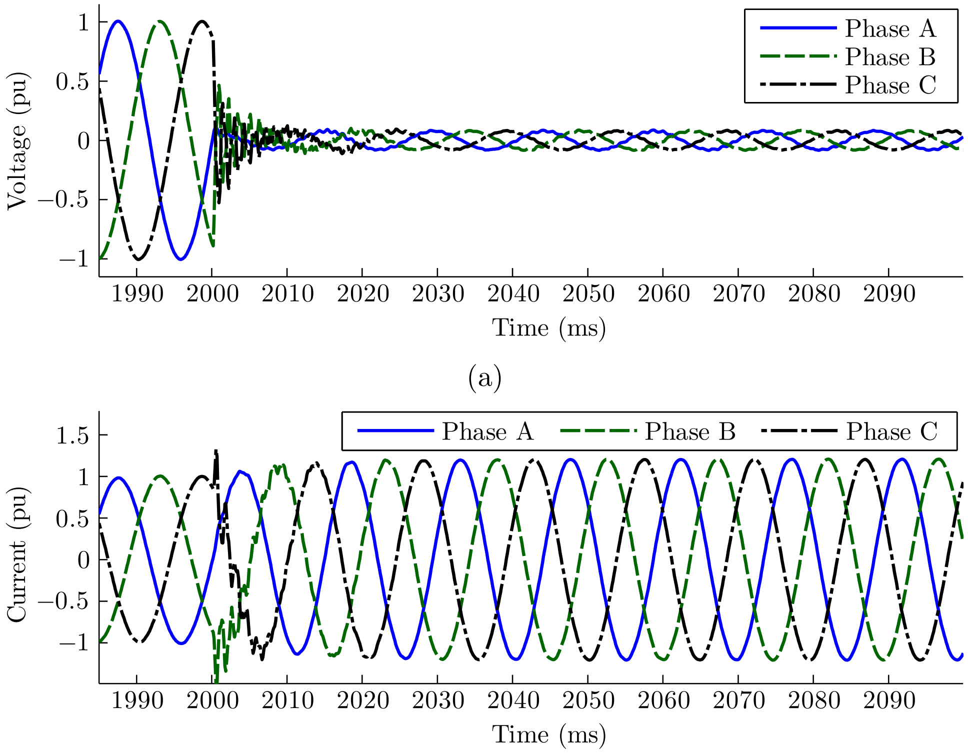

(a)

(b)

Figure 3.7. Measurements at the CIREPP's POI for case 2, (a) Voltage, (b) Current.

control system does not meet its objective, and the PF drops to about 0.09 one cycle after the fault inception. Meanwhile, the low PF is not a failure of the CIREPP's control system. The zero fault resistance causes zero voltage at the fault location for all three phases, and the CIREPP is coupled with an effectively dead circuit. Consequently, the difference between the fault voltage and current angles is dictated by the mainly inductive line impedance, over which the CIREPP has no control. As a result, similar to case 1, the impedances measured by DS25 in Figure 3.9 fall inside zone one in about a cycle.

The above argument can be extended to case 1 as well. In fact, failure or success in GC compliance for all zone one bolted balanced faults is determined not by the control system of the CIREPP, but by the physical properties of line 25 impedance.

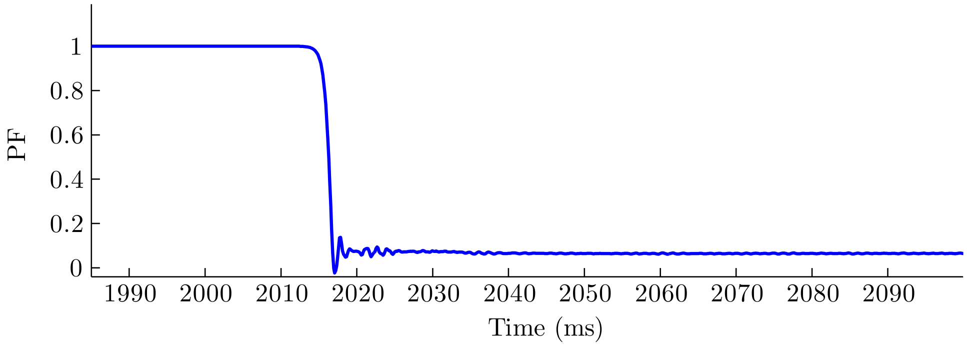

Figure 3.8. PF of the CIREPP for NA-GC compliance in case 2.

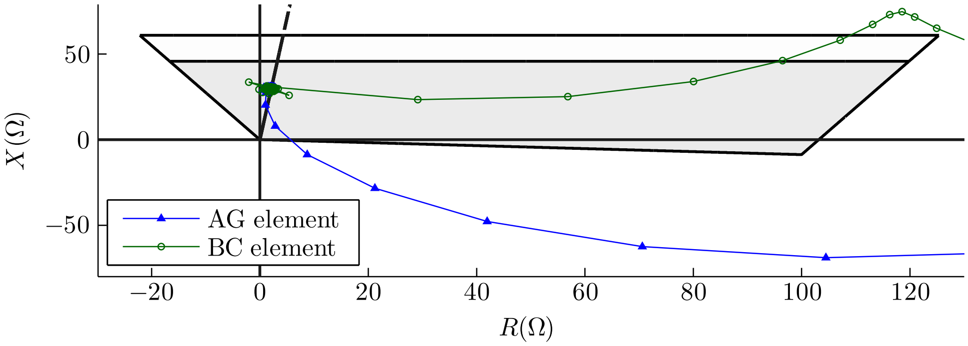

Figure 3.9. The impedance measured by DS25 for case 2.

3.3.3 Case 3

Unlike the above cases, actual faults usually include some level of fault resistance. Case 1 of Section 3.3.1 is repeated, while R_f is increased to 10 Ω. The fault voltage at the POI has risen to 0.29 pu in Figure 3.10(a) compared to less than 0.1 pu in Figure 3.4(a), whereas the fault current in Figure 3.10(b) equals the CIREPP's maximum current limit again. Since the voltage drop is above 50%, the control system attempts to increase the reactive current up to the full capacity. In contrast to Figure 3.5, where the reactive current variation was virtually instantaneous, because it was determined by the line impedance, the I_Q^+ shown in Figure 3.11 undergoes a transient period influenced by the CIREPP's control system.

When the initial transients disappear, the resistance and reactance measured by the AG element of DS25, plotted with respect to time in Figure 3.12(a), are fixed at 0.33 Ω and 124.67 Ω, respectively. The latter is in excess of the actual reactance to the fault by

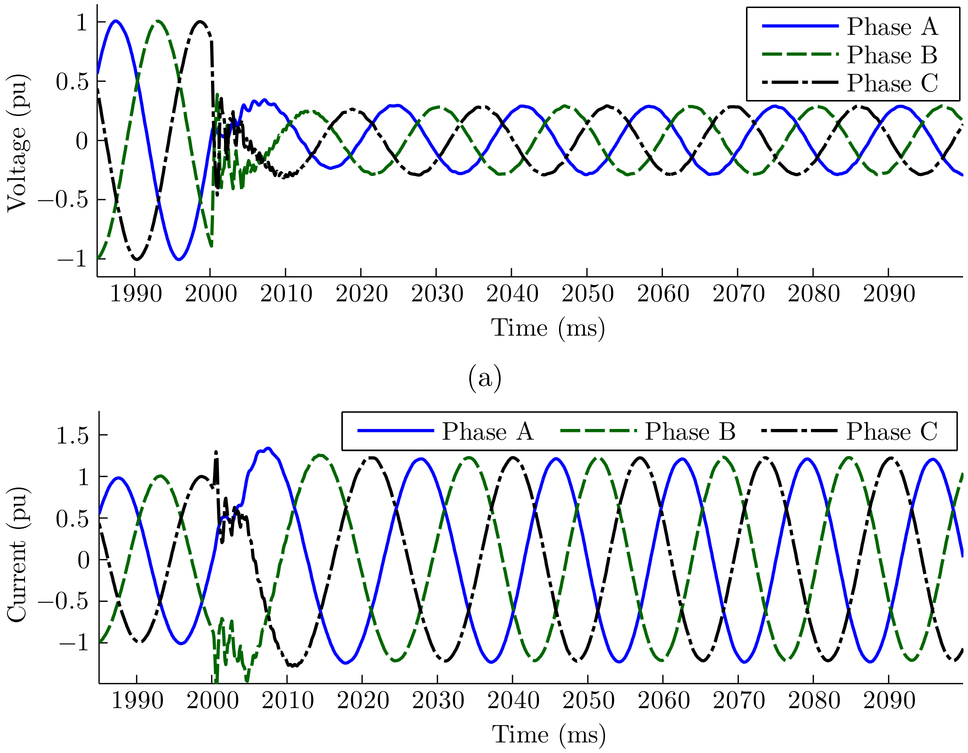

(a)

(b)

Figure 3.10. Measurements at the CIREPP's POI for case 3, (a) Voltage, (b) Current.

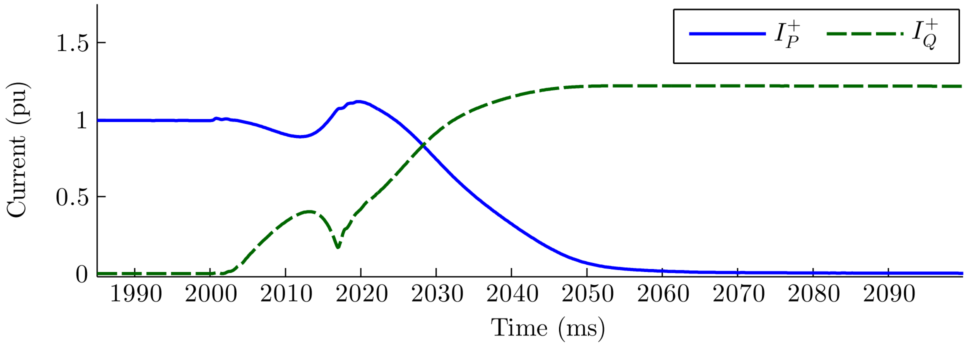

Figure 3.11. The active and reactive current of the CIREPP for EU-GC compliance in case 3.

more than fourfold. Therefore, as shown in Figure 3.12(b), the operating point lies far above zone one, making an impedance-based DS25 fail to trip the line. Unlike case 1, the CIREPP does have full control over its current, as the voltage at the fault location is not

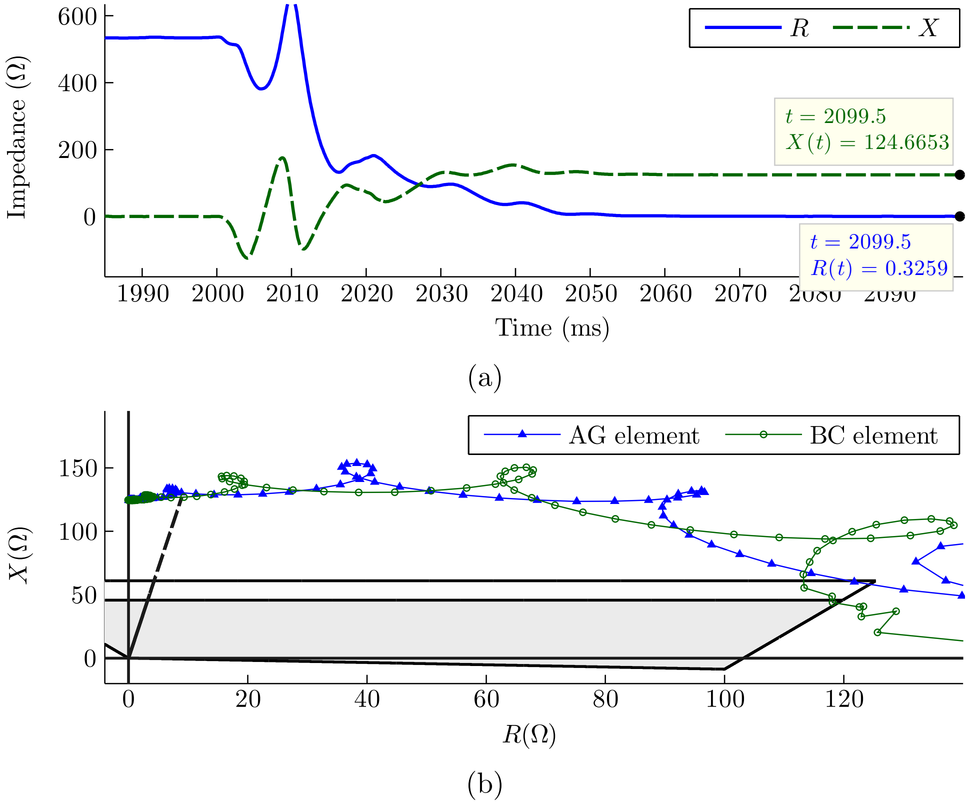

Figure 3.12. Performance of DS25 for case 3, (a) Time variations of R and X measured by the AG element, (b) Impedance plane of the AG and BC elements.

zero and the CIREPP is not completely isolated from the rest of the grid.

Contrary to conventional power plants with SGs, VSCs in RE and HVDC applications are controlled through their currents, due to numerous advantages such as superior dynamic performance and limited overcurrents [60]. Consequently, a CIREPP behaves as a controlled current source that follows certain active and reactive power commands given by the host system GC and/or dc link voltage control loop. The generated P and Q are translated into certain resistance and reactance in the impedance plane, respectively. Take, for instance, the phase A active and reactive power curves of the CIREPP for case 3, displayed in Figure 3.13, which exhibit high correlation with the R and X curves of Figure 3.12(a). Since the control system of the CIREPP makes the current mainly reactive after the transients fade out in Figure 3.11, P and Q are fixed at about 0.03 MW and 11.54 MVAr, respectively,

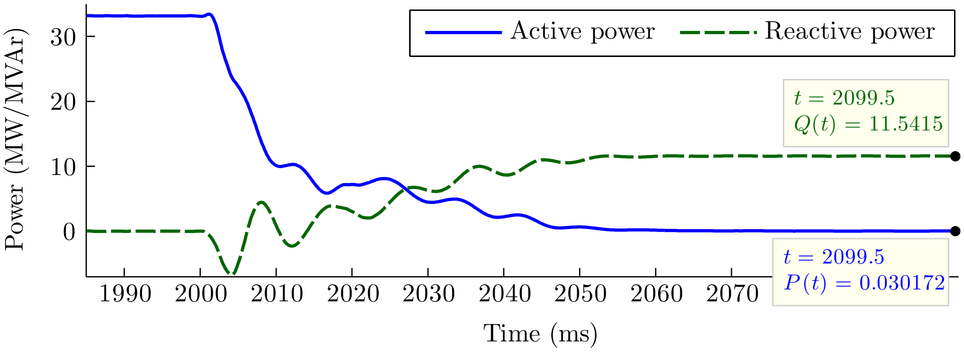

Figure 3.13. Phase A power for case 3.

which correspond to $R = 0.33$ and $X = 127.72\ \Omega$, considering the 1.2 pu current. The tiny difference between these values and the resistance and reactance pinpointed in Figure 3.12(a) arise from the fact that the 1.2 pu limit is for the converter current, while the relay is at the POI.

For the same fault conditions, if the CIREPP's current limit was set to 1.1 pu, Q would decrease to 10.34 MVAr, resulting in X=135.66 Ω; i.e., the reactance calculated by DS25 jumps by about 8 Ω because of a minor change, not in the fault properties, but in the CIREPP's control system. Similarly, increasing the CIREPP's current limit reduces the impedance seen by the relay. In other words, the impedance measured for this case should not be expected to lie along the transmission line replica impedance or inside the correct zone of operation, as it is highly affected by the CIREPP's control system.

Commercial distance relays utilize alternatives to impedance calculation to find the zone in which the fault has occurred. For instance, several relays, such as [61] and [62], compare the angle α between a polarizing and an operating quantity, denoted by V_{pol} and V_{op}, respectively, to form a mho characteristic, i.e., $\alpha = \measuredangle V_{op} - \measuredangle V_{pol}$. V_{pol} is normally the memorized positive sequence voltage, since it is not affected by low fault voltages, and provides a better fault resistance coverage. V_{op} is given by (3.2) for the AG element.

$$V_{op-AG} = V_A - Z_r \left(I_A + K^{\mathrm{o}} I^{\mathrm{o}} \right) \tag{3.2}$$

Z_r is the reach impedance of the respective zone in (3.2). This method, termed as α-based mho in this dissertation, asserts the trip signal of the relay's n-th zone if the

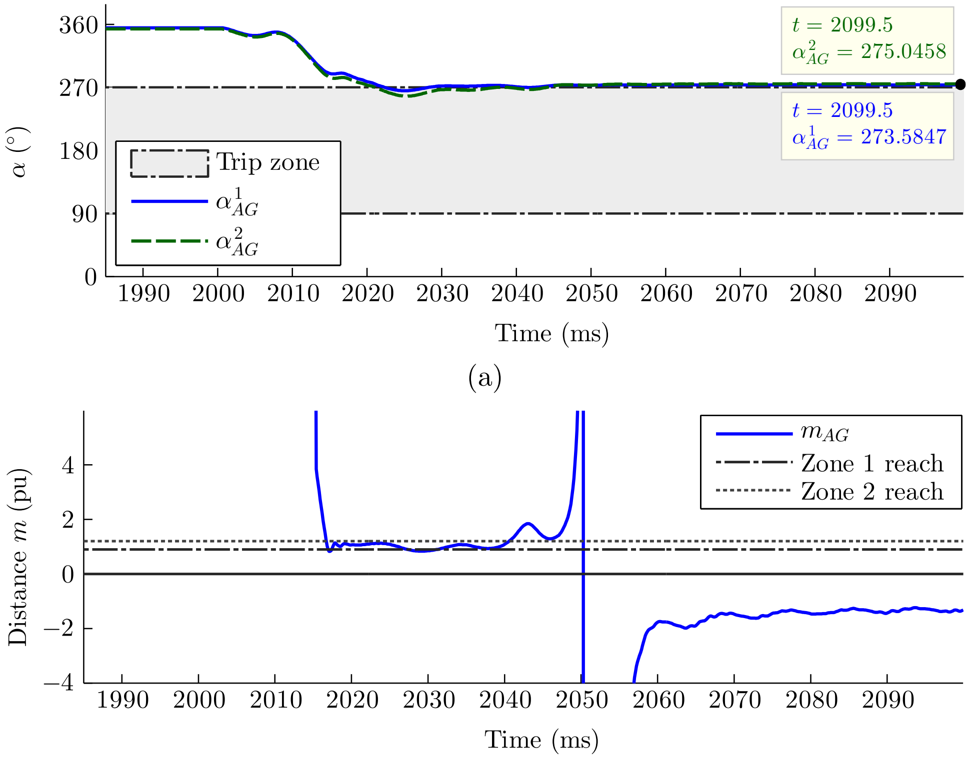

(a)

(b)

Figure 3.14. Operation of the AG element of industrial mho elements for case 3, (a) α-based mho, (b) m-based mho.

corresponding angle, denoted by α^n, is inside the [90°, 270°] interval.

Another group of relays, such as [36] and [39], express the mho characteristic by finding the per-unit distance to an AG fault using (3.3) [63]. This method, referred to as m-based mho in this dissertation, defines similar relations for the other fault loops.

$$m_{AG} = \frac{\text{real}\left(V_A\, V^*_{pol}\right)}{\text{real}\left(Z_r(I_A + K^\circ I^\circ)V^*_{pol}\right)} \tag{3.3}$$

The operation of commercial mho elements for case 3 is illustrated in Figure 3.14. α^1 and α^2 of the AG element of DS25 for case 3 approach the tripping zone in Figure 3.14(a) during the transient response time of the CIREPP's control system, but they maintain 3.5° and 5° distance from the trip boundaries after the transients disappear. m_{AG} decreases

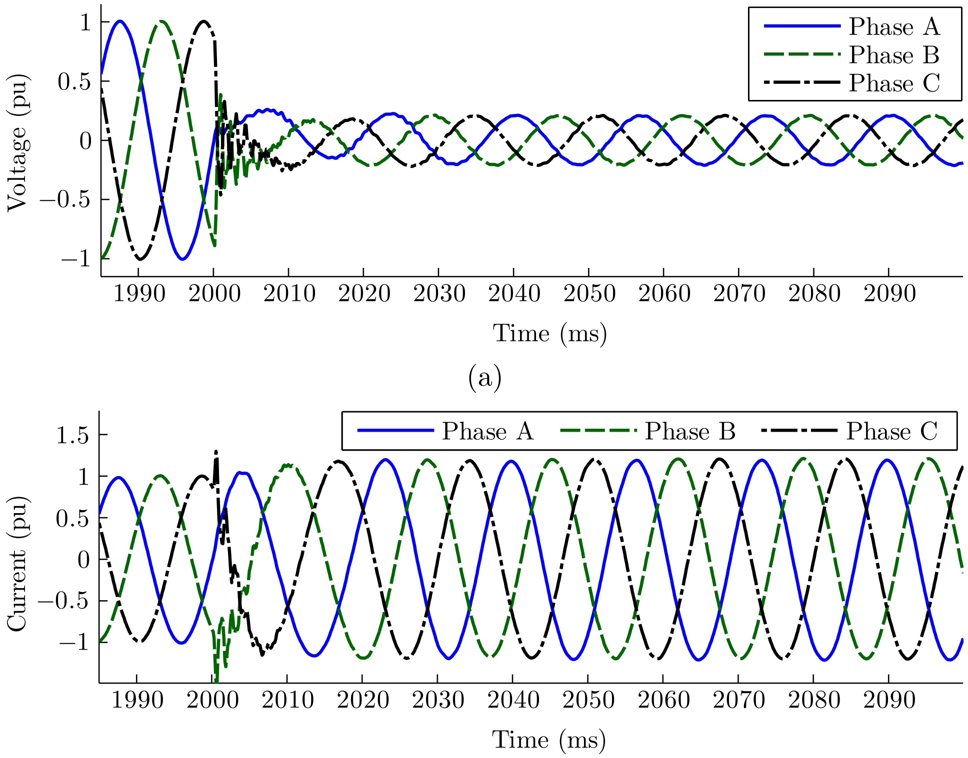

(a)

(b)

Figure 3.15. Measurements at the CIREPP's POI for case 4, (a) Voltage, (b) Current.

down to around zone two reach setting after the fault inception in Figure 3.14(b), but jumps significantly once the CIREPP increases the reactive current, causing a no-trip decision.

For a fault at zone one reach setting, the reactance and α^1 measured by DS25 are 163 Ω and 279°, respectively, which are at even greater distances from their trip zones.

3.3.4 Case 4

Case 2 of Section 3.3.2 is re-simulated, while the fault resistance is increased to 10 Ω. The voltage and current of DS25 are shown in Figure 3.15. In contrast to case 2, where the GC requirement was impossible to meet, the PF curve in Figure 3.16(a) indicates that the CIREPP restores the control over the output current and keeps the PF above 0.95 shortly after the fault inception. As a result, the CIREPP power for phase A in Figure 3.16(b)

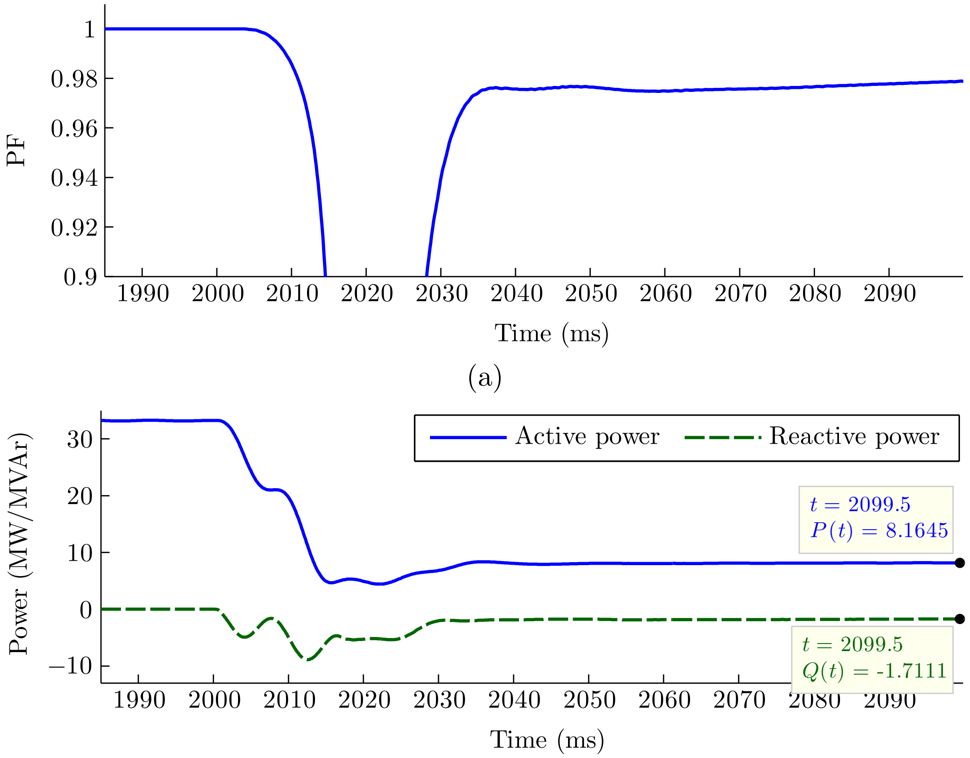

(a)

(b)

Figure 3.16. CIREPP's NA-GC compliance for case 4, (a) PF, (b) Phase A power

is mainly active, and the reactive component takes a small negative value. These power curves are directly reflected in the resistance and reactance measured by the AG and BC elements of DS25, depicted in Figure 3.17(a). A large positive resistance is followed by a small negative reactance, making the operating point fall in the fourth quadrant outside zone one, and putting the dependability of DS25 in jeopardy.

Comparison of totally different impedances measured for the same fault condition in Figures 3.12(b) and 3.17(a) reveals the high dependence of DS25 on the CIREPP's control system. Memory-polarized mho elements do not function properly either. α_{AG}^{1} in Figure 3.17(b) is about 5° above the tripping zone. Only α_{AG}^{2} is on the boundary of the $[90°, 270°]$ interval, which leads to unnecessary delayed tripping. The per-unit distance measured by the m-based mho element in Figure 3.17(c) is also fixed at 1.14, resulting in delayed relay operation.

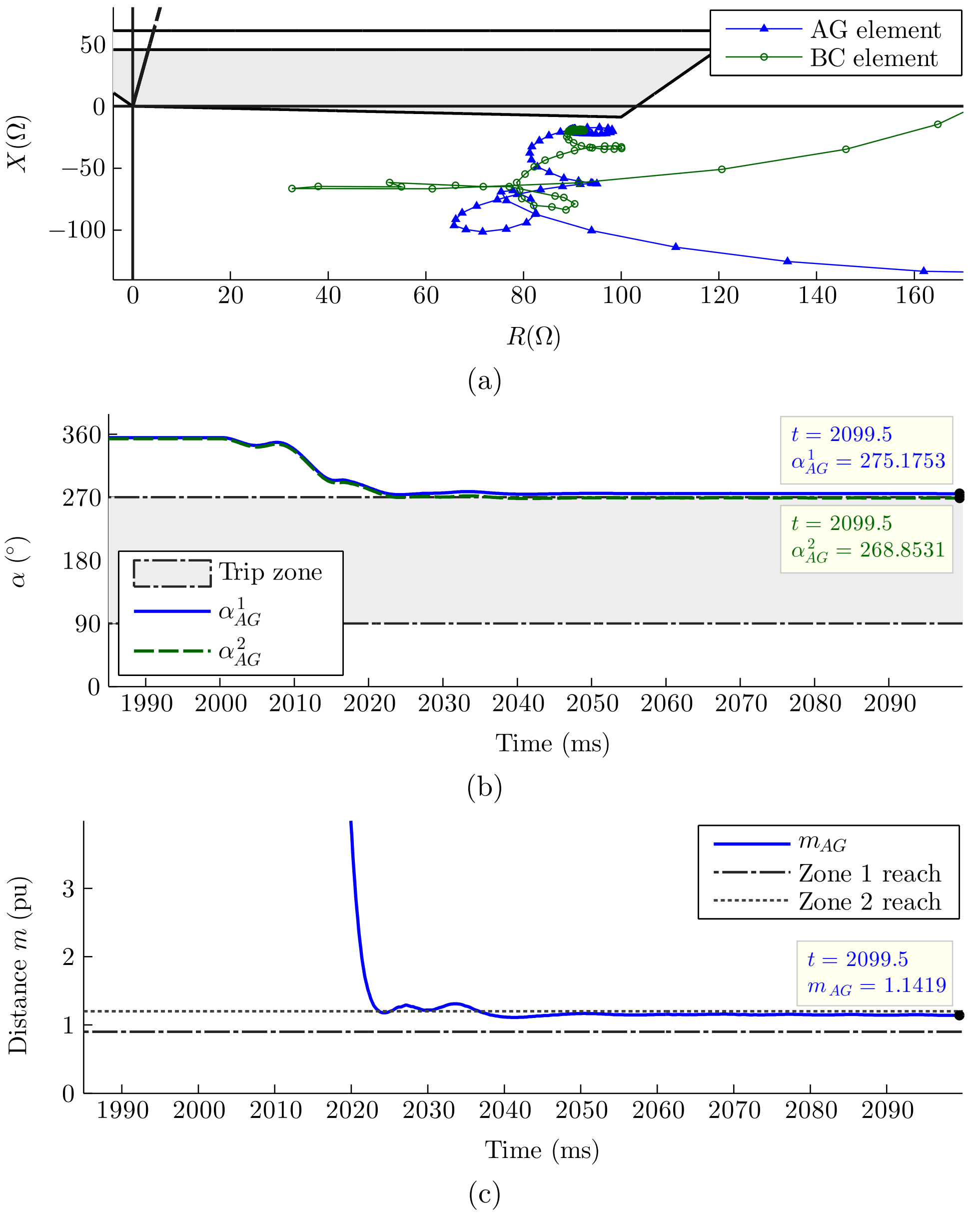

Figure 3.17. Performance of DS25 for case 4,
(a) Impedance measured by AG and BC elements, (b) α-based mho, (c) m-based mho

3.4 Zone One Unbalanced Faults

Discussion of the relay maloperation for balanced faults in the last section was from the viewpoint of the CIREPP's active and reactive power generation. This approach cannot properly explain the relay behavior in the event of unbalanced short-circuits. On the other hand, it is instructive to examine the relay performance using the practices established for studying the impact of remote infeed and fault resistance on distance protection. The insight gained will be helpful in providing a clue to overcome the problems later on. This approach is adopted to analyze zone one unbalanced faults.

3.4.1 Case 5

A phase B to phase C to ground (BCG) fault with 10 Ω fault resistance, the middle of which was grounded, was simulated at 80% of line 25. The fault currents of the CIREPP when it follows the NA-GC are depicted in Figure 3.18(a). Figure 3.18(b) displays the currents at the remote end of the line, which are substantially larger. The impedance of the BC element of DS25 in Figure 3.19(a) falls in the fourth quadrant outside zone one, thereby failing to trip the line. Both the zone one and zone two angles of the BC element of the α-based mho element remain outside the tripping area in Figure 3.19(b), as well. Also, the m-based mho element spuriously measures a per-unit distance far above the reach setting of zone one in Figure 3.19(c).

For the circuit of Figure 3.20, which demonstrates a BCG fault with R_{ph} and R_g as the phase-to-phase and phase-to-ground resistances at the fault, Kirchhoff's voltage law (KVL) can be expressed as

$$V_{BL} - V_{CL} = Z_f I_{BL} - Z_f I_{CL} + R_{ph}\left(I_{BL} + I_{BR}\right) - R_{ph}\left(I_{CL} + I_{CR}\right) \tag{3.4}$$

where Z_f is the positive sequence impedance between the relay and the fault, and the L and R subscripts denote local and remote end quantities, respectively. Rearranging the terms in (3.4) and dividing the two sides over $(I_{BL} - I_{CL})$ yields the impedance measured by the BC element in (3.5).

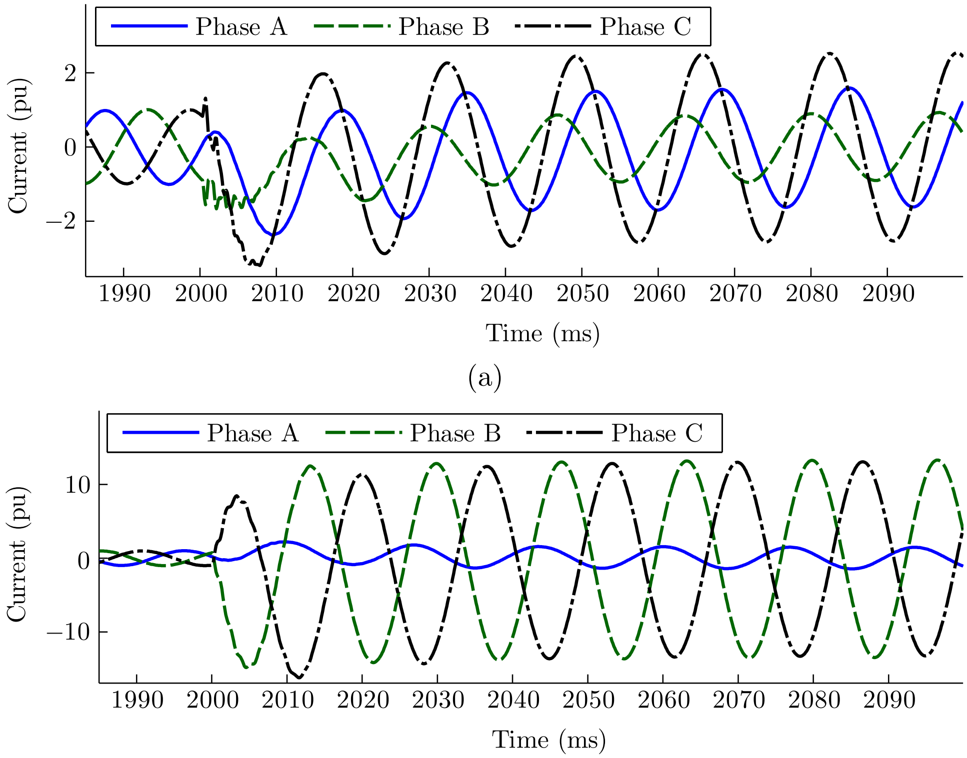

(a)

(b)

Figure 3.18. Current measurements for case 5, (a) Local end, (b) Remote end.

$$Z_{BC} = Z_f + R_{ph} \underbrace{\left(1 + \frac{I_{BR} - I_{CR}}{I_{BL} - I_{CL}}\right)}_{M_{R_f-BC}} \tag{3.5}$$

The primary effect of $R_{ph}M_{R_f-BC}$ is normally on the resistive part of Z_{BC}. That is why a quadrilateral characteristic, whose resistive reach can be set independently, is known to be more robust against the effect of fault resistance. Meanwhile, due to load flow in the system before the fault inception, the phase angles of the local and remote end currents are not identical, making M_{R_f-BC} a complex number, and adding a fictitious reactance to Z_{BC}. A distance relay would, therefore, be in danger of overreach or underreach [22].

Founded upon the voltage source modeling of the systems behind the relays, a basic assumption in distance protection is that the phase difference between the two end currents

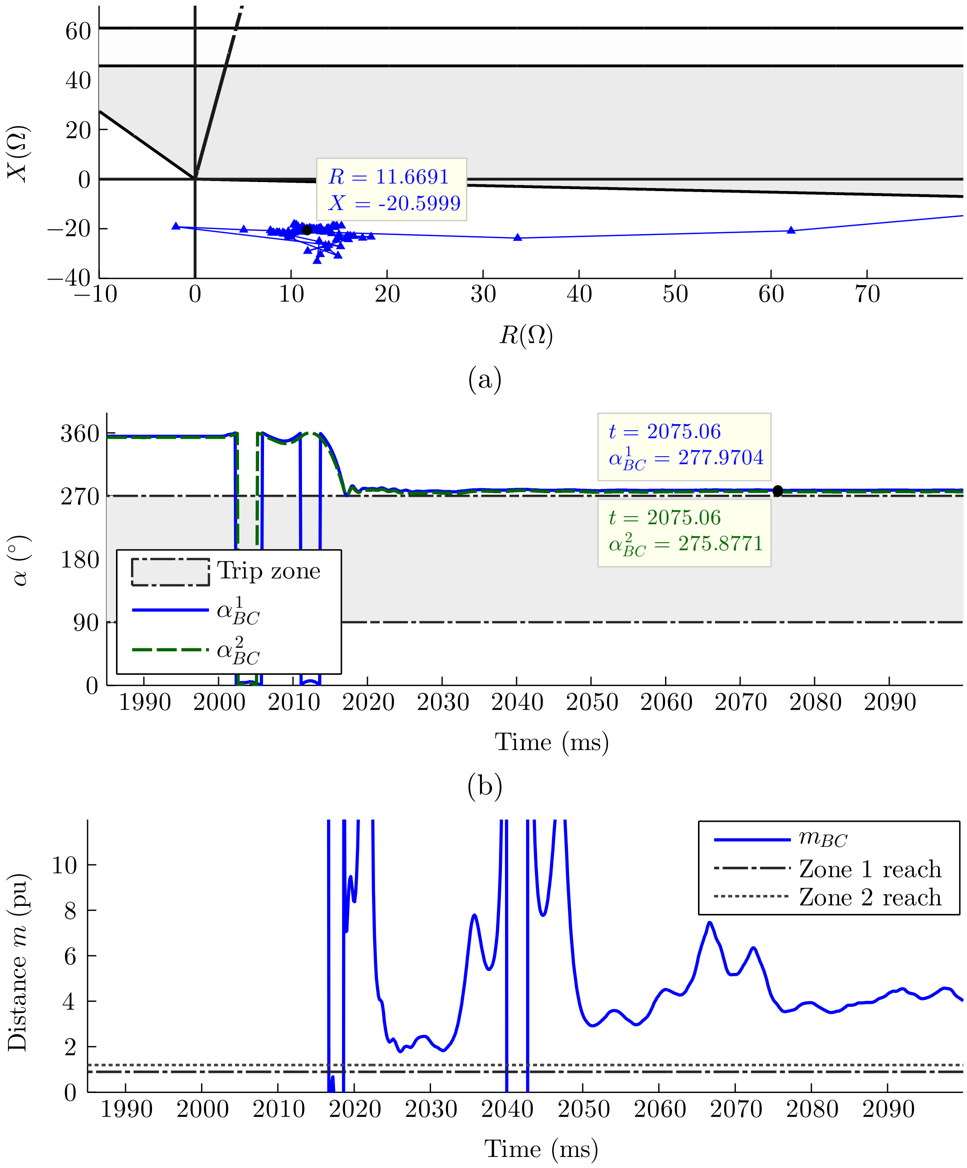

(a)

(b)

(c)

Figure 3.19. Performance of BC element of DS25 for case 5, (a) Measured impedance, (b) α-based mho, (c) m-based mho

is similar to that between the two end pre-fault voltages [64]. As a result, the angles of the two end currents typically differ by only a few degrees, since a sizable phase difference

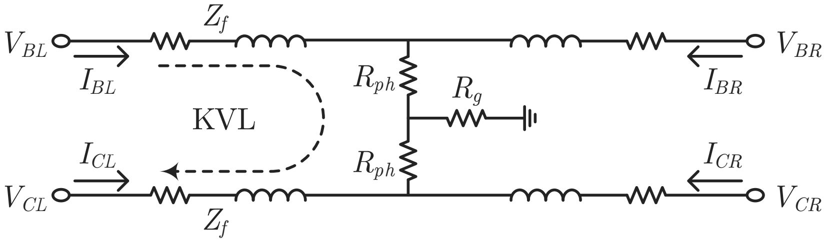

Figure 3.20. Circuit diagram of phases B and C for a BCG fault

between the two end voltages may harbor the risk of instability. Therefore, the fictitious reactance caused by the combined effect of remote infeed and fault resistance is normally insignificant.

In a conventional power plant that operates as a voltage source, the phase angles of fault currents are determined based on the system impedance and the source angle. For a CIREPP, however, the converter current is governed by the control system and according to the host system GC or the internal references. Therefore, the above routine assumption regarding the phase difference between the line end currents does not hold true. The local currents in phases B and C of Figure 3.18(a) are $I_{BL} = 0.893\measuredangle 159.1°$ and $I_{CL} = 2.515\measuredangle 108.4°$ pu. For the remote end currents of Figure 3.18(b), I_{BR} and I_{CR} equal $13.332\measuredangle 165.4°$ and $13.117\measuredangle 20.1°$ pu, respectively. Since the zero-sequence component flowing through the ground of the CIREPP's main transformer constitutes the bulk of the local currents, $(I_{BL} - I_{CL})$, which appears in the denominator of M_{R_f-BC} and is plotted in Figure 3.21(a), is much smaller than $(I_{BR} - I_{CR})$, enlarging the magnitude of M_{R_f-BC}. More importantly, the phase difference between $(I_{BL} - I_{CL})$ and $(I_{BR} - I_{CR})$ in Figure 3.21(b) exceeds 86°. Thus, $R_{ph}M_{R_f-BC}$ becomes $9.02-j60.87\ \Omega$. Considering $Z_f = 2.86+j40.62\ \Omega$, $R_{ph}=5\ \Omega$ and $R_g=0\ \Omega$, the Z_{BC} given by (3.5) would be $11.88-j20.25\ \Omega$, which agrees with the measurements shown in Figure 3.19(a) and causes the relay to overreach.

3.4.2 Case 6

To demonstrate the heavy reliance of the above relay behavior upon the CIREPP's control system, consider the same fault condition when the CIREPP meets the EU-GC. The

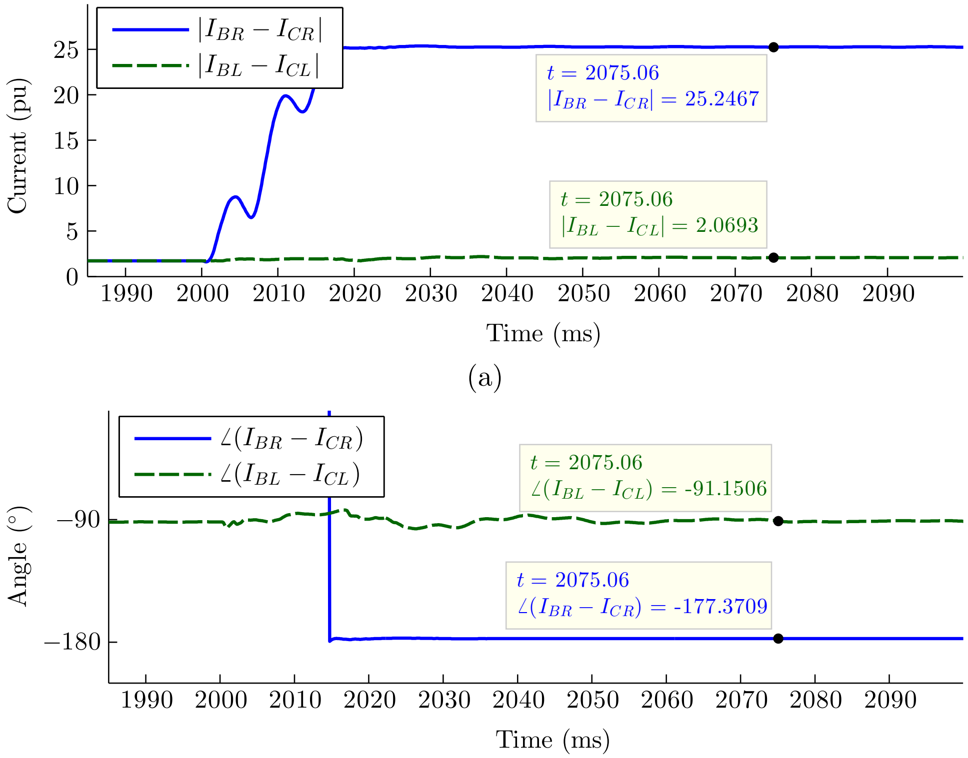

(a)

(b)

Figure 3.21. The numerator and denominator of M_{R_f-BC} for case 5, (a) Magnitude, (b) Angle.

currents at the local and remote end of the line are depicted in Figure 3.22. The resistance and reactance measured by the BC element of DS25 are displayed with respect to time in Figure 3.23(a). Similar to Figures 3.12 and 3.17(a), the two curves undergo notable fluctuations caused by the CIREPP's transient response. Inside the impedance plane of Figure 3.23(b), the operating point initially falls inside zone one for less than 5 ms, and then moves through zone two, eventually lying at $Z = 62.37 + j70.98$ Ω, outside the first two zones. The period during which the impedance passes through the first two zones will be much shorter if the CIREPP does not operate at unity PF and generates reactive power prior to the fault–not an uncommon scenario for the EU-GCs.

$(I_{BL} - I_{CL})$ and $(I_{BR} - I_{CR})$ in Figure 3.24 are $2.080\measuredangle 154.3°$ and $25.619\measuredangle -176.6°$ pu, respectively. Therefore, diametrically opposed to the impedance measured for case 5, where

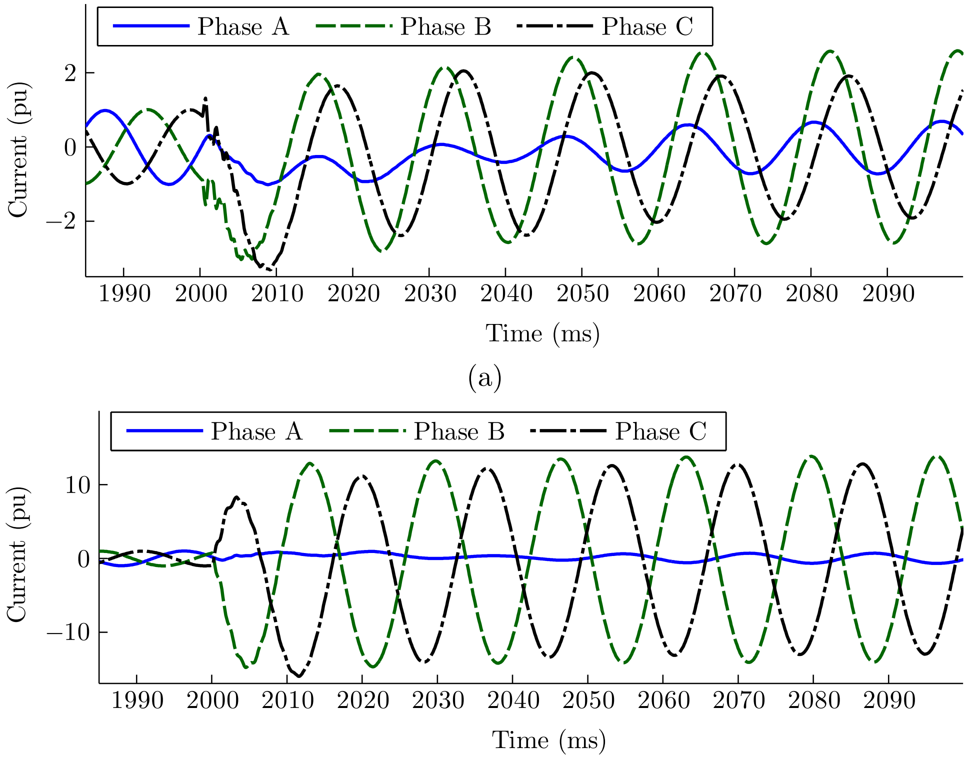

(a)

(b)

Figure 3.22. Current measurements for case 6, (a) Local end, (b) Remote end.

$R_{ph}M_{R_f-BC}$ had a large negative imaginary part, the fictitious reactance added to Z_{BC} is $58.81 + j29.96\ \Omega$, leading to considerable underreach. The marked difference between Z_{BC} for cases 5 and 6 happens despite the identical pre-fault voltage angles at the two line ends and exactly the same fault condition, which should result in equal underreach or overreach according to well-established distance protection principles.

3.4.3 Other Fault Types

The problems associated with LLG faults in relation to the combined effect of remote infeed and fault resistance are valid for LL faults as well. The positive and negative sequence components are basically similar for LLG and LL short-circuits. The main difference is the absence of the zero sequence component in LL fault currents. However, since the phase currents are subtracted in the numerator and denominator of M_{R_f-BC}, the zero-sequence

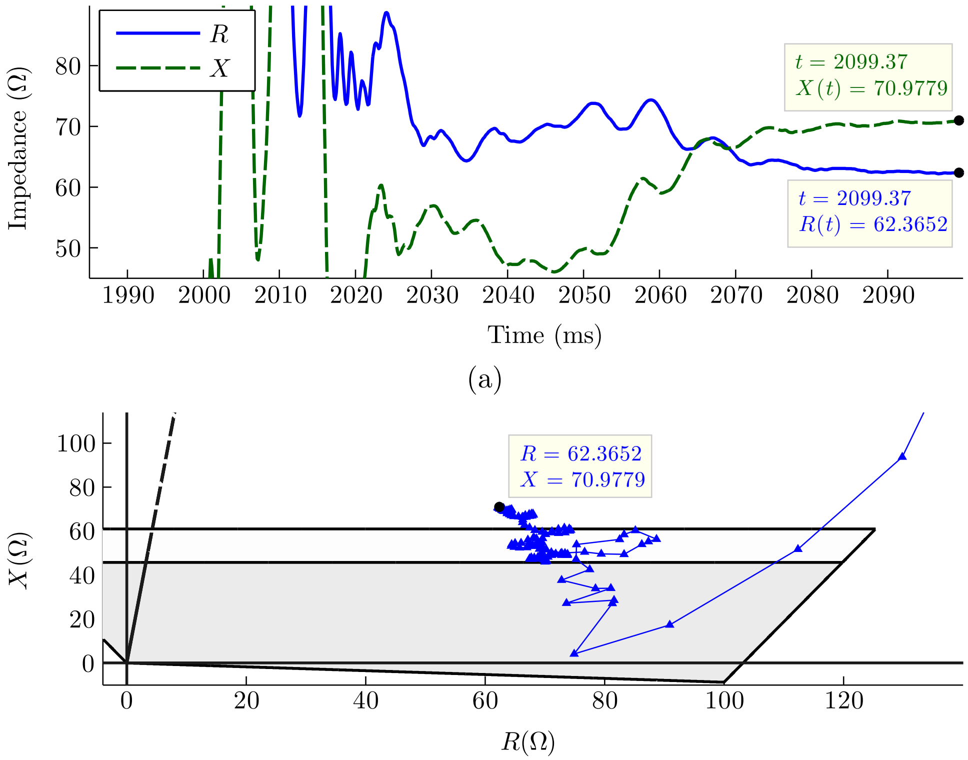

(a)

(b)

Figure 3.23. Performance of the BC element of an impedance-based DS25 for case 6, (a) Impedance versus time, (b) Impedance plane.

current does not impact M_{R_f-BC} and the consequent relay malfunction. Take, for instance, cases 5 and 6 without the ground at the fault, designated as cases 7 and 8, respectively. The resultant Z_{BC} is depicted in Figure 3.25. The impedances pinpointed in this figure are quite close to those previously shown for cases 5 and 6, and are far outside zone one of DS25.

In contrast to balanced, LLG and LL faults, for which the measured reactance may not be even remotely close to the actual fault reactance, a distance relay performs more successfully for SLG faults. That being said, the common countermeasures against underreach and overreach of a ground distance element due to remote infeed does not yield successful results if a CIREPP is connected to the line, requiring special precautions elaborated in Chapter 4.

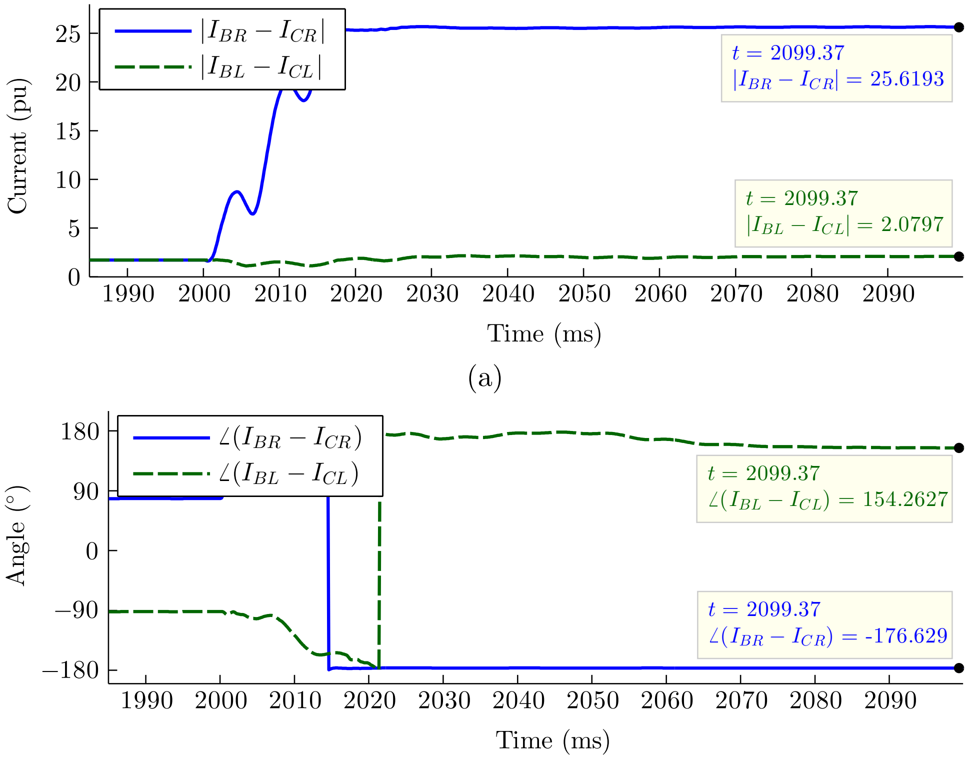

(a)

(b)

Figure 3.24. The numerator and denominator of M_{R_f-BC} for case 6, (a) Magnitude, (b) Angle.

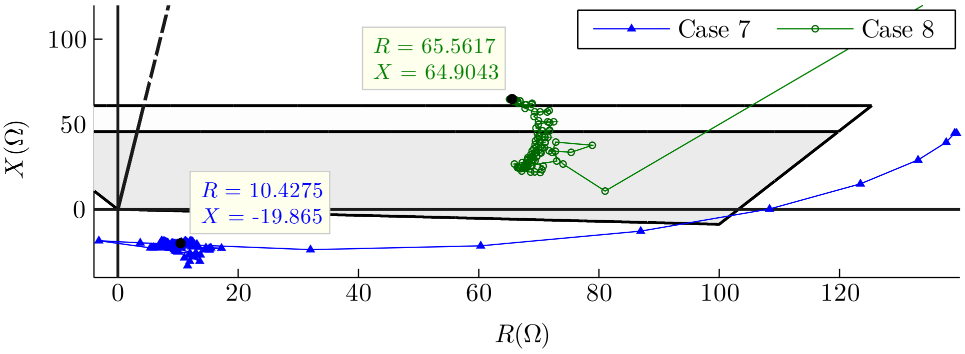

Figure 3.25. The impedance measured by the BC element of DS25 for cases 7 and 8.

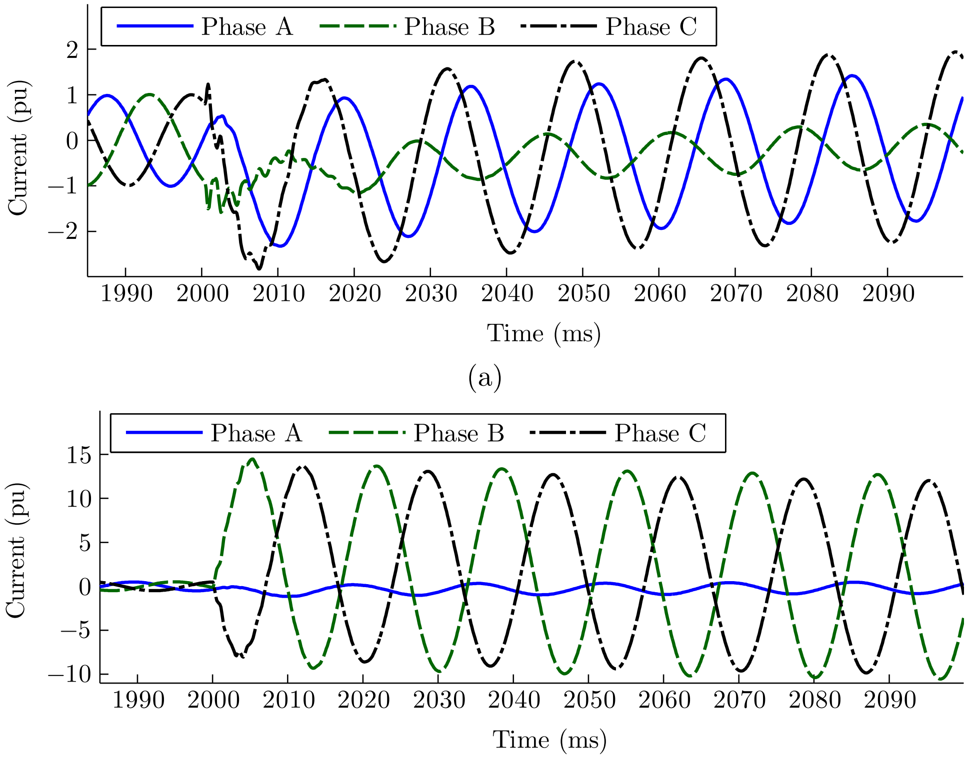

(a)

(b)

Figure 3.26. Current measurements for case 9, (a) Local current, (b) Infeed current.

3.5 Zone Two Faults

In the event of short-circuits on neighboring lines, DS25 is in danger of malfunction even if the fault is bolted. While the relay suffered from lack of dependability in the last two sections, the faults on adjacent lines may jeopardize the security of the protection system and, in turn, neutralize the GCs' FRT articles. The relay may also fail to provide the anticipated back-up protection.

3.5.1 Case 9

The currents recorded by DS25 for a bolted zone two BCG fault on line 45, only 10 km away from bus 5 when the CIREPP complies with the NA-GC are plotted in Figure 3.26(a).

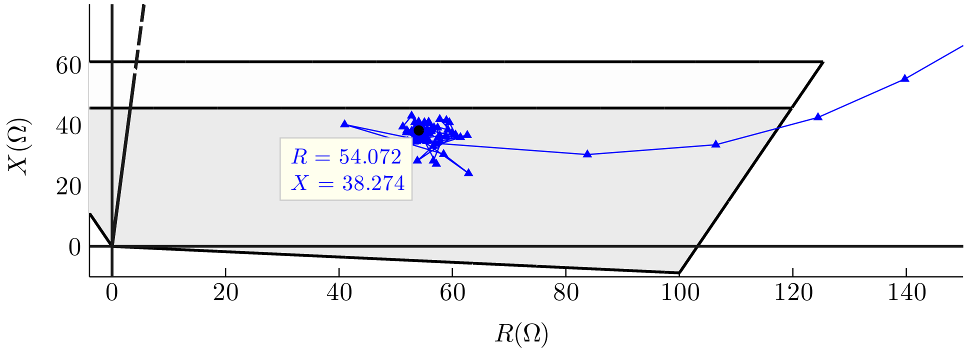

Figure 3.27. The impedance measured by the BC element of DS25 for case 9.

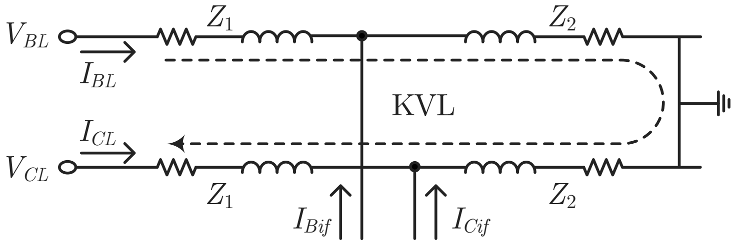

Figure 3.28. Circuit diagram for a bolted BCG fault with intermediate infeed.

While DS25 operation must be delayed to let line 45's relays clear the fault, the impedance measured by the BC element of DS25 in Figure 3.27 illustrates that zone one of the relay is asserted soon after the onset of the fault; thus, the line is tripped immediately. Any FRT scheme implemented in the CIREPP is subsequently negated by the incorrect relay operation.

Since the fault is solid, the relay malfunction is not caused by the currents flowing from the remote end of line 45. The other currents present in the fault loop are the intermediate infeeds, i.e., the currents flowing from lines 15, 35 and the reactor. Figure 3.26(b) shows the sum of the infeed currents, which are appreciably larger than the local currents, due to the CIREPP's modest short-circuit capacity. Meanwhile, intermediate infeed has been known to cause a distance relay to underreach [65, 66], whereas the relay has overreached. To investigate this issue, let us consider the circuit diagram of the fault in Figure 3.28. The KVL for the BC loop can be expressed as

$$V_{BL} - V_{CL} = Z_1 \left(I_{BL} - I_{CL}\right) + Z_2 \left(I_{BL} + I_{Bif} - I_{CL} - I_{Cif}\right) \tag{3.6}$$

where the *if* subscript denotes infeed quantities, Z_1 is the impedance between the relay and infeed location, and Z_2 is the impedance between the infeed and the fault. Dividing (3.6) over $(I_{BL} - I_{CL})$ yields

$$Z_{BC} = Z_1 + Z_2 + Z_2 \underbrace{\left(\frac{I_{Bif} - I_{Cif}}{I_{BL} - I_{CL}} \right)}_{M_{if-BC}} \tag{3.7}$$

$Z_2 M_{if-BC}$ is the fictitious impedance added to Z_{BC} by the intermediate infeed. Similar to the discussion that followed (3.5), the difference between the angles of the local and infeed currents in a conventional power system is considered to be almost equal to the difference between the voltage angles before the fault, which is normally small. Therefore, the imaginary part of M_{if-BC} is insignificant, and the angle of $Z_2 M_{if-BC}$ is very close to that of the fault impedance. That is why a distance relay has been traditionally known to underreach in the presence of intermediate infeed [65, 66].

Since the angles of CIREPP-generated currents are not related to pre-fault voltages and are determined based on the GC requirements or internal references, the above analysis does not hold true in the presence of a CIREPP. Even for the same GC, the angle of a CIREPP fault current may be quite unpredictable. Take, for instance, the Spanish GC where the operating point of a CIREPP can be anywhere inside the shaded area of Figure 3.1, or the German GC where the slope of the reactive current curve versus the voltage drop can vary from 0 to 10 [20], or the NA-GC that allows any PF higher than 0.95. On top of that, the GC reactive current requirements always permit a transient response time, which is longer than operational times of distance relays. For example, the operating point of a WF that complies with the Spanish GC is allowed to be outside the shaded area of Figure 3.1 for 150 ms after the voltage drops, resulting in erratic current angles during distance relay operation time spans.

After the transients fade out, the phase B and C infeed currents in Figure 3.26 are $11.578\measuredangle 158.8°$ and $10.960\measuredangle 11.7°$ pu, respectively. The DS25 current phasors are $I_{BL} = 0.484\measuredangle{-163.5°}$ and $I_{CL} = 2.074\measuredangle 113.5°$ pu. Hence, as shown in Figure 3.29, the numerator and denominator of M_{if-BC} are $21.614\measuredangle 174.8°$ and $2.072\measuredangle{-79.9°}$ pu, respectively, and exhibit a significant phase difference. Therefore, the angle of $Z_2 M_{if-BC}$ lags that of Z_2 by

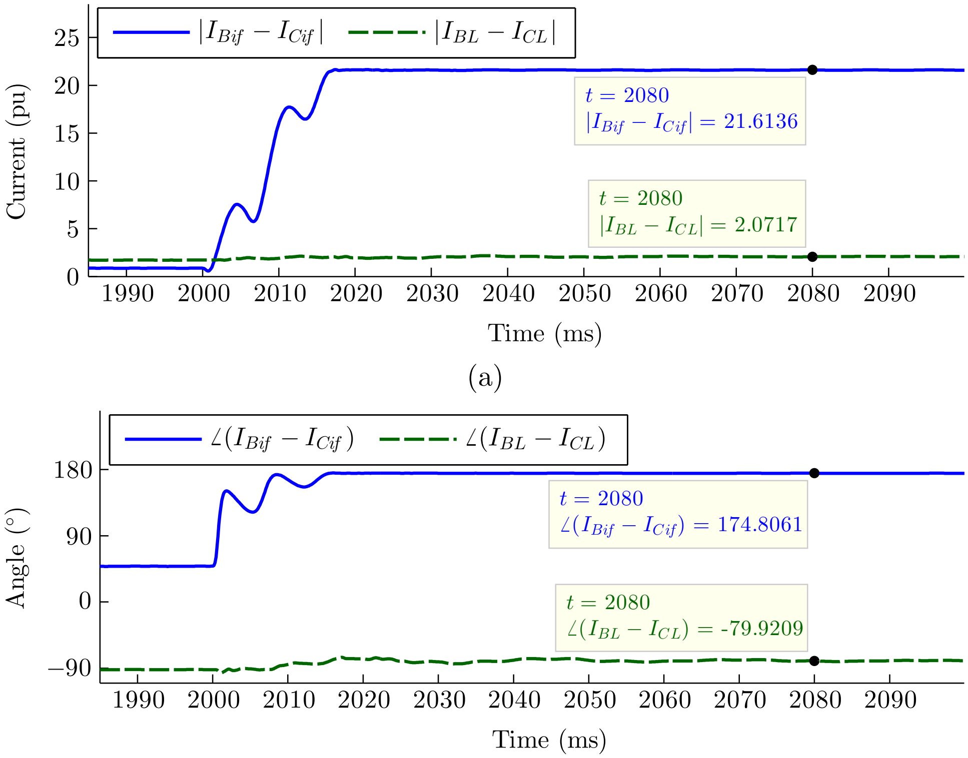

(a)

(b)

Figure 3.29. The numerator and denominator of M_{if-BC} for case 9, (a) Magnitude, (b) Angle.

105.3°, which makes the reactance measured by DS25 smaller than the actual reactance to the fault by about 18 Ω, and induces substantial overreach. Similar incorrect operation is observed for mho elements as well.

3.5.2 Case 10

The fault of case 9 is simulated when the CIREPP conforms to the EU-GC. The local and infeed currents are shown in Figure 3.30. At the relay side, the phase B and C currents are $1.827\measuredangle 130.4°$ and $2.031\measuredangle 65.3°$ pu, respectively, making the denominator of M_{if-BC} in Figure 3.31 equal to $2.083\measuredangle{-167.4}°$ pu. For the infeed quantities, $I_{Bif} = 11.699\measuredangle 160.0°$ and $I_{Cif} = 10.799\measuredangle 11.8°$ pu, leading to $21.638\measuredangle 175.2°$ pu for the numerator of M_{if-BC} in Figure 3.31. Plugging these values into (3.7), the reactance measured by the relay becomes

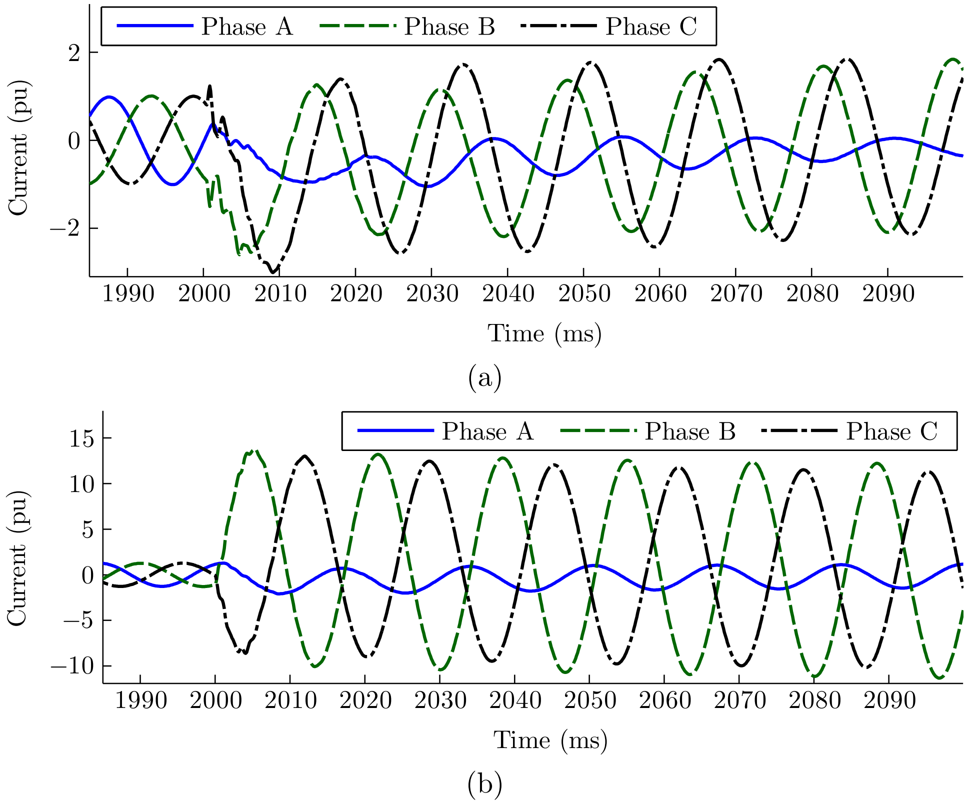

Figure 3.30. Current measurements for case 10, (a) Local current, (b) Infeed current.

105.08 Ω, which is consistent with the impedance measured by DS25 in Figure 3.32, and is almost twice the actual fault reactance. In contrast to case 9, where the intermediate infeed caused overreach, DS25 underreaches for this case. The excessive magnitude of underreach arises from the limited non-zero sequence components of the CIREPP currents and the removal of the zero-sequence component due to the subtraction of the current phasors in (3.7). Apart from the huge underreach, the impedance shown in Figure 3.32 includes a significant resistive part as well, even though the fault is bolted.

These problems exist in spite of the fact that the infeed currents flow through less than 10% of the distance between the fault and DS25. The problems are exacerbated if the fault location is farther from the infeed point or if there is a fault resistance. Cases 9 and 10 have discussed LLG faults, but the same problems also apply to LL and balanced faults.

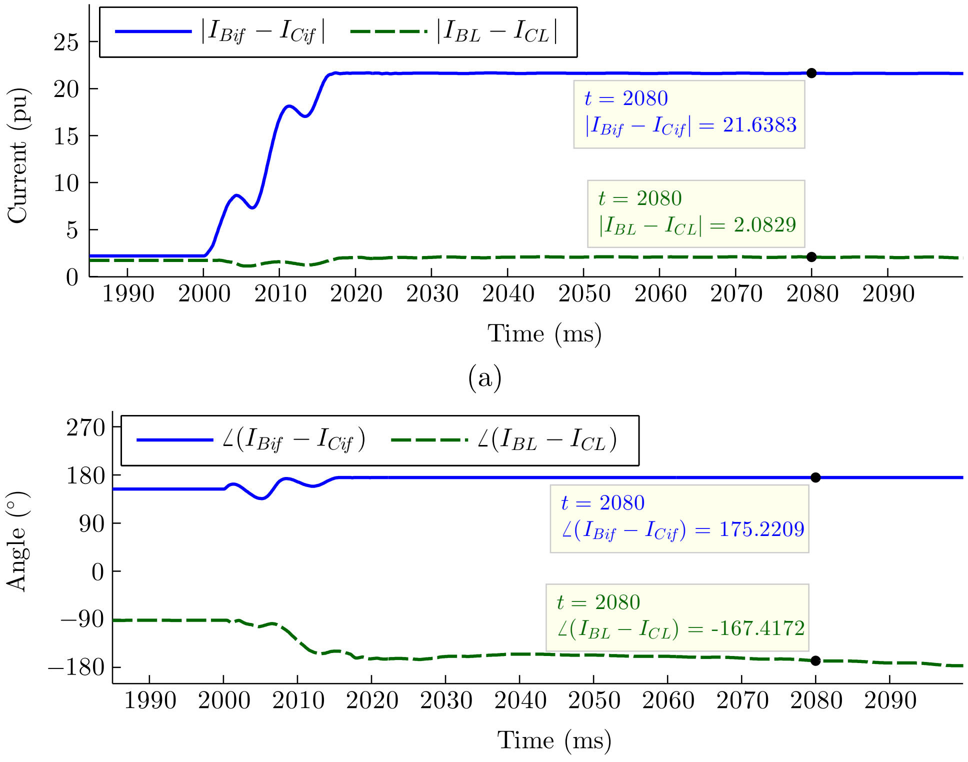

Figure 3.31. The numerator and denominator of M_{if-BC} for case 10, (a) Magnitude, (b) Angle.

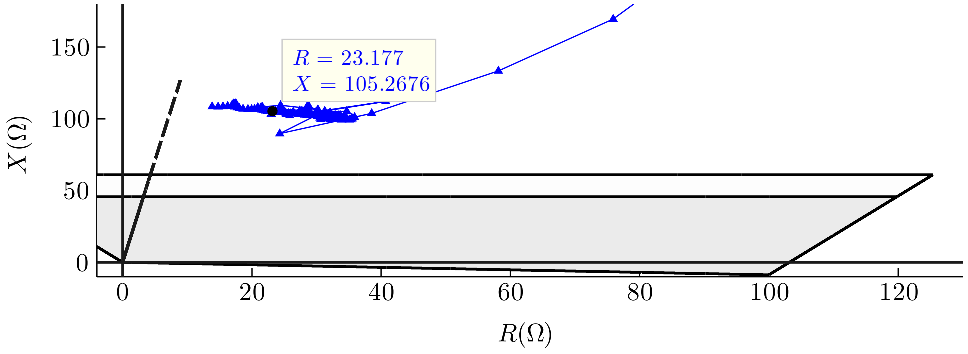

Figure 3.32. The impedance measured by the BC element of DS25 for case 10.

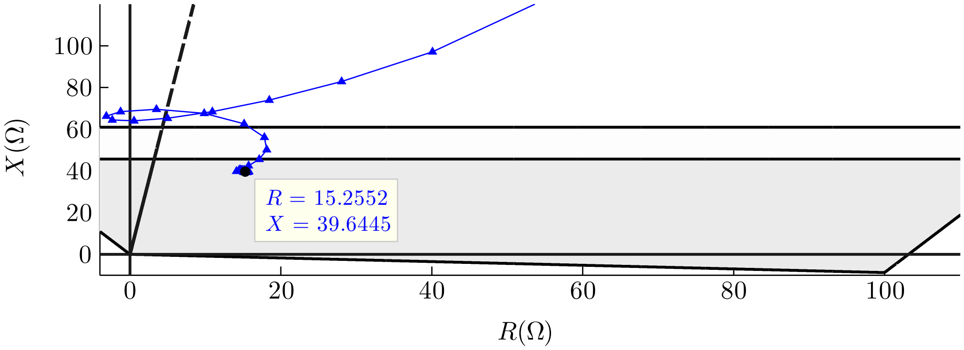

Figure 3.33. The impedance of the BC element of DS25 for the fault of Section 3.4 when the CIREPP is replaced by a conventional source.

3.6 DS25 Operation for a Conventional Source

To further highlight the effect of a CIREPP on line 25 protection, the CIREPP was replaced by a conventional source whose impedance and phase angle are $12.7\measuredangle 88.9°$ Ω and 4.5°. The active and reactive powers of this source are similar to those of the CIREPP. As shown in Figure 3.33, the impedance calculated by DS25 for the zone one fault of Section 3.4 correctly enters zone one in less than one cycle. Unlike Figures 3.19(a) and 3.23(b), which exhibited huge overreach and underreach, a less than 1 Ω overreach is observed. If the fault is on the zone boundary, such small overreach can easily be addressed by tilting the reactance element of the relay by a few degrees. The correct operation of DS25 in Figure 3.33 stems from the relatively close angles of the two line end fault currents. The magnitudes and angles of the terms in the numerator and the denominator of M_{R_f-BC} are plotted in Figure 3.34. In contrast to Figures 3.21(b) and 3.24(b), the current magnitudes and angles in Figure 3.34 are very close. Plugging the values pinpointed in Figure 3.34 into (3.5) yields the impedance shown in Figure 3.33.

The operation of DS25 was tested for the zone two fault of Section 3.5 as well. The impedance in Figure 3.35 is almost at the edge of zone two. Nevertheless, this is the normal underreach expected due to the intermediate infeed. In contrast to Figures 3.29(b) and 3.31(b), the numerator and denominator of M_{if-BC}, displayed in Figure 3.36, are almost aligned, as a result of which the impedance in Figure 3.35 exhibits the normal zone two underreach, and is also situated on the line replica impedance. Moreover, the comparable

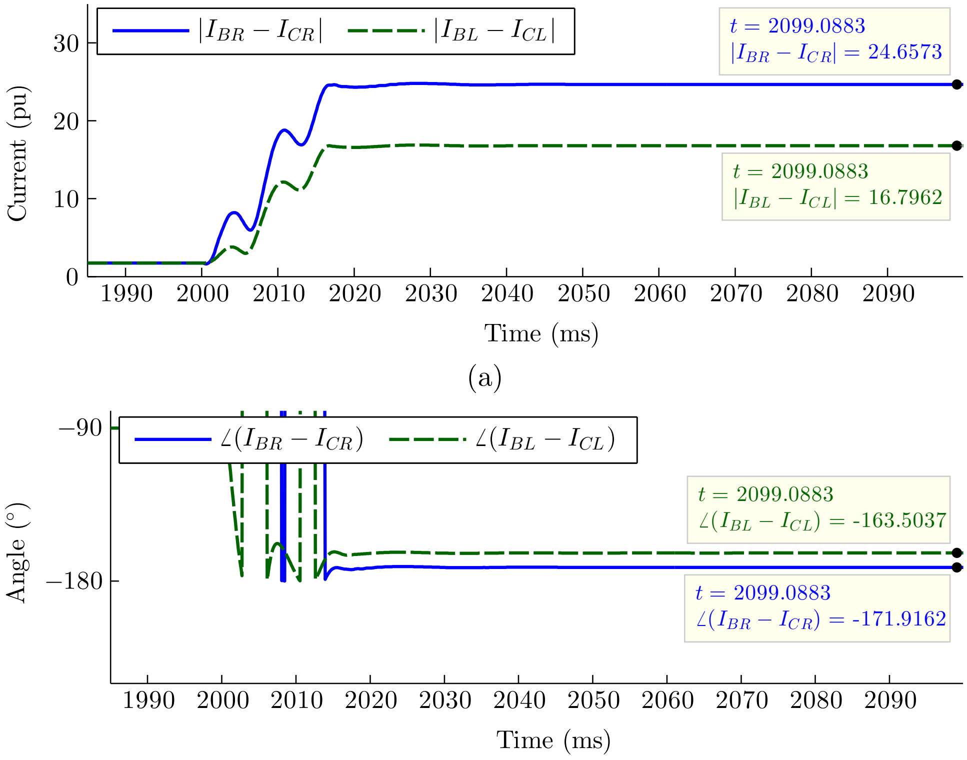

(a)

(b)

Figure 3.34. The numerator and denominator of M_{R_f-BC} for the fault of Figure 3.33, (a) Magnitude, (b) Angle.

magnitudes of the local and infeed currents keep the amount of underreach small.

3.7 Conclusion

For non-bolted balanced faults in zone one of DS25, the CIREPP keeps control over the current. The reactive current for EU-GCs translates into impedances close to the X axis. The CIREPP's large PF for the NA-GCs makes the impedance lie along the R axis. In both cases, the measured impedance can be far away from the actual fault impedance and is highly influenced by the parameters of the CIREPP's control system, such as $i_{\max}$.

The common assumption regarding the phase difference between the line end currents during a zone one fault is not valid for a line that emanates from a CIREPP. Consequently,

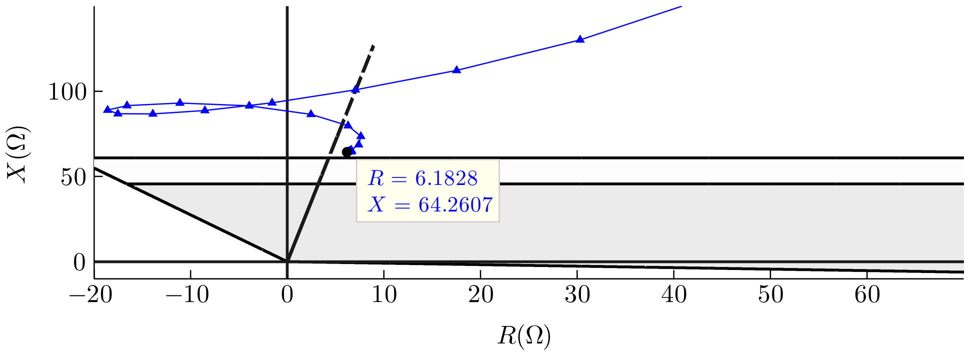

Figure 3.35. The impedance of the BC element of DS25 for the fault of Section 3.5 when the CIREPP is replaced by a conventional source.

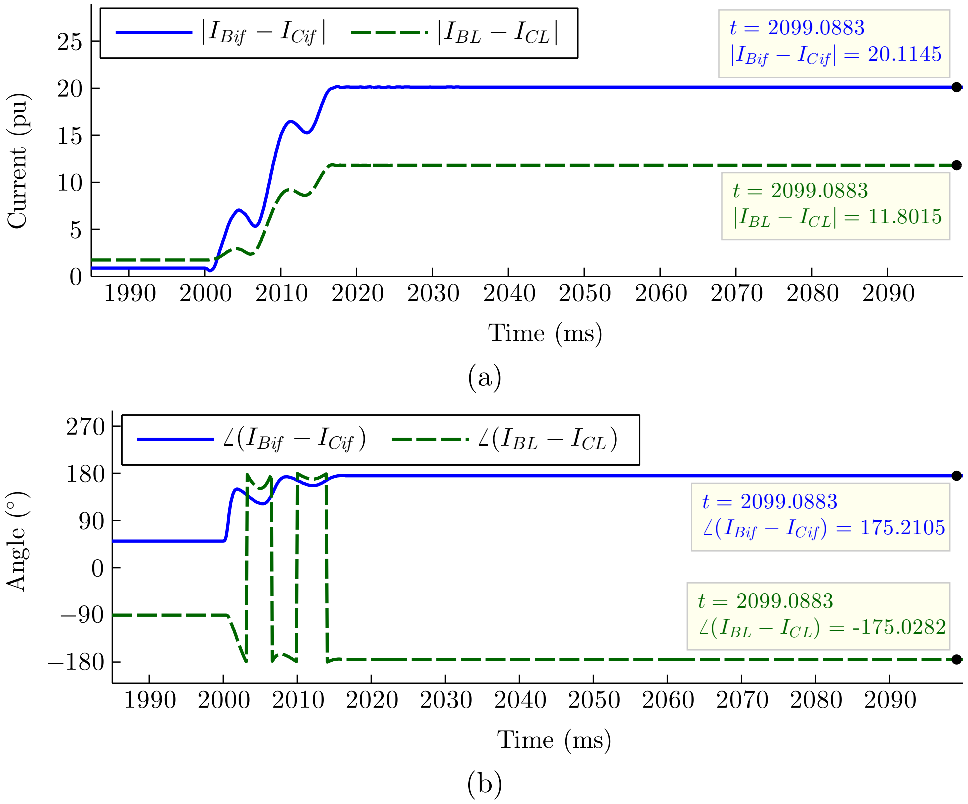

(a)

(b)

Figure 3.36. The numerator and denominator of M_{if-BC} for the fault of Figure 3.35, (a) Magnitude, (b) Angle.

it is highly likely that the underreach or overreach of DS25 due to the remote infeed during LL or LLG faults will become very large. The relay may also underreach for a case where it is normally expected to overreach.

The intermediate infeed has been known to cause distance relays to underreach. However, the angles of the local and infeed currents may be widely apart if a CIREPP is behind the relay. Depending on the CIREPP's control strategy, the relay may overreach during zone two faults, which negates any FRT scheme, or experience a huge underreach and fail to provide back-up operation.

Chapter 4

Distance Protection of Lines Emanating from CIREPPs: Solution Description and Evaluation

Having unveiled the problems associated with distance protection of lines connected to CIREPPs due to remote and intermediate infeed in Chapter 3, Section 4.1 describes why the countermeasures currently deployed by commercial relays to tackle these problems in a conventional power system fail in the presence of a CIREPP. Then, a new formula to calculate impedance is devised in Section 4.2 for the phase element of the relay to prevent maloperation in the event of LLG faults. In addition, Section 4.3 proposes a communication-assisted method with minimal bandwidth requirement for LL and balanced faults. Simplicity and independence from the GC requirements are among the objectives of the presented solutions. Section 4.4 presents the overall trip logic of the proposed relay. Comprehensive performance evaluations are carried out for different fault conditions in Sections 4.5, 4.6 and 4.7 to verify the reliable operation of the proposed methods. Section 4.8 discusses the issues that should be taken into consideration for SLG faults. Section 4.9 concludes this chapter.

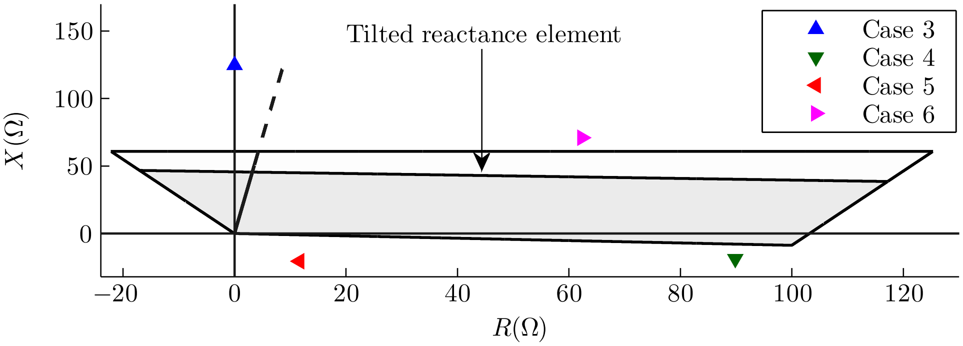

Figure 4.1. The impedances measured by DS25 for cases 3 to 6 of Chapter 3.

4.1 Existing Countermeasures

One solution for the problems discussed in Chapter 3 is to deploy line current differential relays. However, these relays require high-bandwidth communication infrastructure, which is expensive and not always available. Even with a high-bandwidth channel, there is a chance for the link failure [67], in which case the line is protected by the local back-up, that is, the distance relay. Even for a healthy channel, the trip logic applied by many utilities, such as Hydro One in Ontario, Canada, requires at least a zone two pick-up of the distance element in order for the other elements to trip the line.

The following explains why the existing solutions for the impact of remote and intermediate infeed fail to address the problems unveiled in Chapter 3 for the distance relays. Due to close angles of the line end voltages, the combined effect of remote infeed and fault resistance in a conventional system is usually insignificant and is, thus, sometimes even ignored in practice [68]. Meanwhile, the polarizing quantity of mho distance elements includes, at least partially, the memorized positive sequence voltage, which alleviates the effect of fault resistance to some extent. Nevertheless, it was demonstrated in Chapter 3 that the magnitude of the problem in the presence of a CIREPP was great enough to make memory-polarized mho elements malfunction as well. For quadrilateral characteristics, this problem is typically resolved by tilting the top reactance element up or down, depending on the power flow direction [69, 70]. The tilting angle is normally determined according to the phase difference between the line end voltages.

With the 230 kV base voltage and the $50.9\measuredangle 85°$ Ω impedance of line 25 in the test system of Figure 3.2, the 100 MW active power, which was the rated capacity of the CIREPP, can be transmitted through a 5.5° phase difference between the voltages at the ends of line 25. Hence, based on the instruction given in [71], and considering the 45.7 Ω and 100 Ω reactance and resistance reaches of zone one for the quadrilateral DS25, the reactance element should be tilted by less than 2.5°. The tilting direction is clockwise, as DS25 is at the power-sending end of the line. Figure 4.1 shows a quadrilateral characteristic for DS25 with the reactance element of zone one tilted clockwise by 2.5°. The figure also displays the impedances for cases 3 to 6 of Sections 3.3 and 3.4. For cases 4 and 5, the tilting angle is obviously not sufficient to make the two impedances fall inside zone one. Apart from the reactance element, the directional element has to be appreciably rotated for these two cases as well–a function not included in available commercial relays. For cases 3 and 6, the problem is even worse and of a different sort. Although DS25 is located on the power-sending end of the line and should thus be expected to overreach due to the remote infeed, it exhibits major underreach for these two cases. Therefore, tilting the reactance element in the clockwise direction has actually increased the distance between the impedance calculated by the relay and zone one, aggravating the problem further. In other words, the common solutions that address the effect of remote infeed in industrial relays are not successful for the lines emanating from CIREPPs.

Since intermediate infeed is considered to make distance relays underreach [65, 66], for setting zone one of a relay that protects a multi-terminal line or zone two, it is assumed that all of the intermediate paths are out of service [72]. However, as was shown in case 9 of Section 3.5.1, for a CIREPP that complies with the NA-GCs, the intermediate infeed caused the relay to overreach, which makes the above practice not only ineffective, but harmful. In case 10 of Section 3.5.2, where the CIREPP complied with the EU-GCs, DS25 overreached excessively as a result of the intermediate infeed. For a fault at the expected reach of zone two of DS25 on line 45, the reactance seen by the relay exceeds 153 Ω, three times larger than the reactance of the entire line 25. Meanwhile, any reach setting for zone two of DS25 that is larger than 105.6 Ω overlaps with zone two of the relay next to bus 5 protecting line 45 when the infeed paths are not in service, thereby violating the selectivity of the protection system. The problem would be exacerbated for stiffer sources at buses 1 and 3, or shorter lengths for lines 15 and 35.

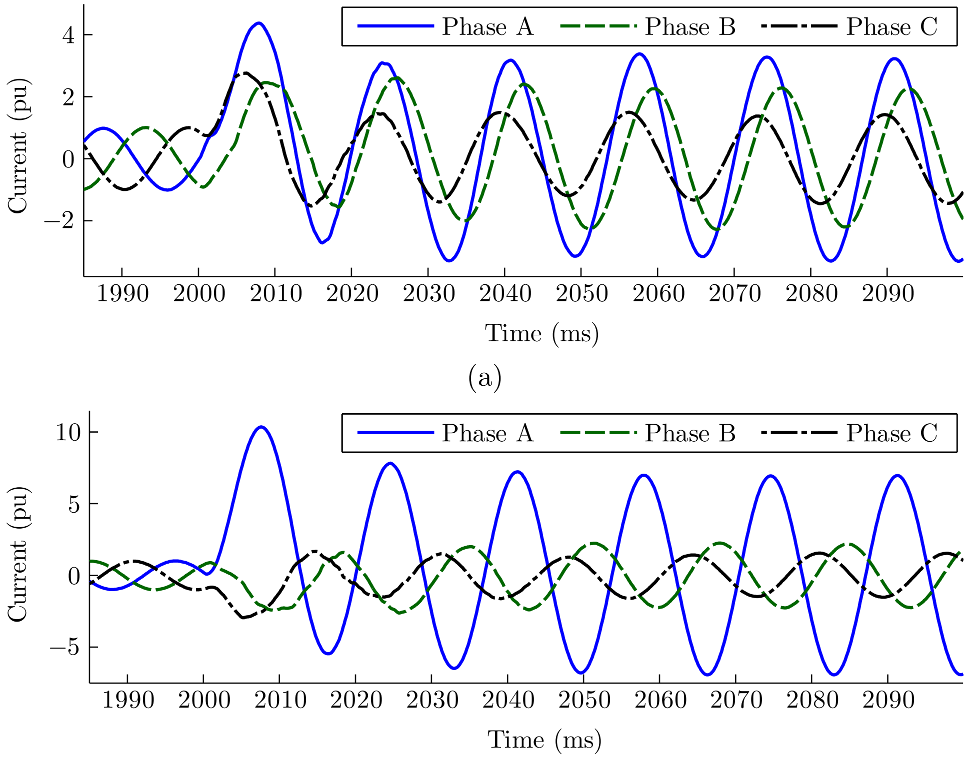

(a)

(b)

Figure 4.2. Current measurements for case 11, (a) Local end, (b) Remote end.

4.2 Proposed Formula for LLG Fault Impedance

As discussed in Section 3.4.3, SLG faults do not pose a great risk to accurate operation of a distance relay located at a CIREPP substation. It is instructive to grasp the reason behind the correct operation of the relay for SLG faults in order to find a solution for LLG faults. The test system used in this chapter is the same as that of Figure 3.2. Let us consider an AG fault at 40% of line 25 with $R_f = 10\ \Omega$. The CIREPP conforms to the EU-GC, generating 80% reactive current 40 ms after the 20% drop in the positive sequence voltage. The local and remote end currents of this fault, denoted as case 11, are depicted in Figure 4.2.

The impedance between the relay and the fault is $1.43 + j20.31\ \Omega$. The reactance calculated by DS25 is only 2.1 Ω larger than the actual reactance to the fault, and the

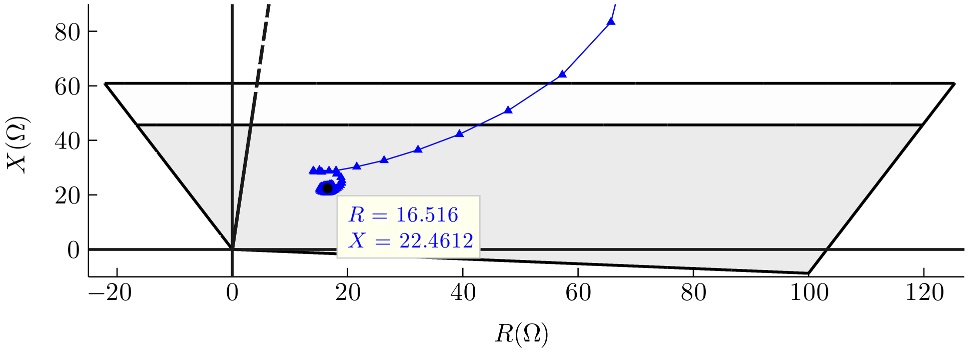

Figure 4.3. Impedance measured by the AG element of DS25 for case 11.

operating point lies correctly inside zone one of Figure 4.3 in less than 13 ms. Similar to the LLG faults studied in Sections 3.4.1 and 3.4.2, the difference between the angles of the positive sequence currents on the two ends of the line is considerable and approximately equals 30°. However, the fictitious reactance seen by DS25 during SLG faults as a result of the remote infeed is not mainly determined by the positive sequence current. The impedance calculated by the AG element of a distance relay is expressed as

$$Z_{AG} = Z_f + R_f \underbrace{\left(\frac{I_{AL} + I_{AR}}{I_{AL} + K^{\circ} I_L^{\circ}} \right)}_{M_{R_f - AG}} \tag{4.1}$$

where K° is $1.726\measuredangle{-17.7^{\circ}}$ for line 25.

The numerator and denominator of M_{R_f-AG} in (4.1), along with the sequence components that build up the denominator of M_{R_f-AG}, for the above-mentioned SLG fault are depicted with respect to time in Figure 4.4. Stemming from the feed-forward compensation of the converter's output voltage, which is necessary to improve the transient response of the control loop [53], the local current contains a negligible amount of negative sequence component. Therefore, the positive sequence component of the local current, I_L^+, is the only component in M_{R_f-AG} that is affected by the CIREPP's control system. In the denominator of M_{R_f-AG}, I_L^+ is added to $(1 + K^{\circ})I_L^{\circ}$. The zero sequence current flows through the ground of the CIREPP's main transformer and is not impacted by the control system. In the numerator, I_L^+ is added to I_L° and the remote end fault current, which is again unaffected by the CIREPP. As shown by the values pinpointed in Figure 4.4(a), $(1+K^{o})I_L^{o}$, as well as the remote end fault current are substantially larger than I_L^{+}, since the CIREPP's control system limits I_L^{+} to 1.2 pu, whereas the other quantities are in the order of normal grid fault currents. Therefore, the effect of I_L^{+} on the phase difference between the numerator and the denominator of M_{R_f-AG} in Figure 4.4(b) is small, and the relay computes an almost true reactance irrespective of the CIREPP's control system. Moreover, in the presence of I_L^{o}, the absolute value of M_{R_f-AG} denominator is comparable with the numerator in Figure 4.4(a), which limits M_{R_f-AG} to a reasonable range and avoids excessive real part for the impedance of Figure 4.3.

On this basis, there follows an attempt to devise a new relation for LLG fault impedance, in which the positive-sequence component of the CIREPP current does not significantly affect the ratio multiplied with the fault resistance. The equivalent circuit for a BCG fault was shown in Figure 3.20. KVL between DS25 and the fault in phases B and C is expressed as

$$V_{BL} = Z_f(I_{BL} + K^{o}I_L^{o}) + R_{ph}(I_{BL} + I_{BR}) + R_g(I_{BL} + I_{BR} + I_{CL} + I_{CR}) \tag{4.2}$$

$$V_{CL} = Z_f(I_{CL} + K^{o}I_L^{o}) + R_{ph}(I_{CL} + I_{CR}) + R_g(I_{BL} + I_{BR} + I_{CL} + I_{CR}) \tag{4.3}$$

The term $K^{o}I_L^{o}$ is considered in the KVL relations to obtain the positive sequence impedance [73]. By adding the above equations and dividing the two sides over $(I_{BL} + I_{CL} + 2K^{o}I_L^{o})$, a new relation is proposed for the BCG fault impedance in (4.4).

$$Z_{BC}^{new} = \frac{V_{BL}+V_{CL}}{I_{BL}+I_{CL}+2K^{o}I_L^{o}} = Z_f + (R_{ph}+2R_g)\underbrace{\left(\frac{I_{BL}+I_{CL}+I_{BR}+I_{CR}}{I_{BL}+I_{CL}+2K^{o}I_L^{o}}\right)}_{M_{R_f-BC}^{new}} \tag{4.4}$$

As a base case study, let us verify the performance of (4.4) during a bolted fault, for which the conventional elements also perform well. The accurate impedance calculation by (4.4) for a bolted BCG fault at 40% of line 25 is illustrated in Figure 4.5(a), where Z_{BC}, given by (3.5), and Z_{BC}^{new} are compared and shown to be situated inside zone one during the fault.

The proposed method can be used to modify the α- and m-based mho elements discussed in Chapter 3, as well. If, instead of $(V_{BL}-V_{CL})$ and $(I_{BL}-I_{CL})$, the BC element of

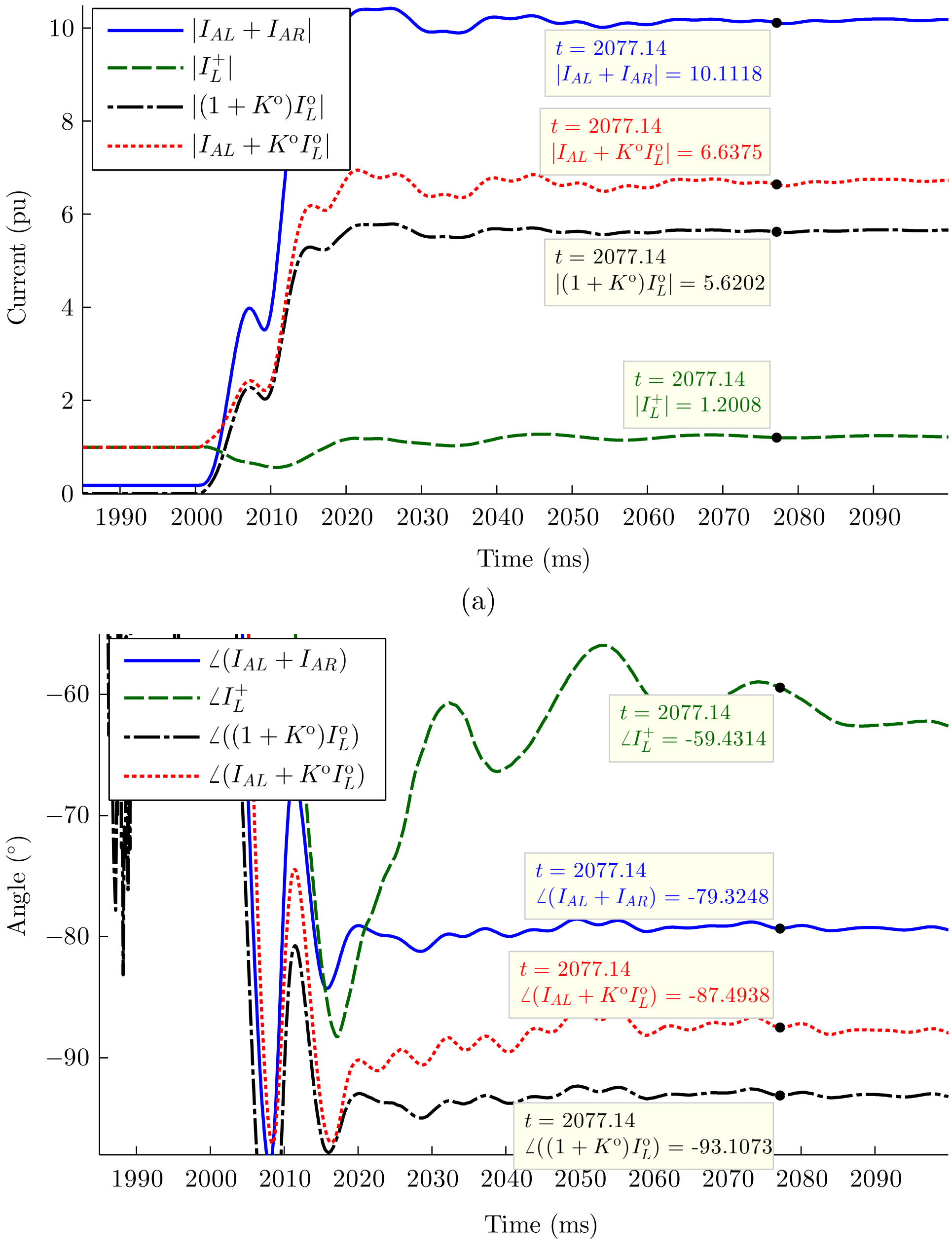

(a)

(b)

Figure 4.4. The numerator and denominator of M_{R_f-AG} for case 11, (a) Magnitude, (b) Angle.

a memory-polarized mho relay is energized by $(V_{BL} + V_{CL})$ and $(I_{BL} + I_{CL} + 2K^{o}I_{L}^{o})$, the angle calculated by the α-based mho for the n-th zone, denoted by α_{BC}^{n-new}, will correctly identify the fault zone. For instance, α_{BC}^{1-new} for the above fault is compared with α_{BC}^{1} in Figure 4.5(b). Similar correct operation has been illustrated for the m-based mho element in Figure 4.5(c). Not only do α_{BC}^{1-new} and m_{BC}^{new} identify the fault accurately, their superiority in terms of speed is evident, although all of the curves in Figures 4.5(b) and (c) are obtained using the same window length. The pinpointed samples demonstrate that α_{BC}^{1-new} and m_{BC}^{new} enter the correct trip zone about 5 ms earlier than α_{BC}^{1} and m_{BC}, respectively.

Akin to Z_{BC}, Z_{BC}^{new} also moves away from Z_f in the presence of remote and intermediate infeed. However, it will be demonstrated in Section 4.5 that this movement is mainly along the R axis in the case of the remote infeed, and any possible underreach or overreach can easily be tackled through the existing remedies. For the intermediate infeed, Section 4.7 will show that Z_{BC}^{new} does not suffer from the overreach or excessive underreach experienced by conventional distance elements.

4.3 Proposed Method for LL and Balanced Faults

Due to the absence of the zero-sequence component, Z_{BC}^{new} introduced in the foregoing section does not address the problems caused by remote and intermediate infeed during LL and balanced faults; thus, a separate method is needed for them. As discussed in Chapter 2, a low-bandwidth communication channel is normally utilized to link the distance relays installed at the two ends of transmission lines. Therefore, if both DS25 and DS52 identify the fault direction correctly, and transmit it to the relay on the other end of the line, the in-zone and out-of-zone faults can be properly differentiated. This strategy is employed by several pilot schemes, such as directional comparison blocking and POTT. These schemes, however, operate for phase faults using only impedance elements, whose autonomous operation for a line connected to a CIREPP was proved to be unreliable. Moreover, as will be shown later on, a conventional directional element is not able to determine the fault direction at a CIREPP substation. The following presents a solution to identify the fault direction by exploiting the exclusive fault behavior of CIREPPs, together

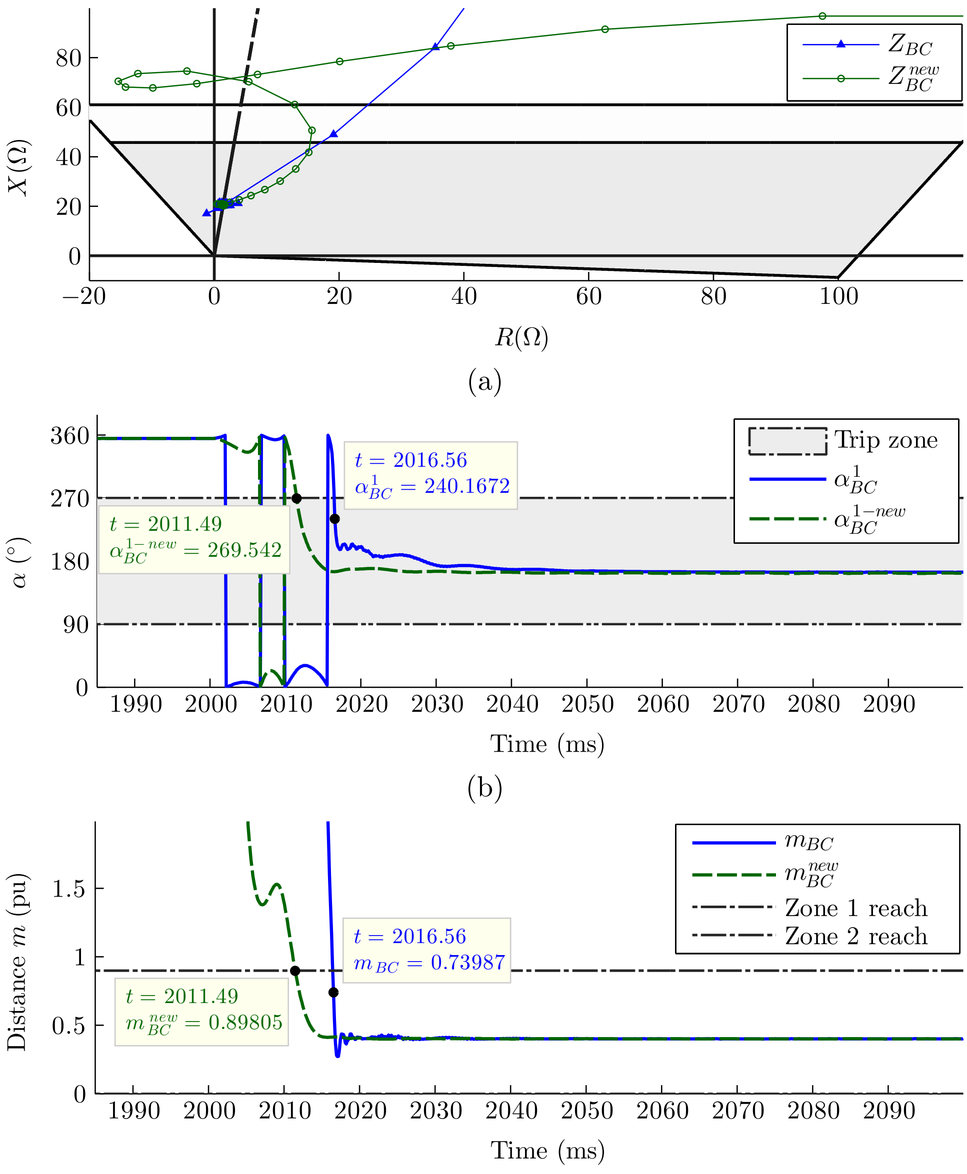

(a)

(b)

(c)

Figure 4.5. Operation of BC element of DS25 based on (4.4) for a bolted fault, (a) Quadrilateral characteristic, (b) α-based mho, (c) m-based mho

with the impedance given by a distance element.

The logic to detect the direction of BC faults by DS25 consists of a four input AND gate. One distinctive feature of a converter fault current is its limited magnitude. The first two inputs of the AND gate are asserted if line B and C's current phasors are larger than a fixed threshold, denoted by I_{PH-th}. The converter fault currents do not normally exceed 120% of the rated value [59]. Considering a safety factor that accounts for possible transient overshoots following a short-circuit, 2 pu is assigned to I_{PH-th}. Comparing the current phasors, not the instantaneous samples or the root mean square (RMS) values, with I_{PH-th}, the impact of fault-induced overshoots becomes minimal.

The current flowing from the bulk power grid toward an internal CIREPP fault is normally above I_{PH-th}, making the first and/or second inputs of the AND gate deasserted, unless the internal fault includes a sufficiently high apparent resistance. In that case, a large negative resistance is seen by a distance relay at the CIREPP substation. Hence, the third input to the AND gate is asserted if the real part of Z_{BC} exceeds a fixed negative threshold, $-R_{BC-th}$. R_{BC-th} should be lower than the maximum resistance seen by DS25 for an internal fault that causes phase currents larger than I_{PH-th}. It should also be large enough to remain unaffected by the noise and other possible transients during forward faults that might result in temporary negative resistances. The low setting for I_{PH-th} makes reaching a reasonable compromise easy. For the test system used in this study, 20 Ω was identified as an effective setting for R_{BC-th}, satisfying both criteria.

The final input to the AND gate secures the relay operation further by checking if the imaginary part of Z_{BC} is larger than a fixed negative threshold, $-X_{BC-th}$. In order to assign X_{BC-th}, let us consider (3.5) expressed in terms of the symmetrical components for a relay at a CIREPP substation, that is,

$$Z_{BC} = Z_f + R_{ph}\left(\frac{(a^2-a)I_R^+ + (a-a^2)I_R^-}{(a^2-a)I_L^+}\right) \tag{4.5}$$

in which I^- is the negative-sequence current and $a = 1\measuredangle 120°$. For a BC fault, the phase angles of I_R^+ and I_R^- differ by about 180°. Therefore, assuming $I_R^- = h.I_R^+$, where h depends on fault condition but is always an approximately real constant, (4.5) can be re-written as

$$Z_{BC} = Z_f + R_{ph}\frac{(1+h)I_R^+}{I_L^+} \tag{4.6}$$

If the CIREPP conforms to the EU-GCs, based on which reactive currents of up to 100% are generated, I_L^+ will lag I_R^+. Hence, as was shown in Figures 3.23(b) and 3.25, the apparent reactance will be higher than the actual reactance to the fault. Therefore, a small value can be assigned to X_{BC-th}, as any negative reactance calculation would be due only to noise and transients and is thus insignificant.

For the CIREPPs meeting the NA-GCs, which maintain a high PF, I_L^+ leads I_R^+, and, as was shown in Figures 3.19(a) and 3.25, the calculated reactance is smaller than the actual fault reactance, potentially resulting in a negative apparent reactance. The largest negative apparent reactance is obtained when the CIREPP operates at the lowest leading PF, so I_L^+ leads I_R^+ more. Moreover, the higher the fault resistance is, the larger the respective term becomes in (4.6), and the longer the impedance moves in the negative direction of the X axis. Meanwhile, determining resistive coverage is a basic requisite for setting up any quadrilateral distance element. The resistive reach setting can be used by a simulation of the system under study for a CIREPP operating at the minimum allowed leading PF to ascertain the appropriate setting for X_{BC-th}. For the system used in this study, and by considering fault resistances of up to 100 Ω and the CIREPP operating at 0.95 leading PF, $X_{BC-th} = 200\ \Omega$ secures accurate protection for line 25.

Considering the same directions for the currents of the two end relays, DS52 also uses the logic used by DS25 to identify the fault direction. Obviously, an asserted output of the AND gate of DS52 indicates a fault outside line 25.

4.4 Proposed Trip Logic

A combination of the proposed methods along with a conventional distance relay is utilized to develop a comprehensive scheme to protect line 25. The schematic diagram of the proposed decision logic for DS25 is displayed in Figure 4.6. TrAG, TrBC and TrABC are the trip signals for AG, BC, and ABC fault loops, respectively. Similar logic is used for other faults. The DDs of commercial relays are usually current-dependent [39, 62]. However, since the variation in the converter current during a fault is minute and might be left unnoticed, it is proposed that the DD in the trip logic of Figure 4.6 detects a

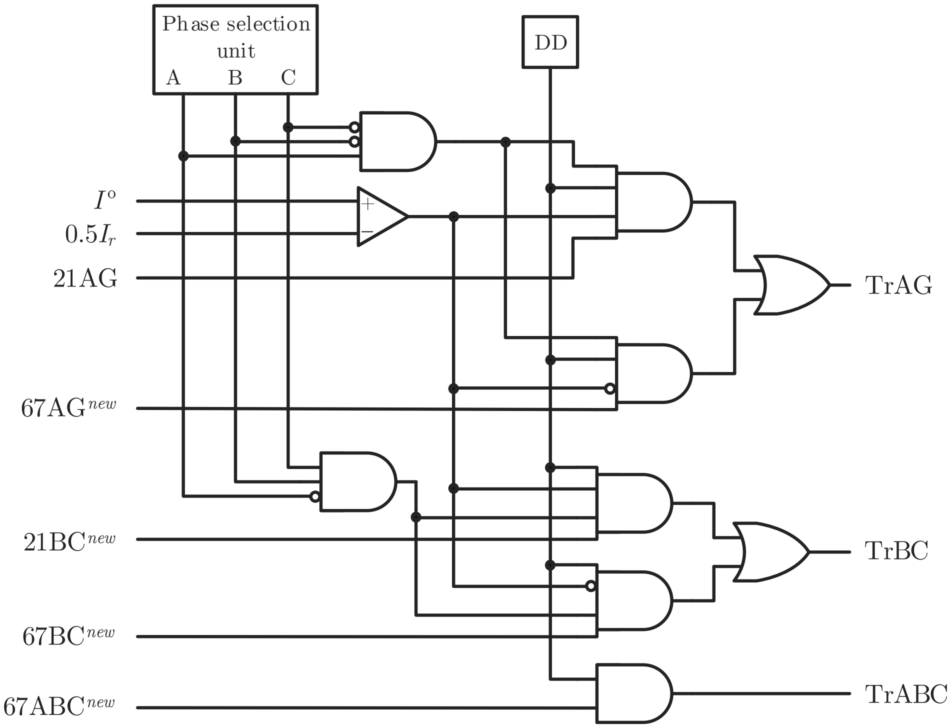

Figure 4.6. Proposed trip logic for DS25.

disturbance if the difference between the one-cycle-apart voltage samples for any of the phases is sufficiently large, and the instantaneous voltage, defined by (4.7), falls below an appropriate threshold, e.g., 0.9 pu.

$$v_{inst} = \sqrt{v_\alpha^2 + v_\beta^2} \tag{4.7}$$

v_α and v_β are obtained by applying the Clarke transform to the three-phase voltages. The output of this DD may also be ORed with a conventional current-dependent DD for increased sensitivity during ground faults. Appropriate element of the relay is activated by this DD along with a phase selection unit, a prevalent element in distance relays [74].

For an AG fault, if the zero-sequence current exceeds 50% of the rated current, I_r, the output of the AG element of a conventional distance relay, denoted by 21AG, is copied into TrAG. Although it is not a very common scenario, the step-up transformer between the grid-side converter and the relay might be ungrounded. For instance, any DG connected to the 44 kV level of the Hydro One network in Ontario, Canada, must be ungrounded, and the system withstands the resultant TOVs during ground faults. As another example, take distance relays installed inside modern WFs, such as the Nordsee-Ost offshore WF in Germany. Off the shelf turbine transformers are not grounded on the HV side [75, 76]. Therefore, if a ground fault occurs between the grounding transformer and one of the turbine relays, the fault current recorded by that relay does not include any zero-sequence current. Therefore, a conventional distance relay fails to properly protect the cable inside the farm for all fault types, including SLG faults. For such cases, the pilot directional logic discussed in Section 4.3, whose output for the AG element is denoted by 67AG^{new}, is deployed.

If phase B and C outputs of the phase selection unit pick up, the magnitude of the zero-sequence current is examined. For a sufficiently large zero-sequence component, the trip decision is up to the distance element devised in Section 4.2, whose output is designated by 21BC^{new}. A low zero-sequence term handles the trip decision to 67BC^{new}, which stands for the directional logic of Section 4.3 with phase B and C quantities. The same method is used to protect the line during balanced faults.

4.5 Performance Evaluation for Zone One LLG Faults

A comprehensive study was carried out to scrutinize the performance of the suggested solutions. A variety of parameters and conditions were inspected, including the fault type, location and resistance, the GC, the CIREPP power at the fault instant, the converter current limit, the winding configuration of the CIREPP's transformer, and the grid stiffness, among others. This section discusses the operation of the formula devised in Section 4.2 for LLG faults inside zone one of DS25.

4.5.1 EU-GC

The proposed method was tested for case 6 in Section 3.4.2, which included a BCG short-circuit at 80 km of line 25, when the CIREPP conformed with the EU-GCs. As discussed earlier, the feed-forward compensation of the control system removes the negative sequence component from the converter current almost completely. Meanwhile, the zero-sequence current flows through the ground of the CIREPP's main transformer. Therefore, the denominator of $M^{new}_{R_f-BC}$ for DS25 is expressed in terms of the symmetrical components as

$$I_{BL} + I_{CL} + 2K^{\text{o}} I^{\text{o}}_L = (a^2 + a)I^+_L + (2 + 2K^{\text{o}})I^{\text{o}}_L \tag{4.8}$$

The magnitude and angle of the two terms on the right-side of (4.8) are plotted versus time in Figure 4.7. It is evident that the zero-sequence term is appreciably larger than the positive-sequence term, because of the converter's limited overcurrent. As a result, both the amplitude and phase angle of the denominator of $M^{new}_{R_f-BC}$ in Figure 4.7 are close to those of the zero-sequence term. If the CIREPP's control system is designed to generate negative sequence current, then the combined magnitude of I^+_L and I^-_L must be lower than $i_{\max}$, maintaining the dominance of I^{o}_L in the $M^{new}_{R_f-BC}$ denominator.

The numerator of $M^{new}_{R_f-BC}$ can also be written in terms of the symmetrical components as

$$I_{BL} + I_{CL} + I_{BR} + I_{CR} = (a^2 + a)I^+_L + 2I^{\text{o}}_L + 2I^{\text{o}}_R + (a^2 + a)I^+_R + (a + a^2)I^-_R \tag{4.9}$$

Similar to (4.8), the first term that includes I^+_L is comparatively negligible. The phase difference between I^{o}_L and I^{o}_R is not impacted by the CIREPP's control system and is thus small. For example, at the time instant pinpointed in Figure 4.7, I^{o}_L and I^{o}_R are $1.454\measuredangle 93.8°$ and $2.484\measuredangle 96.8°$ pu, respectively. $(a^2 + a)$ equals -1, so with the 180° phase difference between I^+_R and I^{o}_R during a BCG fault, the third term of (4.9) is in phase with I^{o}_L, as well. For a BCG fault, I^-_R and I^{o}_R are in phase, so the last term of (4.9) becomes almost 180° out of phase from I^{o}_L. If $|I^-_R|$ is less than the magnitude of the sum of the other terms, which is the most likely scenario, then the whole numerator of $M^{new}_{R_f-BC}$ will be almost in phase with I^{o}_L. If $|I^-_R|$ is larger than the sum of the other terms, then the numerator is 180° out

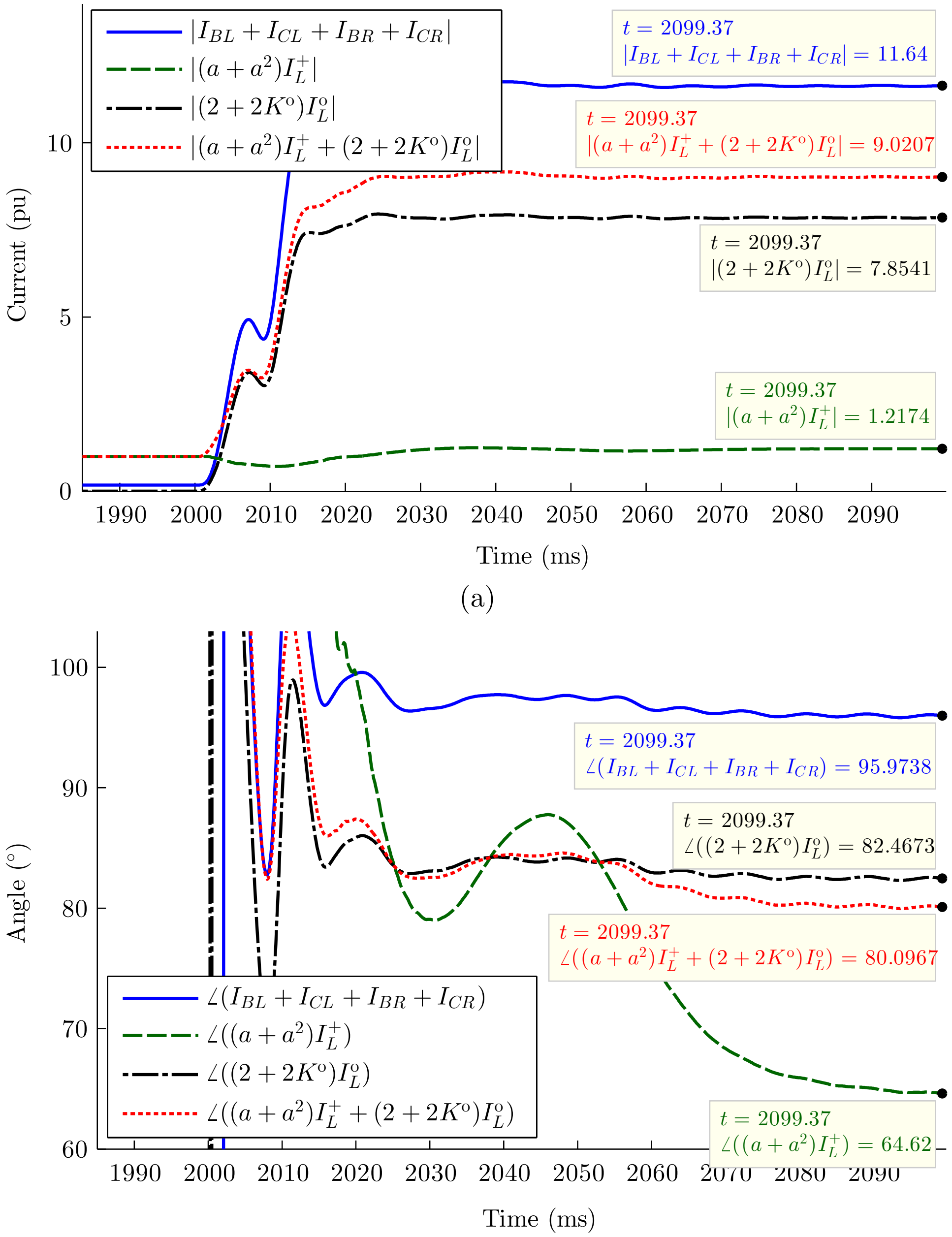

(a)

(b)

Figure 4.7. The numerator and denominator of $M_{R_f-BC}^{new}$ for case 6 in Section 3.4.2, (a) Magnitude, (b) Angle.

of phase from I_L^o. Considering the above discussion on the phase angle of the denominator, the last term on the right side of (4.4) is primarily resistive. For a normal range of $|I_R^-|$, this resistance is positive, while it is negative for excessively large values of $|I_R^-|$.

The last term on the right side of (4.4) includes a small amount of reactance as well, because the angle of the $M_{R_f-BC}^{new}$ denominator is shifted from I_L^o by $\measuredangle(2+2K^o)$. The level of the reactance depends on $\measuredangle K^o$. Distance relays are normally used for HV lines, where $\measuredangle K^o$ is small and negative. For instance, $\measuredangle K^o$ for three typical triangular configurations of single-, twin- and quad-bundle 110 kV, 220 kV and 380 kV overhead lines with Al/St 435/35, 265/35 and 435/55 conductors is $-1.1°$, $-2.3°$ and $-8.3°$, respectively [64]. That is why several credible references consider it safe to approximate K^o with a real number for most overhead transmission lines [22]. Similarly, the default value for $\measuredangle K^o$ in many commercial relays is zero [62,69], and some of them confirm the security of setting K^o to a real number [70]. In addition, the difference between the angles of the $M_{R_f-BC}^{new}$ numerator and denominator is quite smaller than $\measuredangle K^o$, as $2K^o$ is added to 2 in the multiplier of I_L^o in (4.8).

Negative $\measuredangle K^o$ yields a positive imaginary part for $M_{R_f-BC}^{new}$, which will, in turn, result in relay underreach. This is more desirable than overreach for zone one, as it is inherently an underreaching zone [22]. Due to low $\measuredangle K^o$, the relay underreach can simply be addressed by tilting the reactance element of the quadrilateral characteristic similar to [69] and [70]. Having said that, the tilting angle and direction are determined based on K^o, not the power direction and magnitude at the relay location. For a negative $\measuredangle K^o$, the reactance element should be tilted counterclockwise. Moreover, for applications involving underground cable, where $\measuredangle K^o$ might be largely negative, the faults unseen at the end of the line can easily be covered by means of the permissive underreach transfer trip (PUTT) scheme. This solution is effective because the proposed method results in underreach for DS25.

To examine the worst case scenario, the lines of the system were modeled such that the largest possible negative $\measuredangle K^o$ was obtained, while the standards of [77] were met. The resultant K^o was $1.726\measuredangle-17.7°$. Given the magnitudes and angles pinpointed in Figure 4.7, the rightmost term in (4.4) is $6.21+j1.77\ \Omega$. With the $2.86+j40.62\ \Omega$ impedance to the fault, (4.4) yields $9.07+j42.39\ \Omega$, which is the same as the Z_{BC}^{new} calculated by the proposed BCG element, depicted in Figure 4.8(a), validating the above analysis. The α-

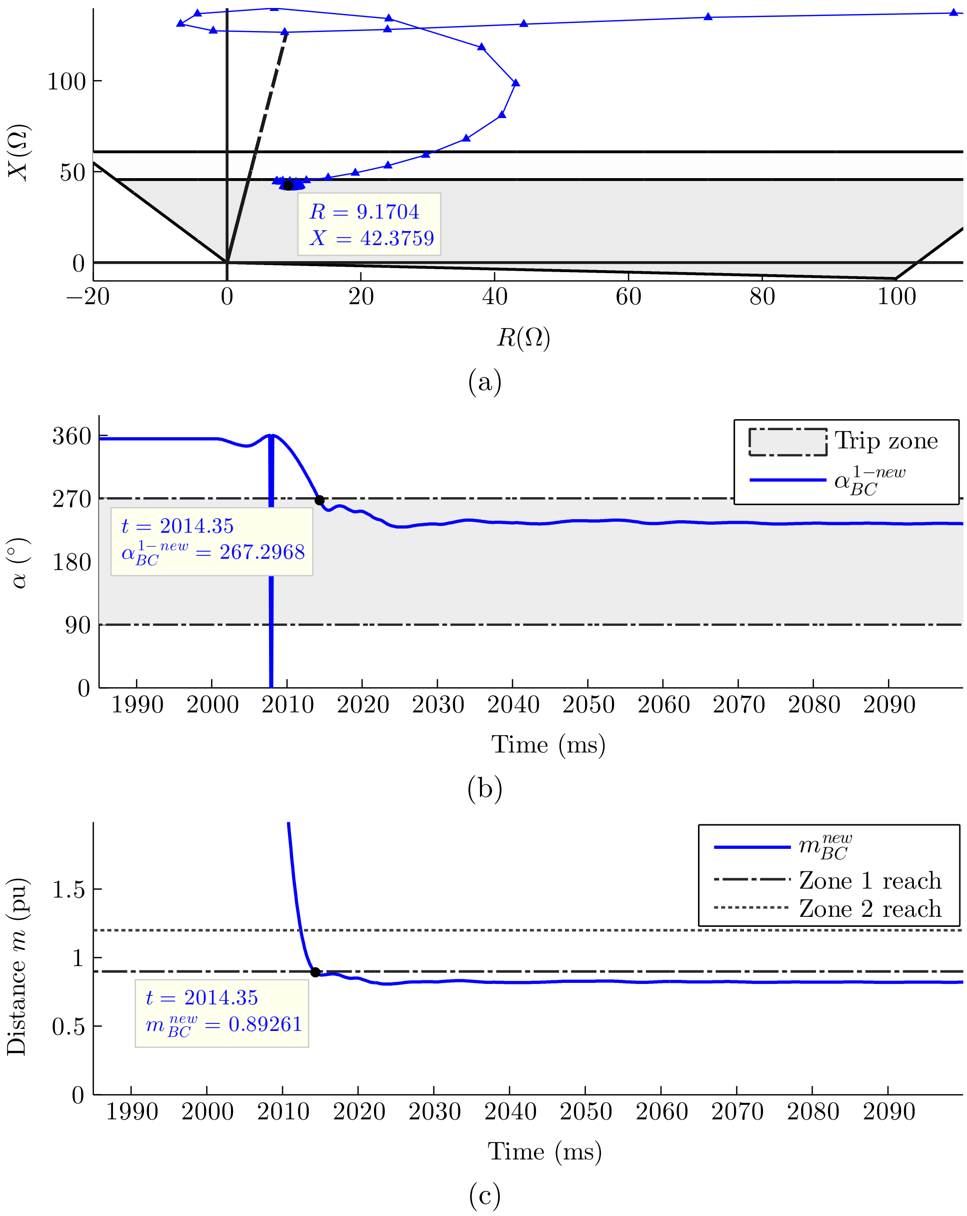

Figure 4.8. Operation of the proposed BC element of DS25 for case 6 in Section 3.4.2, (a) Z_{BC}^{new} with quadrilateral characteristic, (b) α-based mho, (c) m-based mho

and m-based mho elements also provide accurate protection if they are energized by the proposed voltage and current. Both α_{BC}^{1-new} and m_{BC}^{new} enter the trip zone in Figures 4.8(b)

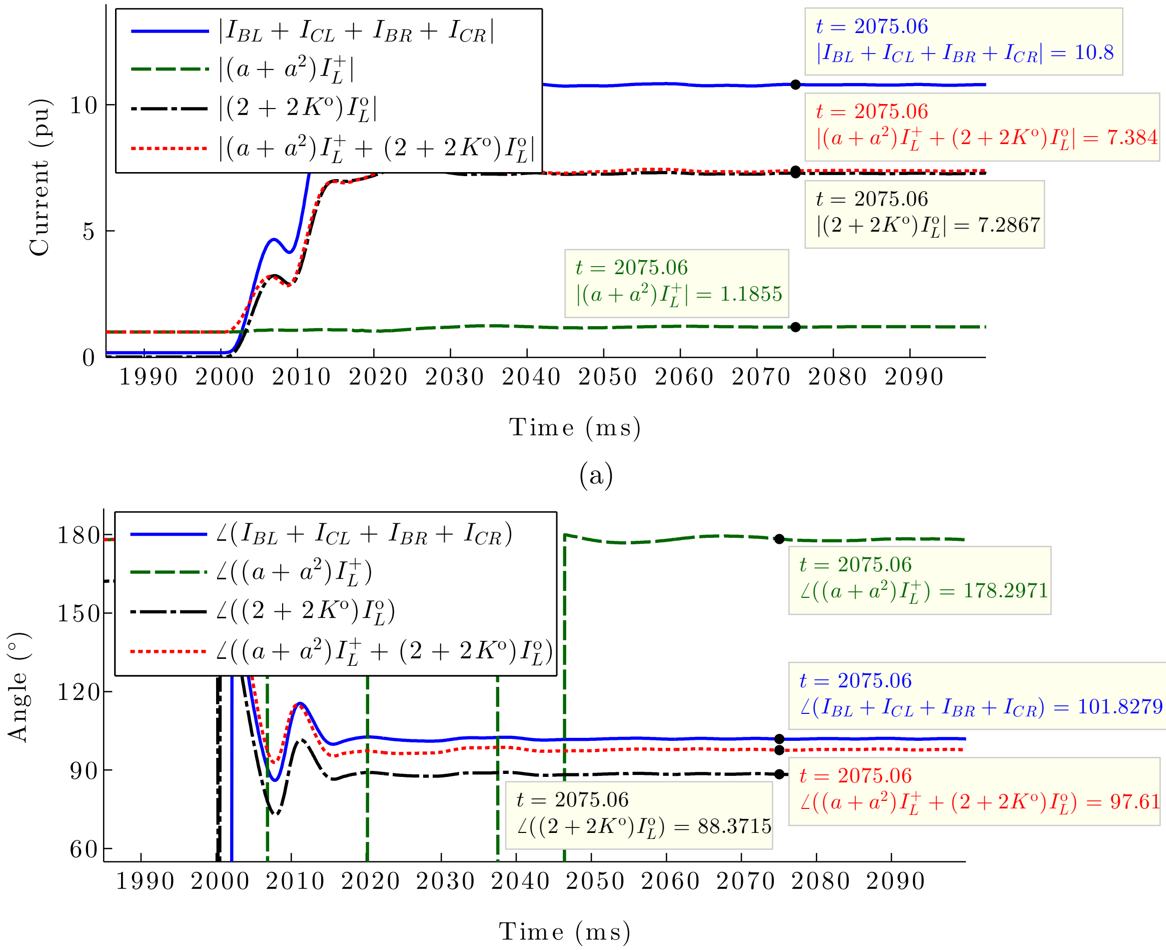

(a)

(b)

Figure 4.9. The numerator and denominator of $M_{R_f-BC}^{new}$ for case 5 in Section 3.4.1, (a) Magnitude, (b) Angle.

and (c) less than 15 ms after the fault inception.

4.5.2 NA-GC

The performance of the proposed method was tested for the same fault when the CIREPP followed the NA-GC, i.e., case 5 of Section 3.4.1. The magnitude and angle of the terms in $M_{R_f-BC}^{new}$ are plotted in Figure 4.9. The presence of the zero sequence component has again confined the phase difference between the numerator and denominator. Furthermore, they are more comparable in magnitude. Therefore, the last term of (4.4) is only $7.29+j0.54\ \Omega$, leading to $Z_{BC}^{new}=10.15+j41.15\ \Omega$, which is in agreement with the impedances provided by the proposed BC element in Figure 4.10(a). The slight $0.53\ \Omega$ underreach is explained as in the foregoing case study.

Comparing different GCs, it was found that the relay underreach was generally milder when the CIREPP operated according to the NA-GCs. The difference between the impacts of the two categories of GCs can be explained by the relative phase angles of the positive- and zero-sequence terms in the denominator of $M_{R_f-BC}^{new}$ in Figures 4.7(b) and 4.9(b). I_L^o leads the zero-sequence voltage by the impedance angle of the CIREPP's main transformer, that is, about 90°. For NA-GCs, I_L^+ is approximately in phase with the positive sequence voltage. Given that the positive- and zero-sequence voltages are almost aligned over a BCG fault, I_L^+ lags I_L^o by about 90°. That is why $(a^2+a)I_L^+$ leads the zero-sequence term in Figure 4.9(b) by 89.9°. Consequently, the backward shift in the I_L^o angle by the $(2+2K^o)$ multiplier is somewhat lessened by $(a^2+a)I_L^+$, and the denominator of $M_{R_f-BC}^{new}$ leads $(2+2K^o)I_L^o$ by 9.2°. Conversely, for EU-GCs, where I_L^+ lags the positive-sequence voltage by up to 90°, $(a^2+a)I_L^+$ may shift the zero-sequence term in the denominator of $M_{R_f-BC}^{new}$ in the backward direction, thereby widening the gap between the numerator and the denominator angles and exacerbating the relay underreach. Indeed, as observed in Figure 4.7, where the difference between the angles of the denominator and its zero sequence term is less than 2°, this effect is limited by the low $i_{\max}$.

This issue can be taken into account by tilting angle of the reactance element of the quadrilateral characteristic adaptively, based on the phase difference between the zero- and positive-sequence currents. A weighting factor proportionate to the relative absolute value of the positive- and zero-sequence currents may also be considered. Generally, as the fault gets closer to DS25, the zero-sequence current increases while the positive sequence component remains equal to $i_{\max}$, so the effect of I_L^+ on the relay underreach declines.

Similar to the quadrilateral characteristic, the new α- and m-based mho elements can also detect the fault correctly. α_{BC}^{1-new} and m_{BC}^{new}, displayed in Figures 4.10(b) and (c), lie inside their trip zones less than one cycle after the fault is initiated.

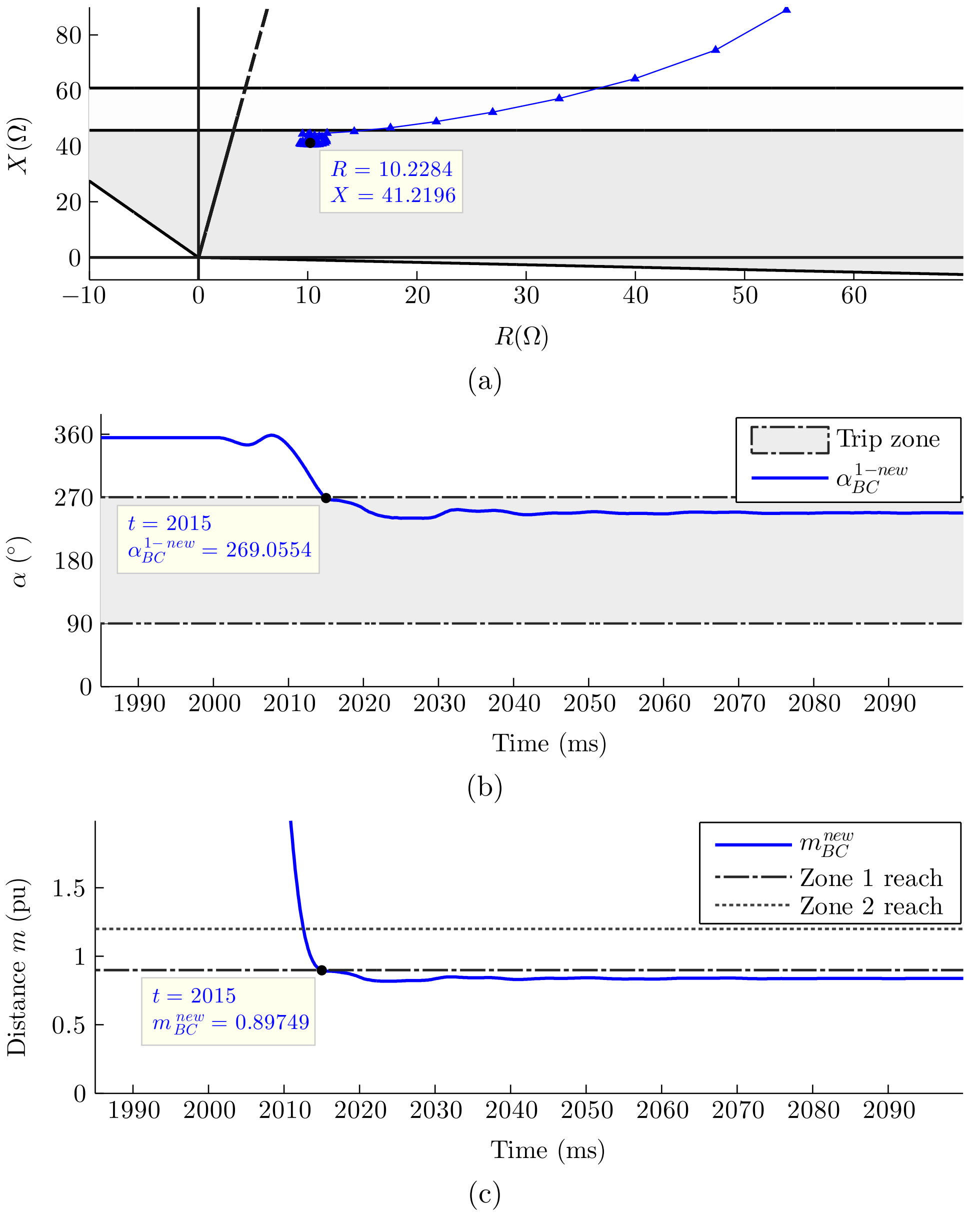

(a)

(b)

(c)

Figure 4.10. Operation of the proposed BC element of DS25 for case 5 in Section 3.4.1, (a) Z_{BC}^{new} with quadrilateral characteristic, (b) α-based mho, (c) m-based mho

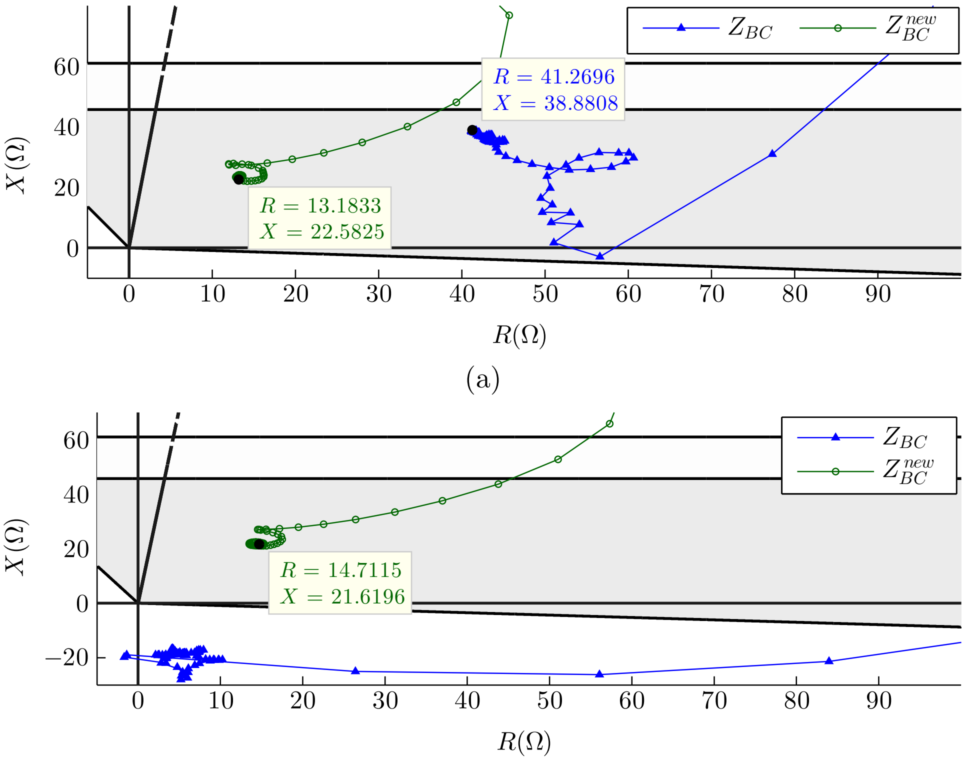

(a)

(b)

Figure 4.11. Z_{BC} and Z_{BC}^{new} for a BCG fault at 40% of line 25 with $R_g = 5\ \Omega$ and $R_{ph} = 5\ \Omega$, (a) EU-GC, (b) NA-GC.

4.5.3 Other Values for Fault Resistance

The operation of the proposed method was tested for other combinations of R_g and R_{ph} as well, and satisfactory performance was observed. As a representative case, a BCG fault at 40% of line 25 with $R_g = 5\ \Omega$ and $R_{ph} = 5\ \Omega$ is reviewed. Figures 4.11(a) and (b) compare Z_{BC}^{new} with Z_{BC} when the CIREPP complies with the EU-GC and NA-GC, respectively. The results obtained from a conventional distance relay are evidently inaccurate and GC-dependent. For the EU-GC, Z_{BC} undergoes a large 18.6 Ω underreach, while the NA-GC leaves Z_{BC} in the fourth quadrant; i.e., the in-zone fault is missed by the relay. The proposed method, conversely, offers an accurate estimation of the fault reactance. Z_{BC}^{new} exhibits only 2.27 Ω and 1.31 Ω underreach for the EU-GC and NA-GC, respectively, indicating its virtual GC independence.

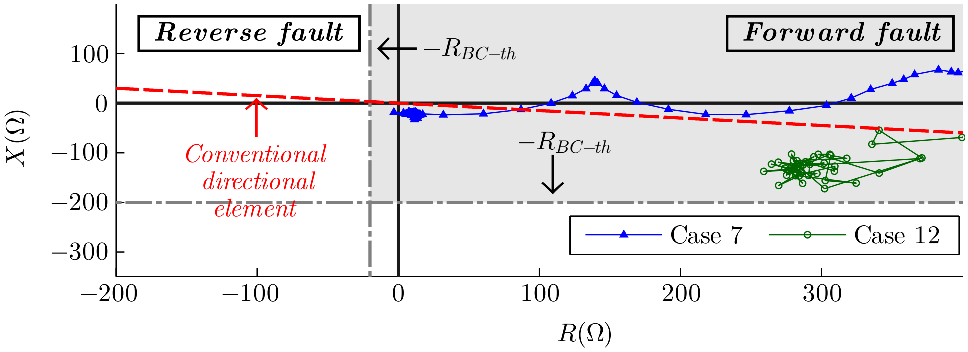

Figure 4.12. Z_{BC} of DS25 for cases 7 and 12.

4.6 Performance Evaluation for LL and Balanced Faults

This section inspects fault direction identification for LL and balanced faults, which was the basic requirement of the pilot scheme developed in Section 4.3, and compares the results with those of conventional directional elements.

4.6.1 In-Zone Faults

For the BC fault in case 7 of Section 3.4.3, DS25 currents are below I_{PH-th}. Therefore, the proposed method compares the real and imaginary parts of Z_{BC} with $-R_{BC-th}$ and $-X_{BC-th}$, respectively. As shown in Figure 4.12, Z_{BC} is safely above both of the thresholds, and DS25 declares a forward fault. Also, the phase B and C currents at the remote end, shown in Figure 4.13(a), exceed 12 and 13 pu, respectively, so the AND gate of DS52 is deasserted, and that relay declares a forward fault as well. Line 25 is, thus, identified to be the fault location.

Z_{BC} moves in the negative direction along the X axis for larger fault resistances. Z_{BC} for the same fault with 100 Ω resistance, denoted as case 12, is displayed in Figure 4.12 as well, indicating the correct operation of DS25. In addition, the remote-end fault currents of phases B and C in Figure 4.13(b) are above 5.5 and 6.0 pu, respectively. Thus, DS52 also identifies a forward fault. Figure 4.12 also shows a conventional directional element and its failure to detect the fault direction for both cases.

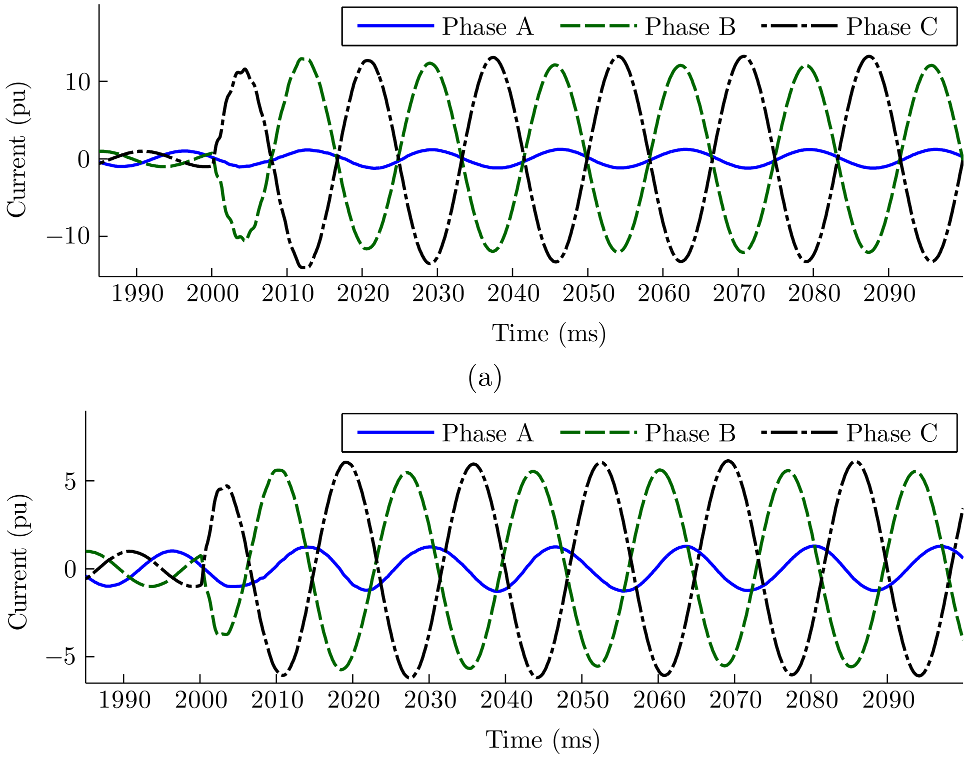

(a)

(b)

Figure 4.13. DS52 current for LL faults, (a) Case 7, (b) Case 12.

Many other LL and balanced forward faults were tested, and the overcurrent limit together with the assigned thresholds for the real and imaginary parts of Z_{BC} were able to correctly identify the fault direction, whereas a conventional directional element was found to be at risk of maloperation.

4.6.2 Out-of-Zone Faults

4.6.2.1 Internal CIREPP Faults

Numerous reverse faults inside the CIREPP were also simulated. A majority of those faults have adequately large overcurrents, thereby deasserting the first two inputs of the AND gate of DS25 and identifying a reverse fault. Two of the simulations that include low

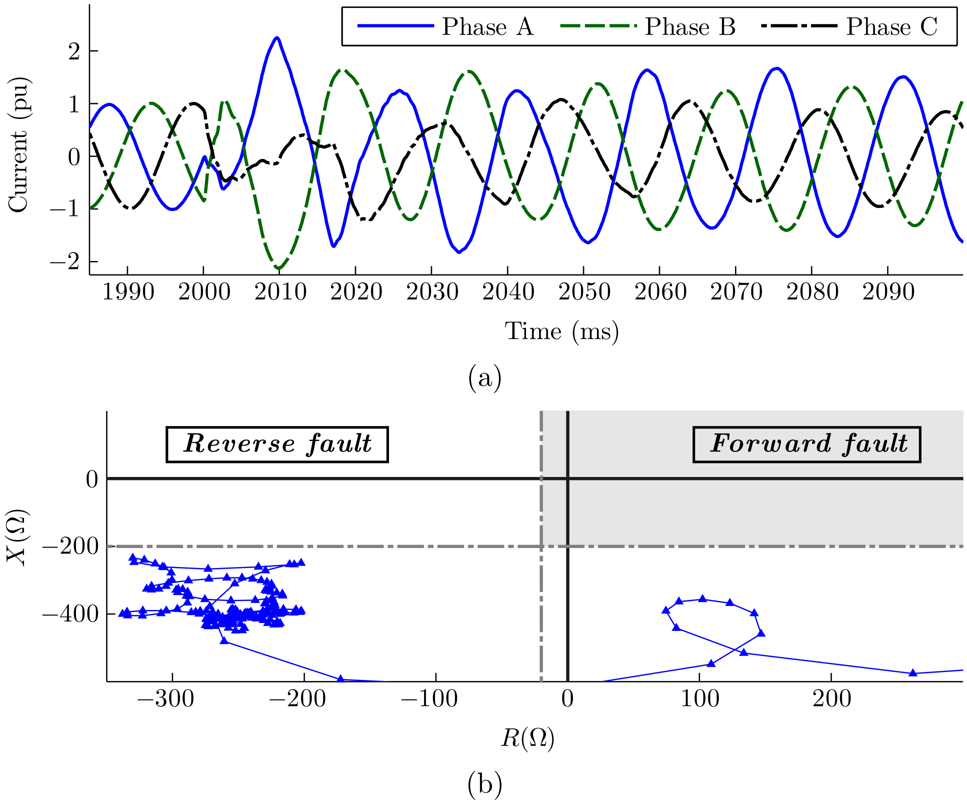

Figure 4.14. DS25 measurements for a reverse BC fault on the LV side of the CIREPP's main transformer, (a) Current, (b) Impedance of the BC element.

currents are reviewed here. Figure 4.14(a) plots DS25 current for a reverse BC fault with 10 Ω resistance on the low-voltage (LV) side of the main transformer. Although the fault does not include a large resistance, the currents are lower than the I_{PH-th} setting, as they are limited not only by the fault resistance, but also by the transformer leakage reactance.

Z_{BC} seen by DS25 is shown in Figure 4.14(b). In spite of the low fault resistance, the real part of Z_{BC} is sizable, as it is determined by the original fault resistance times the square of the transformer winding ratio, which is 14.8, considering the 34.5/230 kV voltage ratio and the ddYG configuration. Thus, Z_{BC} is situated far away on the left side of $-R_{BC-th}$, specifying a backward fault and preventing line 25 tripping.

As discussed earlier, similar to the impedances located in the fourth quadrant for the forward faults in cases 5 and 7 of Sections 3.4.1 and 3.4.3, Z_{BC} may lie in the second quad-

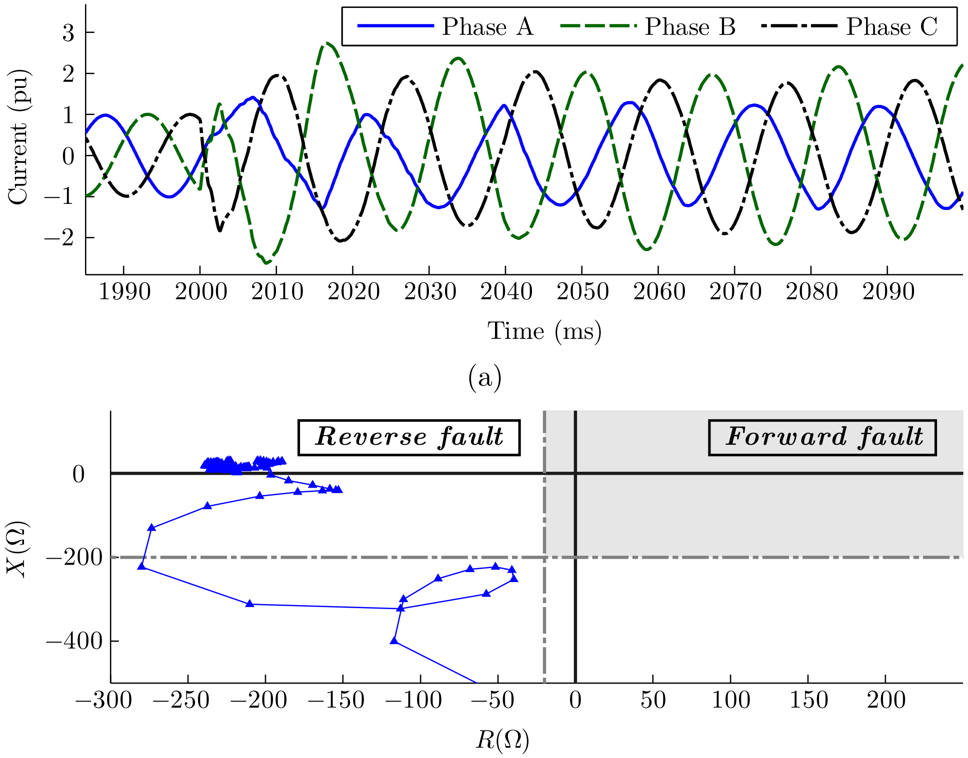

(a)

(b)

Figure 4.15. DS25 measurements for a reverse BC fault on the HV side of the CIREPP's main transformer, (a) Current, (b) Impedance of the BC element.

rant for internal CIREPP faults. Figure 4.15(a) depicts the current for a high resistance BC fault on the HV side of the main transformer behind DS25. The current magnitude is close to I_{PH-th}. The resultant Z_{BC} in Figure 4.15(b) is eventually placed in the second quadrant, endangering the correct operation of a conventional directional element. The proposed method, however, detects the reverse fault direction successfully, as the high fault resistance restrains Z_{BC} from moving to the right of $-R_{BC-th}$.

4.6.2.2 Faults on Subsequent Lines

Similar to cases 3 and 4 of Sections 3.3.3 and 3.3.4, the impedance of DS25 for a balanced zone two fault lies on the positive side of either the R or the X axis depending on the

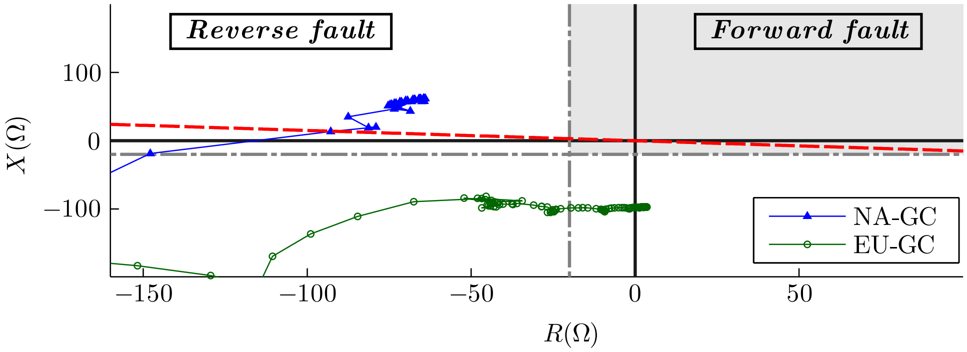

Figure 4.16. Z_{BC} of DS52 for balanced faults on line 45.

GC, and identifies a forward fault. For DS52, however, the apparent impedance is almost symmetrically located on the negative side of the axes. Z_{BC} of DS52 during a bolted balanced fault 20 km away from bus 5 on line 45 is shown in Figure 4.16 for the two GCs. For the NA-GC, the impedance is located well above the R axis due to the 14 MVAr reactive power consumed by line 25, which puts a conventional directional element, shown by dashed red line, at risk. For the same reason, the magnitude of the imaginary part of Z_{BC} given by DS52 when the CIREPP complies with the EU-GC is smaller than that of DS25. Meanwhile, the impedance of DS52 is placed in the reverse region for both GCs, which avoids line 25 tripping.

4.7 Effect of Intermediate Infeed

This section investigates the operation of the formula suggested in Section 4.2 during LLG faults on subsequent lines. KVL in phases B and C of the circuit diagram for a BCG fault involving intermediate infeed, shown in Figure 3.28, yields

$$V_{BL} = (Z_1 + Z_2)(I_{BL} + K^{o} I_{L}^{o}) + Z_2(I_{Bif} + K^{o} I_{if}^{o}) \tag{4.10}$$

$$V_{CL} = (Z_1 + Z_2)(I_{CL} + K^{o} I_{L}^{o}) + Z_2(I_{Cif} + K^{o} I_{if}^{o}) \tag{4.11}$$

where Z_1 and Z_2 are the positive sequence impedance between the relay and the infeed, and from the infeed up to the fault, respectively, and the *if* subscript denotes infeed quantities.

The fault resistance is considered to be zero at this stage to investigate the effect of the intermediate infeed exclusively. Adding (4.10) and (4.11), and dividing the result over $(I_{BL} + I_{CL} + 2K^{\circ}I_L^{\circ})$ determines the effect of the intermediate infeed on Z_{BC}^{new}.

$$Z_{BC}^{new} = Z_f + Z_2 \underbrace{\left(\frac{I_{Bif} + I_{Cif} + 2K^{\circ}I_{if}^{\circ}}{I_{BL} + I_{CL} + 2K^{\circ}I_L^{\circ}} \right)}_{M_{if-BC}^{new}} \tag{4.12}$$

Both the numerator and the denominator of M_{if-BC}^{new} are similar to the denominator of $M_{R_f-BC}^{new}$ and can, in turn, be expressed in terms of the symmetrical components akin to (4.8). Consequently, it is ascertained that the angles of the numerator and the denominator of M_{if-BC}^{new} are close to that of the local zero sequence current, which was absent in M_{if-BC} of (3.7). Any phase difference between the numerator and the denominator arises either from the difference between the angles of I_L° and I_{if}°, which is negligible, particularly for homogeneous systems, or from the radically different angle of I_L^{+}, whose effect is insignificant because of the converters' limited overcurrent.

4.7.1 EU-GC

Case 10 of Section 3.5.2 included a BCG fault 10 km away from bus 5 on line 45 when the CIREPP followed the EU-GC. Figure 4.17 shows the magnitude and angle of the terms in M_{if-BC}^{new}, where the zero sequence component dominates the denominator of M_{if-BC}^{new} and makes it closely aligned with the numerator. Plugging the values pinpointed in Figure 4.17 into (4.12) yields $Z_{BC}^{new} = 4.17 + j64.85\ \Omega$, which is in agreement with Z_{BC}^{new} shown in Figure 4.18, substantiating the above analysis. Z_{BC}^{new} is located slightly above zone two of DS25, while the fault is inside the zone. Nevertheless, this is not a malfunction of the proposed element. The location of Z_{BC}^{new} stems from the regular infeed effect, which should be taken into consideration in any application, with or without CIREPP. The important issue is that, unlike a conventional distance element which suffered from an excessive 50 Ω underreach for this case, DS25 has underreached by less than 10 Ω in Figure 4.18. In addition, despite the zero R_f, the real part of Z_{BC} included a 20 Ω fictitious resistance in Figure 3.32, whereas Z_{BC}^{new} is on the line replica impedance.

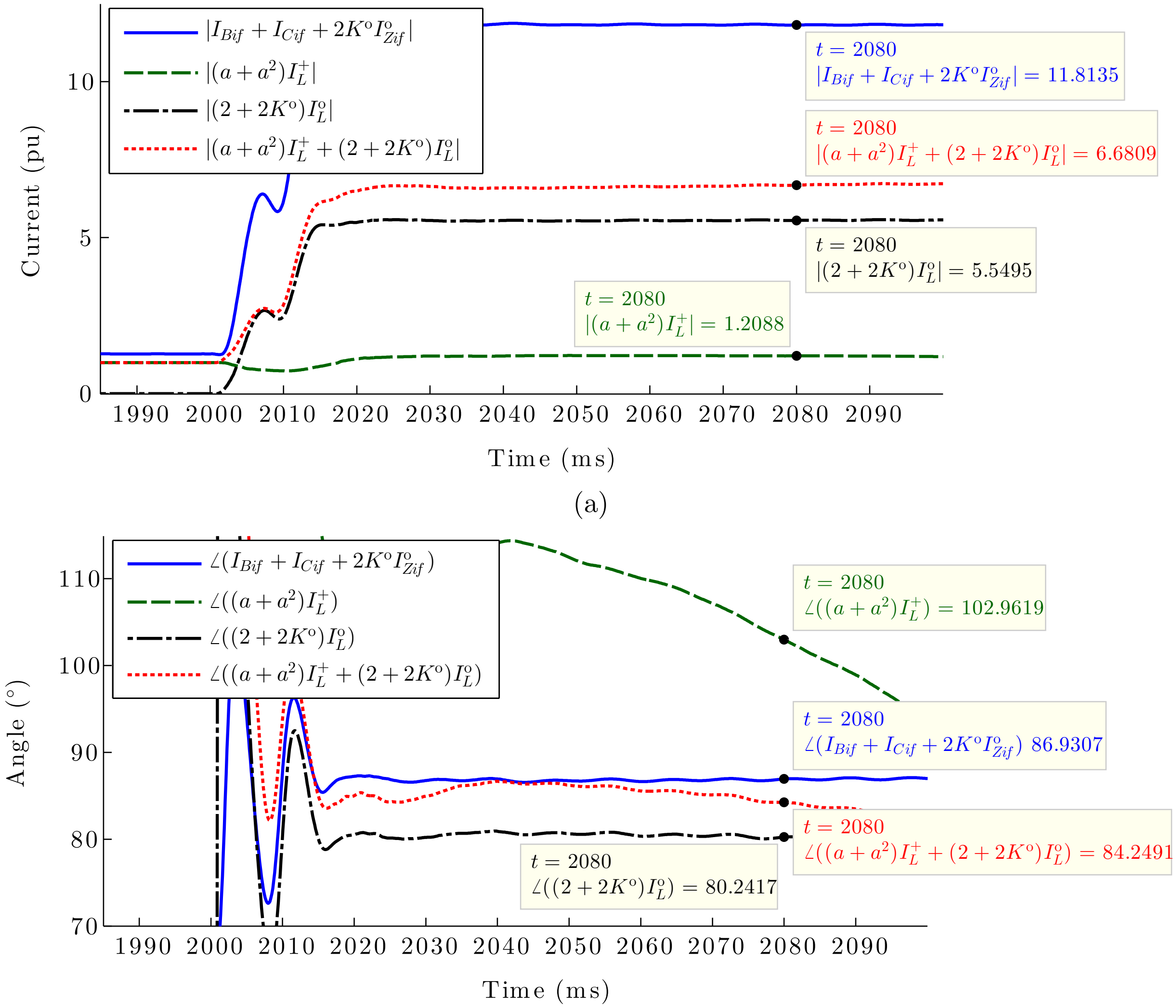

(a)

(b)

Figure 4.17. The numerator and denominator of M^{new}_{if-BC} for case 10 in Section 3.5.2, (a) Magnitude, (b) Angle.

4.7.2 NA-GC

Case 9 of Section 3.5.1 is similar to the above case, with the exception that the CIREPP conforms to the NA-GC. The magnitude and angles of the terms in M^{new}_{if-BC} of DS25 are plotted in Figure 4.19. The positive-sequence component is overshadowed by the zero-

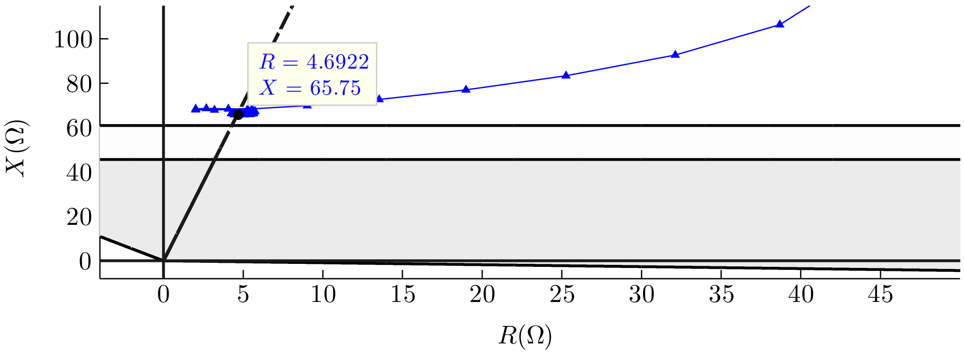

Figure 4.18. Z_{BC}^{new} of DS25 for case 10 of Section 3.5.2.

sequence term in the denominator. Using the values pinpointed in Figure 4.19, Z_{BC}^{new} of (4.12) equals $7.58 + j68.79$ Ω, which is identical with the impedances in Figure 4.20. Z_{BC}^{new} exhibits a normal underreach caused by the intermediate infeed, not the substantial overreach shown by Z_{BC} for this case in Figure 3.27. Furthermore, the similarity between the impedances in Figures 4.18 and 4.20 reveals the superiority of the proposed method over conventional distance elements in terms of GC independence.

4.7.3 Combined Effect of Remote and Intermediate Infeed

To study the combined effect of remote and intermediate infeed, a BCG fault was placed 20 km away from bus 5 on line 45 with 10 Ω resistance. The impedances seen by DS25 for the two GCs are displayed in Figure 4.21. For the EU-GC, there exists a drastic discrepancy between Z_{BC} and the actual fault impedance in both R and X directions in Figure 4.21(a). In contrast, the imaginary part of Z_{BC}^{new} exhibits the natural underreach caused by intermediate infeed. Its real part is also in the order of the actual fault resistance. A similar scenario applies to the Z_{BC}^{new} calculated for the NA-GC in Figure 4.21(b), signifying its GC independence, while Z_{BC} is not even remotely close to its anticipated position in the impedance plane.

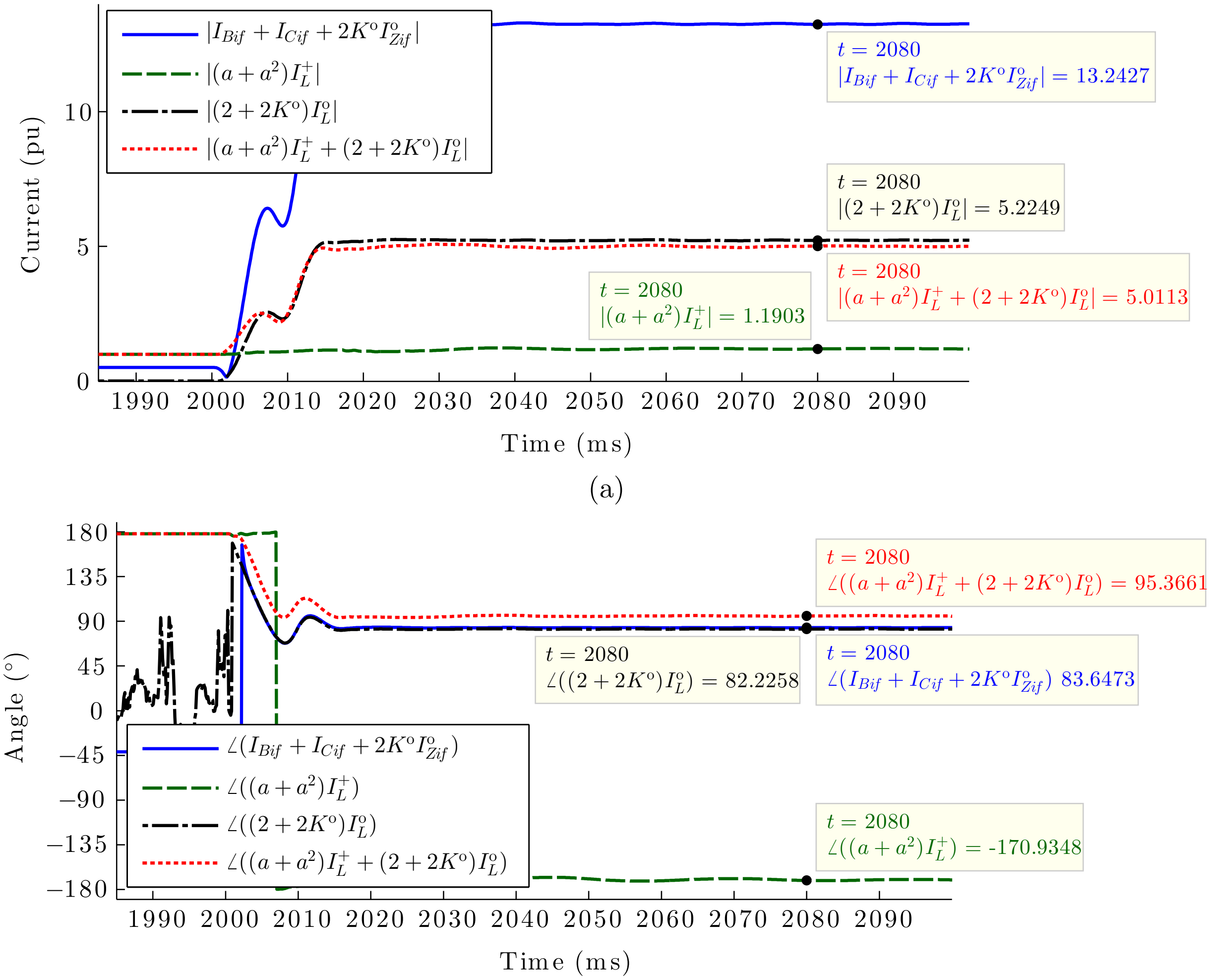

(a)

(b)

Figure 4.19. The numerator and denominator of M^{new}_{if-BC} for case 9 in Section 3.5.1, (a) Magnitude, (b) Angle.

4.8 Relay Setting for SLG Fault Protection

As discussed earlier, ground distance elements generally perform well in the event of SLG faults. Meanwhile, the settings of these elements that address the remote infeed effect should not be similar to those of conventional relays. Let us assume a relay with a quadrilateral characteristic and a tiltable reactance element. The numerator of M_{R_f-AG} in (4.1)

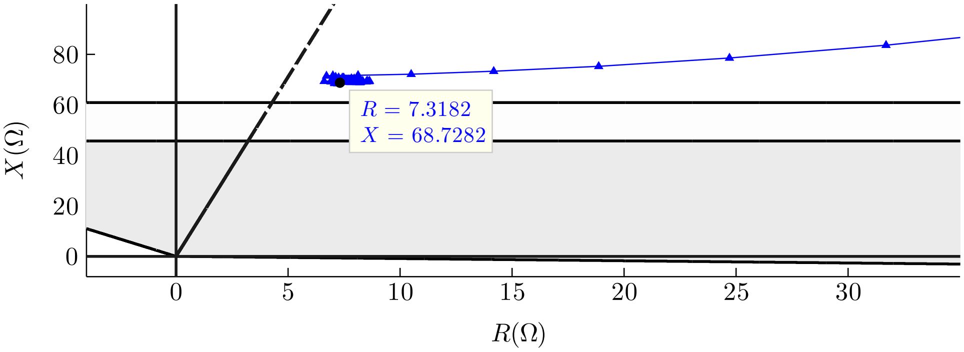

Figure 4.20. Z_{BC}^{new} of DS25 for case 9 of Section 3.5.1.

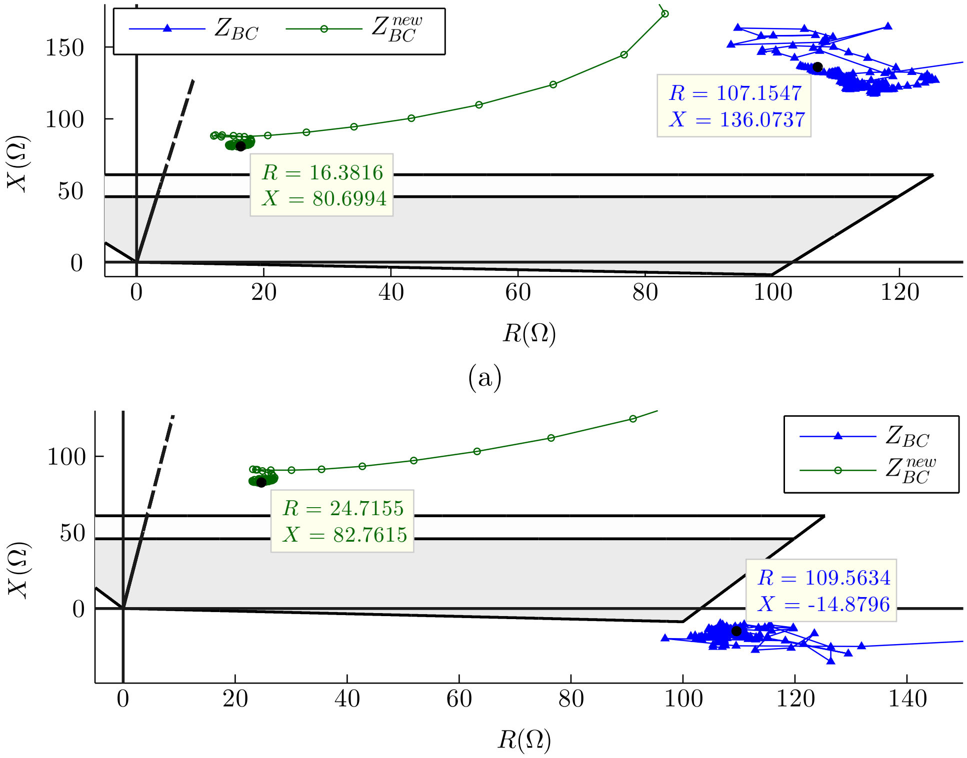

(a)

(b)

Figure 4.21. Operation of DS25 for a fault 20 km away from bus 5 on line 45 with 10 Ω resistance, (a) EU-GC, (b) NA-GC.

is written in terms of the symmetrical components as

$$I_{AL} + I_{AR} = I_L^+ + I_L^{\mathrm{o}} + I_R^+ + I_R^- + I_R^{\mathrm{o}} \tag{4.13}$$

The limited I_L^+ can be neglected in (4.13). The angles of I_L^{o} and I_R^{o} are close, as none of them are affected by the CIREPP's control system. Moreover, I_R^+, I_R^- and I_R^{o} are approximately in phase for an AG fault. As a result, the numerator of M_{R_f-AG} is almost aligned with I_L^{o}. The denominator of M_{R_f-AG} is also described in terms of the symmetrical components as

$$I_{AL} + K^{\mathrm{o}} I_L^{\mathrm{o}} = I_L^+ + (1 + K^{\mathrm{o}}) I_L^{\mathrm{o}} \tag{4.14}$$

Neglecting I_L^+ in (4.14), the denominator's angle is shifted from I_L^{o} by $\measuredangle(1 + K^{\mathrm{o}})$. As discussed, if K^{o} is not a real number, $\measuredangle K^{\mathrm{o}}$ is normally small and negative. Consequently, the numerator leads the denominator, regardless of the power flow direction. This is confirmed by the impedance depicted for the AG fault of case 11 in Figure 4.3. Although DS25 is at the power-sending end of line 25, and should be expected to overreach, it has underreached by 2 Ω. The tilting angle for a relay installed at the CIREPP must therefore be assigned according to $\measuredangle(1 + K^{\mathrm{o}})$.

I_L^+ can also influence the underreach. If I_L^+ leads I_L^{o} appreciably, it alleviates the backward shift in the angle of the zero sequence term in the denominator of M_{R_f-AG}. If the CIREPP meets the NA-GC, I_L^+ leads more and results in less underreach. The effect of I_L^+ on M_{R_f-AG} numerator is trivial, since the sum of the other terms is considerably larger. Thus, the tilting angle chosen based on $\measuredangle(1 + K^{\mathrm{o}})$ can be adaptively modified according to the magnitude and angle of I_L^+ and I_L^{o}.

4.9 Conclusion

The adverse effects of remote and intermediate infeed on a distance relay at a CIREPP substation could not be addressed by existing solutions. A new formula was developed to calculate the line impedance during LLG faults. The term added by the remote infeed and the fault resistance in this formula has a very small imaginary part, which leads to accurate calculation of the fault reactance. Furthermore, the term added by the intermediate infeed in the formula is small and along the line replica impedance.

A pilot scheme with minimal bandwidth requirement, which includes two directional relays, was suggested for balanced and LL faults. Since a conventional directional element was proved unreliable in applications involving CIREPPs, a new directional element was devised using unique features of CIREPP fault currents together with the impedance given by a distance relay. The proposed directional element performed successfully for the faults inside the CIREPP, in zone one and more distant zones.

The underreach or overreach of the relay at the CIREPP substation due to remote infeed during SLG faults is irrespective of the power direction and angle, and depends on the zero sequence compensation factor of the line, as well as the relative magnitude and angle of the local positive sequence current.

Chapter 5

Fault Direction Identification for Distribution Systems with DFIG-Based DG

The previous chapters studied protection of transmission systems with RE sources. The rest of the dissertation focuses on distribution systems with RE-based DGs. Distribution systems have normally been composed of radial feeders supplied from only one end, as a result of which the fault currents have been unidirectional. However, DG introduction has led to fault currents that flow bi-directionally in modern distribution grids, thus necessitating directional overcurrent relays to ensure selectivity of the protection system [78]. Directional overcurrent relays commonly operate according to the angle difference between phasors of the fault current and a polarizing quantity, which is the zero-sequence, a line or a memorized voltage signal [22].

The need for directional relays arises with almost all DG types. Meanwhile, some relaying problems are exclusively associated with specific DGs, such as wind-based ones. DFIG-based wind turbines constitute an appreciable portion of today's wind power [23]. Based upon the findings presented in Chapter 2, the following unveils that conventional directional elements malfunction during balanced short-circuits when a distribution system incorporates DFIG-based wind DG. Section 5.1 shows that the conventional approach of

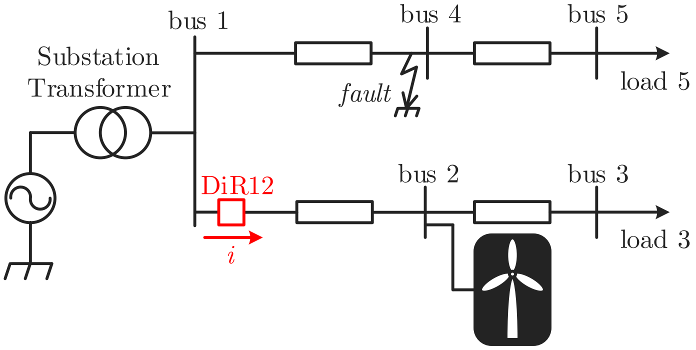

Figure 5.1. Layout of a simple distribution system with a DFIG-based DG.

finding the phase angle between the fault current and a voltage signal fails to provide the correct fault direction. A solution based on discrimination between DFIG and substation short-circuit currents according to their waveshape properties is proposed in Section 5.2. The efficacy of this solution is inspected by simulation results of IEEE 34 bus system in Section 5.3. Concluding remarks are presented in Section 5.4.

5.1 Problem Description

To analyze the basic operation of a directional relay along with a DFIG-based DG, the test system shown in Figure 5.1 is studied in this section. The crowbar resistance of the DFIG is zero at this stage. The effect of non-zero crowbar resistance is studied later on. At $t = 7$ s, a balanced fault is placed on bus 4, i.e., the feeder without the DG. The phase A current recorded by the relay at the beginning of the feeder with the DG is plotted in Figure 5.2 for a sub- and a super-synchronous rotor speed, resulting in positive and negative slips, respectively. The depicted waveshapes agree with the general fault current pattern described by (2.1). Specifically, the dependence of the current frequency on the slip is evident.

The relay installed at the beginning of the feeder with the DG in Figure 5.1, denoted by DiR12, has to be directional in order to avoid unnecessary tripping as a result of the DG contribution to the faults on the other feeder. Following the common directional relaying

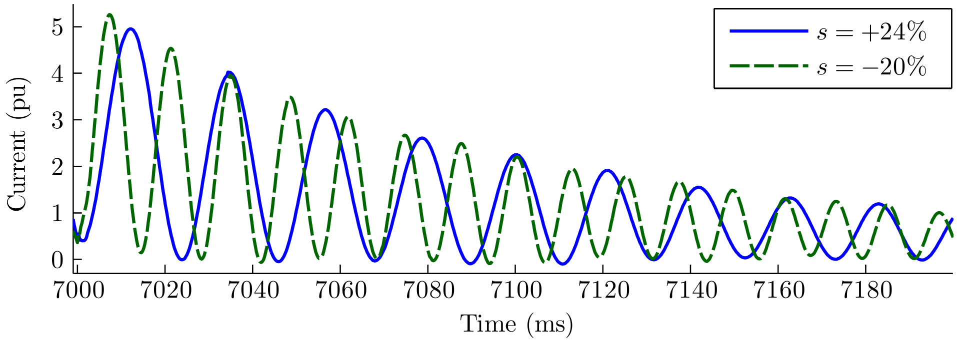

Figure 5.2. Balanced DFIG fault current for two sub- and super-synchronous rotor speeds.

practice for balanced short-circuits implemented in commercial digital directional elements, such as in [79] and [80], DiR12 is memory-polarized, i.e., the angle of each phase current is compared with that of the pre-fault voltage in the same phase. The results of this study are independent of the directional relay characteristic angle; so, for the sake of simplicity, the relay characteristic angle is chosen to be zero degrees. DiR12 measures the voltage phasor using FCDFT. Due to the unconventional properties of a DFIG fault current, the performance of DiR12 is inspected by the following three current phasor measurement techniques (PMTs) developed so as to suppress the impact of the fault current's decaying dc offset on the measured phasor.

- The 1.25 cycles cosine filtering technique [32],
- The one-cycle CLES-based technique, and
- The one-cycle modified least error squares (MLES)-based method of [81].

The first two techniques are termed common PMTs, as they are widely used in modern commercial relays [32]. The MLES method is a modified version of the CLES technique and assumes exponentially decaying amplitude for the fundamental component, which is the case for DFIG short-circuit currents.

Apart from the sampling rate, which is 3840 Hz in this chapter, the frequency of the signal under study is also required to build up the digital filters associated with the above PMTs. As discussed in Chapter 2, the main frequency tracking approach used in modern industrial relays is to find the voltage frequency and update all of the relay subroutines, including the digital filters that compute the current phasor.

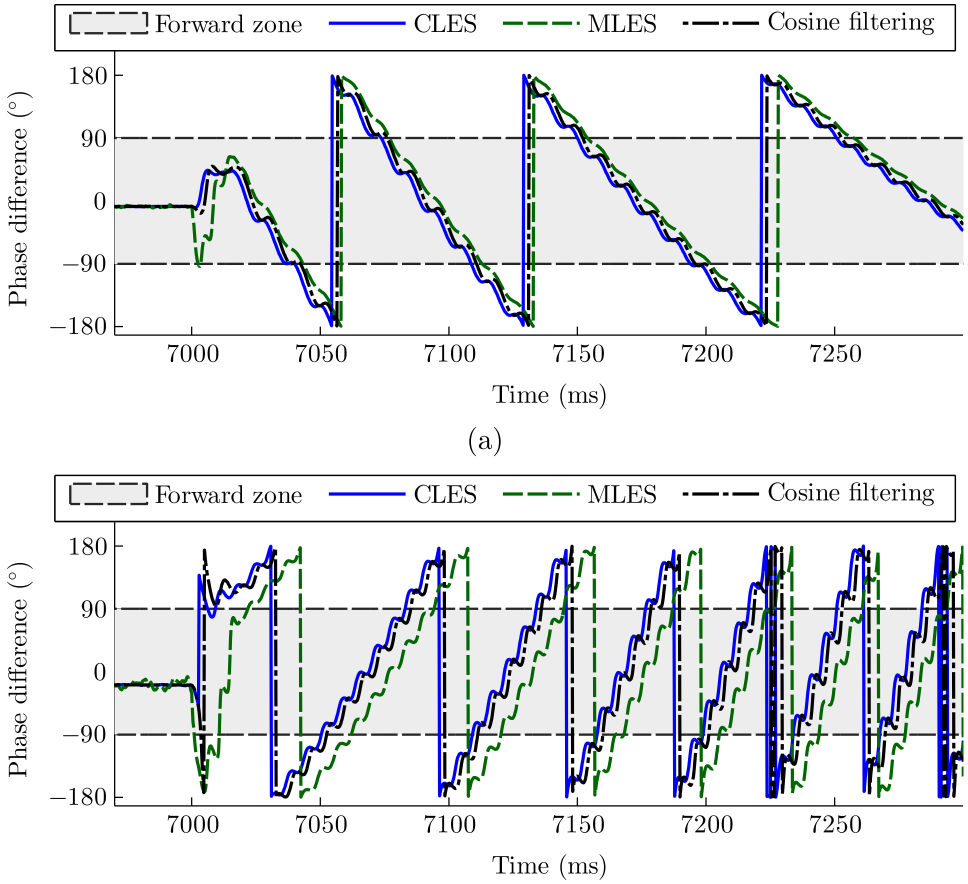

(a)

(b)

Figure 5.3. Phase difference between the current and memorized voltage for the fault of Figure 5.2, considering voltage frequency for all digital filters, (a) $s = +24\%$, (b) $s = -20\%$.

The same frequency tracking approach is adopted to analyze the response of the common directional relaying practice based on the current and voltage phase angle difference. Figure 5.3 plots the angle difference between the phase A memorized voltage and the current recorded by DiR12 during the fault depicted in Figure 5.2 for both the sub- and super-synchronous rotor speeds using the three current PMTs discussed above. The positive direction for the current recorded by DiR12 is assumed to be from bus 1 to bus 2. Prior to the fault, the power flows from the substation to bus 2 and the load connected to bus 3. Thus, the pre-fault phase difference between the voltage and the current of DiR12 is correctly around zero, inside the $[-90°, +90°]$ range. After the fault, however, the current measured at the DiR12 location is the DFIG contribution to the fault on bus 4. In other words, the current direction is reversed and flows towards bus 1, so the phase difference has to normally exit and remain outside the $[-90°, +90°]$ interval following the initial post-fault transient period of the PMTs in order to indicate the backward direction of the fault. However, it is shown that the measured phase difference starts oscillating inside and outside the $[-90°, +90°]$ range for both rotor speeds, regardless of the PMT employed, as a result of which DiR12 operation is utterly unreliable.

These phase oscillations occur because the current frequency is quite different from the voltage's 60 Hz frequency, which is used to build the digital filters that compute the current phasor. Hence, there exists an apparent discrepancy between the current's actual fundamental frequency component and the measured one, which is oscillatory both in magnitude and phase angle.

The above problem cannot be addressed simply by using the actual current frequency to develop the digital filters of the current PMTs. To demonstrate this issue, the phase differences shown in Figure 5.4 for the above fault conditions are obtained by considering the current and voltage frequencies for calculating the current and voltage phasors, respectively. Again, the phase differences for both sub- and super-synchronous cases oscillate inside and outside the $[-90°, +90°]$ interval, irrespective of the PMT utilized, periodically indicating reverse and forward directions for the fault location. The oscillating phase differences stem from the fact that the measured voltage and current phasors correspond to different frequencies, thereby rotating at different speeds and making it theoretically impossible to find a meaningful and fixed phase difference between them.

The problems observed for DFIG-based DGs do not apply to distribution systems with SCIG-based DGs, as their fault current frequency is close to the nominal frequency.

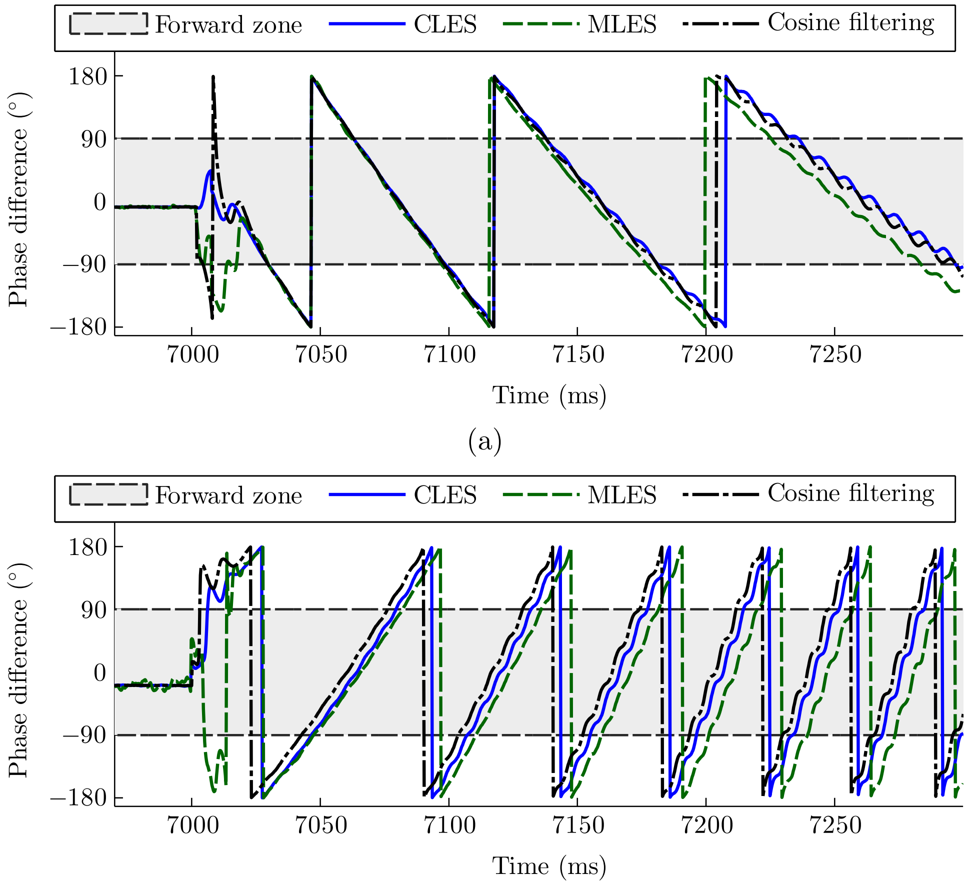

(a)

(b)

Figure 5.4. Phase difference between the current and memorized voltage for the fault of Figure 5.2, considering voltage and current frequencies for their respective digital filters, (a) $s = +24\%$, (b) $s = -20\%$.

5.2 Proposed Solution

5.2.1 Proposed Directional Relaying Scheme

It was demonstrated that the common directional relaying based on comparing the phase difference between voltage and current signals fails to detect the fault direction when a DFIG-based DG is involved. This section proposes a new approach to detect the fault direction for such conditions according to the fault current's waveshape properties. The

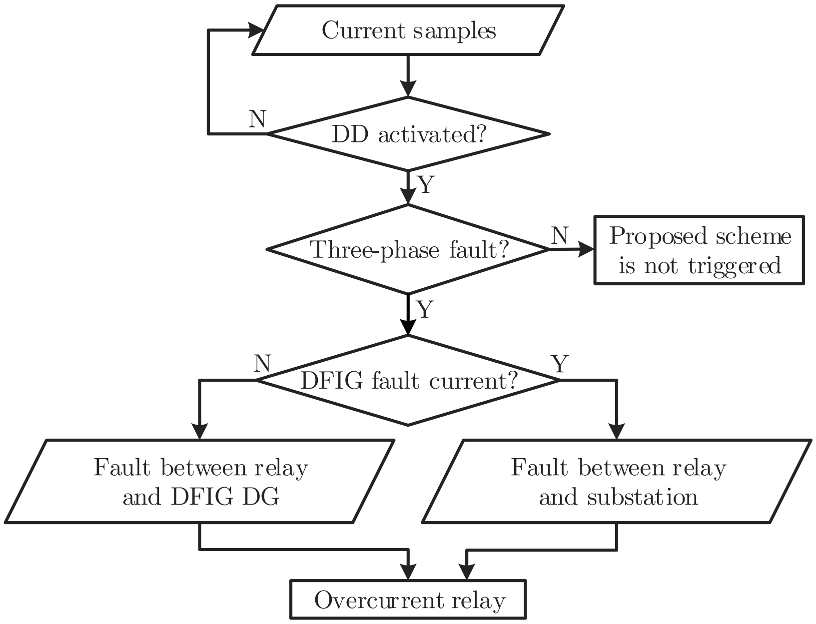

Figure 5.5. Flowchart of the proposed scheme for fault direction identification in the presence of DFIGs.

waveshapes of DFIG balanced fault currents include unique features that can distinguish them from the fault currents flowing from the distribution substation.

Figure 5.5 illustrates the flowchart of the proposed scheme. A typical current-based DD that operates based on the cycle-to-cycle comparison of current samples triggers this scheme. If the fault is balanced, the waveshape recognition technique, discussed in the next subsection, will determine whether the current possesses the distinctive waveshape attributes of DFIG fault currents. The flow of a DFIG fault current at the relay location signifies that the fault is between the distribution substation and the relay location, and the fault direction is determined accordingly. In contrast, the absence of DFIG fault currents' waveshape properties demonstrates that the current recorded by the relay is a substation fault current, and the fault location is between the relay location and the DFIG-based DG. The specified direction is then exported to the overcurrent element to make the final tripping decision.

5.2.2 Proposed Waveshape Recognition Technique

Thevenin equivalent based modeling of aggregate transmission systems results in substation fault currents composed of a constant sinusoidal component and a decaying dc offset with an equal or smaller magnitude, which were expressed by (2.4). The previously discussed PMTs effectively suppress the decaying dc offset and provide the accurate fundamental frequency phasor. For example, the current described by (2.4) is plotted in Figure 5.6(a) for $\theta = 90°$, $\tau = 40$ ms, and $I_m = 1$. The figure also displays the magnitude of the phasors obtained by the three current PMTs mentioned earlier. For all three techniques, the calculated phasor remains virtually fixed at a very narrow margin of the fundamental component's amplitude following their initial response time.

A DFIG fault current and its measured phasor, however, exhibit a different pattern. As a representative case, Figure 5.6(b) shows the current described by (2.1) for identical unity ac and dc component amplitudes, and for dc and ac time constants equal to 40 ms and 80 ms, respectively. The ac component frequency is 60 Hz. The above PMTs are again employed to find the current phasor. The decaying nature of the ac component is directly reflected in the measured phasors. The declining phasors of Figure 5.6(b) are in clear contrast with the uniform pattern observed for the phasors plotted in Figure 5.6(a).

As defined by (5.1), $\rho_{1\phi}$ calculates the relative percentage decline in the magnitude of the measured phasor for the fault current in one phase.

$$\rho_{1\phi} = \frac{|I_{f1}| - |I_{f2}|}{|I_{f2}|} \times |\frac{i_{f-\text{ext}}}{I_{f2}}| \times 100 \tag{5.1}$$

In this relation, I_{f1} is the maximum of the measured fault current phasor within the first half-cycle after the initial response time of the employed PMT. I_{f2} is the minimum magnitude of the measured fault current phasor in the second half-cycle after the response time of the PMT applied to the current. $i_{f-\text{ext}}$ is the largest magnitude for the current samples prior to I_{f2} location and 4 ms after the DD activation. $i_{f-\text{ext}}$ is supposed to be the extremum associated with the fundamental component. The 4-ms delay avoids mistaking the initial current extremums that might be generated due to resonance for the extremum associated with the fundamental component.

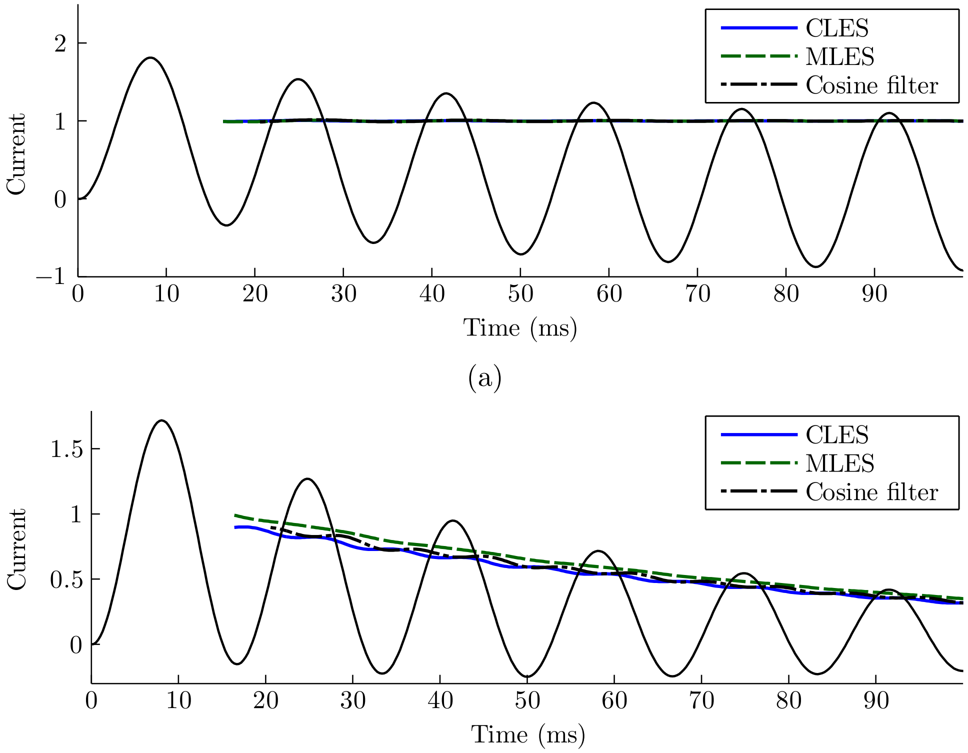

(a)

(b)

Figure 5.6. Comparison of the phasor measured for substation and DFIG fault currents, (a) Current of (2.4) for $\theta = 90°$, $\tau = 40$ ms and $I_m = 1$, (b) Current of (2.1) for identical ac and dc components, with 40 ms and 80 ms time constants, respectively.

I_{f1} and I_{f2} obtained by different PMTs along with $i_{f-\max}$ and the resultant $\rho_{1\phi}$ are tabulated in Table 5.1 for the two currents shown in Figure 5.6. The almost uniform phasor measured for the current of Figure 5.6(a) has led to very small $\rho_{1\phi}$s, whereas the indices obtained for Figure 5.6(b) are large due to the DFIG fault current's decaying trend. In other words, $\rho_{1\phi}$ is capable of differentiating between the fault currents flowing from the distribution substation and a DFIG-based DG. The gap between $\rho_{1\phi}$ for substation and DFIG fault currents is widened by the second ratio on the right side of (5.1), as the dc offset of a substation fault current never exceeds its fundamental component's amplitude, which is not the case for DFIG fault currents.

The choice of PMT for finding the parameters required by (5.1) affects the measured $\rho_{1\phi}$.

TABLE 5.1
PARAMETERS OF (5.1) FOR THE CURRENTS SHOWN IN FIGURE 5.6

Fault current	$i_{f-\max}$	PMT	I_{f1}	I_{f2}	$\rho_{1\phi}$ (%)
Figure 5.6(a)	1.812	CLES	1.006	0.9953	1.96
		MLES	1.007	0.9945	2.29
		COS	1.014	0.9883	4.77
Figure 5.6(b)	1.717	CLES	0.8998	0.7277	55.8
		MLES	0.9902	0.8017	50.35
		COS	0.8956	0.7273	54.63

The MLES technique tailors the CLES technique to cope with a decaying ac component, and provides excellent results for both of the synthetic currents depicted in Figure 5.6. However, the gain responses of the sine and cosine digital filters associated with the MLES technique, displayed in Figure 5.7(a), indicate that this technique is extremely prone to fault current high-frequency contaminations. Harmonics are not considered for developing the filters whose frequency responses are shown in Figure 5.7(a). Considering harmonics reduces the filter gain for the harmonics to zero, but further deteriorates the frequency responses for the non-harmonic components, which are quite likely to be present in the fault current due to noise, resonance, and so on. The frequency responses of the CLES technique's sine and cosine filters, plotted in Figure 5.7(b), illustrate that common PMTs do not suffer from this deficiency.

On the other hand, some oscillations are superimposed on the phasors measured by the common PMTs when the current's fundamental magnitude is variable, because such currents include non-harmonic components in their spectrum. However, as observed in Figure 5.8, which displays the normalized spectrum of the current in Figure 5.6(b), the resultant components are mostly situated in the low-frequency region, and are thereby damped by the sine and cosine filters associated with the common PMTs. As shown in Figure 5.7(b), even for the higher frequency components, except for the cosine filter's response inside a limited interval, the CLES filters' gains are lower than unity. As a result, the mentioned oscillations in the phasors provided by the common PMTs are relatively small and do not obscure the phasors' overall decaying pattern for DFIG fault currents. Among the common PMTs, the CLES technique is chosen for its faster speed than the

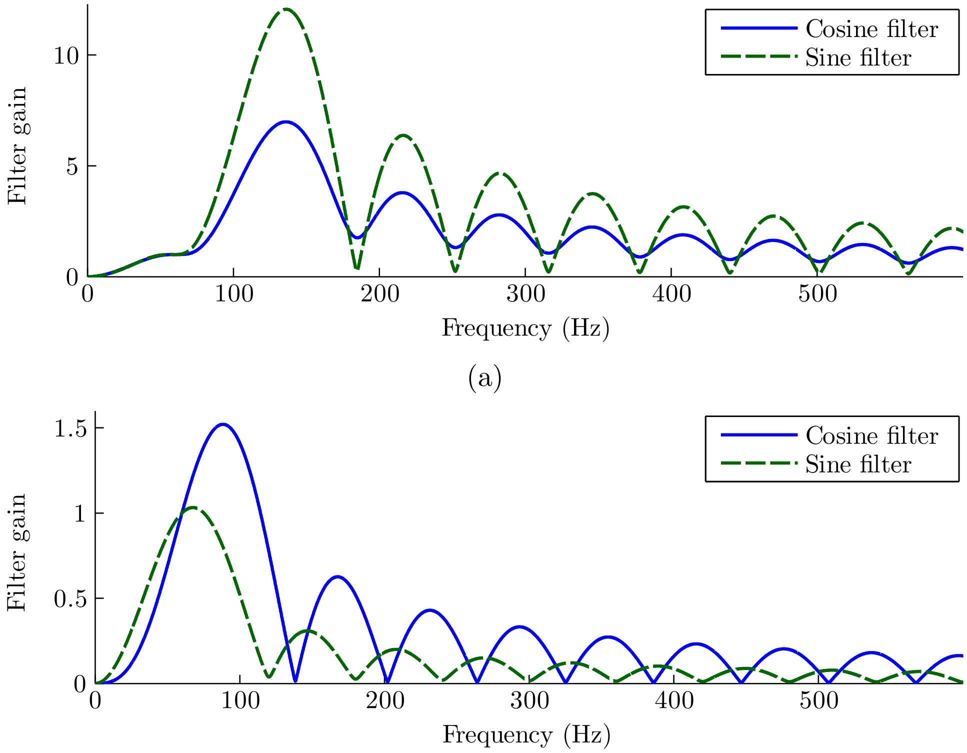

(a)

(b)

Figure 5.7. Frequency response of the digital filters, (a) MLES method, (b) CLES method.

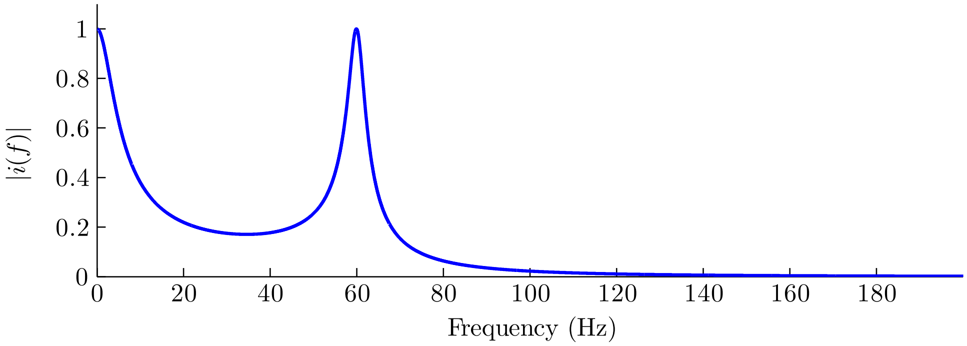

Figure 5.8. Normalized spectrum of the current shown in Figure 5.6(b).

cosine filtering method.

$\rho_{3\phi}$ is defined as the sum of $\rho_{1\phi}$s for the three phase currents. Because of the quite large value of $\rho_{1\phi}$, and subsequently of $\rho_{3\phi}$, for DFIG fault currents, a fixed thresholding

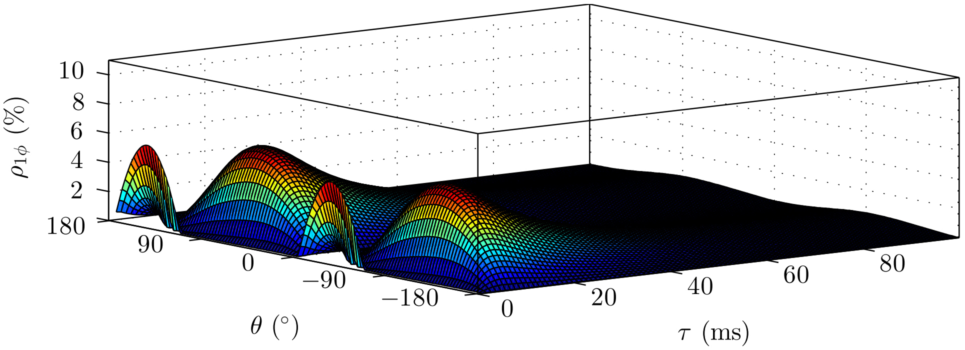

(a)

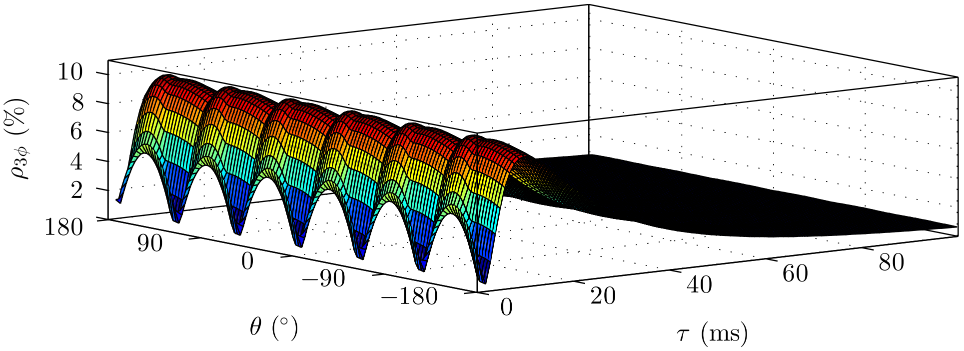

(b)

Figure 5.9. Indices obtained for the currents described by (2.4) with respect to the fault inception angle and dc offset time constant, (a) $\rho_{1\phi}$, (b) $\rho_{3\phi}$.

approach is applied to classify fault currents. The threshold setting criterion is founded upon the maximum indices obtained for the fault currents described by (2.4). The set of three-phase currents expressed by (2.4) is obtained by adding ±120° to θ. In (2.4), θ and τ were varied in the ranges of $[-180°, +180°]$ and $[1, 100]$ ms, respectively, and the phasors for each pair of θ and τ were inspected. The results, plotted in Figure 5.9, show that $\rho_{1\phi}$ of phase A and $\rho_{3\phi}$ reach 6.17% and 9.81% at their maximum, respectively. Considering a 100% plus safety factor to address any effect of noise and other transients, $\rho_{3\phi} = +20\%$ is selected as the threshold for fault current classification.

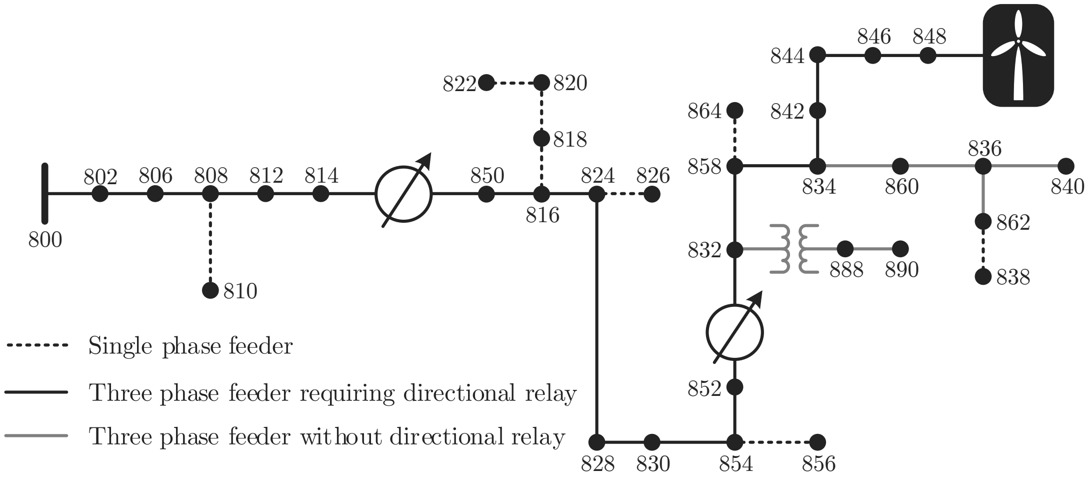

DFIG specifications: S_n=1.5 MW, V_n=0.575 kV,

R_s=0.0071 pu, R_r=0.005 pu, X_m=2.9 pu, X_s=0.1714 pu, X_r=0.1563 pu.

DC-link rated voltage and capacitor: V_{dc}=1200 V, C=2 mF.

Figure 5.10. The diagram of IEEE 34 bus system with a DFIG-based DG.

5.3 Simulation Results

The performance of the proposed method was comprehensively studied for the IEEE 34 bus system, simulated in the PSCAD/EMTDC program, as a benchmark distribution system model. The simulated currents were exported to Matlab, where the proposed method was implemented. The test system as well as the specifications of a DFIG-based DG connected to bus 848 on the far right end of the system are displayed in Figure 5.10. The control mechanism for the DFIG converters along with the wind turbine specification and the pitch angle control system are based on the industrial models of [82]. After the DG is connected, the feeders shown by a black solid line must be protected by directional relays in order to ensure selectivity of the protection system.

Fault direction was determined using the proposed method for a variety of conditions. The tests included different fault locations, wind speeds, fault inception angles, crowbar resistances, etc., and were conducted for different relay locations. The results were promising and corroborated the efficacy of the proposed method. A part of these results that

Table 5.2
Performance of the Proposed Method for Different Faults

Fault location	Relay location	Slip (%)	$\rho_{1\phi}$(%)			$\rho_{3\phi}$(%)	Fault direction
			Phase A	Phase B	Phase C		
B806	B814	+22	19.5	17.9	13.4	50.8	▶ †
B816	B828	+22	22.9	21.6	17.7	62.2	▶
B852	B858	+22	25.4	24.3	20.1	69.8	▶
B840	B844	+22	27.2	25.7	21.8	74.7	▶
B816	B814	+22	0.4	4.7	0.2	5.3	◀ ‡
B806	B814	0	18.3	16.2	12.1	46.6	▶
B816	B828	0	22.2	20.3	16.6	59.1	▶
B852	B858	0	24.6	22.7	18.4	65.7	▶
B840	B844	0	26.3	24.5	20.8	71.6	▶
B816	B814	0	0.3	4.7	0.3	5.3	◀
B806	B814	-25	17.5	14.9	11.0	43.4	▶
B816	B828	-25	21.7	19.5	15.5	56.7	▶
B852	B858	-25	23.3	21.3	17.1	61.7	▶
B840	B844	-25	25.4	23.6	20.0	69	▶
B840	B858	-25	0.4	4.8	0.3	5.5	◀

† Towards the substation.

‡ Towards the DG.

corresponds to zero crowbar resistance is reported in Table 5.2. Some of the performed tests are graphically presented in this section. First, two case studies that include different fault locations and wind speeds are reviewed. Then, the effect of crowbar resistance is analyzed, and finally, the operation of the proposed method for a fault current flowing from the substation is demonstrated.

5.3.1 Case Studies

5.3.1.1 Fault on Bus 842

A balanced fault is placed on bus 842 at $t = 9$ s, when the DFIG slip is +6.7%, and the crowbar resistance is zero. The three phase currents recorded at bus 844 are depicted in

Figure 5.11. A relay at bus 844 must classify the current as a DFIG fault current and, in turn, identify the fault direction towards the distribution substation, that is, bus 800. The decaying pattern of the ac component and the measured phasor is obvious for all phases, and $\rho_{1\phi}$ equals 38.58%, 22.59% and 16.47% for phases A, B and C, respectively, which is fairly above the maximum $\rho_{1\phi}$ found in Figure 5.9(a). As a result, $\rho_{3\phi}$ becomes 77.64%, i.e., about four times larger than its threshold, and the current is correctly labeled as a DFIG one.

5.3.1.2 Fault on Bus 802

The current recorded by the relay located at bus 832 for a fault on bus 802 at $t = 9$ s is shown Figure 5.12. Due to the increased wind speed, the DFIG slip at the fault instant is −20%. Here again, the crowbar resistance of the DFIG is zero. Unlike the last-studied fault, which was relatively close to the DG, this fault is located farthest from the DFIG, and therefore the short-circuit is not severe, leaving higher voltage at the DG terminal and a lower level of demagnetization for the DFIG. Therefore, the decline rate of the phasors in Figure 5.12 has reduced, compared to those of the previously discussed fault currents. Nevertheless, $\rho_{1\phi}$ is still as large as 20.86%, 22.14% and 11.27% for phases A, B, and C, respectively, adding up to $\rho_{3\phi} = 54.27\%$, which is more than twice the 20% threshold, and can reliably identify the DFIG type of the fault current.

5.3.2 Effect of Crowbar Resistance

For all of the faults studied so far, the crowbar resistance was zero. However, in practice, some resistance is added to the crowbar circuit, as it improves the DFIG operation during disturbances by decreasing the short-circuit current level, dampening generator's torsional oscillations, etc. [33]. Figure 5.13 shows the currents recorded at bus 842 for a fault on bus 860, while the machine slip is −18% and the crowbar resistance is 0.1 pu. The decaying rate of the sinusoidal component in Figure 5.13 is significantly larger than that of the previously shown fault currents, as a result of which $\rho_{1\phi}$ has grown to 853.64%, 478.90% and 465.80% for phases A, B and C, respectively, and $\rho_{3\phi}$ equals 1798.34%, which is considerably in

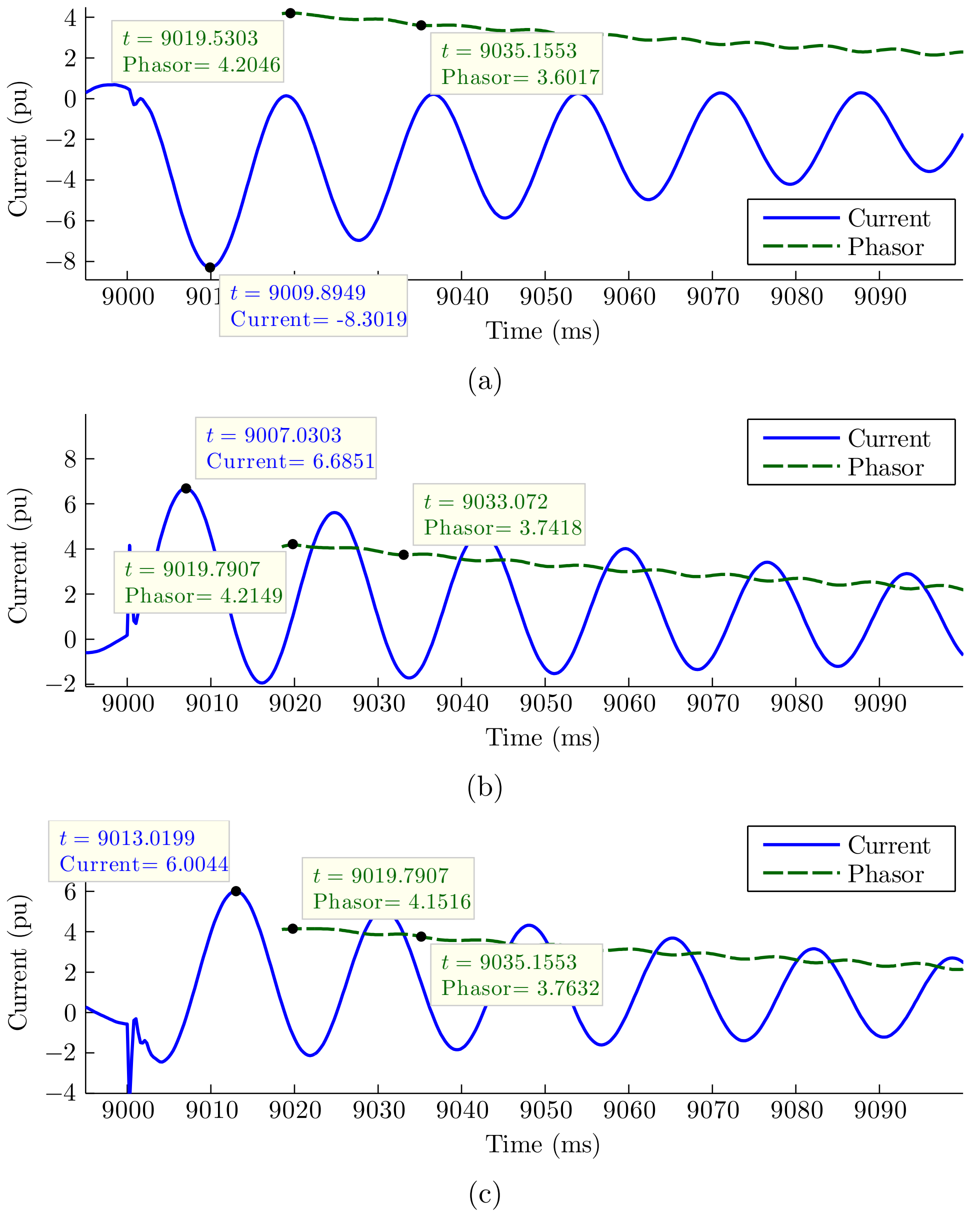

Figure 5.11. Currents recorded at bus 844 for a fault on bus 842, (a) Phase A, (b) Phase B, (c) Phase C.

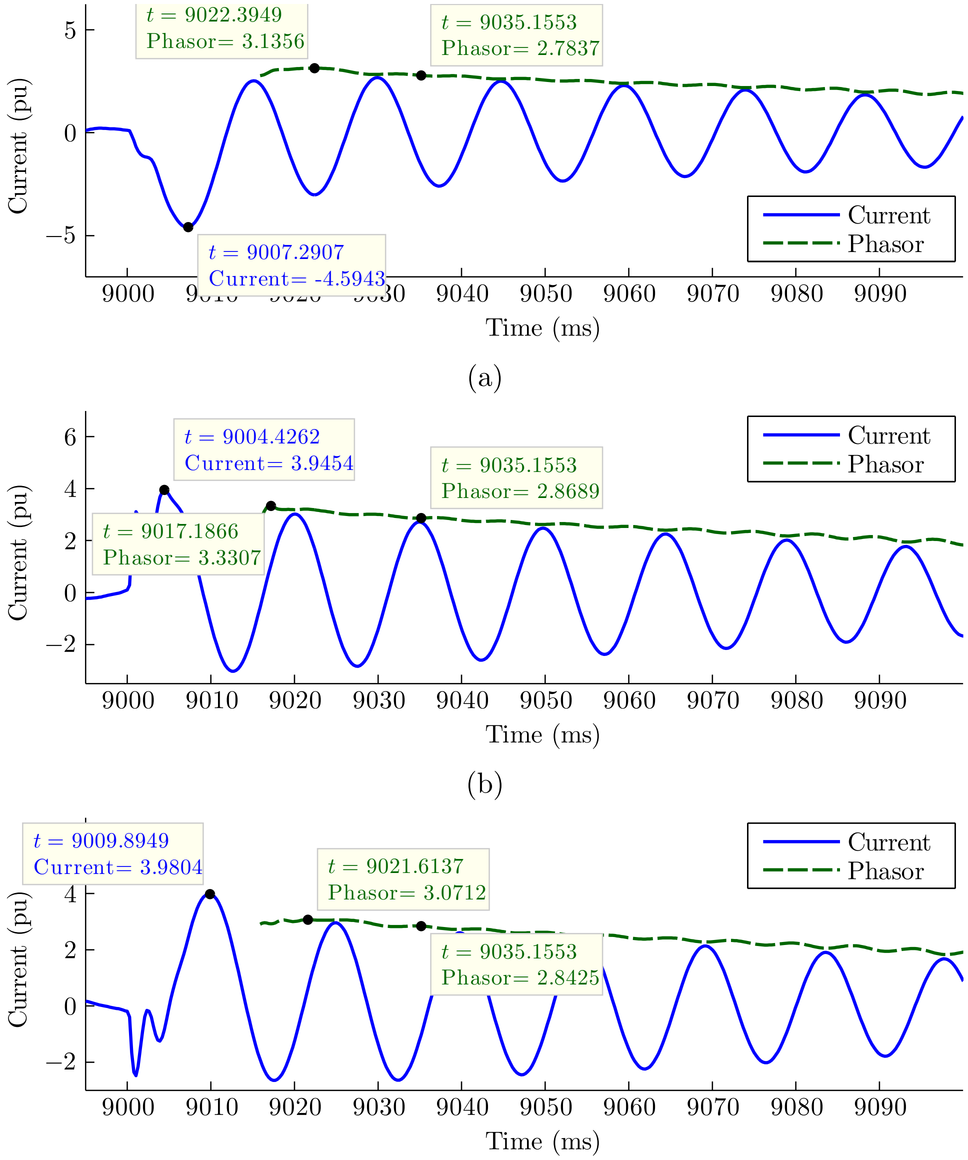

(a)

(b)

(c)

Figure 5.12. Currents recorded at bus 832 for a fault on bus 802, (a) Phase A, (b) Phase B, (c) Phase C.

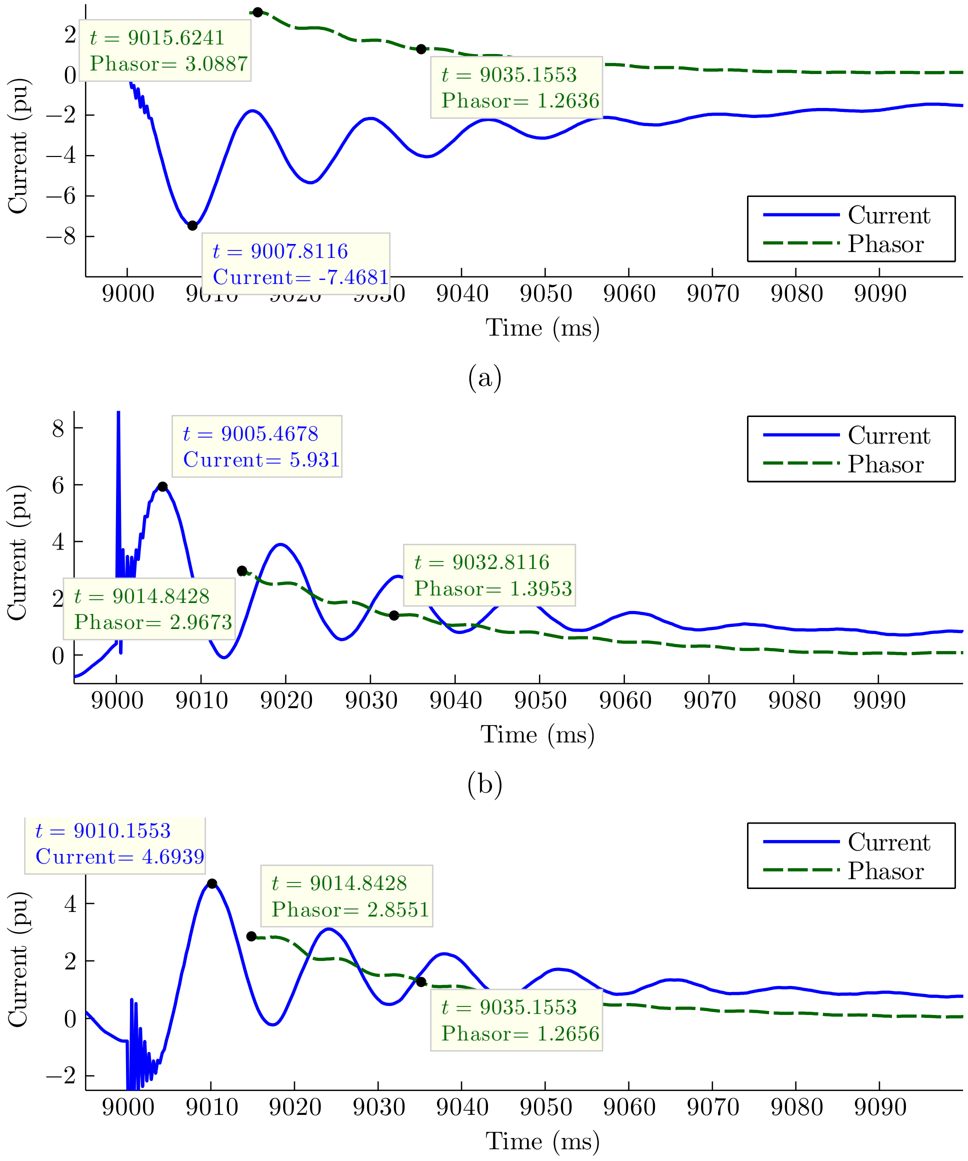

(a)

(b)

(c)

Figure 5.13. Currents recorded at bus 842 for a fault on bus 860 with non-zero resistance for the crowbar, (a) Phase A, (b) Phase B, (c) Phase C.

excess of the assigned threshold. The improved performance of the proposed method when resistance is inserted into the crowbar path was expected. The crowbar resistance raises the effective resistance of the rotor circuit. Thus, the short-circuit transient time constant, i.e., T' in (2.1), is decreased, and the amplitude of the ac component declines faster. Consequently, $\rho_{3\phi}$ grows excessively, and the proposed method performs exceptionally well for the more commonly observed shape of DFIG fault currents.

5.3.3 Substation Fault Currents

The almost constant ac magnitude for the substation short-circuit currents leads to very small values for $\rho_{3\phi}$. For the fault studied in Section 5.3.2, the current flowing through bus 852, which originates from the substation, is shown in Figure 5.14. The measured phasors exhibit constant magnitudes for all three phases, and $\rho_{1\phi}$ is as small as 0.24%, 4.86% and 0.10% in phase A, B and C respectively, resulting in $\rho_{3\phi} = 5.2\%$, which is safely below the set threshold. Hence, the proposed method identifies the fault location to be between the relay location and the DG. The proposed method was tested for several other substation fault currents, and $\rho_{3\phi}$ did not reach even half of its threshold.

5.4 Conclusion

The frequency of memorized voltage that polarizes directional elements during balanced short-circuits is closely tied with the nominal frequency. The fault current frequency for DFIG-based wind DGs, however, may considerably deviate from the nominal frequency depending on wind speed. On this basis, the impossibility of finding fault direction through the common method of phase angle comparison between the current and voltage phasors was demonstrated. In addition, a novel method was proposed to address this problem by classifying fault currents according to their waveshape properties. The decaying pattern of the ac component for DFIG fault currents proved to be a key feature in discriminating such currents from the short-circuit currents that originate from the distribution substation. The index $\rho_{1\phi}$ measured the percentage decline in the current phasor within the two cycles after the fault inception. The sum of $\rho_{1\phi}$ for the three phases was able to reliably classify fault currents. Operation of the proposed method was tested for the IEEE 34 bus system.

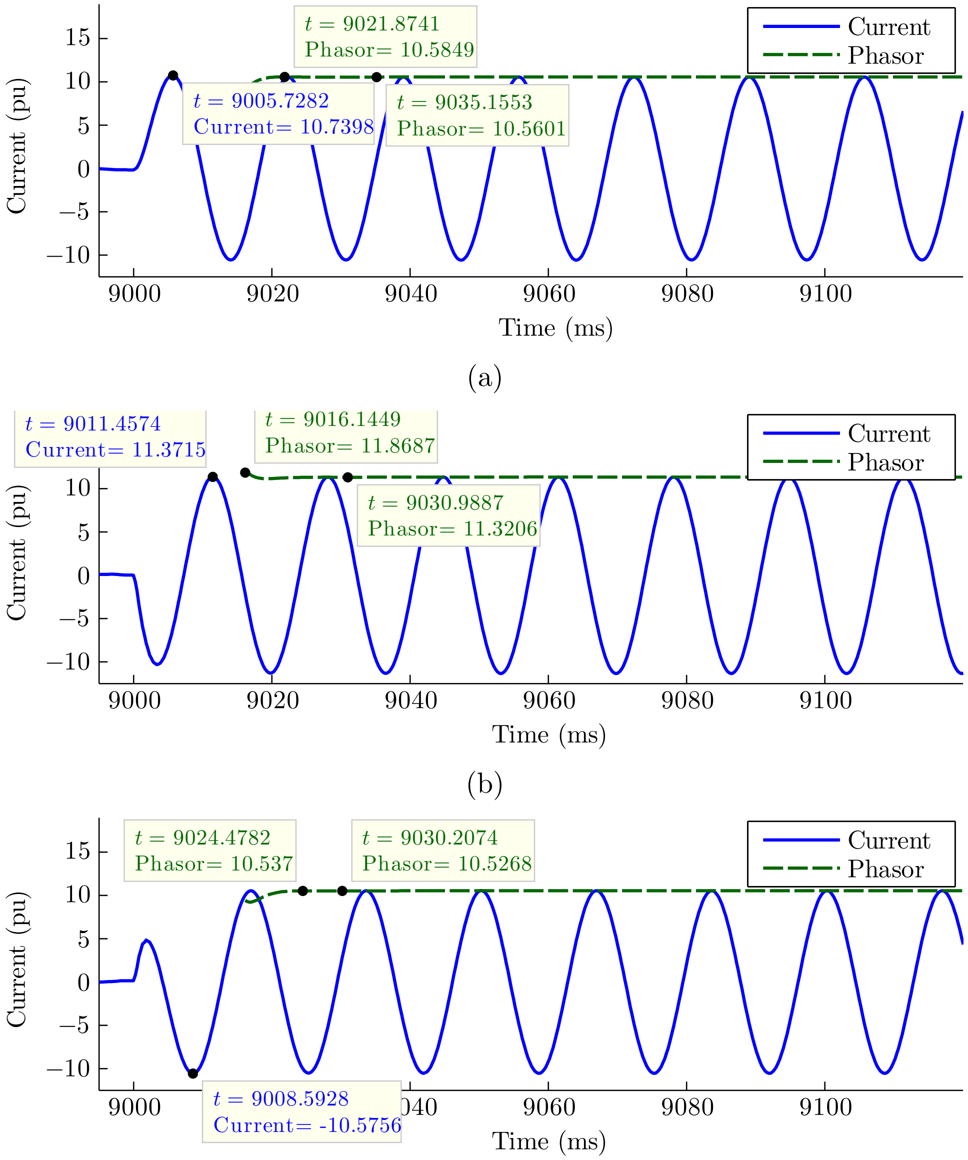

(a)

(b)

(c)

Figure 5.14. Currents recorded at bus 852 for a fault on bus 860, (a) Phase A, (b) Phase B, (c) Phase C.

Successful results were obtained regardless of the relay and fault location. Particularly promising performance was observed when a resistance is placed along the DFIG's crowbar path, which is the most likely situation in practice.

Chapter 6

Fault Type Classification in Microgrids with PVDGs

Stemming from the different operation modes and the diversity of generation technologies, the protection of a microgrid can be challenging [83]. Traditional relaying schemes for LV and medium voltage systems may fail to protect a microgrid, particularly if converter-interfaced renewable DGs, such as photovoltaic DGs (PVDGs), are involved, as is often the case. Similar to CIREPPs discussed in Chapters 3 and 4, PVDGs have limited fault currents, to which the overcurrent elements are normally insensitive [84]. Various publications offer protection solutions for microgrids by means of adaptive and communication-assisted techniques [84–89]. Despite their successful fault detection, these methods do not provide information on the fault type.

Next-generation microgrids are expected to be smart and fault-resilient, and should thus maintain the operation of sound phases during the unbalanced short-circuits, which account for the majority of faults. On the other hand, single-phase protective devices are increasingly installed in modern distribution systems. That is why several proposals have been put forward by the industrial community to apply single- and double-pole tripping in distribution systems [90]. With the prospect of substantial improvement to system reliability, this plan has already been put into practice by some utilities and relay manufacturers [91,92]. The Alabama Power Company and Progress Energy Florida are cases in point [92, 93].

Selective phase tripping requires fault type classification by the microgrid protection system. In transmission system relays, fault type classification is an imperative subroutine, the output of which is needed for several functions, e.g., single-pole autoreclosure and blocking of ground distance elements during phase faults. An early fault type identification method still used by some relay manufacturers is based on the magnitudes of the impedances measured for different fault loops [94]. The inaccuracy of this approach for short lines, among other shortcomings, led to the development of several classifiers exploiting the phase differences between the superimposed sequence currents [95–97], which have been proven effective for conventional power systems. Some of these methods, however, need high-bandwidth communication infrastructure [96, 97], which is not normally available in LV and medium voltage systems. Another group of relays utilize overcurrent-based methods using phase and sequence currents with satisfactory performances for conventional systems [69, 98]. Many classifier based on artificial intelligence, decision tree, mathematical morphology, pattern recognition and wavelet transform, among other methods, have also been proposed in the literature [99–103], but have remained without industrial application to date, due to practical limitations, including noise sensitivity, complexity and high computational burden.

This chapter studies fault selection for a microgrid. The test microgrid is overviewed in Section 6.1. Section 6.2 reveals that the existing fault type classifiers malfunction for microgrids that include PVDGs. The analogy between the grid-side converters makes this study equally applicable to the systems with Type IV wind DG. The unveiled problems can also be encountered in transmission systems to which CIREPPs are connected. Two new methods are developed in Section 6.3 to determine the fault type for not only a microgrid with PVDG, but any three-phase system. Section 6.4 verifies the performance of the proposed classifiers. It is shown that they perform successfully for both the autonomous and grid-connected modes of a microgrid, and do not require communication facility. Their other salient features include robustness against fault resistance and high-frequency noise, as well as independence from PVDG's PF in the course of faults. Section 6.5 concludes this chapter.

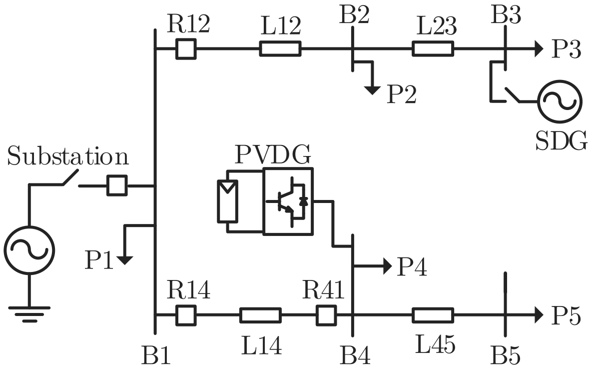

- V_n=34.5 kV, f=60 Hz,
- Feeder impedance:
  Positive sequence: 0.0178+j0.314 Ω/km,
  Zero sequence: 0.295+j1.04 Ω/km,
- Feeder lengths:
  L12=8 km, L23=12 km, L14=8 km, L45=12 km,
- Loads:
  P1=1.0 MW, P2=4.5 MW+0.6 MVAr,
  P3=3 MW+0.3 MVAr, P4=4.5 MW+0.6 MVAr,
  P5=6 MW+0.15 MVAr,
- Substation: $Z_{th}=4\measuredangle 80^\circ$ Ω, $\measuredangle V=0^\circ$,
- SDG: $Z_{th}=27.5\measuredangle 80^\circ$ Ω, $\measuredangle V=0.5^\circ$,

Figure 6.1. Single line diagram of the test microgrid.

6.1 Test Microgrid

Simulated by PSCAD/EMTDC program, the 34.5 kV, 60 Hz system of Figure 6.1 is used for this study. The system parameters are shown in the figure. The system is balanced at this stage. The 9.2 MW PVDG at bus 4 along with a synchronous DG (SDG) connected to bus 3 can supply all of the loads. Therefore, the substation breaker can be opened, allowing the system to operate as an isolated microgrid. During the grid-connected mode, the SDG is normally open. R14 is one of the relays that protect the feeder between buses 1 and 4. The fast dynamics of the photovoltaic source are essentially decoupled from the grid by the dc capacitor. Thus, the photovoltaic source together with the dc-dc converter are represented by a controllable current source. The specifications of the PVDG transformer are 14 MVA, 4.16/34.5 kV, X=0.1 pu and dYG. The PVDG can ride through faults using a braking chopper circuit [56].

6.2 Performance of Existing Fault Type Classifiers

6.2.1 Current Angle-based Methods

The relative angles of the superimposed sequence currents are utilized by many relays, e.g., [62], to determine the fault type. The approach developed in [95] and adopted by [62]

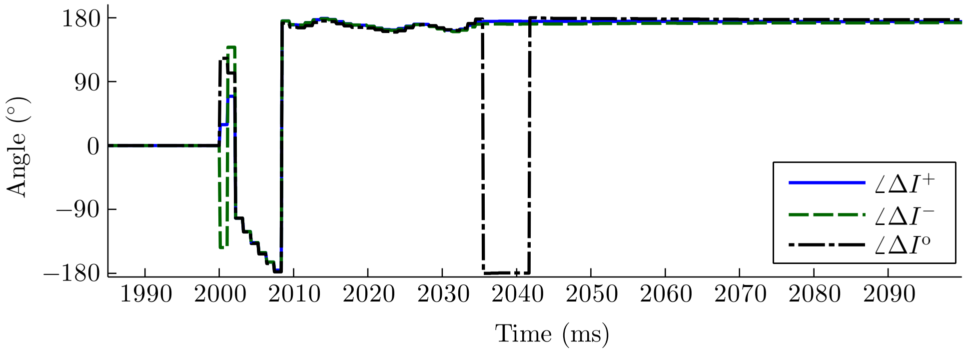

Figure 6.2. Angles of superimposed sequence currents of R14 for a bolted AG fault at bus 2 when the PVDG is not in service.

ensures accuracy for all conditions, including a microgrid with conventional sources. Take, for instance, the system of Figure 6.1 in the grid-connected mode when the PVDG is not in service. The angles of the three superimposed sequence currents of R14 for a bolted AG fault at bus 2 are within approximately 4° of each other in Figure 6.2, identifying the fault type accurately.

Proper classification for this AG fault when the PVDG is in service entails aligned sequence components for the superimposed currents flowing from the PVDG. Conventional power plants connected to transmission networks, where the method of [62] has been utilized for years, deploy SGs, modeled by voltage sources for fault studies [41]. Therefore, the characteristics of fault currents, including their angles, are determined by the fault properties, such as its type and impedance. A PVDG, in contrast, is connected to the grid/microgrid through a VSC, which operates as a current source [45]. If the HV winding of the PVDG transformer is grounded star, as is normally the case, then the angle of the PVDG zero-sequence current is still mainly determined by the fault properties. The positive and negative sequence currents, however, are regulated by the control system of the VSC and its internal references.

Figure 6.3 displays the PVDG's grid interface and the current control loop for its grid-side converter in the rotating reference frame with PI controllers [45]. A PLL similar to that of [55] provides the *dq* quantities. The *d*-axis reference current is given by an outer control loop that regulates the dc link voltage. The reactive power of the converter is

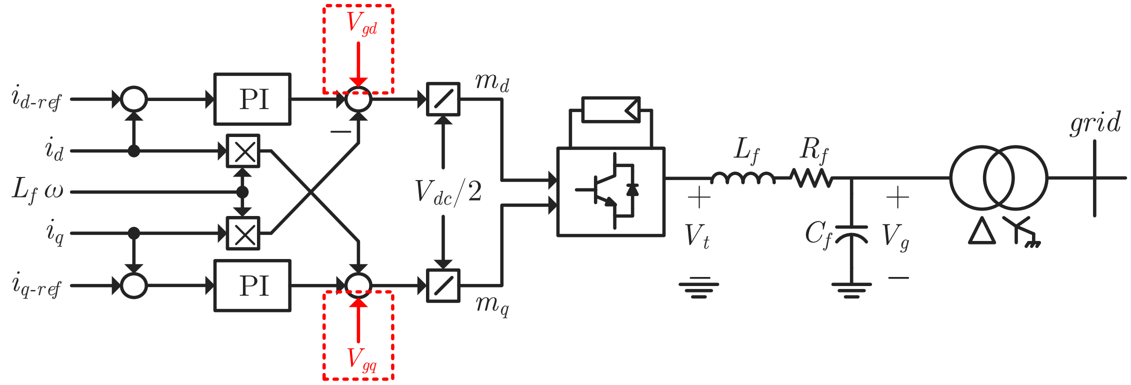

Figure 6.3. The PVDG's current control loop and grid interface.

controlled through the q-axis reference current. PVDGs operate at 0.95 plus PF in North America. Meanwhile, requirements in Europe for reactive current generation by the RE-based sources up to the rated capacity during faults, mentioned in Chapter 3, result in non-zero i_{q-ref} [55].

The signals added to the outputs of the PI controllers in Figure 6.3 include V_{gd} and V_{gq}, which denote the d and q components of the grid voltage, V_g. Besides the decoupling function, the addition of V_{gd} and V_{gq} to the controllers' outputs also improves the transient response of the converter [45, 59]. That is why voltage feed-forward is normally present in the stationary reference frame controllers as well. In fact, the voltage feed-forward makes the disturbances and transients of V_g also appear in the voltage of the converter side of the LC filter, V_t.

For example, consider the above AG fault at $t = 2$ s when the PVDG is connected to the system and generates its rated power at unity PF before the fault. After the fault inception, the converter generates equal active and reactive powers, complying with EU-GCs. The unbalanced voltages on the LV side of the PVDG transformer are displayed in Figure 6.4(a). As a result of the voltage feed-forward, V_t exhibits similar imbalance. Therefore, the difference between the power-frequency content of V_g and V_t, which is the voltage across the LC filter and determines the converter current, becomes balanced. Figure 6.4(b) shows this voltage for the above fault after being passed through an LPF to eliminate the switching pulses. This disturbance-free voltage leads to the converter current of Figure 6.5(a). Figure 6.5(b) illustrates that the magnitude of the negative and zero sequence

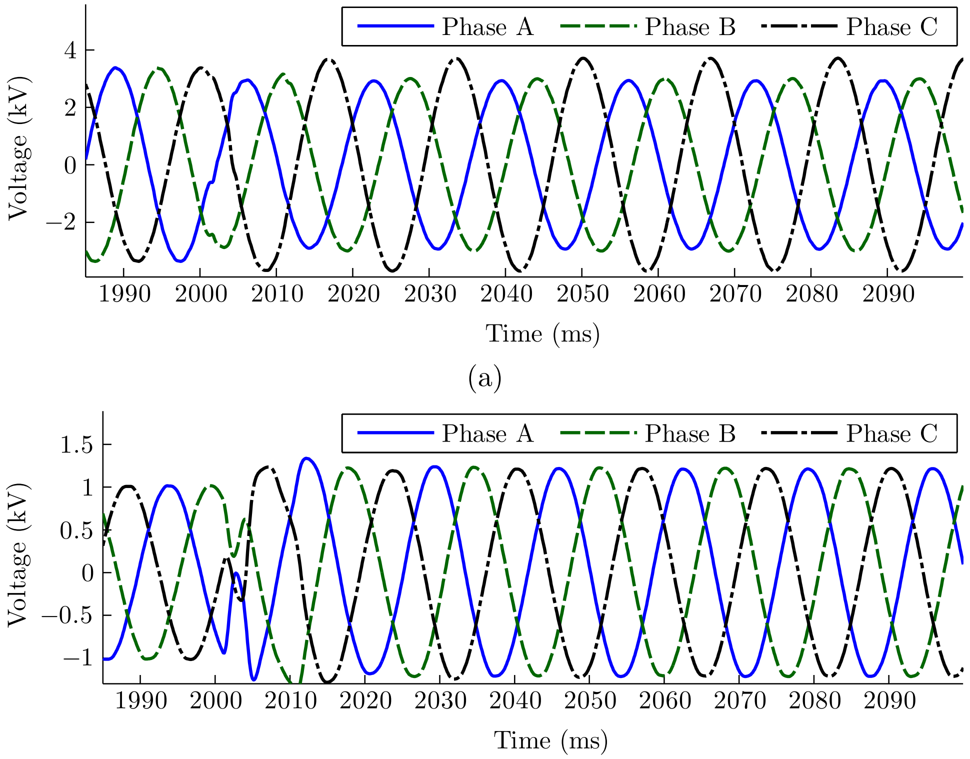

(a)

(b)

Figure 6.4. PVDG voltage for a bolted AG fault at bus 2,
(a) Voltage at the LV side of the transformer, (b) Voltage across the inverter's LC filter.

components of the current are negligible, and only the positive sequence current increases by about 20% following the fault. The limited rise in the current comes from a saturation block applied to the reference currents to protect the converter against overcurrents.

Since the currents injected by the PVDG do not follow the regular pattern of AG fault currents, the angles of the superimposed sequence currents of R14, shown in Figure 6.6, do not select the faulted phase correctly. The Δ sign in the figure designates the superimposed signals. ΔI^- leads ΔI^+ by 128.0°, which falls under the sector defined for BG faults in [62]. Meanwhile, ΔI° lags ΔI^- by 110.6°, indicating a CG or an ABG fault. Hence, the method of [62] is unable to identify the fault type. The same scenario applies to other sequence current-based classifiers.

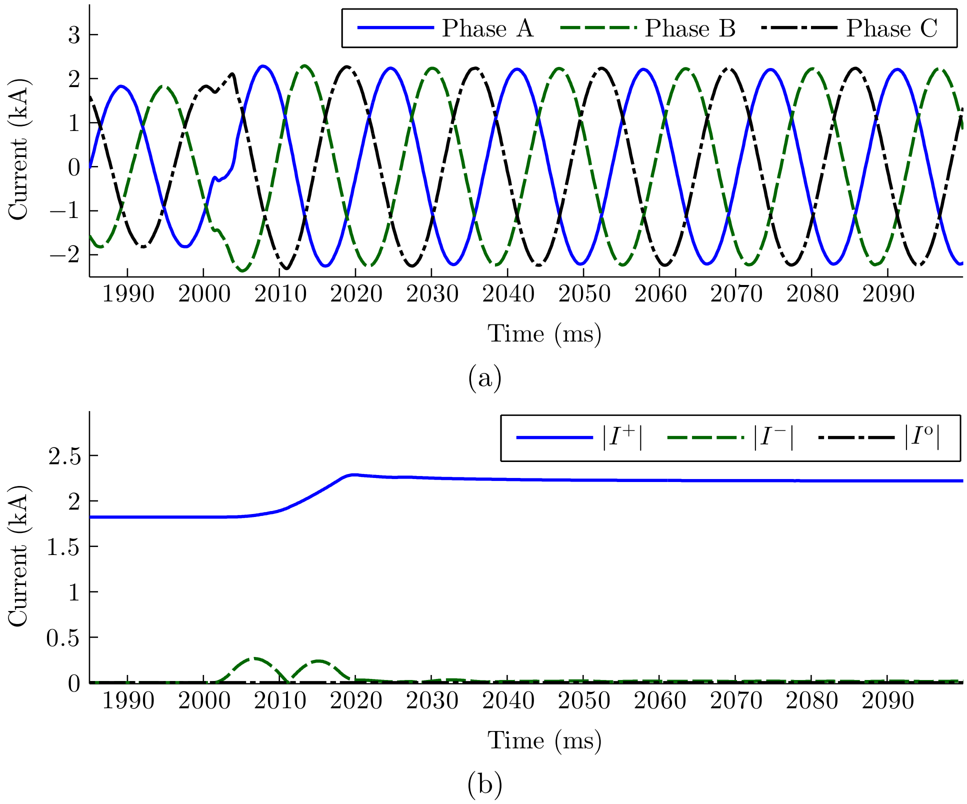

Figure 6.5. PVDG current at the LV side of the transformer for the fault of Figure 6.4, (a) Instantaneous current, (b) Magnitude of sequence components.

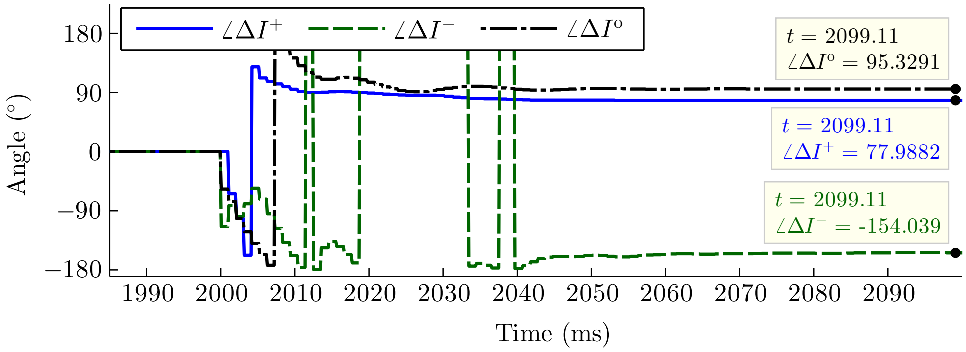

Figure 6.6. Angles of superimposed sequence currents of R14 for the fault of Figure 6.4.

6.2.2 Current Magnitude-based Methods

Another classification approach is based on the changes in the magnitudes of the phase or LL currents after a fault. Let us first analyze the basic current magnitude-based approach, according to which the phases with the largest overcurrents are the faulted ones [104]. This method is employed by the existing selective phase tripping devices utilized in distribution systems [91, 93]. However, it is not used by transmission system relays, as it is vulnerable to weak infeeds and might suffer from system imbalance, particularly for high resistance faults. Meanwhile, it will be unveiled that the presence of PVDGs makes this method unreliable even for a perfectly balanced microgrid with no weak infeed. The following demonstrates that,

1. the unfaulted phases may have larger overcurrents when the system includes PVDGs, and
2. the overcurrent levels are highly dependent on PVDG's reactive current level during faults.

Figure 6.7(a) shows the HV-side current of the PVDG transformer when it operates at unity PF during a bolted BCG fault at bus 2 of the grid-connected microgrid. Although phase A is healthy, its current is 0.27 kA, exceeding phase B's current by about 0.1 kA. The larger phase A current originates from the angle between the converter-generated fault current and the zero sequence current flowing through the ground of the PVDG transformer. As discussed, the converter's negative sequence current is negligible, and the current of Figure 6.7(a) consists of only the positive and zero sequence components, whose magnitudes and angles are plotted in Figures 6.7(b) and (c), respectively. The sequence components have been measured with respect to phase A. The positive sequence current of phase B lags the $-2.9°$ positive sequence angle in Figure 6.7(c) by $-120°$. As a result, the phase difference between the positive and zero sequence components for phase B current becomes 139.7°, whereas the same quantity for phase A is 100.4°. In other words, the two sequence components nearly cancel each other in phase B current, which drops below even the pre-fault level. Unlike the case of weak infeed, for which the close phase current magnitudes make phase selection difficult, the basic overcurrent-based classifier clearly

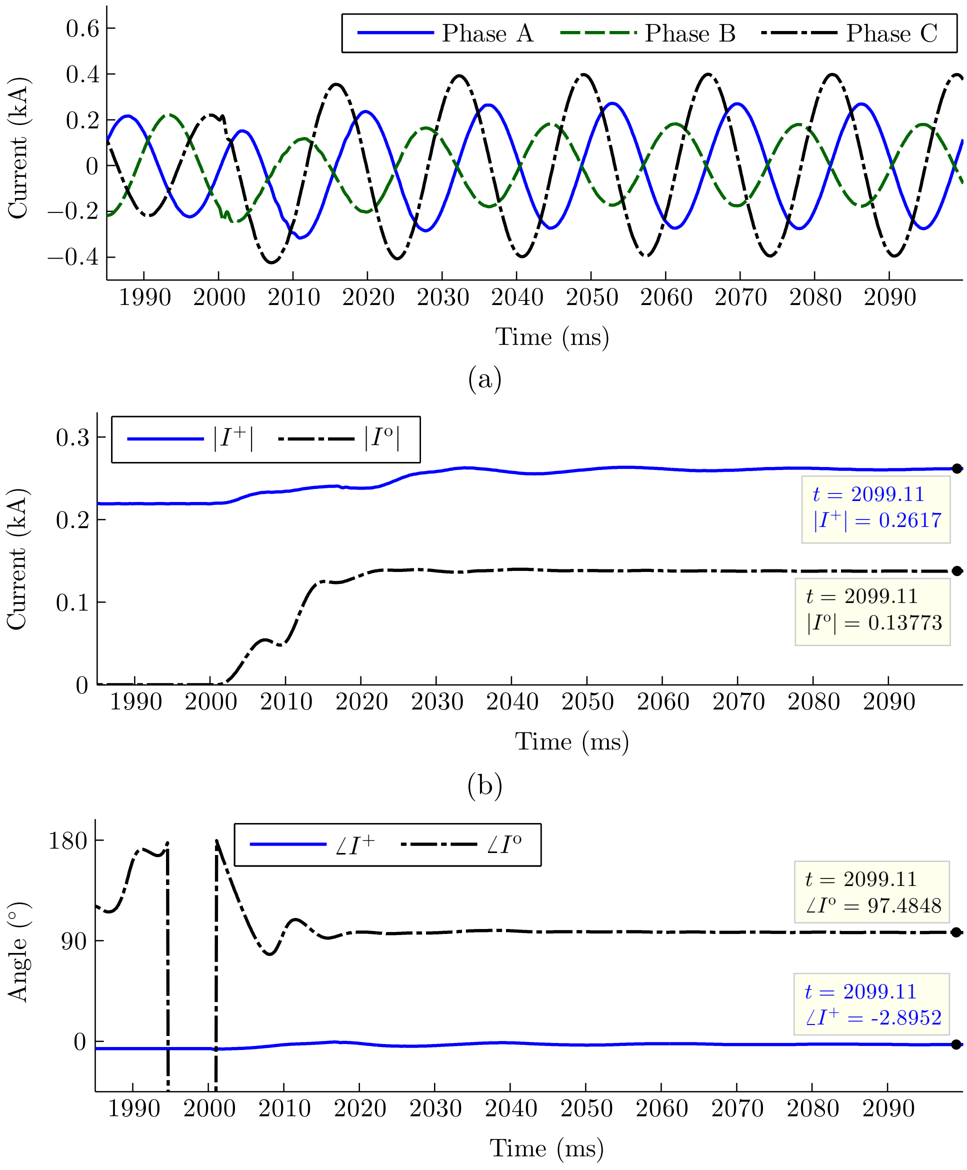

(a)

(b)

(c)

Figure 6.7. PVDG current at the HV side of the transformer during a BCG fault when the PVDG's PF is unity, (a) Instantaneous current, (b) Magnitude of sequence components, (c) Angle of sequence components.

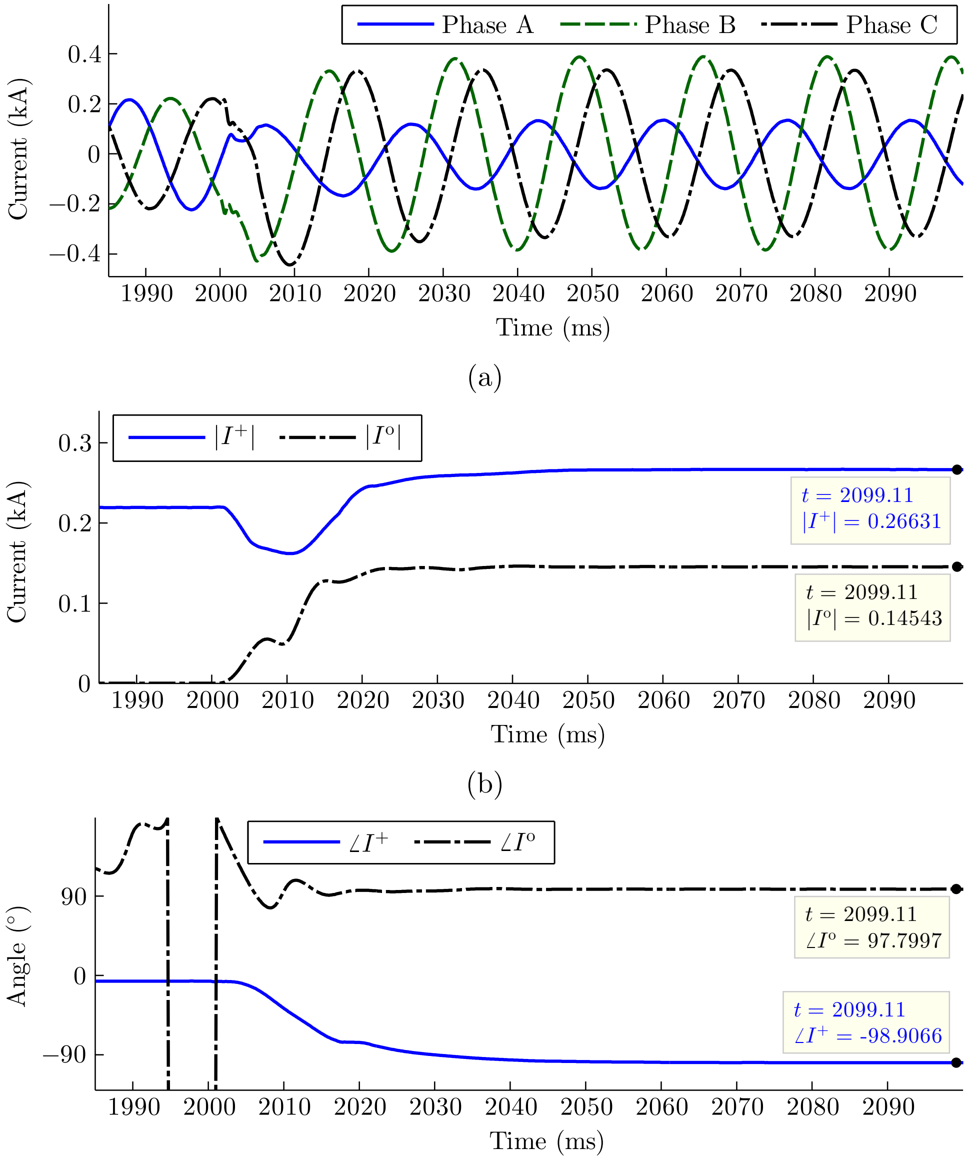

(a)

(b)

(c)

Figure 6.8. PVDG current at the HV side of the transformer during a BCG fault when the PVDG generates rated reactive current, (a) Instantaneous current, (b) Magnitude of sequence components, (c) Angle of sequence components.

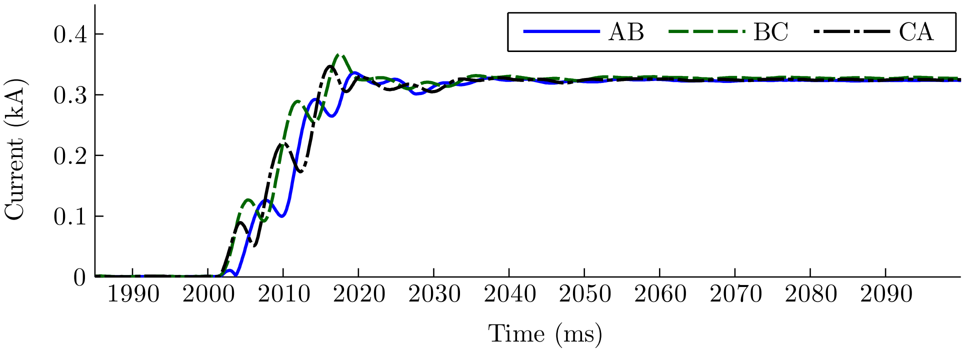

Figure 6.9. Superimposed LL currents of the PVDG for the fault of Figure 6.4.

misidentifies the fault type, even though the zero sequence component does not dominate the PVDG current in Figure 6.7.

Figure 6.8 depicts the PVDG current for the same fault when the PVDG complies with the requirements of EU-GCs and generates the rated reactive current during the fault. Figure 6.8(a) shows that the change in the reactive current of the PVDG raises phase B current beyond the other currents. The zero sequence term in Figures 6.8(b) and (c) is similar to that in Figure 6.7. Conversely, the angle of the positive sequence component is shifted backwards by about 90° to meet the reactive current requirement. As a result, the phase difference between the zero and positive sequence terms of phase B current has reduced to 43.3°, i.e., these two components do not cancel each other anymore. The classification provided by the basic current magnitude-based method is thus dependent on the PVDG's PF and unreliable.

To address the effect of weak infeeds, current magnitude-based classifiers of commercial relays normally remove the zero sequence current. Hence, the variable angle between the positive and zero sequence currents should no longer be a problem. Meanwhile, these methods select incorrect phases for other reasons. Take, for instance, the classifier of [69], which compares the magnitudes of the superimposed LL currents. In a conventional system, an SLG fault results in two large superimposed LL currents that include the faulted phase, and the third signal is zero. However, the superimposed LL currents of the PVDG for the AG fault of Figure 6.4, displayed in Figure 6.9, are identical in magnitude since the zero sequence component is not present in the LL quantities and the negative sequence term is removed from the PVDG current by the voltage feed-forward signal. A three-phase fault would consequently be detected by [69]. Similar maloperation is observed for LLG faults.

The current magnitude-based method of [98] defines the following two delta signals for each phase current.

$$DEL_{\Phi} = |I_{\Phi} - I_{\Phi-prf} - I^{\mathrm{o}}|^2 \tag{6.1}$$

$$DEL1_{\Phi} = |I_{\Phi} - I_{\Phi-prf}|^2 \tag{6.2}$$

The prf subscript denotes pre-fault quantities, and Φ is the respective phase. To detect an SLG fault, DEL of the faulted phase must be larger than 2.25 times DEL of each of the remaining phases. For an LLG fault, $2.25DEL$ of the unfaulted phase is lower than the DEL of the other phases. If DEL signals do not identify an unbalanced fault, then $DEL1$ signals are used with the same rule to identify an LLG fault. If none of these conditions are met, a balanced fault is deduced.

DEL and $DEL1$ for the PVDG current during the BCG fault of Figure 6.7 are shown in Figure 6.10. The base to per-unitize the currents is the rated current of the PVDG. The removal of the zero-sequence term in (6.1) and the absence of the negative sequence current have made the DEL of all phases identical in Figure 6.10(a). Hence, $DEL1$ signals are checked for an LLG fault. Since $DEL1$ includes the zero sequence term, it is affected by the angle between the positive and zero sequence currents, which was previously proved to be dependent on the PVDG's reactive current level. That is why the relation between the $DEL1$ curves of Figure 6.10(b) is similar to the current magnitudes of Figure 6.7, and the method of [98] mistakes them for the $DEL1$'s of a CAG or a balanced fault, depending on when the decision is made. Even for the BCG fault of Figure 6.8, where phase A has a lower current, $2.25DEL1_A$ is larger than $DEL1_C$, and the fault type is misidentified again.

6.3 Proposed Solutions

This section presents two new fault type classifiers that work for not only the microgrids with PVDGs, but for any three-phase system. Let us first investigate the relations between the angles of the sequence voltages for two SLG and LLG faults. Unlike the methods

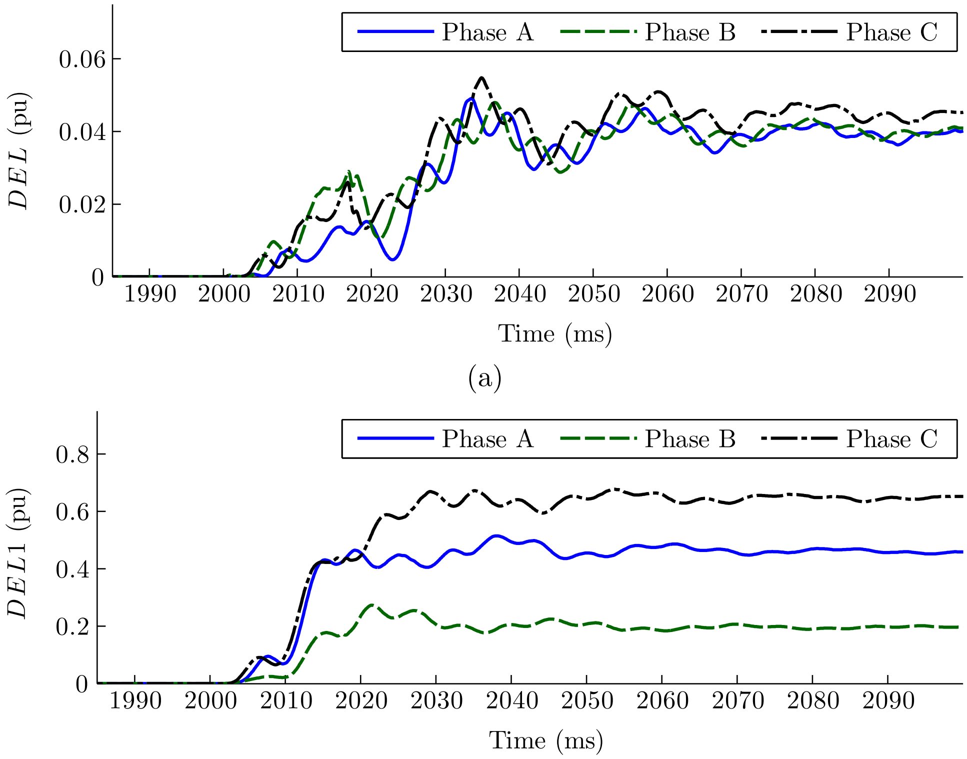

(a)

(b)

Figure 6.10. The parameters of [98] for the fault of Figure 6.7, (a) DEL, (b) $DEL1$.

reviewed in the last section, which relied on superimposed quantities, the following analysis focuses on total fault voltages, as the angles of the superimposed voltages will later be shown to be affected by the PVDG's PF over faults. As displayed by Figure 6.11(a), in which the f and n subscripts designate the fault location and the system neutral, the sequence circuits calculated with respect to phase A are connected in series for an AG fault. KVL for the outer loop is expressed by (6.3).

$$V_f^+ + V_f^- + V_f^{\mathrm{o}} - 3R_f I_f^{\mathrm{o}} = 0 \tag{6.3}$$

Neglecting R_f at this stage, the sum of the negative and zero sequence voltages is out of phase from V_f^+ in (6.3) by 180°. On the other hand,

$$V_f^- = -Z_{tot}^- I_f^- \tag{6.4}$$

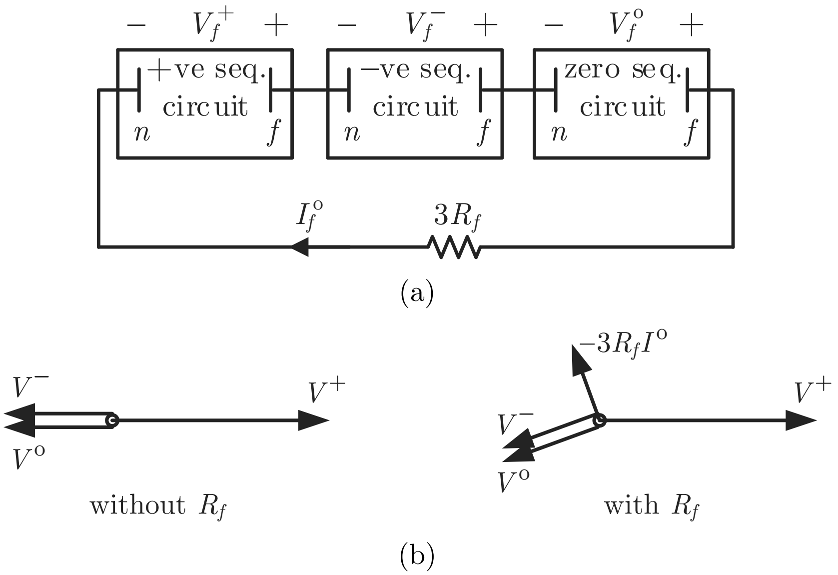

Figure 6.11. Sequence elements for an AG fault,
(a) Sequence circuits connection, (b) Voltage phasors.

$$V_f^o = -Z_{tot}^o I_f^o \tag{6.5}$$

Z_{tot}^- and Z_{tot}^o are the total impedances of the negative and zero sequence circuits, respectively. Since I_f^- and I_f^o are equal for an AG fault, phase lead of the negative sequence voltage over the zero sequence voltage, denoted by δ^o, is similar to the phase difference between Z_{tot}^- and Z_{tot}^o, which is very small [22]. Consequently, as illustrated by Figure 6.11(b), δ^o and the phase lead of the negative sequence voltage over the positive sequence voltage, designated by δ^+, are around 0° and 180°, respectively, for a bolted AG fault. The phase differences between the sequence voltages of R14 for the AG fault of Figure 6.4, plotted in Figure 6.12(a), are in close proximity of 0° and 180°. Stronger sources in a system provide stiffer positive sequence voltages, as a result of which δ^+ and δ^o equal these angles more precisely.

In the presence of fault resistance, $3R_fI_f^o$ leads the aligned V_f^- and V_f^o by the zero sequence impedance angle. Thus, as shown by Figure 6.11(b), in order for $V_f^- + V_f^o - 3R_fI_f^o$ to be out of phase from V_f^+ by 180°, V_f^- and V_f^o advance in phase. The higher R_f is, the larger δ^+ should be. The distribution utilities traditionally consider 40 Ω as the maximum resistance between a downed conductor and the ground [105]. Larger fault resistances have

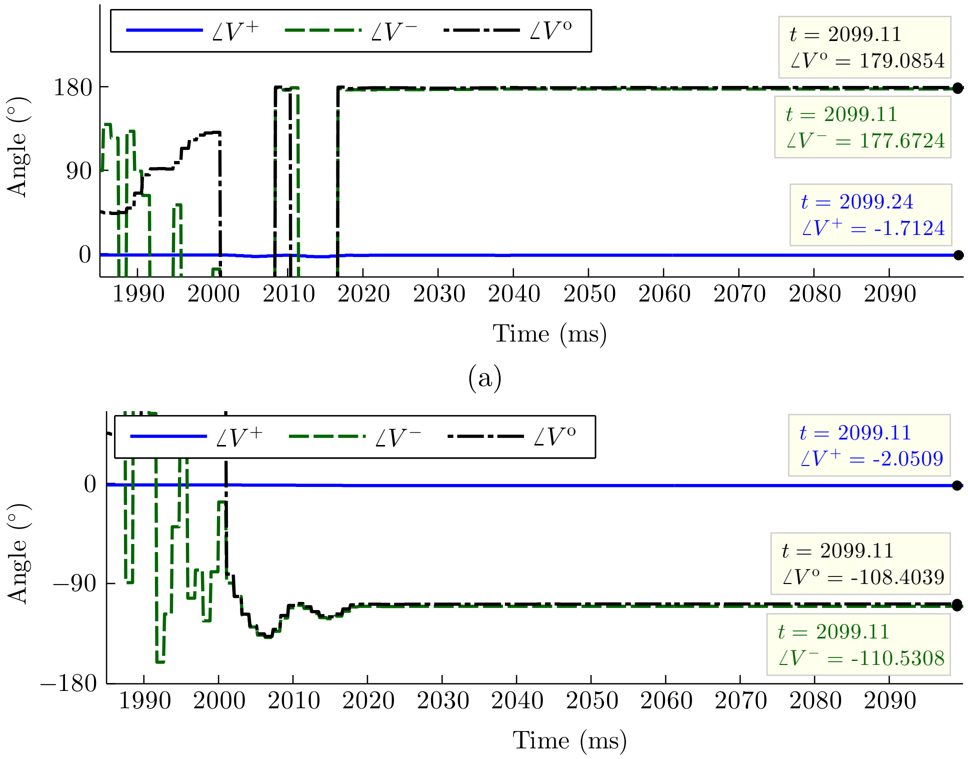

(a)

(b)

Figure 6.12. R14 voltage angles for the fault of Figure 6.4, (a) $R_f = 0\ \Omega$, (b) $R_f = 100\ \Omega$.

also been reported in the literature [106]. For $R_f = 100\ \Omega$, Figure 6.12(b) depicts the angles of R14 sequence voltages during the AG fault of Figure 6.12(a). The high R_f makes the voltage drop at the PVDG terminal small, and the converter continues to operate at unity PF. δ^+ has reduced to $-108.5°$ compared to Figure 6.12(a).

To study extreme scenarios, significantly larger fault resistances were also tested. It was found that variations of $\measuredangle V_f^-$ and $\measuredangle V_f^o$ with respect to R_f do not follow a linear pattern, and increasing R_f further has virtually no effect on the angles between the sequence voltages. Figure 6.13 plots δ^+ and δ^o versus R_f for unity PF operation of the PVDG during the above AG fault. The saturation-like curve of δ^+ arises from the fact that elevated levels of resistance to the ground result in lower zero sequence current, thereby preventing the $3R_f I_f^o$ term in (6.3) from growing unboundedly large. Also, δ^o is shown to be independent of R_f.

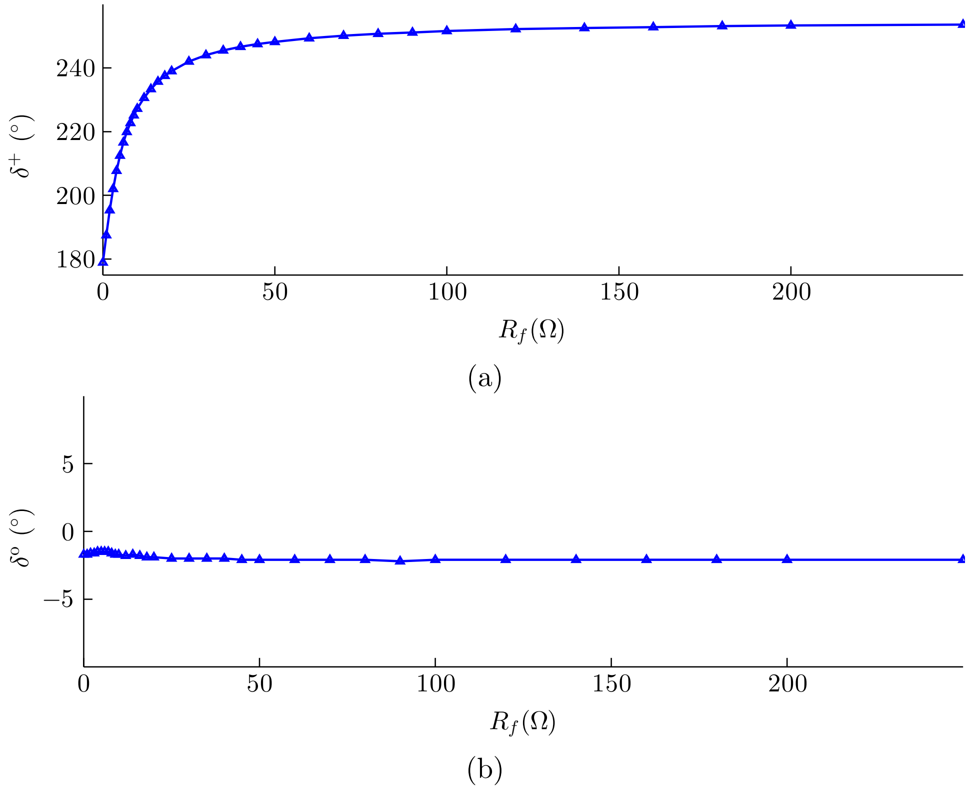

Figure 6.13. Voltage angle variations with respect to fault resistance for an AG fault on bus 2 during unity PF operation of PVDG, (a) δ^{+}, (b) δ^{o}.

Figure 6.14(a) shows parallel connection of the sequence circuits calculated with respect to phase A for a BCG fault. The resistance between the two phases at the fault location is $2R_{ph}$, the middle of which is grounded through R_f. KVL for the left loop is

$$V_f^{+} = V_f^{-} + R_{ph}\left(I_f^{+} - I_f^{-}\right) \tag{6.6}$$

R_{ph} consists of mainly the arcing resistance, which is relatively small in microgrids due to the short spacing between the conductors. Thus, the effect of R_{ph} will later be analyzed by simulations and is neglected at this point. As a result, δ^{+} becomes zero for a BCG fault. KVL for the right loop in Figure 6.14(a) is

$$V_f^{-} = V_f^{o} - 3R_f I_f^{o} + R_{ph}\left(I_f^{-} - I_f^{o}\right) \tag{6.7}$$

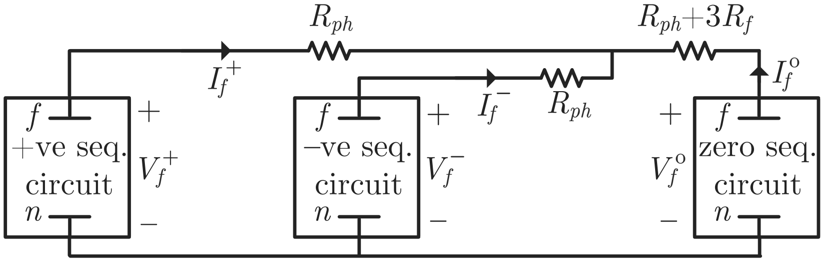

(a)

(b)

Figure 6.14. Sequence elements for a BCG fault,
(a) Sequence circuits connection, (b) Voltage phasors.

Neglecting R_{ph}, V_f^- and V_f^o are aligned for zero R_f, and as depicted in Figure 6.14(b), δ^o is zero for a solid BCG fault as well. As an example, the similar angles of R14 sequence voltages for the BCG fault of Figure 6.7 are displayed in Figure 6.15(a).

The zero sequence current leads V_f^o by $\measuredangle Z_{tot}^o$. Therefore, as shown by Figure 6.14(b), in order for $V_f^o-3R_fI_f^o$ to be aligned with V_f^- during resistive faults, V_f^o advances in phase and raises δ^o in the negative direction. To study a severe condition, the fault of Figure 6.15(a) is re-simulated with $R_f=100\ \Omega$, and the angles are shown in Figure 6.15(b), where δ^+ remains unchanged, but δ^o has grown by $-77.6°$ compared to Figure 6.15(a). Akin to SLG faults, increasing R_f further for LLG faults does not alter the voltage angles. δ^+ and δ^o of R14 for the above BCG fault, plotted versus R_f in Figure 6.16, exhibit uniform curves for large fault resistances.

6.3.1 Voltage Angle and Magnitude-based Classifier

Similar values are obtained for δ^o during other fault types if the sequence components are calculated with respect to the faulted phase for SLG faults and the unfaulted phase for

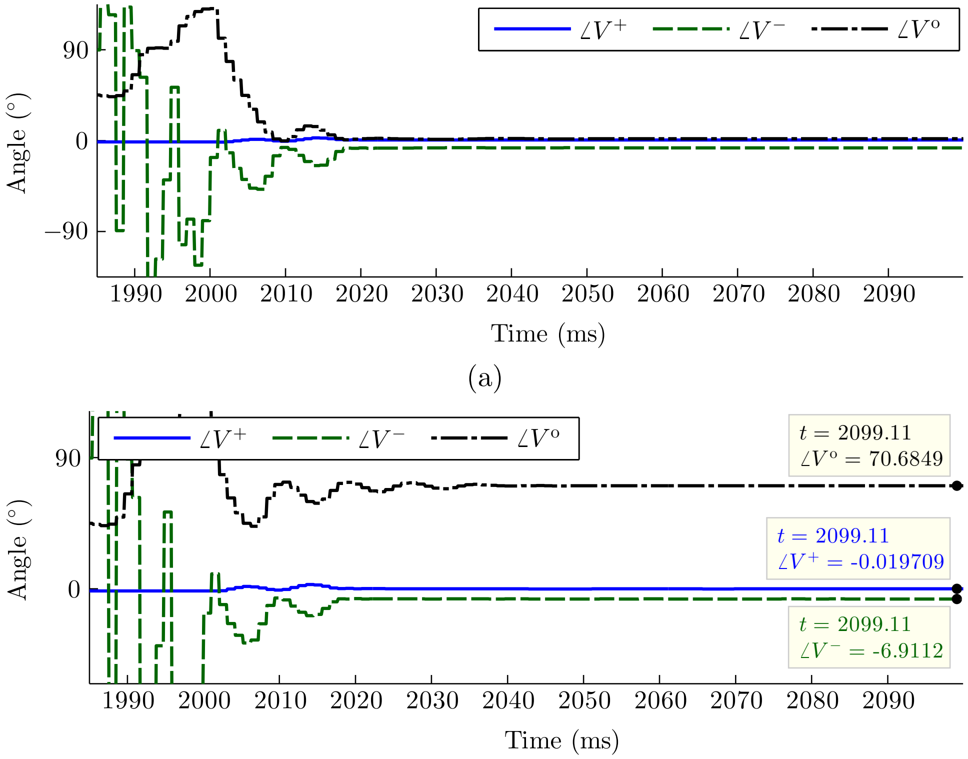

(a)

(b)

Figure 6.15. R14 voltage angles for the fault of Figure 6.7, (a) $R_f = 0\ \Omega$, (b) $R_f = 100\ \Omega$.

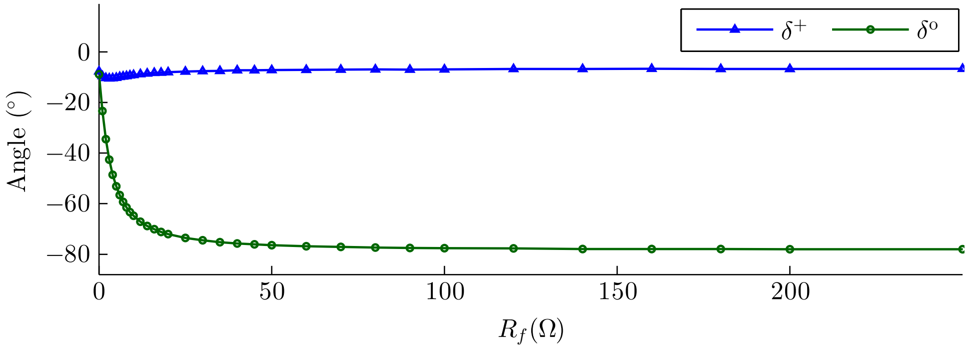

Figure 6.16. δ^+ and δ^o versus fault resistance for a BCG fault on bus 2 during unity PF operation of PVDG.

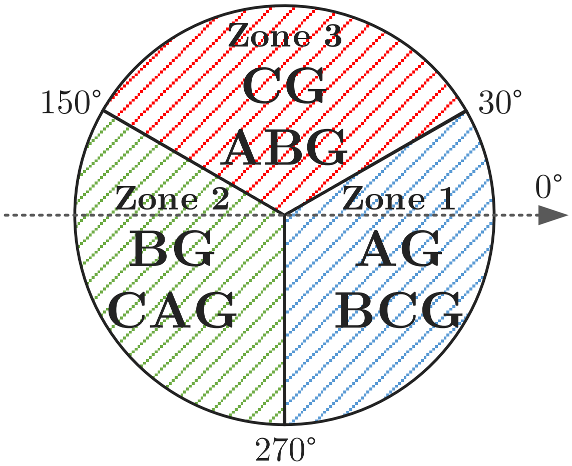

Figure 6.17. δ^o zones for different fault types.

LLG faults. As a result, when phase A is the reference phase, δ^o lies in the vicinity of 240° and 120° during BG and CG faults, respectively. For ABG and CAG faults, δ^o is close to 120° and 240°, respectively. Hence, three zones, each corresponding to one SLG and one LLG fault, are defined around the mentioned angles for δ^o in Figure 6.17. Given that R_f makes the zero sequence voltage lead the negative sequence voltage during LLG faults, the three zones of δ^o have been shifted backward from the symmetrical position around the above angles by 30°.

A key feature of δ^o zones in Figure 6.17 is that the two faults associated with each zone include opposing phases. Classification of such faults can effectively be carried out by means of phase voltage magnitudes. For instance, δ^o is situated inside zone 1 during both AG and BCG faults. Meanwhile, the change in the magnitude of phase A voltage compared to that for the other two phases is a characteristic difference between these two faults. This feature, along with the value of δ^o, is the basis for the proposed classification logic illustrated by Figure 6.18. Magnitudes of phase voltages are inspected using (6.8).

$$\Delta V_\Phi = |V_\Phi| - |V_{\Phi-prf}| \tag{6.8}$$

To identify an AG fault, δ^o must be in zone 1, and ΔV_A has to be lower than both ΔV_B and ΔV_C. For a BCG or BC fault, a zone 1 δ^o is accompanied by a ΔV_A exceeding

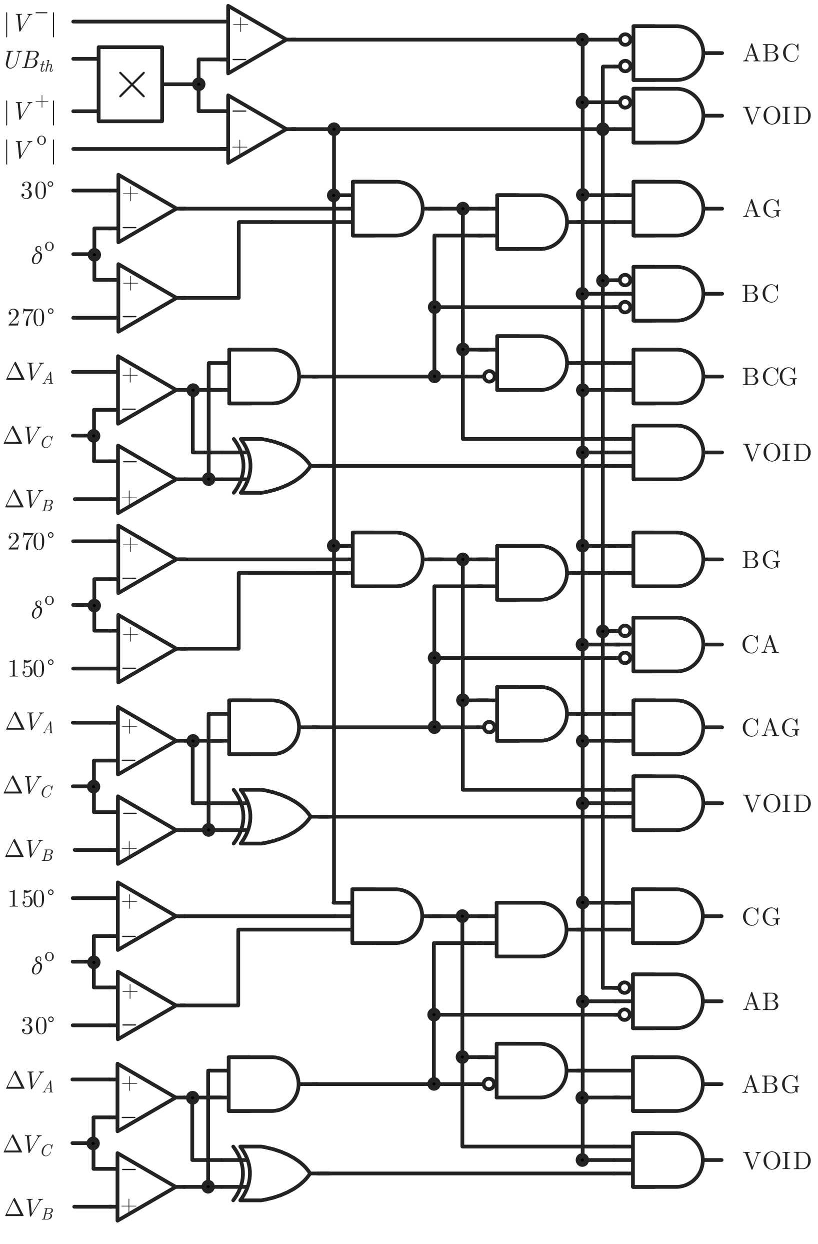

Figure 6.18. Logic circuit of the voltage angle and magnitude-based classifier.

both ΔV_B and ΔV_C. To differentiate between LL and LLG faults, $|V^o|$ is compared with the unbalance threshold, UB_{th}, which equals the %Imbalance, defined by [107], before the

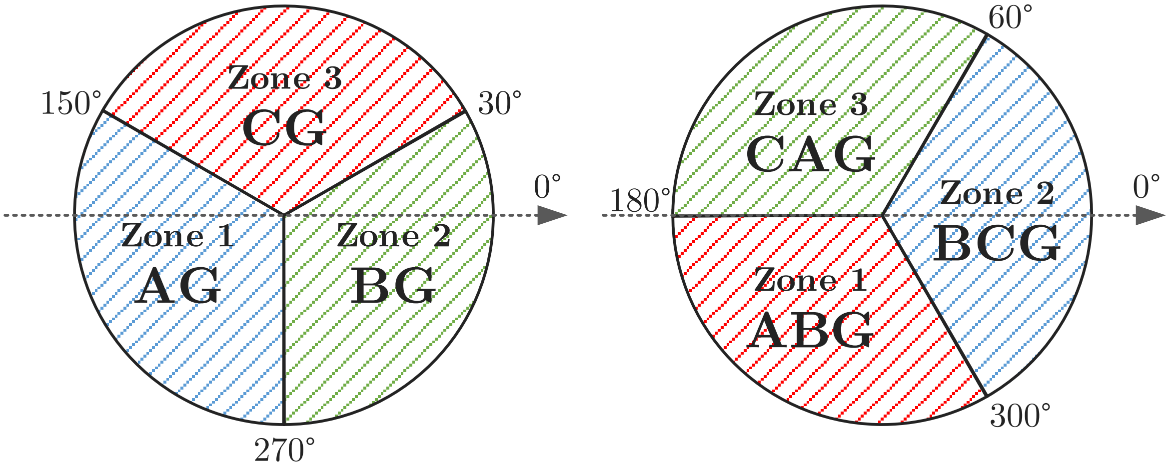

Figure 6.19. δ^+ zones for different fault types.

fault detection plus a safety factor, say 2% of the rated voltage. UB_{th} is thus immune to load imbalance and does not need to be set by the user. Moreover, $|V^-|$ must be higher than UB_{th} to identify an asymmetrical fault. Fault classifiers of commercial relays raise a VOID flag if the fault signals follow none of the known signatures [62]. The same approach is adopted by the proposed method.

6.3.2 Voltage Angle-based Classifier

The values of δ^+ for other fault types are similar to those of the previously discussed AG and BCG faults if sequence components are calculated with respect to the faulted phase for SLG faults and the unfaulted phase for LLG faults. Therefore, when phase A is the reference phase, δ^+ is close to 120° and 240° for CAG and ABG faults, respectively. For BG and CG faults, δ^+ lies in the neighborhood of 300° and 60°, respectively. Figure 6.19 defines appropriate zones for δ^+ around these angles. The δ^+ zones for SLG faults are shifted forward from the symmetrical position about the respective angles to take the effect of fault resistance into account. R_f does not affect δ^+ during LLG faults, so the zones in Figure 6.19 are symmetrical about their corresponding angles.

Positions of δ^o and δ^+ inside the zones in Figures 6.17 and 6.19 are the basis for the classification logic proposed in Figure 6.20. No δ^+ and δ^o pair follows more than one of

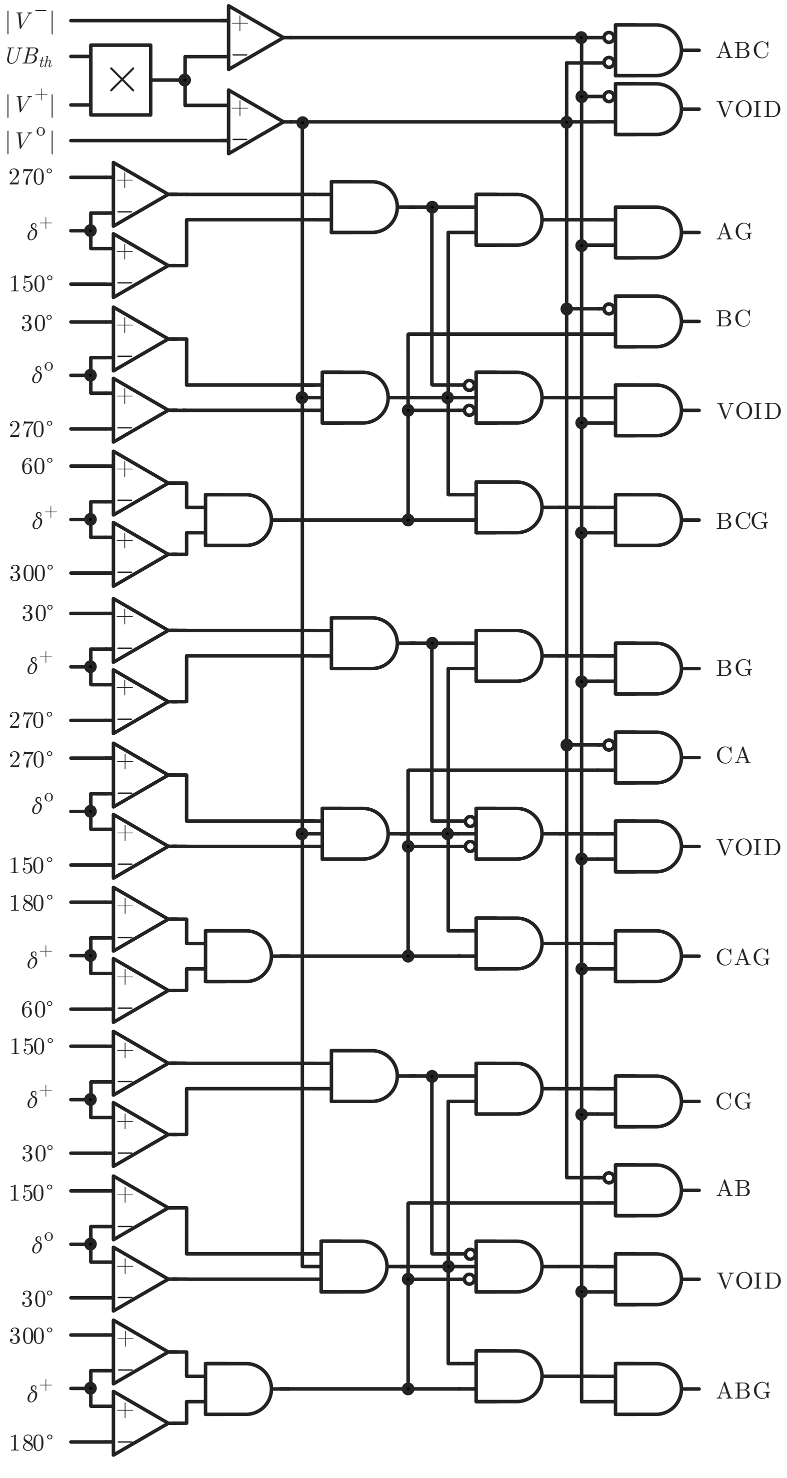

Figure 6.20. Logic circuit of the voltage angle-based classifier.

the patterns in Figures 6.17 and 6.19, so this classifier can reliably identify the fault type. As in Figure 6.18, $|V^-|$ and $|V^o|$ are used to determine balanced faults and discriminate between LL and LLG faults.

Unlike the classifier proposed in the last subsection, this new method exploits the angle of the positive sequence voltage, which varies along the path from the fault location to the relay due to load flow. Phase difference between positive sequence voltages along a feeder is small, as its large amounts harbor the risk of instability. For distribution systems, in particular, voltage phase differences along feeders are in the order of a fraction of a degree, as the load levels are not high [108, 109]. Even for HV systems with higher load levels and larger phase variations, enough allowance has been made through sufficiently large security margins in the δ^+ zones of Figure 6.19.

6.4 Performance Evaluation

The proposed methods were tested for a variety of conditions in the microgrid of Figure 6.1. The studies included various fault and relay locations, fault resistances and PVDG's PF, and were carried out for both autonomous and grid-connected modes. The fault type could be identified within a cycle after fault inception. This speed is enough even for instantaneous overcurrent relays. The angle and magnitude-based classifier can make a reliable decision in half a cycle if the system is not severely unbalanced.

6.4.1 Grid-Connected Mode

Tables 6.1 and 6.2 report the angles of the sequence voltages and the changes in the phase voltage magnitudes, respectively, for R14 during different SLG and LLG faults at bus 5. The microgrid is in the grid-connected mode, and the PVDG operates at unity PF. It was found that $R_f = 50\ \Omega$ sufficed to observe the maximum effect of fault resistance on the voltage angles, a conclusion in line with the findings from Figures 6.13 and 6.16. LL faults are excluded because they result in almost the same δ^+ and voltage changes that are given for LLG faults.

Table 6.1
Voltage Angles for Grid-Connected Mode During Faults at Bus 5 when PVDG's PF Is Unity

Fault type	$2R_{ph}$ (Ω)	R_f (Ω)	$\measuredangle V^+$ (°)	$\measuredangle V^-$ (°)	$\measuredangle V^\circ$ (°)
AG	N/A	0	-1.0	177.7	-173.1
		50	-2.6	-120.6	-113.1
BG	N/A	0	-1.0	-62.3	66.9
		50	-2.6	-0.5	126.9
CG	N/A	0	-1.0	57.7	-53.1
		50	-2.6	119.4	6.9
ABG	0	0	0.0	-128.3	129.8
		50	-0.6	-129.5	-170.2
	10	0	-5.6	-101.6	146.7
		50	-5.2	-104.6	-173.3
BCG	0	0	0.0	-8.3	9.8
		50	-0.6	-9.5	69.8
	10	0	-5.6	18.4	26.7
		50	-5.2	15.4	66.8
CAG	0	0	0.0	111.7	-110.2
		50	-0.6	110.6	-50.2
	10	0	-5.6	138.4	-93.3
		50	-5.2	135.4	-53.3

The results in Table 6.1 identify the fault type correctly with a high margin between δ^+ and δ° and their corresponding zone boundaries. For example, for the high-resistance AG fault shown in the second row, δ^+ and δ° maintain distances of 28° and 37.5° from the boundaries of the associated zone boundaries. Also, the variations in the phase voltage magnitudes in Table 6.2 can correctly discriminate between the SLG and LLG faults.

6.4.2 Autonomous Mode

Similar correct classification is observed for the bus 2 faults of Tables 6.3 and 6.4, which display the angles and magnitude variations of R14 voltages during the autonomous mode. The PVDG complies with the reactive current requirements of EU-GCs during the faults. Sustained voltages below 90% are categorized as undervoltage disturbance by [107]. Since

Table 6.2
Voltage Magnitude Variations for Grid-Connected Mode During Faults at Bus 5 when PVDG's PF Is Unity

Fault type	$2R_{ph}$ (Ω)	R_f (Ω)	ΔV_A (kV)	ΔV_B (kV)	ΔV_C (kV)
AG	N/A	0	-6.623	-0.611	-0.984
		50	-0.657	-0.370	0.217
BG	N/A	0	-0.986	-6.624	-0.612
		50	0.218	-0.650	-0.370
CG	N/A	0	-0.613	-0.986	-6.624
		50	-0.370	0.217	-0.658
ABG	0	0	-9.039	-7.761	-1.478
		50	-8.077	-6.284	-0.137
	10	0	-5.780	-7.453	-1.094
		50	-4.521	-6.879	0.017
BCG	0	0	-1.477	-9.036	-7.757
		50	-0.137	-8.074	-6.281
	10	0	-1.093	-5.778	-7.452
		50	0.018	-4.520	-6.879
CAG	0	0	-7.761	-1.479	-9.037
		50	-6.285	-0.139	-8.075
	10	0	-7.453	-1.093	-5.778
		50	-6.879	0.017	-4.521

the SDG at bus 3 is a weak source, the voltage level before the fault is 86.6% of the rated value. Although such a weak voltage support is not practical, it is considered to study the worst case scenario. As a sample case in Tables 6.3, the angles for the BCG fault with $R_f = 50\ \Omega$ and $R_{ph} = 0\ \Omega$ are displayed in Figure 6.21. δ^+ and δ^o equal 0.9° and $-67.6°$, respectively, identifying a BCG fault. Also, ΔV_B and ΔV_C are substantially lower than ΔV_A for this case in Table 6.4. Similar to the cases studied in Section 6.2, current-based methods malfunction for most of the cases in Tables 6.3 and 6.4.

Some relays that specify the fault type using the angles of the superimposed currents switch to the angles of the superimposed voltages if the current-based approach does not recognize any of the known fault patterns [62]. The classification criterion for the superimposed voltages is the same as that of the currents. The following studies the superimposed voltage-based approach. Take, for instance, the angles of the superimposed sequence volt-

TABLE 6.3
VOLTAGE ANGLES FOR AUTONOMOUS MODE DURING FAULTS AT BUS 5 WHEN PVDG GENERATES REACTIVE CURRENT

Fault type	$2R_{ph}$ (Ω)	R_f (Ω)	$\measuredangle V^{+}$ (°)	$\measuredangle V^{-}$ (°)	$\measuredangle V^{\circ}$ (°)
AG	N/A	0	-39.4	132.4	160.1
		50	-22.6	-156.2	-148.7
BG	N/A	0	-39.5	-107.6	39.9
		50	-22.6	-36.2	91.3
CG	N/A	0	-39.3	12.5	-79.8
		50	-22.6	83.8	-28.8
ABG	0	0	-38.1	-156.7	87.0
		50	-48.7	-167.8	140.1
	10	0	-58.5	-153.4	96.5
		50	-57.0	-161	138.6
BCG	0	0	-38.1	-36.7	-33.0
		50	-48.7	-47.8	19.9
	10	0	-58.5	-33.4	-23.5
		50	-57.0	-41.0	18.6
CAG	0	0	-38.1	83.3	-153.0
		50	-48.6	72.2	-99.9
	10	0	-58.5	86.6	-143.5
		50	-57.0	79.0	-101.4

ages for the above BCG fault, plotted in Figure 6.22(a). ΔV^{-} leads ΔV^{+} by 120.5°; the signature of a BG fault in [62]. In addition, $\measuredangle\Delta V^{-}-\measuredangle\Delta V^{\circ}=-67.6°$, which is closer to the sector of ABG and CG faults in [62]. This method's failure stems from the fact that the angles of the superimposed voltages are determined by the superimposed PVDG currents, whose angles differ from those of conventional sources, and are regulated by the PVDG control system. Thus, changing the reactive current of the PVDG alters the phase difference between the superimposed voltages. If the PVDG operates at unity PF, the angles of the superimposed voltages change to the curves of Figure 6.22(b). The 170.1° phase difference between ΔV^{-} and ΔV^{+} indicates a BCG fault in [62], whereas ΔV^{-} lags ΔV° by 68.2°, which is closer to the sector of BG and CAG faults in [62].

Proper operation of the proposed method, however, is unaffected by changes in the PVDG's reactive current level. The angles of the sequence voltages for the above fault

Table 6.4
Voltage Magnitude Variations for Autonomous Mode During Faults at Bus 5 when PVDG Generates Reactive Current

Fault type	$2R_{ph}$ (Ω)	R_f (Ω)	ΔV_A (kV)	ΔV_B (kV)	ΔV_C (kV)
AG	N/A	0	-21.436	1.463	-3.029
		50	-5.148	-1.659	0.103
BG	N/A	0	-3.073	-21.437	1.395
		50	0.104	-5.147	-1.657
CG	N/A	0	1.502	-3.002	-21.438
		50	-1.657	0.107	-5.146
ABG	0	0	-21.293	-21.431	-4.937
		50	-13.099	-13.295	-1.169
	10	0	-17.309	-19.076	-6.136
		50	-10.786	-15.229	-2.255
BCG	0	0	-4.936	-21.293	-21.431
		50	-1.171	-13.100	-13.297
	10	0	-6.136	-17.309	-19.076
		50	-2.265	-10.791	-15.234
CAG	0	0	-21.430	-4.934	-21.293
		50	-13.286	-1.148	-13.091
	10	0	-19.076	-6.135	-17.308
		50	-15.225	-2.243	-10.781

during unity PF operation, shown in Figure 6.23, yield $\delta^{+} = -4.2°$ and $\delta^{o} = -68.2°$, which are similar to those of Figure 6.21 and inside their respective zones for a BCG fault. Also, ΔV_A, ΔV_B and ΔV_C are -1.999, -14.335 and -12.943 kV; i.e., both of the proposed methods select the faulted phases correctly.

6.4.3 Unbalanced Microgrid

Microgrids might not be perfectly balanced during normal operation. To verify the performance of the proposed classifiers for an unbalanced system, the loads at different buses of the test microgrid were changed to the values displayed in Table 6.5. The resultant voltage and current at R14 location for the autonomous mode along with their sequence components are displayed in Figures 6.24 and 6.25. The pinpointed samples in Figures 6.24(b)

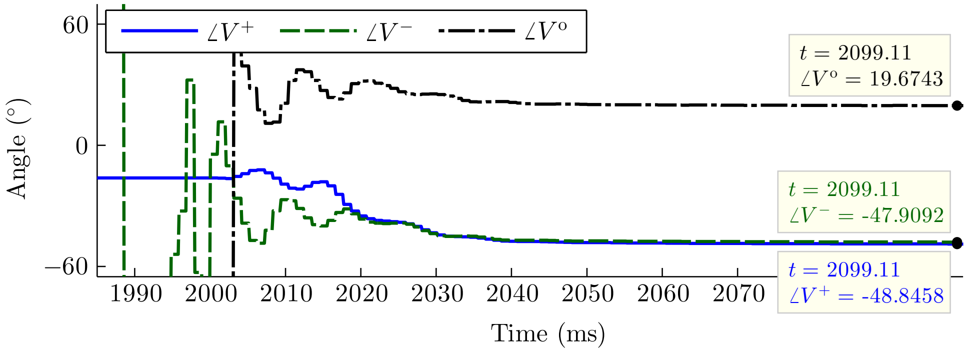

Figure 6.21. R14 voltage angles for the autonomous microgrid when the PVDG generates reactive current during a BCG fault at bus 2 with $R_f = 50\ \Omega$.

TABLE 6.5
LOADS OF THE UNBALANCED MICROGRID IN MW AND MVAR

	P_A	Q_A	P_B	Q_B	P_C	Q_C
Bus 1	0.30	0.05	0.40	0.07	0.35	0.00
Bus 2	1.50	0.00	1.20	0.30	1.00	0.25
Bus 3	1.20	0.10	0.80	0.20	0.70	0.30
Bus 4	1.20	0.11	1.70	0.20	1.40	0.30
Bus 5	0.60	0.08	1.70	0.30	1.30	0.05

and 6.25(b) indicate that the percentage voltage and current imbalances exceed 6.2% and 88%, respectively, which are categorized as severe imbalance [107]. The weak SDG, again, results in low pre-fault phase voltages, equal to 26.590, 24.174 and 24.483 kV in phases A, B and C, respectively. The angles and magnitude variations of R14 voltages for bus 5 faults when the PVDG meets the reactive current requirements of EU-GCs are displayed in Tables 6.6 and 6.7. These results indicate accurate operation of the proposed methods for highly unbalanced systems. As an example, the angles of the sequence voltages during the bolted AG fault of Table 6.4 are plotted in Figure 6.26.

The failure of superimposed voltages to classify faults was earlier shown for a high-impedance fault. Similar inaccuracy is observed for faults with lower resistances as well. For example, the angles of the superimposed voltages for the above AG fault are shown in Figure 6.27. The 73.1° difference between $\measuredangle \Delta V^{-}$ and $\measuredangle \Delta V^{+}$ signifies a CAG fault and

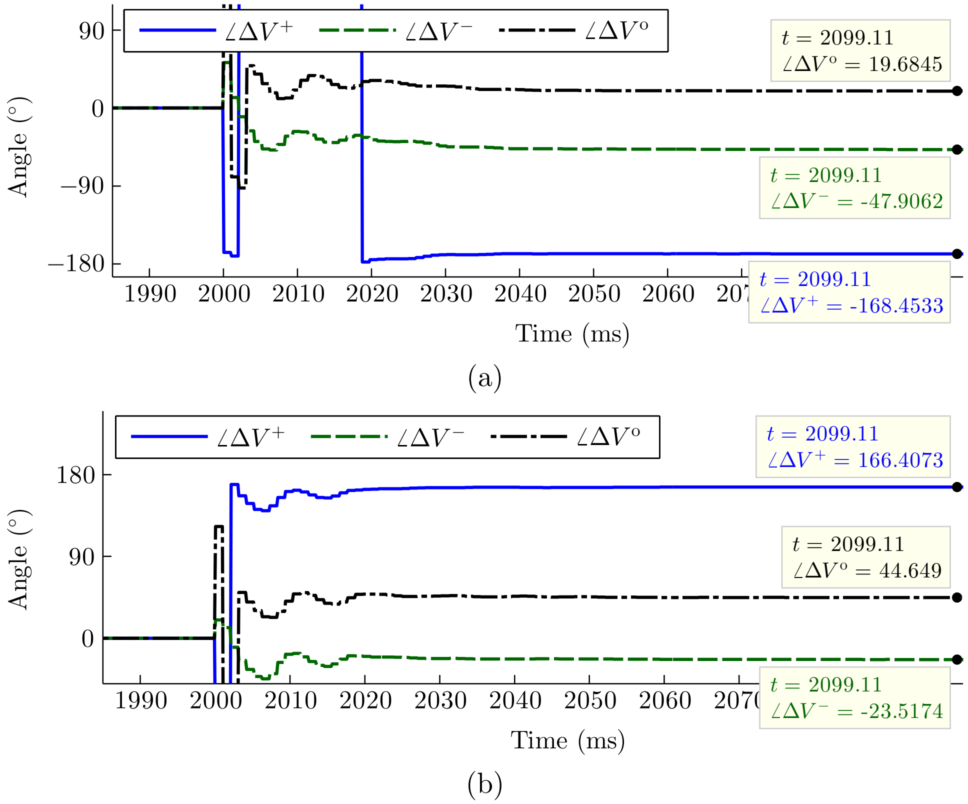

Figure 6.22. Angles of R14 superimposed voltages during the fault of Figure 6.21, (a) PVDG generates reactive current, (b) PVDG operates at unity PF.

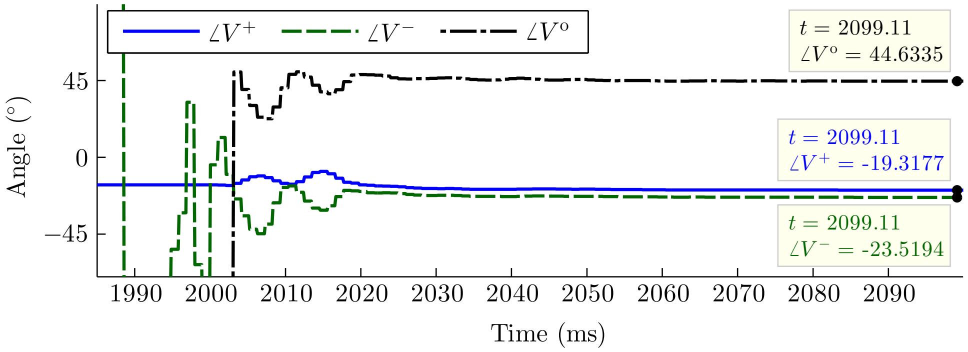

Figure 6.23. R14 voltage angles for the fault of Figure 6.21 when the PVDG's PF is unity.

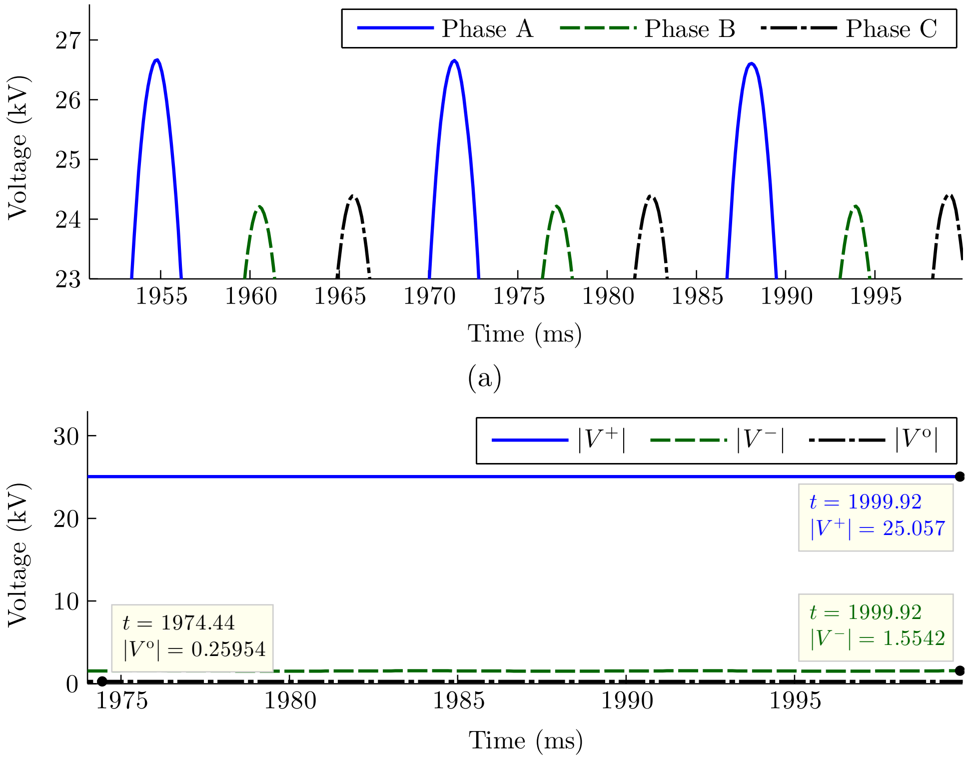

(a)

(b)

Figure 6.24. R14 voltage in the autonomous unbalanced microgrid during normal operation, (a) Phase voltages, (b) Sequence voltages.

leads to misclassification by [62].

6.5 Conclusion

The voltage feed-forward of the current control loop eliminates the negative sequence current of PVDGs. In addition, the angle of positive sequence current of a PVDG is determined by the internal references of the control system. Consequently, the fault type classifiers based on the angles of the superimposed sequence currents were shown to malfunction in systems with PVDG. Current magnitude-based classifiers also were found to be adversely affected by the variable phase difference between the positive and negative sequence currents, as well as the identical phase overcurrents of a PVDG converter.

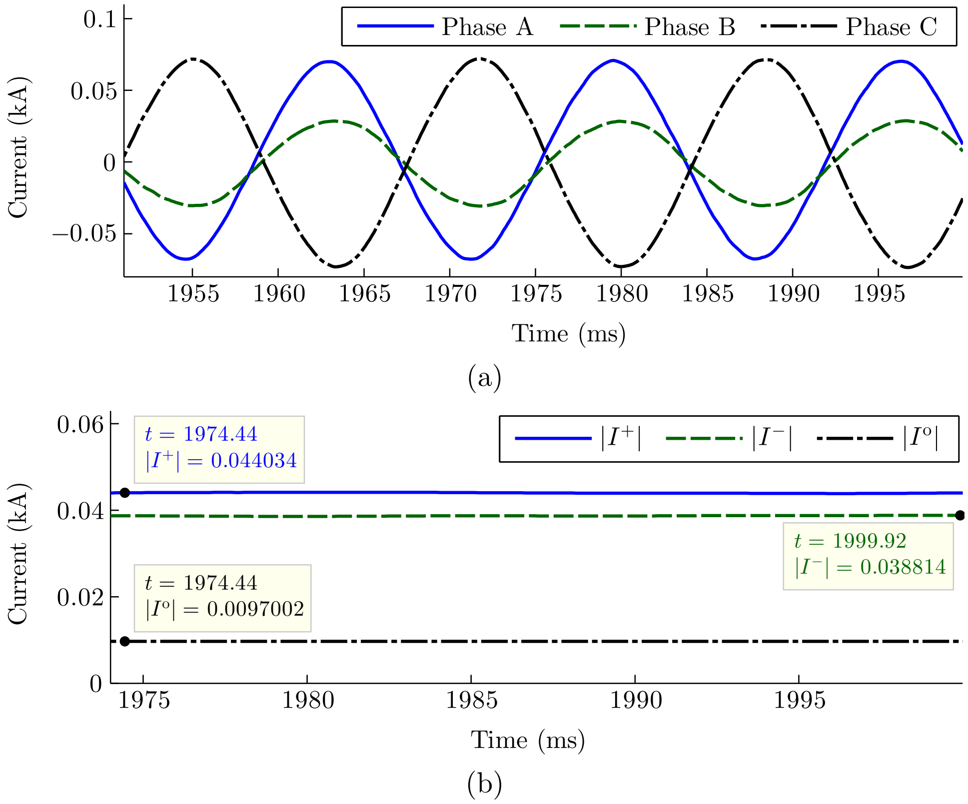

(a)

(b)

Figure 6.25. R14 current in the autonomous unbalanced microgrid during normal operation, (a) Phase currents, (b) Sequence currents.

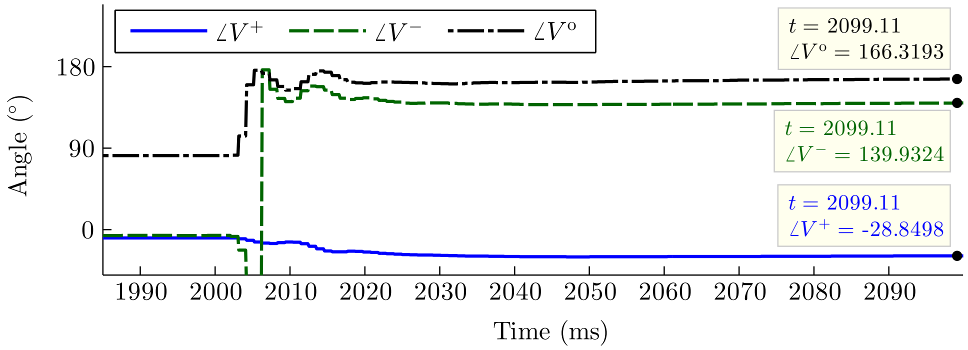

Figure 6.26. R14 voltage angles for the autonomous unbalanced microgrid when the PVDG generates reactive current during a bolted AG fault at bus 5.

TABLE 6.6
VOLTAGE ANGLES FOR AUTONOMOUS UNBALANCED MICROGRID DURING FAULTS AT BUS 5 WHEN PVDG GENERATES REACTIVE CURRENT

Fault type	$2R_{ph}$ (Ω)	R_f (Ω)	$\measuredangle V^+$ ($^\circ$)	$\measuredangle V^-$ ($^\circ$)	$\measuredangle V^\circ$ ($^\circ$)
AG	N/A	0	-28.7	138.9	166.6
		50	-16.7	-129.7	-154.0
BG	N/A	0	-23.9	-92.8	50.4
		50	-13.8	-28.3	86.9
CG	N/A	0	-27.7	16.7	-59.7
		50	-15.2	71.4	-10.9
ABG	0	0	-20.5	-152.8	97.0
		50	-31.7	-162.3	156.0
	10	0	-37.5	-153.4	103.6
		50	-38.6	-156.3	155.1
BCG	0	0	-19.8	-31.8	-25.8
		50	-31.3	-42.1	25.1
	10	0	-36.6	-33.9	-20.4
		50	-38.1	-37.8	23.3
CAG	0	0	-22.6	81.9	-148.3
		50	-35.2	71.5	-86.2
	10	0	-39.7	81.9	-141.9
		50	-42.8	75.6	-87.3

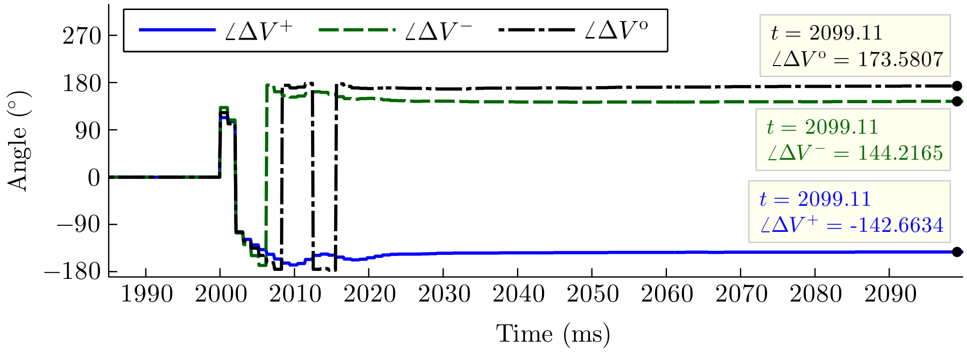

Figure 6.27. Angles of R14 superimposed voltages during the fault of Figure 6.26.

Distinctive zones were defined for the phase difference between the total sequence voltages. The first proposed classifier relied on the fact that each zone defined for δ° corre-

Table 6.7
Voltage Magnitude Variations for Autonomous Unbalanced Microgrid During Faults at Bus 5 when PVDG Generates Reactive Current

Fault type	$2R_{ph}$ (Ω)	R_f (Ω)	ΔV_A (kV)	ΔV_B (kV)	ΔV_C (kV)
AG	N/A	0	-18.793	2.795	-1.339
		50	-5.855	-2.739	1.361
BG	N/A	0	-0.370	-16.204	4.943
		50	0.241	-5.108	-1.735
CG	N/A	0	2.396	-0.693	-16.956
		50	-2.464	1.079	-5.067
ABG	0	0	-20.592	-15.652	-5.224
		50	-15.397	-8.489	2.328
	10	0	-18.577	-16.031	-5.942
		50	-12.828	-10.608	1.734
BCG	0	0	-6.432	-17.984	-15.851
		50	1.016	-12.940	-8.623
	10	0	-7.243	-16.089	-16.197
		50	0.348	-10.666	-10.483
CAG	0	0	-18.201	-5.922	-18.896
		50	-11.447	0.605	-14.316
	10	0	-18.524	-6.742	-16.929
		50	-13.441	-0.521	-12.159

sponded to two SLG and LLG faults that included opposing phases. The voltage magnitude was thus exploited to differentiate between the two possible faults. The unique pair of δ^o and δ^+ zones associated with each fault type was utilized to devise the second classification logic. Correct operation of the proposed methods for the grid-connected and autonomous modes of a microgrid, together with their robustness against various PVDG control strategies, fault resistance, system imbalance and load levels were validated by simulation studies.

Chapter 7

Conclusions

7.1 Summary

The effect of the FRT requirement of modern GCs for REPPs on protective relaying systems has been investigated. The studies were based on time-domain simulation of complete REPP models using PSCAD/EMTDC program and relaying algorithms implemented in the MATLAB environment. The objective of the studies was twofold: Detecting the problems that are exclusively associated with RE systems and left unnoticed by other studies, and devising modified relaying algorithms to circumvent these problems without the need for extra hardware or change in the GC articles for REPPs. The studies were divided into two main parts: transmission and distribution system protection.

- For transmission systems, this dissertation has focused on the following subjects.

1. *Distance protection of lines adjacent to SCIG- and DFIG-based WFs*: It was proved that the impedance measurements provided by a distance relay installed at the substation of an IG-based WF do not truly represent the actual distance between the relay and the location of a balanced fault. The problem arises from the unconventional fault behavior of these sources, which affects the relations employed by a distance relay to measure impedance. A computationally efficient method has been proposed to address

this problem such that fast non-delayed tripping of distance relays over the entire length of the line is restored using the commonly available communication links with minimal bandwidth between the two line end relays.

2. *Distance protection of lines connected to CIREPPs and VSC-based HVDC substations*: A variety of operating conditions and faults on the lines that are in close proximity to CIREPPs underwent scrutiny. It was shown that the control system operation and different GC requirements about the fault current contribution of REPPs clearly influenced the fault behavior of CIREPPs and, subsequently, the impedance measured by distance relays installed at CIREPP substations. The relay malfunctions led to delayed or no-trip decisions during zone one faults, together with instantaneous tripping or failure to provide back-up protection for faults on subsequent lines. Once the scenarios resulting in maloperation of protection systems had been pinpointed, simple yet effective solutions were devised to modify the operation of the two line end relays.

- For distribution systems, this research work included the topics listed below.

1. *Impact of DFIG-based wind DGs on directional relays*: Directional relays are indispensable components of DG-equipped distribution grids. The conditions in which the existing relays fail to determine the fault direction correctly were detected, and the root causes for their failure were identified. Modifications were proposed to rectify directional relay maloperations.

2. *Protection of distribution systems in the context of smart microgrids*: The new trends adopted by distribution utilities and relay manufacturers in North America were presented to corroborate how improved reliability has heightened the need for selective phase tripping and, thus, fault type classification in smart microgrids. However, the available literature on microgrid protection has ignored selective phase tripping. Meanwhile, it was revealed that fault behavior of photovoltaic and Type IV wind DGs prevents the existing relays from accurate fault type classification. Two new classifiers developed in this study are immune to the fault characteristics of RE-based DGs and can therefore be applied in microgrid protection systems, as well as any other three-phase system.

7.2 Contributions

The contributions fall roughly into two categories: the diagnosis of previously unknown relay failures and the proposal of solutions to address these problems.

7.2.1 Diagnosis of Relay Failures

The followings are among the failures of the existing protection systems in the presence of the RE-based sources that this dissertation has identified.

1. Based on the constant flux linkage theorem, an SCIG operates as a voltage source immediately after a balanced fault. After a few cycles, however, the SCIG generates some active power but absorbs reactive power, as the reactive power generated by the PF correction capacitors of an SCIG-based WF falls sharply due to the substantial voltage drop. For a distance relay at the WF substation, the positive active and negative reactive powers of an SCIG are translated into impedances situated in the fourth quadrant of the complex plane, not along the line replica impedance. In its way towards the fourth quadrant, the impedance measured during a fault on a subsequent line passes through zone one of the relay, causing immediate spurious tripping, whereas only back-up protection is required.
2. The fault current expression of DFIGs is similar to that of SCIGs once the crowbar circuit is activated to ride through balanced faults. In this expression, the frequency of the ac component is related to the machine slip, which is commensurate with the wind speed. As a result, the fault current frequency ranges between 42 Hz to 78 Hz for 60 Hz systems. Meanwhile, the frequency of fault voltage is dictated by the grid and equal to the nominal frequency. In addition, the polarizing quantity of commercial distance relays is mainly comprised of the memorized voltage, whose frequency is also closely tied with the nominal frequency. Different current and voltage frequencies make the phasor-based relations on which distance protection is founded fail to calculate a meaningful impedance, regardless of the relay's frequency tracking approach. Hence,

the measurements obtained from a distance relay at the substation of a DFIG-based WF are chaotic and unreliable.

3. Despite the received wisdom within the protective relaying community, a Thevenin equivalent circuit does not suffice to model CIREPPs. For solid lines, the relay at a CIREPP substation can measure the impedance to the fault correctly. In the presence of fault resistance, however, the CIREPP regains control over the fault current angle and attempts to satisfy the host system GC. For EU-GCs, the domination of the reactive component of the fault current during balanced faults results in impedances located along the reactance axis. For NA-GCs, conversely, the measured impedance approaches the resistance axis due to the high PF requirement. For both cases, the relay measurement can be utterly remote from the actual impedance between the relay and the fault location. Furthermore, the current saturation limit of the CIREPP's control system is among the internal CIREPP parameters that impact the measured impedance considerably.

   The phase difference between the two line end currents in the event of zone one faults in conventional systems is similar to that between the two end pre-fault voltages. Moreover, this phase difference is normally small, as large values endanger stability. As a result, for distance relays in a conventional system,

   a) the level of overreach and underreach caused by the remote infeed is typically insignificant, and
   b) using pre-fault voltage angles, it is easy to predict whether the relay overreaches or underreaches, and by how much.

   The above premises and neither of the subsequent conclusions hold true when CIREPPs are involved. The angle of the local fault current for the relay at the CIREPP substation is determined by the control system and may be radically different from the angle of the remote end current. Therefore, the term added by the fault resistance effect to the impedance measured by a phase distance element is most likely to include a large imaginary component, leading to incorrect fault reactance calculation and delayed tripping or no-trip decisions during zone one faults. This problem is exacerbated by the limited amplitude of CIREPP fault currents. For SLG faults, on the other hand, the ground distance elements in the CIREPP substation consistently underreach, even though they are located at the power sending end of the line.

4. For a relay at a CIREPP substation, the odds are that the angles of the local and intermediate infeed currents differ enormously. Consequently, intermediate infeed may unexpectedly result in relay overreach for NA-GCs, while it is known to cause relay underreach in conventional systems. For EU-GCs, on the other hand, the substantial difference between the magnitude of the intermediate infeed current and the limited CIREPP current can make the relay underreach so excessive that zone two of the CIREPP relay may overlap with zones two and three of the relays on subsequent buses, jeopardizing the selectivity of the protection system.

5. Commercial directional relays currently determine the fault direction by comparing the angle between the fault current and a polarizing quantity, which is normally a fault or memorized voltage. Meanwhile, the frequency of balanced DFIG fault currents can significantly deviate from the nominal frequency. The conventional elements fail to identify the fault direction in distribution systems that include DFIG-based DGs, as it is impossible to measure the angle between two phasors that correspond to different frequencies.

6. The following two groups of fault type classification approaches that are currently deployed by transmission system relays can also be applied at the distribution level.

    a) Approaches that are built upon the angle difference between sequence currents,
    b) Approaches that rely on the phase and sequence current magnitude.

    A PVDG converter operates as a current source that suppresses the negative sequence current during asymmetrical faults using voltage feed-forward compensation in its control loops. Moreover, the angle of the PVDG's positive sequence current is regulated such that the target PF is achieved. Therefore, the angle of the sequence currents cannot select the faulted phase(s) correctly in microgrids that include PVDGs.

    The magnitudes of PVDG phase currents depend on the angle between the converter-generated positive sequence current and the zero-sequence current that flows through the ground of the PVDG transformer. This angle is affected by the PVDG's PF. As a result, the current of the unfaulted phase may exceed fault currents. Hence, the methods that are founded upon the phase currents' magnitudes fail to identify the faulted phase(s) in microgrids with PVDGs. The non-zero sequence portion of phase currents is not able to classify faults either, as the only non-zero sequence term of PVDG currents is the positive sequence component.

7.2.2 Proposal of Solutions

This dissertation has presented the following solutions for the above-discussed relay failures.

1. IG balanced fault currents were discriminated from the bulk grid fault currents by inspecting the current waveshape properties. The relay at the substation of the IG-based WF determined the fault direction by comparing the two initial consecutive peak-to-peak values of the current. Accurate fault direction identification by the two line end relays along with a modified POTT scheme with minimal bandwidth requirement was used to distinguish between the faults on the line connected to an IG-based WF and the WF internal faults and the faults on subsequent lines. The result was fast non-delayed protection over the entire line length. Successful performance of this solution was observed particularly for DFIG-based WFs with non-zero crowbar resistance, which is the most probable scenario in practice.

2. By adding the KVL relations of the two faulted phases during LLG faults, a new formula was developed to measure the impedance by phase distance elements. This formula includes the zero sequence current of the two line ends in the numerator and denominator of the factor multiplied with the fault resistance. Since the zero sequence current is not affected by the CIREPP's control system, the angles of the numerator and the denominator are similar, and the fictitious impedance added by the fault resistance is mainly along the R axis, leaving the measured reactance largely unaffected. For the relay at the CIREPP substation, the proposed element underreaches, which is the preferred behavior for zone one faults, as it does not affect the relay security. In addition, the amount of underreach is very small.

Furthermore, the term added by the intermediate infeed to the impedance calculated using this new formula is almost a real number. As a result, the effect of intermediate infeed on the measured impedance is always the expected underreach. Moreover, the presence of the zero sequence component in the denominator of the term added due to the intermediate infeed effect keeps this term relatively small. Thus, the relay at the CIREPP substation can be coordinated with subsequent relays without violating the protection system selectivity.

3. A new directional relaying scheme for LL and balanced faults was proposed for the relays that protect the line adjacent to a CIREPP. This new element specifies fault direction based on the phase current magnitudes together with the impedance measured by a conventional distance element. New zones inside the impedance plane are defined to distinguish between forward and reverse faults. The line is protected by means of a pilot scheme, such as directional comparison blocking or POTT, equipped with two of these directional elements. The same strategy can be applied to protect the line during SLG and LLG faults if the HV winding of the CIREPP's transformer is not grounded.

4. The direction of the reactance element tilting for a conventional quadrilateral distance characteristic, used to address the effect of fault resistance during SLG faults, should be counterclockwise. The tilting angle is determined based on the angle of the zero-sequence compensation factor of the protected line.

5. The decline rate of the fundamental frequency phasor of fault currents was proposed to detect the balanced fault direction in distribution systems with DFIG-based wind DG. Even though the ac component of DFIG fault currents exhibits a decaying nature, the digital filters that assume constant amplitude for the current were shown to provide more reliable and less noisy phasors. The currents that have the decaying property of DFIG-based DGs are the ones flowing toward a fault located between the relay and the substation, that is, the reverse direction. Other current waveshapes indicate forward faults.

6. During solid AG faults, the positive sequence voltage is 180° out of phase from the in-phase negative and zero sequence voltages calculated with respect to phase A. The-

oretical and simulation analysis verified that the negative and zero sequence voltages advance in phase almost equally in the presence of fault resistance; meanwhile, this phase shift exhibits a saturation-like relationship with R_f. Similar relations hold true over other SLG faults if the sequence voltages are computed with respect to the faulted phase. During a bolted BCG fault, the three sequence voltages remain in-phase. The fault resistance makes the zero sequence voltage advance in phase, while the angles of the other sequence voltages remain almost intact. Similar relations are obtained during other types of LLG fault if the sequence voltages are measured with respect to the unfaulted phase.

On this basis, two fault classifiers using the sequence and phase voltages were introduced. The angle and magnitude-based classifier defines three zones for the phase difference between the zero and negative sequence voltages. Each zone corresponds to one SLG and one LLG fault that include opposing phases, and can thus be differentiated using the phase voltage magnitudes. The angle-based classifier defines six zones for the phase difference between the positive and negative sequence voltages besides the already defined zones for the phase difference between the negative and zero sequence voltages. Each pair of these zones is related to only one fault type. These techniques are immune to high-impedance faults and specify the fault type correctly in microgrids with PVDGs during both the grid-connected and isolated modes of operation, as well as in highly unbalanced systems.

7.3 Future Work

Further research on the protection of RE systems may include the topics listed below.

1. Protection of microgrids using communication-assisted techniques,
2. Effect of REPPs on line current differential relays,
3. Operation of wide area protection systems in the presence of REPPs.

APPENDICES

Appendix A

Description of the Test System in Chapter 2

The details of the 69 kV, 60 Hz test power system shown in Figure 2.1 are as follows. The line constants along with the source parameters are as follows.

Lines: $Z_{l1} = 0.3621\measuredangle 84.4^\circ\ \Omega/\text{km}$, $Z_{l0} = 1.6130\measuredangle 72.9^\circ\ \Omega/\text{km}$,

Sources: $Z_{S3} = 24.7\measuredangle 89^\circ\ \Omega$, $Z_{S4} = 6.4\measuredangle 89^\circ\ \Omega$

Either an SCIG-based or a DFIG-based WF, whose specifications are given below, is connected to bus 1.

A.1 SCIG-Based WF

The SCIG-based WF consists of ten wind turbines. The collector system includes two parallel paths, each having five wind turbines that are 0.5 km apart. The collector system is comprised of underground cables with the following impedances, taken from [51].

$R = 3.51 \times 10^{-5}\ \Omega/\text{m}$, $X = 2.804 \times 10^{-5}\ \Omega/\text{m}$.

The specifications of the SCIGs are

IG rating: $S_n = 2.5$ MVA, $V_n = 0.480$ kV, $R_s = 0.010$ pu, $R_r = 0.0053$ pu, $X_m = 4$ pu, $X_s = 0.106$ pu, $X_r = 0.12$ pu.

PF correction capacitor: $C = 4.5$ μF.

Transformer for each turbine: 2.6 MVA, 0.480/34.5 kV, ygD.

WF main transformer: 27.5 MVA, 34.5/34.5/69 kV, ygdYG.

A.2 DFIG-Based WF

The DFIG-based WF is comprised of eight wind turbines with the following specifications.

IG rating: $S_n = 1.5$ MVA, $V_n = 0.575$ kV, $R_s = 0.0071$ pu, $R_r = 0.005$ pu, $X_m = 2.9$ pu, $X_s = 0.1714$ pu, $X_r = 0.1563$ pu.

DC-link rated voltage and capacitor: $V_{dc} = 1200$ V, $C = 2$ mF.

Transformer for each turbine: 1.6 MVA, 0.575/34.5 kV, ygD.

WF main transformer: 13 MVA, 34.5/34.5/69 kV, ygdYG.

The collector system is similar to that of the SCIG-based WF, with the exception that each of the two paths includes four wind turbines.

The control system for the DFIG converters as well as the wind turbine specifications and control loops are based on the industrial models of [82].

Appendix B

List of Publications

The following is a list of publications by the author during doctoral studies.

[1] A. Hooshyar, M. Azzouz, and E. F. El-Saadany, “Distance protection of lines connected to induction generator-based wind farms during balanced faults,” *IEEE Trans. Sustain. Energy*, vol. 5, no. 4, pp. 1193–1203, Oct. 2014.

[2] A. Hooshyar, M. Azzouz, and E. F. El-Saadany, “Distance protection of lines emanating from full-scale converter-interfaced renewable energy power plants—Part I: Problem statement,” *IEEE Trans. Power Del.*, Accepted for publication.

[3] A. Hooshyar, M. Azzouz, and E. F. El-Saadany, “Distance protection of lines emanating from full-scale converter-interfaced renewable energy power plants—Part II: Solution description and evaluation,” *IEEE Trans. Power Del.*, Accepted for publication.

[4] A. Hooshyar, M. Azzouz, and E. F. El-Saadany, “Three-phase fault direction identification for distribution systems with DFIG-based wind DG,” *IEEE Trans. Sustain. Energy*, vol. 5, no. 3, pp. 747–756, Jul. 2014.

[5] A. Hooshyar, M. Azzouz, and E. F. El-Saadany, “Addressing IEC flickermeter deficiencies by digital filtration inside a sliding window,” *IEEE Trans. Instrum. Meas.*, vol. 62, no. 9, pp. 2476–2491, Aug. 2013.

[6] A. Hooshyar and E. F. El-Saadany, “Development of a flickermeter to measure non-incandescent lamps flicker” *IEEE Trans. Power Del.*, vol. 28, no. 4, pp. 2103–2115, Oct. 2013.

References

[1] M. Hossain, T. Saha, N. Mithulananthan, and H. Pota, “Control strategies for augmenting LVRT capability of DFIGs in interconnected power systems,” *IEEE Trans. Ind. Electron.*, vol. 60, no. 6, pp. 2510–2522, Jun. 2013.

[2] J. L. Blackburn and T. J. Domin, *Protective Relaying: Principles and Applications*, 3rd ed. Boca Raton, FL, USA: CRC Press, 2006, ch. 8.

[3] M. Tsili and S. Papathanassiou, “A review of grid code technical requirements for wind farms,” *IET Renew. Power Gen.*, vol. 3, no. 3, pp. 308–332, Sep. 2009.

[4] “Implementation guideline for network code: Requirements for grid connection applicable to all generators,” European Network of Transmission System Operators for Electricity (ENTSO-E), Brussels, Belgium, Oct. 2013. [Online]. Available: http://networkcodes.entsoe.eu/wp-content/uploads/2013/08/131016-NC-RfG-implementation-guideline.pdf (Accessed on: 2014-11-01)

[5] A. Morales, X. Robe, M. Sala, P. Prats, C. Aguerri, and E. Torres, “Advanced grid requirements for the integration of wind farms into the Spanish transmission system,” *IET Renew. Power Gen.*, vol. 2, no. 1, pp. 47–59, Mar. 2008.

[6] J. Morren and S. de Haan, “Ridethrough of wind turbines with doubly-fed induction generator during a voltage dip,” *IEEE Trans. Energy Convers.*, vol. 20, no. 2, pp. 435–441, Jun. 2005.

[7] K. Okedu, S. Muyeen, R. Takahashi, and J. Tamura, "Wind farms fault ride through using DFIG with new protection scheme," *IEEE Trans. Sustain. Energy*, vol. 3, no. 2, pp. 242–254, Apr. 2012.

[8] S. Xiao, G. Yang, H. Zhou, and H. Geng, "An LVRT control strategy based on flux linkage tracking for DFIG-based WECS," *IEEE Trans. Ind. Electron.*, vol. 60, no. 7, pp. 2820–2832, Jul. 2013.

[9] J. Yang, J. Fletcher, and J. O'Reilly, "A series-dynamic-resistor-based converter protection scheme for doubly-fed induction generator during various fault conditions," *IEEE Trans. Energy Convers.*, vol. 25, no. 2, pp. 422–432, Jun. 2010.

[10] M. Bollen and F. Hassan, "Protection," in *Integration of Distributed Generation in the Power System*, 1st ed. Hoboken, NJ, USA: Wiley-IEEE Press, 2011, ch. 7, pp. 299–366.

[11] W. Najy, H. Zeineldin, and W. Woon, "Optimal protection coordination for microgrids with grid-connected and islanded capability," *IEEE Trans. Ind. Electron.*, vol. 60, no. 4, pp. 1668–1677, Apr. 2013.

[12] H. Wan, K. Li, and K. Wong, "An adaptive multiagent approach to protection relay coordination with distributed generators in industrial power distribution system," *IEEE Trans. Ind. Appl.*, vol. 46, no. 5, pp. 2118–2124, Sep. 2010.

[13] T. Sulawa, Z. Zabar, D. Czarkowski, Y. TenAmi, L. Birenbaum, and S. Lee, "Evaluation of a 3ϕ bolted short-circuit on distribution networks having induction generators at customer sites," *IEEE Trans. Power Del.*, vol. 22, no. 3, pp. 1965–1971, Jul. 2007.

[14] "Renewables 2014 – Global status report," Renewable Energy Policy Network for the 21st Century, Paris, Apr. 2014. [Online]. Available: http://www.ren21.net/portals/0/documents/resources/gsr/2014/gsr2014_full%20report_low%20res.pdf (Accessed on: 2014-11-01)

[15] R. Parkes, "Can the UK meet its renewables targets?" *Renewable Energy Focus*, vol. 13, no. 1, pp. 24–27, Jan.–Feb. 2012.

[16] M. Ni and Z. Yang, “By leaps and bounds: Lessons learned from renewable energy growth in China,” *IEEE Power Energy Mag.*, vol. 10, no. 2, pp. 37–43, Mar. 2012.

[17] A. Pradhan and G. Joos, “Adaptive distance relay setting for lines connecting wind farms,” *IEEE Trans. Energy Convers.*, vol. 22, no. 1, pp. 206–213, Mar. 2007.

[18] L. He, C.-C. Liu, A. Pitto, and D. Cirio, “Distance protection of AC grid with HVDC-connected offshore wind generators,” *IEEE Trans. Power Del.*, vol. 29, no. 2, pp. 493–501, Apr. 2014.

[19] H. Yazdanpanahi, Y. W. Li, and W. Xu, “A new control strategy to mitigate the impact of inverter-based DGs on protection system,” *IEEE Trans. Smart Grid*, vol. 3, no. 3, pp. 1427–1436, Sep. 2012.

[20] “Ordinance on system services by wind energy plants (System service ordinance SDLWindV),” Jun. 2010. [Online]. Available: http://www.bmub.bund.de/fileadmin/bmu-import/files/english/pdf/application/pdf/sdl_windv_en.pdf (Accessed on: 2014-11-01)

[21] K. Corfee *et al.*, “Distributed generation in Europe – Network planning and operational impacts – Memorandum #2,” KEMA, Inc., Oakland, CA, USA, Apr. 2011. [Online]. Available: http://www.energy.ca.gov/2011_energypolicy/documents/2011-05-09_workshop/documents/Memo%202%20DG%20Network%20Planning%20and%20Operational%20Impacts.pdf (Accessed on: 2014-11-01)

[22] S. H. Horowitz and A. G. Phadke, *Power System Relaying*, 3rd ed. New York, NY: Wiley, 2008, ch. 4–5.

[23] A. D. Hansen, “Generators and power electronics for wind turbines,” in *Wind Power in Power Systems*, 2nd ed., T. Ackermann, Ed. Hoboken, NJ, USA: Wiley, 2012, ch. 5, pp. 73–104.

[24] C. Wessels, N. Hoffmann, M. Molinas, and F. Fuchs, “StatCom control at wind farms with fixed-speed induction generators under asymmetrical grid faults,” *IEEE Trans. Ind. Electron.*, vol. 60, no. 7, pp. 2864–2873, Jul. 2013.

[25] M. Slepchenkov, K. Smedley, and J. Wen, "Hexagram-converter-based STATCOM for voltage support in fixed-speed wind turbine generation systems," *IEEE Trans. Ind. Electron.*, vol. 58, no. 4, pp. 1120–1131, Apr. 2011.

[26] J. Carrasco, L. Franquelo, J. Bialasiewicz, E. Galvan, R. Guisado, M. Prats, J. Leon, and N. Moreno-Alfonso, "Power-electronic systems for the grid integration of renewable energy sources: A survey," *IEEE Trans. Ind. Electron.*, vol. 53, no. 4, pp. 1002–1016, Jun. 2006.

[27] J. Morren and S. W. H. De Haan, "Short-circuit current of wind turbines with doubly fed induction generator," *IEEE Trans. Energy Convers.*, vol. 22, no. 1, pp. 174–180, Mar. 2007.

[28] E. Muljadi, N. Samaan, V. Gevorgian, J. Li, and S. Pasupulati, "Different factors affecting short circuit behavior of a wind power plant," *IEEE Trans. Ind. Appl.*, vol. 49, no. 1, pp. 284–292, Jan. 2013.

[29] N. D. Tleis, *Power Systems Modelling and Fault Analysis.* Oxford, U.K.: Newnes, 2008, ch. 5.

[30] R. E. Doherty and C. A. Nickle, "Three-phase short circuit synchronous machines-V," *Trans. AIEE*, vol. 49, no. 2, pp. 700–714, Apr. 1930.

[31] C. B. Cooper, D. MacLean, and K. Williams, "Application of test results to the calculation of short-circuit levels in large industrial systems with concentrated induction-motor loads," *Proc. Inst. Electr. Eng.*, vol. 116, no. 11, pp. 1900–1906, Nov. 1969.

[32] M. S. Sachdev *et al.*, "Understanding microprocessor-based technology applied to relaying," Report of Working Group I-01 of the Relaying Practices Subcommittee, IEEE Power System Relaying Committee, Jan. 2009. [Online]. Available: http://www.pes-psrc.org/Reports/UNTAR-Ed2.pdf (Accessed on: 2014-11-01)

[33] R. Cardenas, R. Pena, S. Alepuz, and G. Asher, "Overview of control systems for the operation of DFIGs in wind energy applications," *IEEE Trans. Ind. Electron.*, vol. 60, no. 7, pp. 2776–2798, Jul. 2013.

[34] D. Campos-Gaona, E. Moreno-Goytia, and O. Anaya-Lara, "Fault ride-through improvement of DFIG-WT by integrating a two-degrees-of-freedom internal model control," *IEEE Trans. Ind. Electron.*, vol. 60, no. 3, pp. 1133–1145, Mar. 2013.

[35] D. Hart, Y. Hu, D. Novosel, and R. Smith, "System and method for phasor estimation and frequency tracking in digital protection systems," U.S. Patent 5 721 689, Feb. 24, 1995.

[36] *Instruction Manual for SEL-321-3,-4: Phase and Ground Distance Relay*, Schweitzer Engineering Laboratories (SEL), Pullman, Washington, USA, 2012, Date Code 20120127. [Online]. Available: www.selinc.com/SEL-321/ (Accessed on: 2014-11-01)

[37] *Application Manual for ABB Transformer Protection Terminal RET 521*2.5*, ABB, Vasteras, Sweden, 2003, Version 2.5, DocID: 1MRK 504 037-UEN. [Online]. Available: http://www05.abb.com/global/scot/scot354.nsf/veritydisplay/72557c65acb0b97dc12578570041dc1b/$file/1mrk504037-uen_en_application_manual_transformer_protection_terminal_ret_521_2.5.pdf (Accessed on: 2014-11-01)

[38] *IEEE Guide for Protective Relay Applications to Transmission Lines*, IEEE Std. C37.113-1999, 1999.

[39] *Instruction Manual for SEL-411L Advanced Line Differential Protection, Automation, and Control System*, Schweitzer Engineering Laboratories (SEL), Pullman, Washington, USA, 2012, Date Code 20121005. [Online]. Available: https://www.selinc.com/SEL-411L/ (Accessed on: 2014-11-01)

[40] J. Pan, K. Vu, and Y. Hu, "An efficient compensation algorithm for current transformer saturation effects," *IEEE Trans. Power Del.*, vol. 19, no. 4, pp. 1623–1628, Oct. 2004.

[41] P. M. Anderson, *Analysis of Faulted Power Systems*, IEEE Reissued ed. Hoboken, NJ, USA: Wiley-IEEE Press, 1995, ch. 6.

[42] J. D. Glover, M. S. Sarma, and T. J. Overbye, *Power System Analysis and Design*, 4th ed. Toronto, Canada: Thomson Learning, 2008, ch. 7.

[43] A. Kasem, E. El-Saadany, H. El-Tamaly, and M. Wahab, "An improved fault ride-through strategy for doubly fed induction generator-based wind turbines," *IET Renew. Power Gen.*, vol. 2, no. 4, pp. 201–214, Dec. 2008.

[44] N. Flourentzou, V. Agelidis, and G. Demetriades, "VSC-based HVDC power transmission systems: An overview," *IEEE Trans. Power Electron.*, vol. 24, no. 3, pp. 592–602, Mar. 2009.

[45] J. Rocabert, A. Luna, F. Blaabjerg, and P. Rodriguez, "Control of power converters in AC microgrids," *IEEE Trans. Power Electron.*, vol. 27, no. 11, pp. 4734–4749, Nov. 2012.

[46] "ENTSO-E network code for requirements for grid connection applicable to all generators," European Network of Transmission System Operators for Electricity (ENTSO-E), Brussels, Belgium, Mar. 2013. [Online]. Available: http://networkcodes.entsoe.eu/wp-content/uploads/2013/08/130308_Final_Version_NC_RfG1.pdf (Accessed on: 2014-11-01)

[47] "Procedure for verification validation and certification of the requirements of the PO 12.3 on the response of wind farms and photovoltaic plants in the event of voltage dips," May 2011, Version 9. [Online]. Available: http://www.aeeolica.org/uploads/documents/1306-pvvc-n9-english.pdf (Accessed on: 2014-11-01)

[48] "Interconnection for wind energy," United States of America Federal Energy Regulatory Commission, Dec. 2005, Docket No. RM05-4-001, Order No. 661-A. [Online]. Available: www.ferc.gov/EventCalendar/Files/20051212171744-RM05-4-001.pdf (Accessed on: 2014-11-01)

[49] M. P. LeBlanc, L. Evans, P. Gardner, and N. C. Scott, "Canadian grid code for wind development – Review and recommendations," Canadian Wind Energy Association, Oct. 2005. [Online]. Available: www.nrcan.gc.ca/energy/publications/sciences-technology/renewable/smart-grid/6081 (Accessed on: 2014-11-01)

[50] "ENTSO-E draft network code on high voltage direct current connections and DC-connected power park modules," European Network of Transmission

System Operators for Electricity (ENTSO-E), Brussels, Belgium, Nov. 2013. [Online]. Available: www.entsoe.eu/fileadmin/user_upload/_library/resources/HVDC/131107-NC_HVDC_-_for_public_consultation.pdf (Accessed on: 2014-11-01)

[51] E. Muljadi, S. Pasupulati, A. Ellis, and D. Kosterov, "Method of equivalencing for a large wind power plant with multiple turbine representation," in *Proc. IEEE Power Energy Soc. Gen. Meet.*, Pittsburgh, PA, USA, Jul. 2008, pp. 1–9.

[52] J. Brochu, C. Larose, and R. Gagnon, "Validation of single- and multiple-machine equivalents for modeling wind power plants," *IEEE Trans. Energy Convers.*, vol. 26, no. 2, pp. 532–541, Jun. 2011.

[53] A. Timbus, M. Liserre, R. Teodorescu, P. Rodriguez, and F. Blaabjerg, "Evaluation of current controllers for distributed power generation systems," *IEEE Trans. Power Electron.*, vol. 24, no. 3, pp. 654–664, Mar. 2009.

[54] S. Li and T. A. Haskew, "Converter control of variable-speed wind turbines," U.S. Patent 8 577 508 B2, Nov. 5, 2013.

[55] P. Rodriguez, R. Teodorescu, I. Candela, A. Timbus, M. Liserre, and F. Blaabjerg, "New positive-sequence voltage detector for grid synchronization of power converters under faulty grid conditions," in *Proc. IEEE 37th Power Electronics Specialists Conf.*, Jun. 2006, pp. 1–7.

[56] J. Conroy and R. Watson, "Low-voltage ride-through of a full converter wind turbine with permanent magnet generator," *IET Renew. Power Gen.*, vol. 1, no. 3, pp. 182–189, Sep. 2007.

[57] *Hardware manual for PVS800-MWS megawatt stations*, ABB, Switzerland, Nov. 2012. [Online]. Available: www05.abb.com/global/scot/scot232.nsf/veritydisplay/afc6e27d5ba8be86c1257b94002ba837/$file/EN_PVS800_MWS_HW%20manual_B.pdf (Accessed on: 2014-11-01)

[58] M. Asmine, J. Brochu, J. Fortmann, R. Gagnon, Y. Kazachkov, C.-E. Langlois, C. Larose, E. Muljadi, J. MacDowell, P. Pourbeik, S. Seman, and K. Wiens, "Model

validation for wind turbine generator models," *IEEE Trans. Power Syst.*, vol. 26, no. 3, pp. 1769–1782, Aug. 2011.

[59] A. Yazdani and R. Iravani, *Voltage-Sourced Converters in Power Systems: Modeling, Ccontrol, and Applications*. Hoboken, NJ, USA: Wiley-IEEE Press, 2010, p. 370.

[60] M. Kazmierkowski and L. Malesani, "Current control techniques for three-phase voltage-source PWM converters: A survey," *IEEE Trans. Ind. Electron.*, vol. 45, no. 5, pp. 691–703, Oct. 1998.

[61] *Line distance protection REL670 application manual*, ABB, Vasteras, Sweden, Dec. 2012, Doc. ID: 1MRK 506 315-UEN, Revsion: C. [Online]. Available: www05.abb.com/global/scot/scot387.nsf/veritydisplay/1d6bacf573307830c1257b0c0046292a/$file/1MRK506315-UEN_C_en_Application_manual__REL670_1.2.pdf (Accessed on: 2014-11-01)

[62] D90$^{\text{Plus}}$ *line distance protection system*, General Electric (GE), Markham, Canada, Mar. 2012, GE publication code: GEK-113240B. [Online]. Available: www.gedigitalenergy.com/products/manuals/d90plus/gek-113240b.pdf (Accessed on: 2014-11-01)

[63] E. O. Schweitzer, "Computationally-efficient distance relay for power transmission lines," U.S. Patent 5 325 061, Jun. 28, 1994.

[64] G. Ziegler, *Numerical Distance Protection: Principles and Applications*, 4th ed. Erlangen, Germany: Publicis Publishing, 2011, ch. 3.

[65] W. A. Elmore, *Protective Relaying: Theory and Applications*, 2nd ed. New York, NY, USA: Marcel Dekker Inc., 2004, p. 260.

[66] *Network Protection & Automation Guide – Protective Relays, Measurement & Control*, 2nd ed. Stafford, UK: Alstom Grid Publication, 2011, ch. 11, pp. 17–18.

[67] K. Zimmerman and D. Costello, "A practical approach to line current differential testing," 2013. [Online]. Available: https://www.selinc.com/workarea/downloadasset.aspx?id=21474837050 (Accessed on: 2014-11-01)

[68] C. R. Mason, *Art and Science of Protective Relaying*, 1st ed. New York, NY: Wiley, 1956, ch. 14.

[69] *Technical manual: MiCOMho P446 – Distance relay*, Alstom, Stafford, UK, 2011, Alstom Publication Reference: P446/EN/TM/E. [Online]. Available: ftp://ftp.alstom.com/Alstom_Manuals/P446_EN_TM_E.pdf (Accessed on: 2014-11-01)

[70] *Manual: SIPROTEC, Distance Protection, 7SA522*, Siemens, Germany, Sep. 2013, Version 4.7. [Online]. Available: http://w3.siemens.com/smartgrid/global/en/products-systems-solutions/protection/distance-protection/pages/7sa522.aspx (Accessed on: 2014-11-01)

[71] J. Holbach, V. Vadlamani, , and Y. Lu, "Issues and solutions in setting a quadrilateral distance characteristic," in *Proc. of 61st Annual Conf. for Protec. Relay Eng.*, College Station, Texas, USA, Apr. 2008, pp. 89–104.

[72] "Application of overreaching distance relays," Report by Line Protection Subcommittee, IEEE Power System Relaying Committee, 2009. [Online]. Available: www.pes-psrc.org/Reports/D4_Application_of_Overreaching_Distance%20_Relays.pdf (Accessed on: 2014-11-01)

[73] J. Roberts, A. Guzman, and E. O. Schweitzer, "$Z = V/I$ does not make a distance relay," in *20th Annual Western Protec. Relay Conf.*, Spokane, Washington, USA, Oct. 1993.

[74] D. Costello and K. Zimmerman, "Determining the faulted phase," in *63rd Annual Conf. for Protec. Relay Eng.*, Texas, USA, Mar. 2010.

[75] R. van de Sandt, J. Lowen, J. Paetzold, and I. Erlich, "Neutral earthing in off-shore wind farm grids," in *IEEE PowerTech Conf.*, Bucharest, Romania, Jun. 2009, pp. 1–8.

[76] C. Feltes, R. van de Sandt, F. Koch, F. Shewarega, and I. Erlich, "Neutral grounding in wind farm medium voltage collector grids," in *IEEE/PES Power Systems Conf. and Expos.*, Phoenix, Arizona, USA, Mar. 2011, pp. 1–7.

[77] "Electric transmission specifications and drawings – 115 kV through 230 kV," United States Department of Agriculture, Apr. 1998. [Online]. Available: www.rurdev.usda.gov/supportdocuments/uep_bulletin_1728f-811.pdf (Accessed on: 2014-11-01)

[78] T. Abdel-Galil, A. Abu-Elanien, E. El-Saadany, A. Girgis, Y. Mohamed, M. Salama, and H. Zeineldin, "Protection coordination planning with distributed generation," National Resources Canada, Jun. 2007. [Online]. Available: http://www.nrcan.gc.ca/sites/www.nrcan.gc.ca/files/canmetenergy/files/pubs/2007-149e.pdf (Accessed on: 2014-11-01)

[79] *Instruction Manual for GRE140 Directional Overcurrent Protection Relay*, Toshiba, Japan, 2012, Version 2.1. [Online]. Available: http://www.toshiba-tds.com/tandd/pdf/pcsystems/Manual/6F2T0177_r2.1_GRE140_manual.pdf (Accessed on: 2014-11-01)

[80] *Complete Technical Manual for 7SG11 Argus 1-6 Overcurrent Protection Relay*, Siemens, Erlangen, Germany, Apr. 2013. [Online]. Available: https://w3.siemens.com/smartgrid/global/en/products-systems-solutions/Protection/overcurrent-feeder-protection/Pages/7SG111-7SG116.aspx (Accessed on: 2014-11-01)

[81] D.-G. Lee, S.-H. Kang, and S.-R. Nam, "Modified dynamic phasor estimation algorithm for the transient signals of distributed generators," *IEEE Trans. Smart Grid*, vol. 4, no. 1, pp. 419–424, Mar. 2013.

[82] K. Clark, N. W. Miller, and J. J. Sanchez-Gasca, "Modeling of GE wind turbine-generators for grid studies," General Electric (GE), Apr. 2010, Version 4.5. [Online]. Available: http://www.creps.com.cn/web973/images_1/2012082054141805.pdf (Accessed on: 2014-11-01)

[83] A. Oudalov, T. Degner, F. Overbeeke, and J. Yarza, "Microgrid protection," in *Microgrids: Architectures and Control*, 1st ed., N. Hatziargyriou, Ed. West Sussex, United Kingdom: Wiley-IEEE Press, 2014, ch. 4, pp. 117–164.

[84] E. Sortomme, S. S. Venkata, and J. Mitra, “Microgrid protection using communication-assisted digital relays,” *IEEE Trans. Power Del.*, vol. 25, no. 4, pp. 2789–2796, Oct. 2010.

[85] H. Zeineldin, Y.-R. Mohamed, V. Khadkikar, and V. Pandi, “A protection coordination index for evaluating distributed generation impacts on protection for meshed distribution systems,” *IEEE Trans. Smart Grid*, vol. 4, no. 3, pp. 1523–1532, Sep. 2013.

[86] L. Che, M. Khodayar, and M. Shahidehpour, “Adaptive protection system for microgrids: Protection practices of a functional microgrid system,” *IEEE Electrific. Mag.*, vol. 2, no. 1, pp. 66–80, Mar. 2014.

[87] E. Casagrande, W. Woon, H. Zeineldin, and D. Svetinovic, “A differential sequence component protection scheme for microgrids with inverter-based distributed generators,” *IEEE Trans. Smart Grid*, vol. 5, no. 1, pp. 29–37, Jan. 2014.

[88] I. Xyngi and M. Popov, “An intelligent algorithm for the protection of smart power systems,” *IEEE Trans. Smart Grid*, vol. 4, no. 3, pp. 1541–1548, Sep. 2013.

[89] M. Zamani, A. Yazdani, and T. Sidhu, “A communication-assisted protection strategy for inverter-based medium-voltage microgrids,” *IEEE Trans. Smart Grid*, vol. 3, no. 4, pp. 2088–2099, Dec. 2012.

[90] J. Aguero, J. Wang, and J. Burke, “Improving the reliability of power distribution systems through single-phase tripping,” in *IEEE PES Transm. and Distrib. Conf. and Expo.*, New Orleans, USA, Apr. 2010, pp. 1–7.

[91] G. Hataway and R. Moxley, “Distribution single-phase tripping and reclosing,” *Protection, Automation and Control World*, pp. 28–33, Spring 2009.

[92] T. Fahey and N. Burbure, “Single-phase tripping,” *IEEE Power Energy Mag.*, vol. 6, no. 2, pp. 46–52, Mar. 2008.

[93] R. Cheney, J. Thorne, and G. Hataway, “Distribution single-phase tripping and reclosing: Overcoming obstacles with programmable recloser controls,” in *Proc. of*

62nd Annual Conf. for Protec. Relay Eng., Austin, Texas, USA, Mar. 2009, pp. 214–223.

[94] M. Hori, Y. Saita, and M. Inukai, “Short-circuit distance relay,” U.S. Patent 2011/0 149 448 A1, Jun. 23, 2011.

[95] B. Kasztenny, B. Campbell, and J. Mazereeuw, “Phase selection for single-pole tripping: Weak infeed conditions and cross-country faults,” in *27th Annual Western Protec. Relay Conf.*, Spokane, Washington, USA, Oct. 2000.

[96] J. Roberts and E. Schweitzer, “Fault identification system for use in protective relays for power transmission lines,” U.S. Patent 5 515 227, May 7, 1996.

[97] M. Mynam and Y. Gong, “Fault-type identification for electric power delivery systems,” U.S. Patent 2013/0 088 239 A1, Apr. 11, 2013.

[98] L. Yang, “Fault type classification algorithm,” U.S. Patent 5 783 946, Jul. 21, 1998.

[99] S. Valsan and K. Swarup, “High-speed fault classification in power lines: Theory and FPGA-based implementation,” *IEEE Trans. Ind. Electron.*, vol. 56, no. 5, pp. 1793–1800, May 2009.

[100] A. Jamehbozorg and S. Shahrtash, “A decision-tree-based method for fault classification in single-circuit transmission lines,” *IEEE Trans. Power Del.*, vol. 25, no. 4, pp. 2190–2196, Oct. 2010.

[101] L. Zhang, M. Li, T. Ji, Q. Wu, L. Jiang, and J. Zhan, “Morphology singular entropy-based phase selector using short data window for transmission lines,” *IEEE Trans. Power Del.*, vol. 29, no. 5, pp. 2162–2171, Oct. 2014.

[102] B. Mahamedi and J. G. Zhu, “Fault classification and faulted phase selection based on the symmetrical components of reactive power for single-circuit transmission lines,” *IEEE Trans. Power Del.*, vol. 28, no. 4, pp. 2326–2332, Oct. 2013.

[103] J.-A. Jiang, C.-L. Chuang, Y.-C. Wang, C.-H. Hung, J.-Y. Wang, C.-H. Lee, and Y.-T. Hsiao, “A hybrid framework for fault detection, classification, and location—Part

I: Concept, structure, and methodology," *IEEE Trans. Power Del.*, vol. 26, no. 3, pp. 1988–1998, Jul. 2011.

[104] T. Adu, "An accurate fault classification technique for power system monitoring devices," *IEEE Trans. Power Del.*, vol. 17, no. 3, pp. 684–690, Jul. 2002.

[105] S. Ekles, "Detecting high-impedance faults," Utility Automation and Electric Light and Power El-Paso Electric Company, 2008. [Online]. Available: http://www.elp.com/articles/powergrid_international/print/volume-13/issue-10/features/detecting-high-impedance-faults.html (Accessed on: 2014-11-01)

[106] P. Maezono, E. Altman, K. Brito, V. Alves dos Santos Mello Maria, and F. Magrin, "Very high-resistance fault on a 525 kV transmission line – Case study," in *Proc. of 62nd Annual Conf. for Protec. Relay Eng.*, Austin, Texas, USA, Mar. 2009, pp. 322–332.

[107] *IEEE Recommended Practice for Monitoring Electric Power Quality*, IEEE Std. 1159-2009, 2009.

[108] A. Borghetti, C. Nucci, M. Paolone, G. Ciappi, and A. Solari, "Synchronized phasors monitoring during the islanding maneuver of an active distribution network," *IEEE Trans. Smart Grid*, vol. 2, no. 1, pp. 82–91, Mar. 2011.

[109] D. Petri, D. Fontanelli, and D. Macii, "A frequency-domain algorithm for dynamic synchrophasor and frequency estimation," *IEEE Trans. Instrum. Meas.*, vol. 63, no. 10, pp. 2330–2340, Oct. 2014.